Seismic assessment of a detached masonry building using non-linear analyses

Adarsha Kadaba Srinivasan

Master of Science Thesis

Delft University of Technology

Civil Engineering and Geo-Sciences

Seismic assessment of a detached masonry building using non-linear analyses

MASTER OF SCIENCE THESIS

For the degree of Master of Science in Civil Engineering, Track - Structural Engineering at Delft University of Technology

Adarsha Kadaba Srinivasan

August 21, 2017

Faculty of Civil Engineering and Geo-Sciences (CiTG) · Delft University of Technology

DELFT UNIVERSITY OF TECHNOLOGY
DEPARTMENT OF
CIVIL ENGINEERING AND GEO-SCIENCES (CITG)

The undersigned hereby certify that they have read and recommend to the Faculty of Civil Engineering and Geo-Sciences (CiTG) for acceptance a thesis entitled

SEISMIC ASSESSMENT OF A DETACHED MASONRY BUILDING USING NON-LINEAR ANALYSES

by

ADARSHA KADABA SRINIVASAN

in partial fulfillment of the requirements for the degree of

MASTER OF SCIENCE CIVIL ENGINEERING, TRACK - STRUCTURAL ENGINEERING

Dated: August 21, 2017

Supervisor(s):

Prof. Dr. Ir. J.G.Rots

Dr. Ir. M.A.N.Hendriks

Dr. Ir. P.C.J.Hoogenboom

Dr. Ir. G.J.P. Ravenshorst

Dr. V. Mariani

Abstract

Masonry is one of the oldest and popular building materials used world over. The constituent materials are readily available and hence are cheap in most areas. So it serves as an economically viable building material. Though, its load bearing capacity under compression is high, it does not perform well under tensile forces, cyclic and lateral loads.

In the Netherlands, specifically around the Groningen area, where natural gas is being extracted from the 1960*s*, masonry structures are currently prone to artificial seismic excitation due to excessive gas extraction and the resulting soil liquefaction. Such residential buildings having stood there for about a 100 years are being affected by these seismic vibrations and have developed cracks which can prove detrimental to both life and property if unchecked.

To this end, Nederlandse Aardolie Matschappij (NAM) has spearheaded a research group along with TUDelft, ARUP and others to get a thorough insight into the strength and durability aspects of these existing buildings. Since there are different configurations and types of structures, it has been divided into several typologies. Further research, using shake table tests, has also been taken up at the TUDelft Stevin lab using these different typologies and/or scaled models.

This project deals with the study of type *T3a* detached type villa, which is asymmetric in plan. This structure consists of clay brick masonry walls and timber floors and beams. Effectively, the current thesis project is a blind prediction on the strength and behaviour aspects of this particular structure. For the same, the structure is modelled and analysed using Finite Element application DIANA 9.6.

Firstly, modelling of the structure is done according to macro-modelling technique with smeared cracking. Shell elements are used for walls and floors, and beam elements for timber beams. It is noted here that all the non-linearities have been focused only on the masonry part. Linear static checks and Eigenvalue checks are carried out. The time-history record was provided by the supervisor.

Variational studies were performed on the structure to check their influence on the seismic resistance. These variations are - model without roof and with the roof part, the latter modelled under fair assumptions. Different type of beam end connections, seismic excitation along different directions of the structure were also included. Finally, as a check, monotonic mass-proportional pushover analyses were conducted.

The results show that the given input signal at $0.16g$ scaling is not able to inflict serious damage, hence higher scaling is used. It is observed that the seismic resistance of the structure is higher along the X-direction of the structure than in Y-direction. Influence of beam ends on the seismic resistance is not significant. However, coupling between floors has been observed, by comparing their displacements at multiple time instants. The presence of roof part has a significant influence on the (box) behaviour of the structure, due to increase in overburden load. The pushover curves validate the time-history analyses by forming an envelope over the hysteresis curves from the latter.

All the beams are provided along the X-direction of the structure, which provides significant stiffness to out-of-plane walls (X-direction excitation). It is also interesting to find that the same wall ($IP1$) undergoes maximum cracking for analyses along either X or Y directions. The pushover curves are in agreement with the hysteresis curves from time-history analyses which proves the validity of the results.

Acknowledgements

I'd like to humbly thank the support of my committee members in helping me throughout this project with their time and invaluable guidance, specially **Prof. Rots** for providing me with the opportunity. I'd like to specially thank **Dr. Max** for all the help, clinical supervision, and for inspiring me throughout the length of the project. I express my gratitude to **Dr. Pierre** for all the help in the project. I'm grateful to **Dr. Geert** for being a part of my thesis committee and supporting my work. Also, I thank **Dr. Valentina** for her timely advice and guidance. Lastly, I shall forever remain indebted to **TUDelft** for everything I have learnt in my years of study here.

“To my biggest inspirations - Gurus, Appa, Amma, Poovi, all my teachers and every one of my friends.”

— *Adarsha*

Table of Contents

List of Figures

List of Tables

Chapter 1

Introduction

1-1 An Introduction to Masonry

Masonry is one of the oldest building materials in the world. It has been used by ancient civilizations in various forms and configurations, some of which can be seen even to this day. They have been used to build structures ranging through arches, bridges, temples, cathedrals, dams, dikes, pyramids, gardens, houses, cottages and more. With the advancement of technology, masonry construction has only improved for the better. Such widespread application of masonry implies its worthiness and durability as a good building material since long ago.

Masonry construction is carried out by laying individual units and binding them using a fluid mortar. Based on the different types of individual units used, masonry can be widely differentiated into Adobe, Stone, Brick, Cement Block or Reinforced. Generally used materials for mortar are mud, lime, clay, cement etc.

1-2 Context of Present study

In the Netherlands, burnt brick masonry structures are a common sight. Masonry has been used since long for the construction of dikes, churches, dams, royal palaces and residential buildings among others. The thesis topic is based out of the current scenario in and around the North-eastern Groningen area in the Netherlands, where the locals are experiencing dangerous "triggered" quakes as a consequence of extensive natural gas exploitation.

During the 1960s, a giant natural gas field was discovered in the Groningen area of the Netherlands and since then natural gas extraction is being carried out. It has become a lucrative project and contributes heavily to the national economy. The Dutch government has reaped an estimated €250bn from the sale of this natural resource. In 2012 alone, the Dutch government made about €14bn(£12bn; $18bn) from the Groningen gas fields. [17].

This gas field is being operated by *Nederlandse Aardolie Maatchappij* (NAM). As an effect of long-term extraction, the soil is under subsidence, the result of which are shallow tremors originating at depths of $3km$. It is also important to take note that the seismic activity has accelerated in recent times. The Groningen area has experienced numerous tremors measuring upto 3.6 on the Richter Scale, from 1986 to 1997. However, studies estimate that an earthquake, of the magnitude 6.5 on Richter scale, with a 0.65 probability of exceedance could occur in the next 10 years, whereas the estimated intensity is VI-VII on the European Macroseismic Scale [18]. Due to these tremors, walls of a few old houses have undergone cracking (small and detrimental) and this might prove life-threatening for the local population.

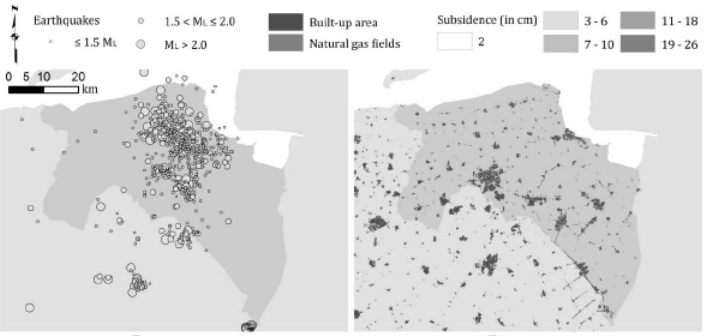

A. EARTHQUAKES B. BUILT-UP AREA

C. NATURAL GAS FIELDS D. SOIL SUBSIDENCE IN 2008

Figure 1-1: Subsidence of Soil due to Gas Extraction adapted from [19]

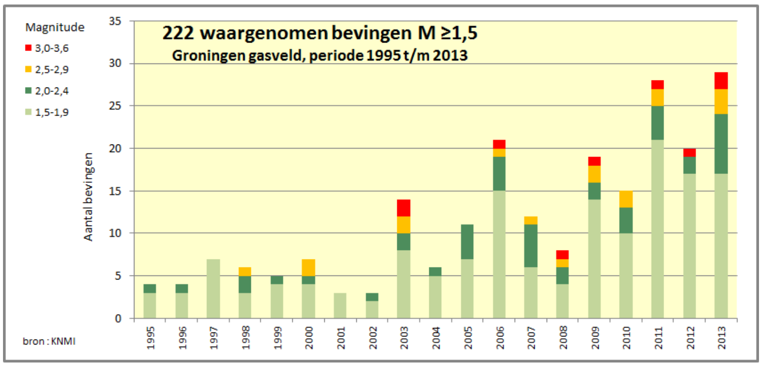

Figure 1-2: Increase in number of quakes [20]

In this regard, NAM has created a research consortium with EUCENTRE, ARUP, TUDelft to carry out an in-depth study to analyse the current situation and provide most efficient

solutions at the earliest. This involves studying the current state of the existing houses and their response towards seismic forces, ground motion studies etc. Since most of the houses are old, retrofitting these structures will improve their seismic resistance.
To this end, TU Delft's Stevin Lab is carrying out shake table analyses. It requires a physical model to be tested using an appropriate test setup. This involves building of the real-size or scaled models of walls and performing analyses on them. Comparatively, numerical modelling is advantageous as it is quick and requires lesser resources. Moreover, it also provides accurate results in comparison to the real behaviour, given the structure is modelled to mimic the real structure closely. Numerical modelling is a popular choice due to this reason.

1-3 Scope of study

Understanding the current state of the structures is important to provide efficient, cost-effective and long-term solutions. To this end, numerical modelling has proved effective owing to its accuracy to predict the real behaviour. However, shake table tests are regarded the most accurate since it involves analyses on models (full size or scaled) built using physical constituent materials. The objective of the thesis is to model the detached masonry house and study its seismic behaviour as accurately as possible using the Finite Element Application called DIANA developed by TNO-DIANA.
This study examines the effects of application of seismic forces on a detached villa built using unreinforced burnt brick masonry. The primary goals of the project are as follows-

1. Prepare an accurate finite element model of the detached villa (or type 3A typology).
2. Perform seismic assessment of structure based on uni-directional non-linear time history analyses using the corresponding real time earthquake data.
3. Study the structural behaviour using variational studies
    - Uni-directional non-linear time-history analyses with earthquake signal along each of the X and Y directions, using base excitation.
    - Use multiple levels of scaling of input signal to analyse the level of damage.
    - Study the influence of beam end connections on the seismic response of the structure.
    - Influence of the roof on the seismic response (without and with roof part)
    - Comparative validation of time-history analyses using monotonic mass proportional pushover analyses.

It is a humble hope that this thesis contributes to the bigger goal of computationally estimating the capacity of the Groningen masonry buildings under seismic loads in the current state.

1-4 Outline of the project

This MSc. thesis is divided into five chapters with the following subjects:

Chapter 1: The current chapter serves a bird's eye view of the entire project. It offers a brief summary of the work taken up in the subsequent chapters.

Chapter 2: This chapter investigates the past experimental and other research work in the area relating to masonry. It details the general aspects and behaviour of unreinforced masonry, connections used in masonry. It also describes the material modelling, load characteristics and computational strategies available to accurately and efficiently model the structure and simulate the dynamic response of the structure. Modelling approaches for the study including constitutive models and other finite element options associated are discussed. It also elaborates on the numerical modelling of the current structure used for subsequent analyses

Chapter 3 This chapter deals with the general description of the structure used in this study.

Chapter 4 This chapter presents the model along with characteristic properties, loading cases and initial checks to validate the working of the model in the linear elastic regime and the specific choices made for the non-linear analyses.

Chapter 5 This chapter depicts the main results of this thesis, relating to the non-linear time history analyses and the variational studies carried out along with it. It also deals with the non-linear uni-directional pushover analyses carried out on the model.

Chapter 6 The final chapter describes the results, conclusions drawn from this project and recommendations for future work on the same.

Chapter 2

Literature Study

The goal of this part of the thesis is to provide insight into existing literature on Masonry, modelling of Masonry including connections. Firstly, the general use of masonry in buildings and some general configurations of burnt brick masonry have been described.

2-1 Unreinforced Masonry

Masonry is one of the oldest building materials being used to-date. It is built by placing the masonry units adjacent to each other or atop one other and binding them with mortar. This process is carried out in layers. Masonry has appreciable resistance under compression and suitable for bearing gravity loads. When subjected to lateral loads like wind or seismic loads, the resistance is comparatively low. This is due to low tensile strength of masonry and its quasi-brittle nature. This might lead to sudden collapse particularly in the case of seismic loads. This led to the use of steel reinforcements and other fibre-reinforced polymers in Masonry (called *R*einforced Masonry) to improve the tensile strength of Masonry and in-turn the mechanical behaviour of masonry in response to lateral loads.
However, the aim of the thesis is to contribute to the research program that focuses on the unreinforced burnt clay brick masonry buildings in Groningen, and hence the study is restricted to unreinforced brick masonry, which is referred to as "Masonry" from here on.

A typical unreinforced masonry (URM) wall consists of the following parts- Bricks/Units, Joints- Vertical Head joints and Horizontal Bed joints and brick-mortar interface. Bed joints are continuous throughout the width of the wall, whereas bricks act as discontinuities along head joints. This explains the difference in effective behaviour of masonry in vertical and horizontal directions which is called *Orthotropy*

Depending on the stacking of bricks, different bond patterns are in common practice- Stack bond, American (or Common) bond, Stretcher (or Running) bond which is quite common

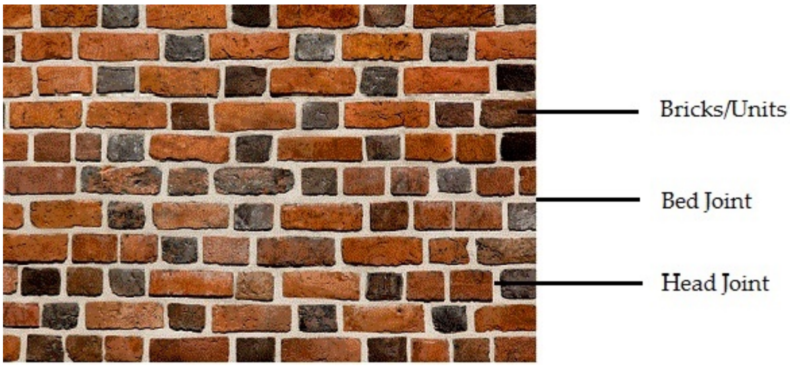

Figure 2-1: Parts of Masonry Wall (with Flemish Bond)

in the Netherlands. The following figure shows the different parts of masonry and types of bond patterns.

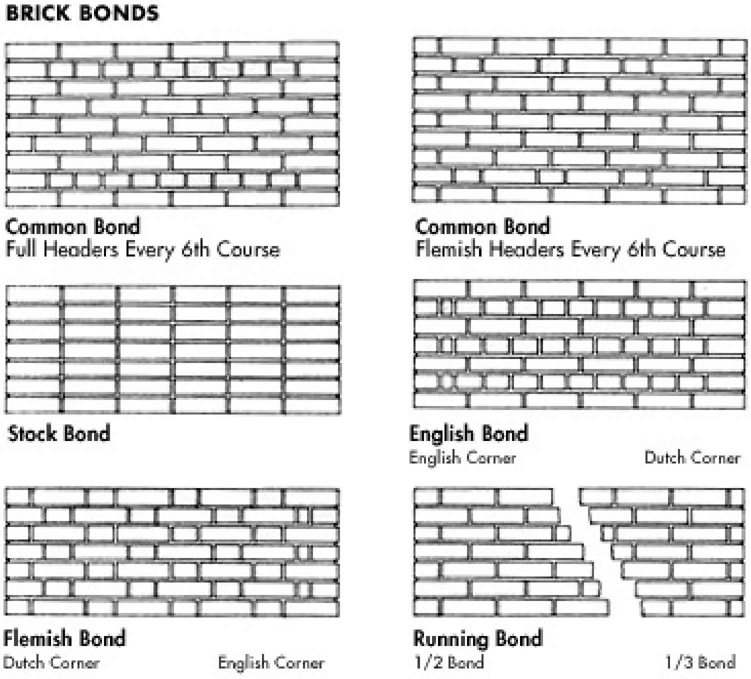

Figure 2-2: Types of Bond in Masonry

2-2 Material properties and Behaviour

General behaviour of both masonry and mortar are similar. Both perform sufficiently well under compression but behave like a "quasi-brittle" material- displays a cracking point followed by exponential softening. Under compression, initial crushing is observed which is followed by strain hardening after which parabolic softening occurs. However, they can model to suit the requirements of the model and the materials used. For this reason, constitutive models are employed to generate stress-strain relationships.

2-2-1 Constitutive models

Constitutive models or equations spell the relationship between two physical quantities in any system for a given set of conditions, in this case stress and strain states of masonry material in linear and non-linear regimes. Examples of such models are Hooke's law for linear materials, plasticity model for non-linear materials, Boltzmann equation for transport phenomena, etc. This is a very material specific property. Similarly, the behaviour of masonry under different conditions are discussed further in chapter 3.

2-2-2 Behaviour under tensile forces

Masonry behaves very similar to concrete in tension. In a tensile test of a quasi-brittle material like concrete, masonry-units or mortar-joints is controlled beyond the maximum load and the constitutive relation is obtained, which help us in modelling masonry under tension/flexure. Quasi-brittle behaviour is referred to a situation where the transferred force does not immediately drop back to zero, but gradually decreases. This kind of behaviour is often described by the term "softening". The initial behaviour prior to maximum loading is predominantly linear. The post peak behaviour is more important to understand the ultimate failure of the structure. There are several approaches to describe the constitutive relation / softening behaviour like linear, multi-linear and non-linear softening, exponential as shown in Figure 2-3 [11]. The parameters G_f, h, σ_{nn}, ϵ_{nn}^{cr} and f_t refer to the fracture energy in tension, the crack bandwidth, the stress sigma, the ultimate crack strain and the tensile strength of the material.

2-2-3 Behaviour under compressive forces

Under compression, masonry exhibits hardening behaviour after initial crushing followed by a parabolic softening. This softening relation is used depending upon the availability of parameters for behaviour in compression. In the absence of adequate parameters, an elastic or Ideal behaviour (with only the compressive strength) can be used safely. The material models for compression are shown in Figure 2-4. The parameters G_c, h and f_c refer to the fracture energy in compression, the crack bandwidth and the compressive strength of the material respectively. The mortar-brick interface is the weakest part and a typical failure is the stepped diagonal cracking pattern as described in 2-3. Anthoine(1992)[21] has described the uni-axial compression stress strain curve for masonry. See figure 2-5

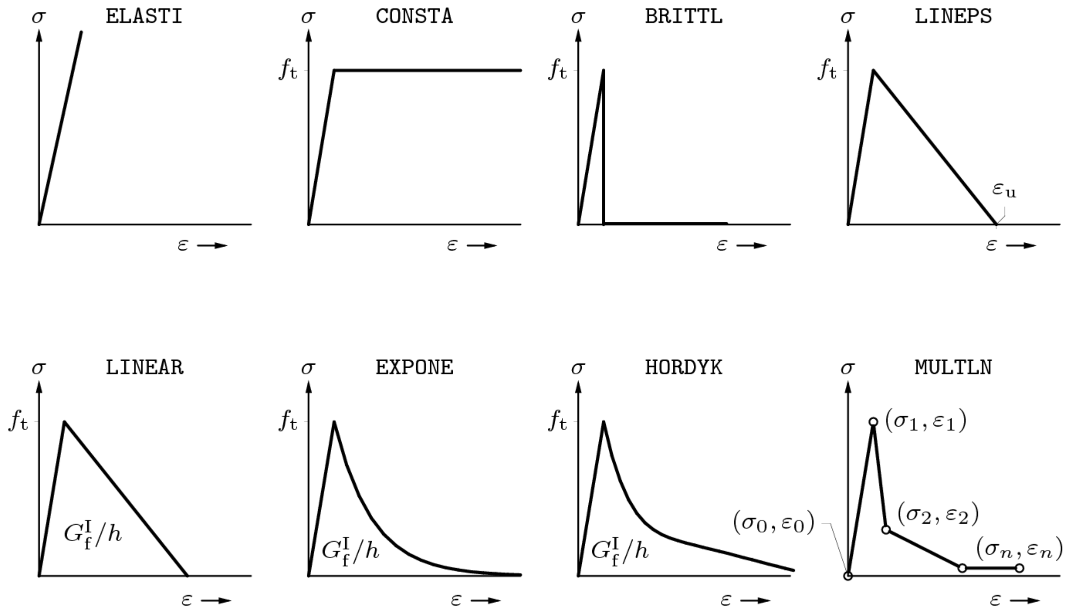

Figure 2-3: Material models in Tension including post peak behaviour

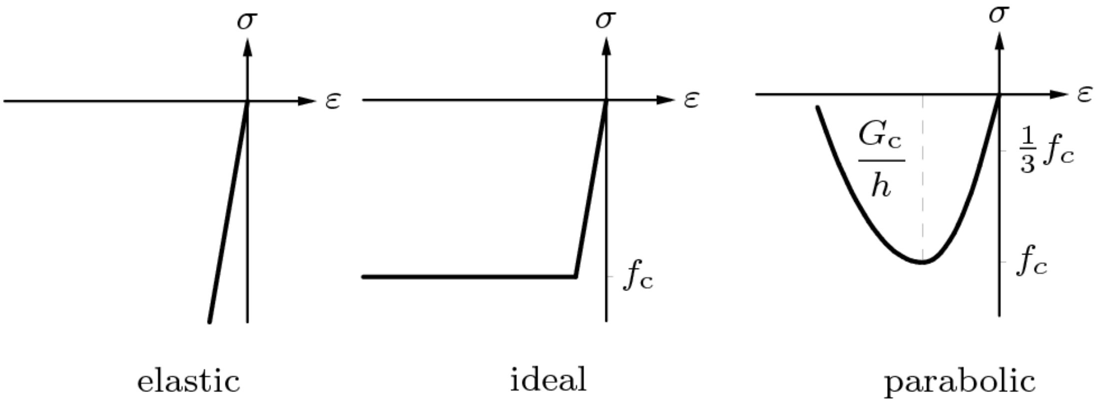

Figure 2-4: Material models in Compression

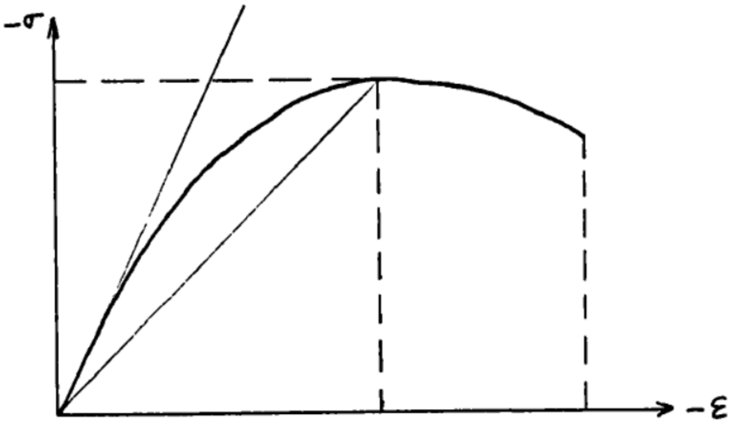

Figure 2-5: Stress-strain curve for masonry under uni-axial vertical Compression

2-3 Behaviour under Lateral Loads

Masonry structures have to be designed for lateral forces like wind and seismic actions apart from the general vertical loading due to overburden, dead and live loads. Quite a lot of research has been conducted to study about the behaviour of masonry walls under cyclic, seismic and lateral loads. Under seismic or earthquake loading, it is not easy to determine the direction of the loading since these loads are stochastic in nature. In reality, complex deformation occurs in all three directions. In a masonry building subjected to earthquake loads, the walls, floor and roof systems which transfer lateral loads to the lateral load resisting system develop horizontal inertial forces due to earthquakes which is proportional to their structural mass and acceleration at that height. Depending on how the horizontal load is applied to a masonry structure, two types of behaviour is observed generally. They are *In-plane loading* and *Out-of-plane loading*.

However, it is almost impossible to subject a real structure to a real earthquake or wind load i.e. perform a true test to study its real behaviour. This is impractical. Hence, to understand the behaviour of masonry walls, simplicity is sought by experimentally testing a single wall or a scaled model of the complete structure under different conditions. With the advancement in computer technology, it has become much more easy to simulate and study these structures, with prior knowledge of numerical methods. In as early as 1930, masonry specimens were tested experimentally as an attempt to study its tensile, flexural and shear resistances by Norman Kelch[22]. Priestley[1] and Doherty(2000)[2] have described the seismic energy load path for URM structures as depicted below in figure 2-7 and has also studied both in-plane and out-of-plane seismic response of URM walls.

2-3-1 Experimental studies on In-plane behaviour

When seismic loading is applied parallel to a wall, then it is said to undergo in-plane loading. Such a wall is also called a "Shear Wall". The capacity of a shear wall is derived from high moment of inertia about one of its axis, compressive strength of the brickwork, tensile capacity of masonry through bond strength between brick and mortar, along with

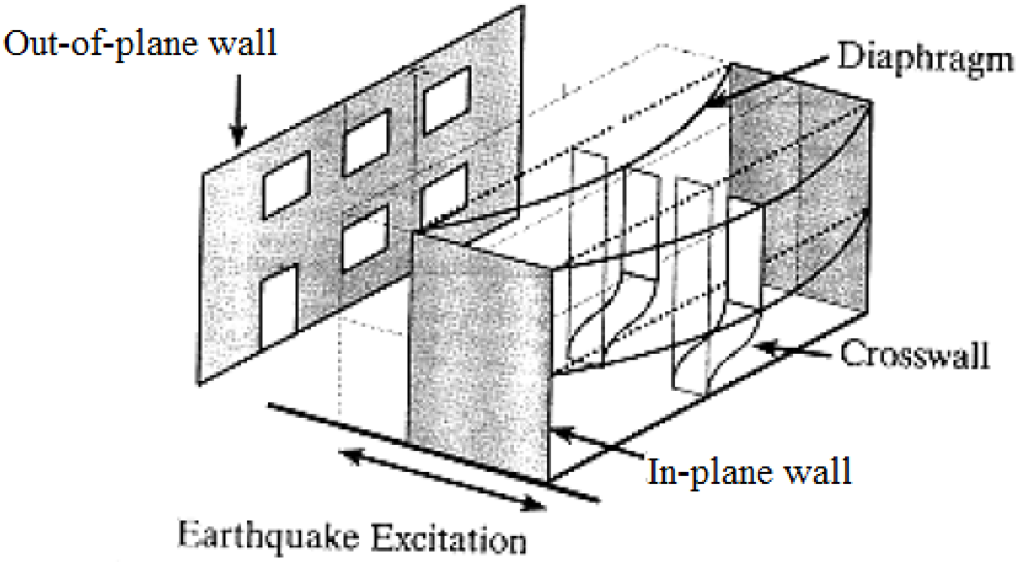

Figure 2-6: Behaviour of the walls due to cyclic random nature of the loading

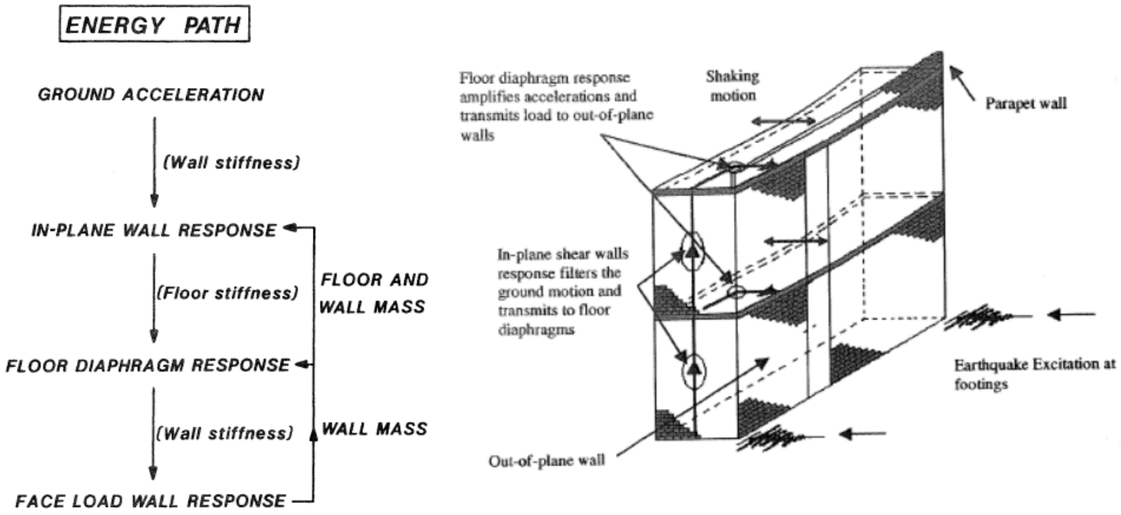

Figure 2-7: Sesimic Energy Path in URM structures (Priestley and Doherty)[1][2]

compressive overburden stresses due to dead load[23]. Lateral loads are mainly carried by the shear walls and hence the importance.

Numerous researchers have developed various methods to study in-plane shear behaviour. Among these are Norman Kelch[22], Benjamin and Williams, Abrams and Shah[24] and Anthoine[21] etc. The differences in each of their testing were with respect to length-height aspect ratio of masonry specimen, vertical overburden compressive stress, reinforcements, boundary conditions of set-up, loading- cyclic, direct loading, dynamic, quasi-static loading etc. Different type of panels with unreinforced, reinforced and pre-stressed masonry was also used. Predominantly, three types of in-plane shear testing could be differentiated as illustrated below.

- Diagonal Compression Loading: This type of testing consists of applying only compressive force at an angle to the bed joints by which masonry is loaded in both compression and shear, also called biaxial compression test.
- Shear-Compression Loading: This type of testing consists of in-plane horizontal loading of masonry wall which is loaded at its bottom and top sides to simulate overburden loads, with bed joints parallel to the horizontal loading direction. Corradi et al.[25] have performed such a test among others.
- Compression Loading: This test consists of applying uniform compressive stresses simulating just the overburden pressure, also called uni-axial compressive test.

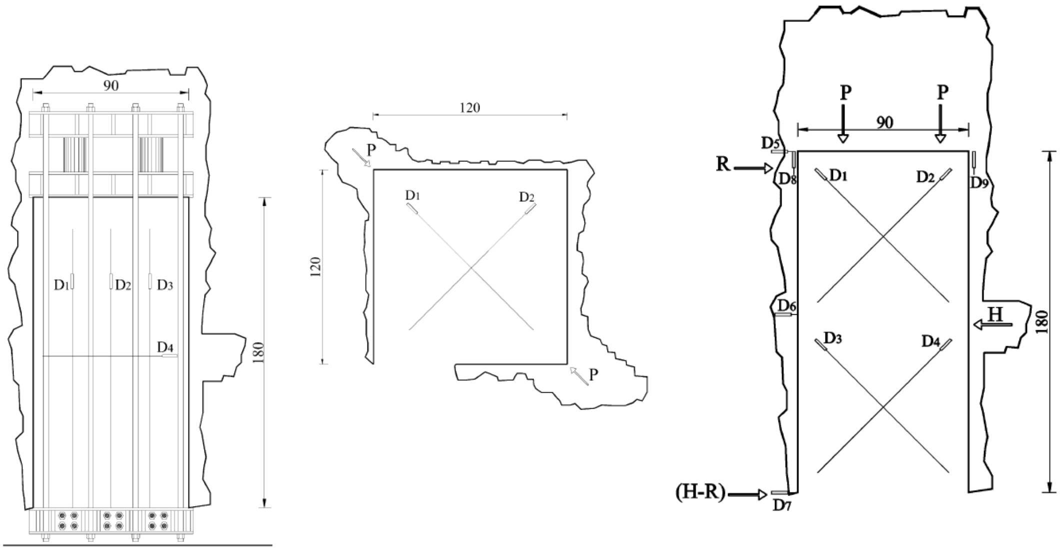

a) b) c)

Figure 2-8: In-plane Shear Tests on Masonry: a)Compression loading, b)Diagonal compression loading, c)Shear-Compression loading, symbols- D: Inductive transducers; P,R,H: Forces.

The in-plane shear strength tests yield commonly observed typical shear failures which are shown below in figure 2-9.

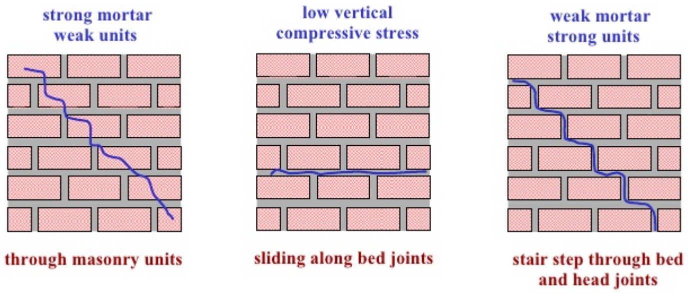

Figure 2-9: Typical in-plane shear wall failures

- Diagonal failure: Also known as shear failure, it is caused either by weak mortar or unit or both. This is associated with low aspect ratios and high axial loads. Cracks go through unit-mortar interface or the unit itself or both as it is a case of biaxial tension compression state. Principal tensile stresses developed in the wall exceeds the tensile strength of masonry.
- Sliding shear failure: This kind of failure occurs when low vertical loads are present. This kind of failure occurs along the bed joint if the mortar is weak. Hence, a part of the wall slides long the bed joint.
- Flexure failure: In the presence of low compressive stresses, after the loss of bond between mortar and brick by tensile failure and owing to the overturning moment due to lateral loads, the section resisting tensile failure displays a "rocking behaviour" and topples and such a failure due to combination of compression and tension is called "toe crushing". Refer figure 2-10.

Another typical pattern seen is the double diagonal cracking, however, flexure and sliding shear failures are more favourable as they are able to withstand gravity loads even after significant energy dissipation, whereas double diagonal results in a brittle collapse often [2].

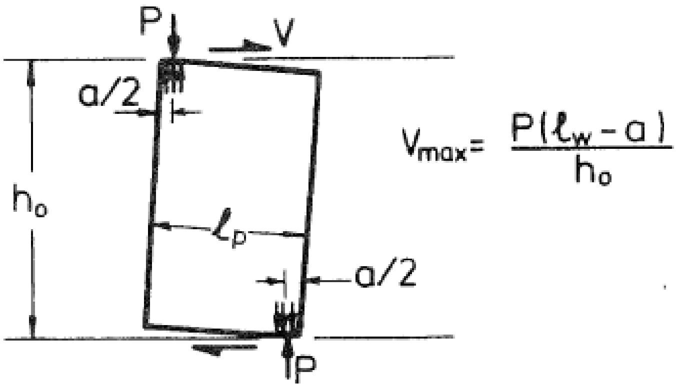

Figure 2-10: Rocking of wall and toe crushing described by Priestley (1985)

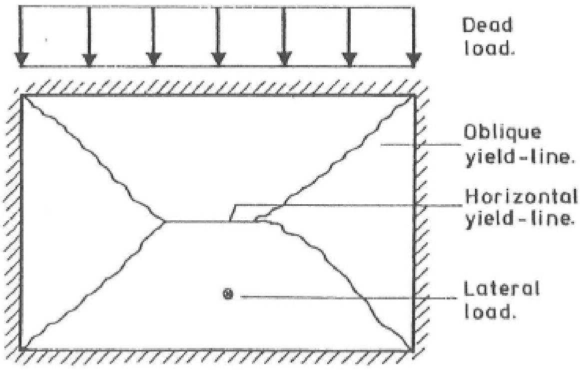

Figure 2-11: Yield lines as described by Brincker(2008)

2-3-2 Experimental studies on Out-of-Plane behavior - Flexure walls

The past research in the field of masonry behaviour has been dominated by the in-plane shear behaviour studies due to the fact that it provides the primary load path for transfer of seismic loads to the foundation. The out-of-plane behaviour is considerably more complex than in-plane behaviour of walls but does not contribute much to the load path. However, the out of plane failure of Masonry walls is critical as it can lead to partial collapse or global collapse if it is a load bearing wall. It has been experimentally studied by various researchers with keen interest in the past like Anderson(1984) [26], Paulay and Priestley(1992) [27], D P Abrams(1996) and have agreed on the out of plane behaviour as a critical one. The presence of flexible diaphragms and the lack of proper connections between walls and/or diaphragm are some of the primary reasons which cause detrimental effects due to out-of-plane bending.

Anderson(1984) studied the arching action of transverse laterally loaded masonry walls and its effects prior to cracking and post cracking and has found that masonry walls, which can bear arch action within the thickness of the wall, can have high resistance in excess of its flexural strength against lateral loading.

Brincker(1984) [28] studied a failure behaviour of URM walls subjected to lateral load (out-of-plane) with overburden pressure (in-plane dead load) of small values. He had proposed to use yield-line theory as a design method for such a structure, stating that masonry is not entirely brittle and that the failure criterion closely matches the Coulomb type. This is shown in figure 2-11.

Priestley (1985) [1] has described the results of face-loading (out-of-plane) and has shown that failure occurs by rocking behaviour of two halves of the wall, if adequate anchoring is provided. He has also proposed a method based on energy equivalence to predict out-of-plane stability of wall. General test set-up is shown in figure 2-12

Meisl et al.(2007) [29] had similar results from shake table tests on unreinforced masonry flexure walls connected at the top by rigid supports. They tested four full scale double-leaf walls, with an uniform aspect ratio of 12, for out-of-plane bending. Variations included construction quality of walls and three different ground motions. They found that connections

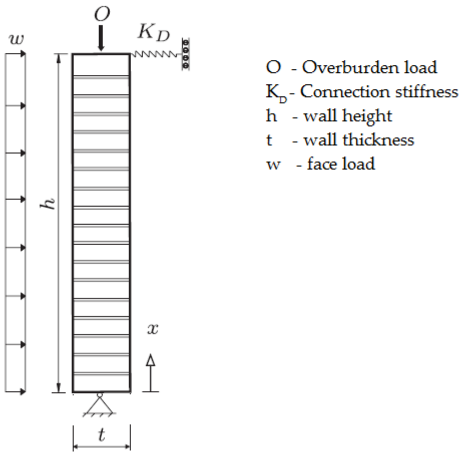

Figure 2-12: General test set-up for Out-of-plane testing adapted from Derakshan et al.(2013)

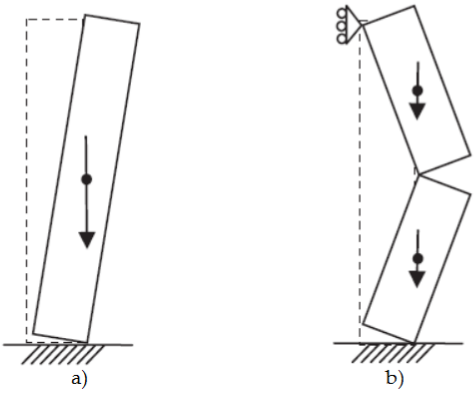
a)

b)

Figure 2-13: Two modes of failure in flexure walls (based on connections)

of the walls play an important role. Accordingly they have described two different failure modes. In the first mode, where there are poor or no connections, the wall behaves like a cantilever beam shown in Figure 2-13a) whereas good connections will allow it to behave like a simple beam where it displays a bending behaviour at approximately mid-height of the section. This is called "Rocking behaviour" shown in Figure 2-13b)

Derakshan et al.(2013) [30] also found similar test results. However, variations on overburden pressure, horizontal crack height and stiffness properties of connections to diaphragms were studied and they found that crack height highly influenced out-of-plane behaviour in terms of displacement and lateral resistance. Also, they have observed that overburden pressure greatly reduces lateral resistance of the cracked wall and displacement due to instability.

2-4 Behaviour under Cyclic and Dynamic Loads

Apart from the static and dynamic in-plane and out-of-plane tests, a variety of other tests have been performed and the results studied. A few of the reviewed test types are discussed below.
Benedetti et al.(1980)[31] compared a static model of a masonry structure to a non-linear dynamic numerical model and proposed that the latter provides a good margin of safety over the former case. They insist that the out-of-plane ductility and resistance may be the critical for the wall.
Tomazevic(1987)[32] performed shake table tests on scaled masonry structures by simulating N-S acceleration spectrum of 1940 El Centro earthquake by using hydraulic actuators. Though not completely successful, he compared the dynamic behaviour to analytical methods by assuming lumped mass multi degree of freedom representation and found adequate closeness. He also suggests the inclusion of stiffness-degrading hysteresis rules to calculate dynamic response in non-linear regime. In 1994 Tomazevic et al. repeated the study with masonry structures, this time reinforced with horizontal and vertical reinforcement applied to bed joints and borders of the wall respectively, to find that coupled shear-wall mechanism was critical, as opposed to storey mechanism in the former case.
Again in 1996, Tomazevic et al.[3] studied seismic behaviour of reinforced URM walls, this time varying the load input by imposing monotonic, cyclic and simulated earthquake loads on the load actuators. This is shown in figure 2-14. In this study, the difference between the cyclic loads is that in case 1, amplitude increases step-wise in pre-defined blocks, repeated three times at each amplitude peak, whereas in case 2 amplitudes are increasing step-wise, repeated three times at each peak but with decrease in amplitude between two consecutive blocks. He has observed that dynamic analyses offers higher lateral resistance and rigid initial behaviour than that of static analyses. However, he also notes that monotonic loading offers higher resistance and larger ultimate displacements than by loading cyclically.

AlShebani et al.(2001) conducted uni-axial cyclic loading test on half-scale URM panels, with loading parallel to, and normal to the bed joint respectively. They performed monotonic uni-axial loading to derive the envelope stress-strain curve and cyclic uni-axial loading to obtain hysteresis behaviour. In cyclic tests, two cases were studied, the latter of which had reloading and unloading were repeated many times in a single cycle. Refer figure 2-15.
Griffith et al.(2007)[33] have studied cyclic testing of URM walls in two-way bending using airbags, Derakshan et al.(2013)[34]

The reviews of many researchers reveal that monotonic/static and cyclic tests, being simple and inexpensive, are mostly performed to understand fairly the behaviour of masonry. However, to study the real seismic resistance of a masonry structure, it is advised to use shake table tests and/or dynamic tests[35]. For these tests scaled or full size models can be set up. These tests reveal much more accurate seismic behaviour. Nevertheless, these tests require expensive set-up and skilled technicians. To make it simpler, but to have more control over the dynamic tests, Paqutte et al.[36] used a pseudo-dynamic method. This method is described by Mahin et al.[37] as very similar to conventional quasi-static tests with the only difference that an on-line computer imposes the displacements. The response is measured from the test specimen whose inertia and damping properties are prescribed.

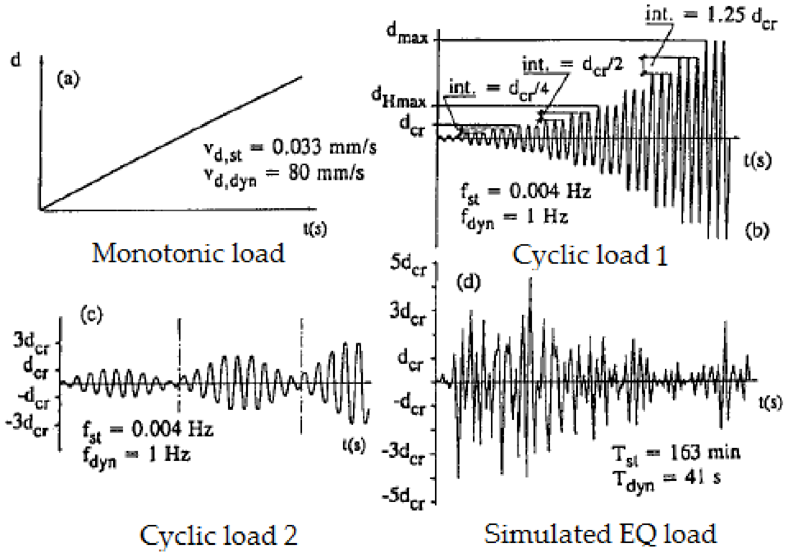

Figure 2-14: Test inputs used to simulate seismic loading (adapted from [3])

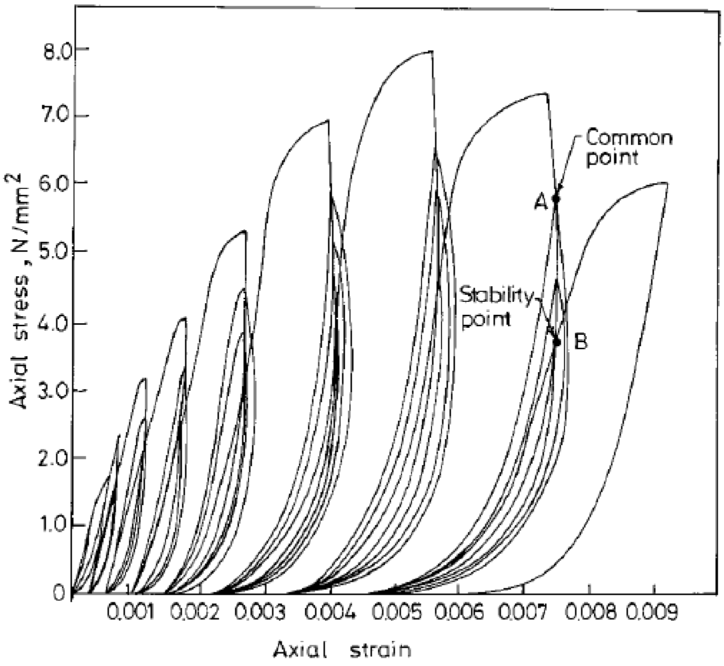

Figure 2-15: Typical hysteresis curve for cyclic loading (adapted from [4])

Such a test gives the researcher freedom to manipulate the input according to the desired study. Paquette et al. successfully studied full-scale models with a wooden diaphragm fixed to the wall at its corners. Their specimen displayed combined rocking and sliding mechanism without losing much strength.

2-4-1 Pushover Analyses

Pushover analysis is a static type of analysis in which the intended structure is laterally "pushed over" monotonically in steps using either mass proportions of the structure or with respect to the structures' dominant modes of vibration. The former is called mass proportional pushover analysis whereas the latter is called modal pushover analysis. It was firstly introduced by Freeman et al.(1975)[38] using capacity spectrum design method and since then has undergone several advancements. It is a very popular method to estimate the seismic demand of the structure under consideration. Mass proportional pushover analysis is carried out by applying gravity loading in the lateral direction in increments to study the linear and nonlinear behaviour of the structure until ultimate capacity is reached. It has been demonstrated clearly by Anil Chopra et al. (2001)[39]. This method of analysis is popular because a close estimate of the actual behaviour can be obtained without extensive requirement of computation time or resources. However, this method successfully predicts the structural behaviour until ultimate capacity is reached. Furthermore, it is difficult to predict post peak behaviour due to convergence issues. As an example in mass proportional analysis, no structure is designed to undertake gravity loading in the lateral directions and hence it is difficult to accurately predict the response for every incremental step. But, this can be overcome upto an extent by using tools such as displacement control, arc-length control and line search criteria. The result is a capacity curve with force or acceleration plotted against lateral displacement of the structure. Though pushover analysis is not as robust compared to the more complex time-history analysis, a non-linear pushover analysis generally provides a quick insight and close estimate of seismic behaviour of the structure such as- peak structural response, ductility behaviour of the structure, relative drift of different storeys, cracking process etc. at lesser computation cost. This is best suited for a computational model and hence is one of the primary advantages of using the pushover analysis. This analysis can also be used as a comparative tool to validate the dynamic behaviour of the structure when comparing with other dynamic non-linear analyses such as time-history and response spectrum analyses.

2-4-2 Time-History Analyses

As the name suggests, it is an analysis in which, load is applied in steps of time. This way, any earthquake acceleration data can be input with appropriate units of time and acceleration. Such step-by-step time-integration methods were developed for dynamic analysis of non-classically damped structures using mode-acceleration algorithms by Singh et al.(1986)[40].

Time-History dynamic analyses on structures have been carried out by Salajegheh et al.(2005)[41]

by the application of filter banks and wavelet transforms. Filters are used to split the ground acceleration data into two parts consisting of low and high frequencies, and low frequency values which are more effective for the input are converted into a signal with small points using fast wavelet transforms. These transforms are computed by using certain algorithms. The authors have demonstrated through this study that using the described method computational time and costs can be reduced.
Similarly, Lam et al.(2003)[42] have made a comparison of the dynamic behaviour of an analytical model to experimental shake table tests using time-history data of several earthquakes. They have also written a computer-program to analyse non-linear behaviour of flexure walls. They have also demonstrated that the use of computational modelling is advantageous owing to reduced computational time and effort, accuracy of results in comparison with shake table tests using physical specimens.
Similar to their objective of cutting testing costs which include materials, machinery, skilled labour, this thesis uses a computational model to understand the seismic behaviour of a masonry structure, using a set of time-history data. This is executed by base excitation of the structure, to simulate real behaviour under the earthquake input in steps of time. The advantage of this project is it will be a benchmark to further tests that would be carried out in the future in TU Delft Stevin Lab. The non-linear time history analyses being the centrepiece of this project, it will be dealt with in extensive detail in section 4-4.

2-5 Connections in Masonry Buildings

Several researchers who have studied the out-of-plane behaviour of masonry walls in a structure have emphasised that “adequate”connection between these walls and diaphragms are critical to reduce damage caused by it. Due to earthquake loading, the out-of-plane wall undergoes bending and proper connection will impose a rocking behaviour as pointed out in section 2-3-2. Doherty(2000) has described the different connections commonly observed in masonry structures- figure 2-16. In clockwise order from top left, they indicate the following respectively.

- Internal partition wall cornice connection
- Cavity wall to roof truss connection 1
- Cavity wall to roof truss connection 2
- Wall to inter storey floor slab Damp Proof Course (DPC) connection
- Wall to ground floor slab DPC connection

Bonucci et al.(1996)[5] have presented three anchorage designs which are shown in figure 2-17 as follows

a) - Wall slab connection with continuous reinforced concrete rib- steel plate

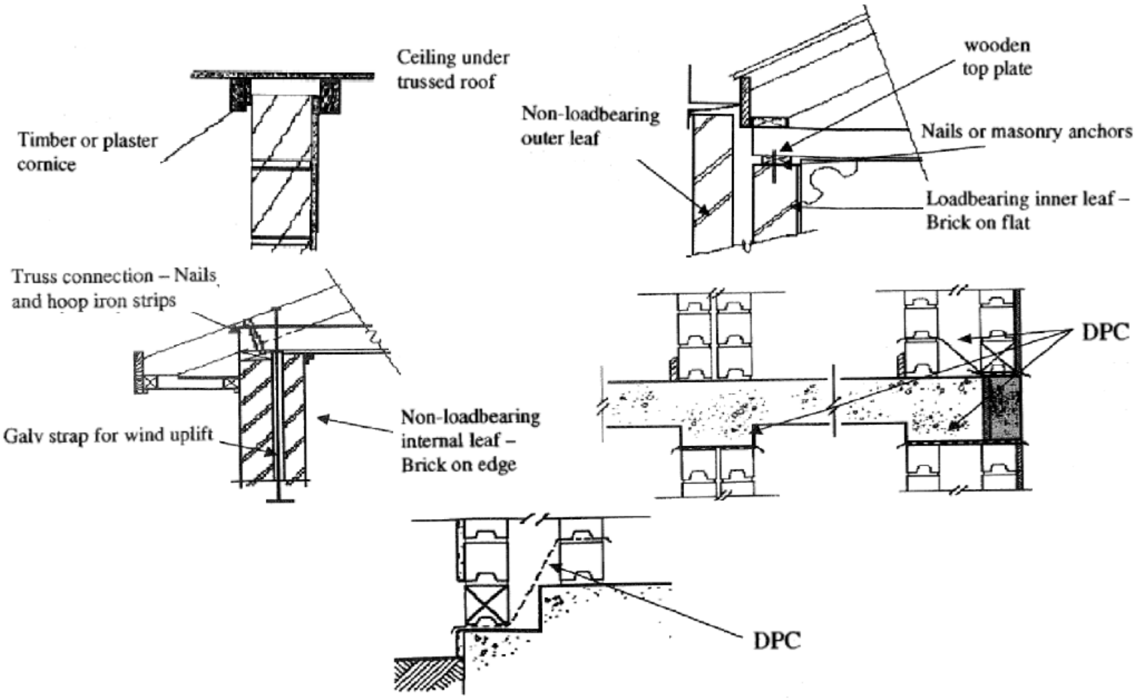

Figure 2-16: Typical connections between wall-diaphragms (adapted from [2])

b) - Timber floors with/without internal tendons to wall using various anchorages-steel hook

c) - Wall slab connection with reinforcing bars tied to brickwork- steel loop

They have performed cyclic pull out tests on full scale masonry walls with various steel reinforcements as shown in 2-17 to understand the punching limit state of anchorages. The test set up is shown in figure 2-18. They have found out that the addition of anchorage , their shape greatly influence their failure. Large displacements and a number of cycles take place before yielding of anchorage. They also suggest that easy design rules can be formulated by using simple theoretical models to predict the limit state.

Parisi et al.(2002) performed tests on old timber roof joists of a 19^{th} century building and full scale experimentation on roof section, with and without retrofit, and compared it with a numerical model to find matching results. The post-elastic response of their retrofit (with simple bolts) tests were comparable to that of new structures.
Moreira et al.(2012)[6] studied anchorages of two different types generally found in Portugal. Former *Pombalino* type of building used embedded metal ties along the wall and carpentry joints to firmly fix the floor slab to the wall. However, the newer *Gaioleiro* type of building used metal ties to nail the floor onto the beam or was simply supported and carpentry joints were omitted. The anchorages relied only on friction, adhesion and shear resistance of masonry. Refer figure 2-19. Pull-out test set up is depicted in figure 2-20 and the results as a force-displacment curve in figure 2-21. They found that bending of bolt or crushing of timber beam against the bolts were present always in anchorage behaviour.

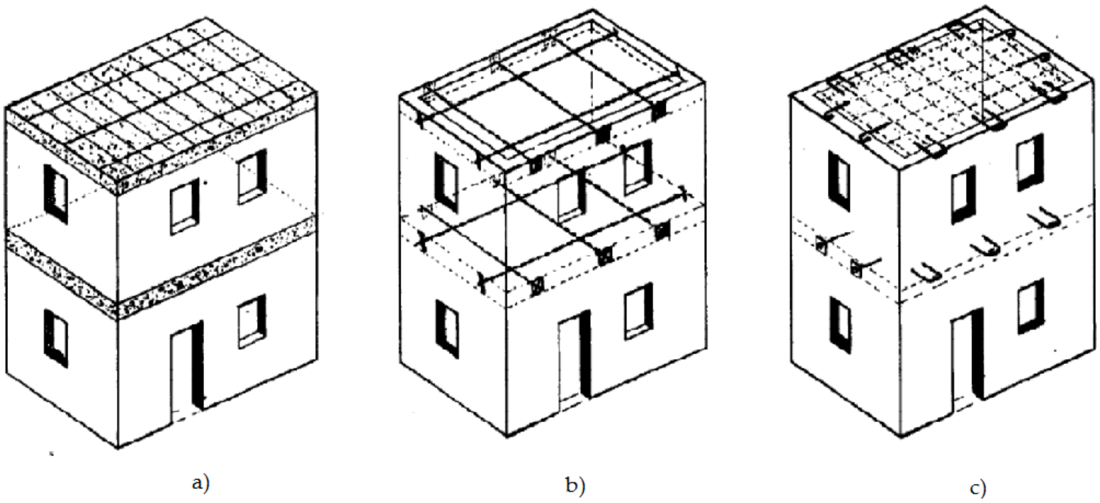

Figure 2-17: Typical connections between wall-diaphragms (adapted from [5])

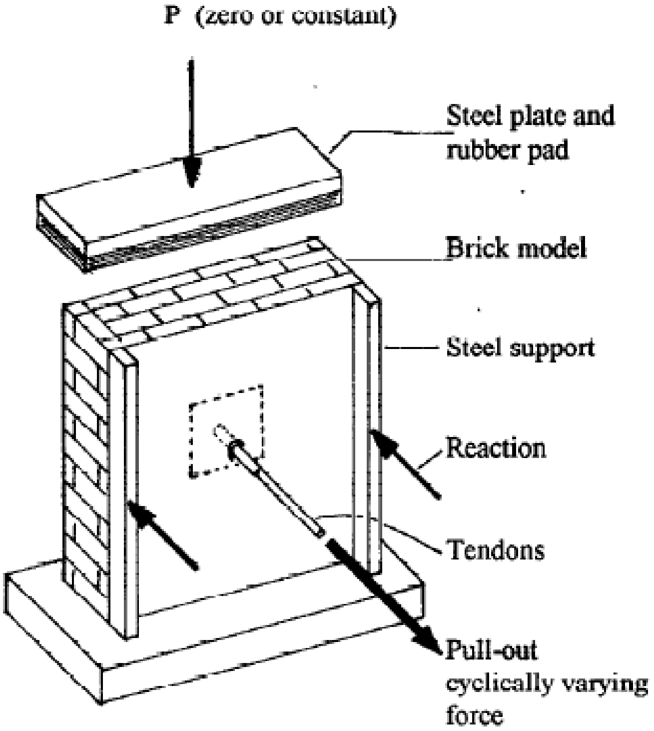

Figure 2-18: Cyclic punching limit state test set up (adapted from [5])

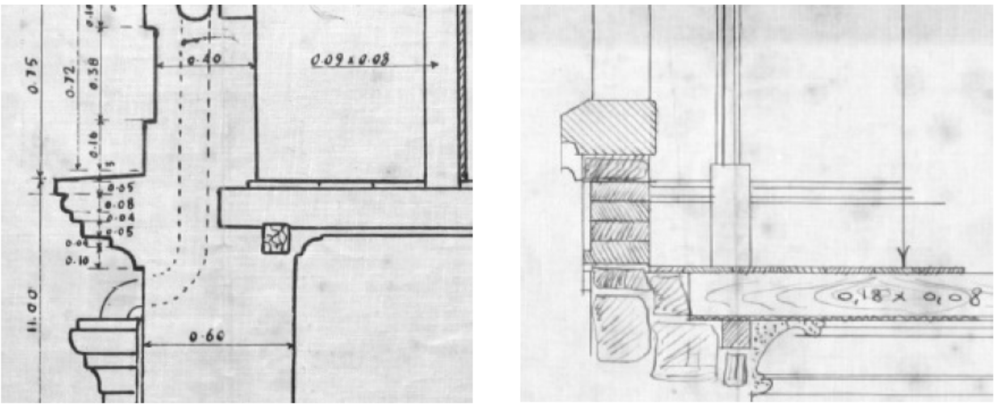

a) b)

Figure 2-19: Floor-wall connections in -a)Pombalino building and b)Gaioleiro building (adapted from [6])

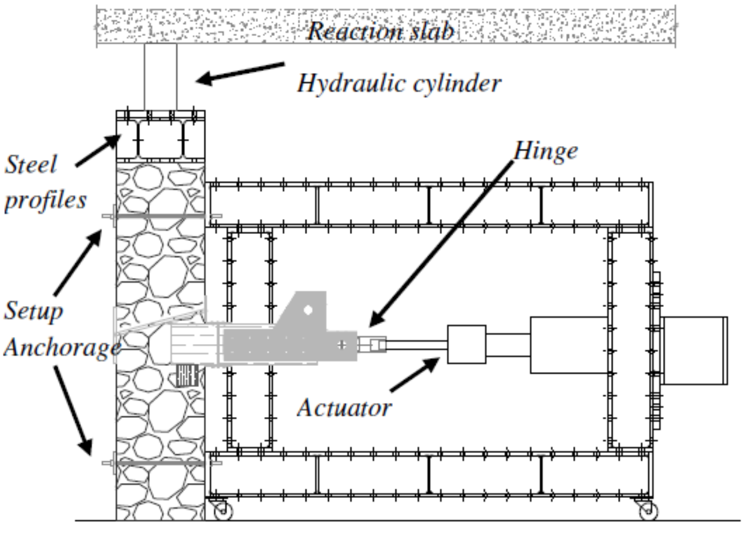

Figure 2-20: Pull out test set up [6])

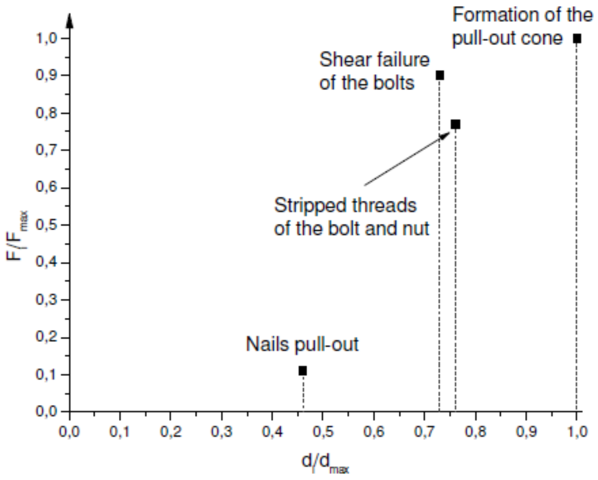

Figure 2-21: Pull out test results [6])

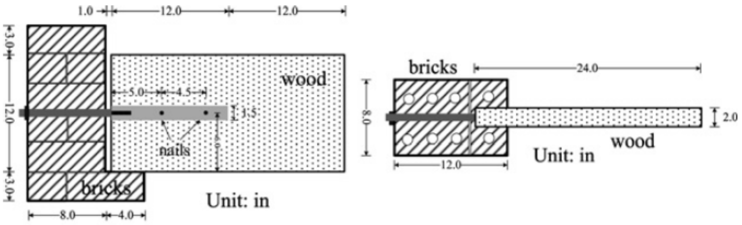

Side C/S view

Plan view

Figure 2-22: Test specimen [7])

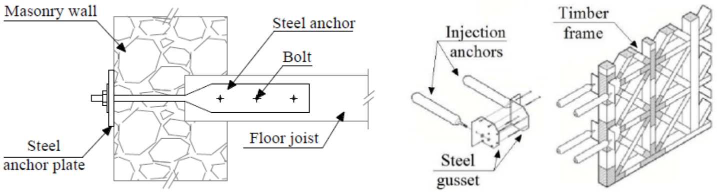

Figure 2-23: Testing of brick-timber joist connections with injection anchors [8])

Lin et al.(2012)[7] performed static monotonic and dynamic analyses on connections between brick wall and wood diaphragm. Variations used were- presence of nailed strap anchor and test methods. They have determined the force-displacement envelope and hysteresis response of the brick wall. It was found that joist-brick connection displayed brittle behaviour under dynamic loading than that compared to monotonic and quasi-static analyses. It is also suggested to use these test results to calibrate nonlinear numerical modelling of connections.

2-6 Introduction to Numerical Modelling

Behaviour of unreinforced masonry in tension and compression associated with Unreinforced masonry has been reviewed. Masonry walls subjected to in-plane, out of plane testing were reviewed, ranging from testing methods, loading histories. Behaviour under lateral loads, cyclic and dynamic loads were surveyed. The constitutive models available to simulate the behaviour of masonry have been presented in the next chapter.

Numerical modelling of structures is a recent advancement in the field of structural engineering developed from 1950s, but its applications are widespread. One such numerical method is *Finite Element Analysis*. It is a general methodology to estimate approximate solutions to boundary value problems for partial differential equations. Its first usage has been to solve complex analyses in structural and aeronautical fields of engineering. Eventually, it has found multitude of applications in the fields bio-mechanics, materials, medicine, among various other fields. Finite Difference Method, Boundary Element Method are two other major numerical techniques used for the same purpose.
There are multiple commercially available Finite Element Applications (FEA). Some of them are *ABAQUS, SAP2000, SCIA, ANSYS, DIANA, LS-DYNA*. The commercially developed applications offer simple user interface, library of standards for materials, failure models, constitutive equations, easy input and output, graphical representation of results etc. These things make it easier for the user to perform studies and interpret the results accordingly.
DIANA (DIsplacement ANAlyser) is a finite element package developed by *TNO-DIANA B.V.*. It contains three parts-

- A pre-processor called *FX+ for DIANA* developed by MIDAS IT.
- Finite Element Analyser Application called *DIANA and/or iDIANA*
- Post processor for interpretation of results, which in this case is included in FX+.

This application is also included in the master curriculum of Structural Engineering at the TUDelft. Familiarity, its simple user interface, powerful pre- and post-processor are some of the reasons for me to choose the application. *DIANA* 9.6 is the version of the software used for the analyses in this thesis work.

Several URM walls have been analysed using analytical and experimental methods. These have discussed above. However, analytical models fail to depict the post-peak behaviour. Experimental shake table tests, though, require expensive set up. With the increased use of computers, it has become easier to compute different configurations of masonry walls at a low operation cost since physical models need not be prepared or tested. Numerical modelling predicts very accurately the behaviour of structures provided, material properties, physical dimensions and failure models are input precisely.
Masonry is a composite material that can be modelled in three ways as suggested by Rots(1991)[43].

- Joints are represented by continuum elements

- Joints are represented by discontinuum elements
- Joints are smeared out.

This has been described by Lourenco et al.(1995)[9] as follows. Each of the following alternative is directly related to those described by Rots(1991) and Lourenço(1996)[44].

- Detailed Micro modelling : Units and joints are represented by continuum elements and the brick mortar interface is modelled as discontinuum elements. The material properties of both the units and the joints like the Young's modulus, poisson's ratio and the inelastic properties are taken into account and the interface is provided with high initial dummy stiffness and acts as a potential crack/slip plane.
- Simplified Micro modelling : Units are represented by continuum elements and the mortar joint and the brick mortar interface are lumped into discontinuous elements. Here each joint consisting of the mortar and two brick mortar interface is depicted by an average interface keeping the global geometry consistent. This type of modelling thus represents masonry system as a set of elastic blocks bonded by slip lines at the joint.
- Macro modelling : Units, mortar and unit-mortar interface are lumped into continuum. Masonry is treated here as a homogeneous anisotropic continuum. Relationship between average masonry stresses and strains are established. However, material parameters have to be evaluated from masonry tests under homogeneous stress state.

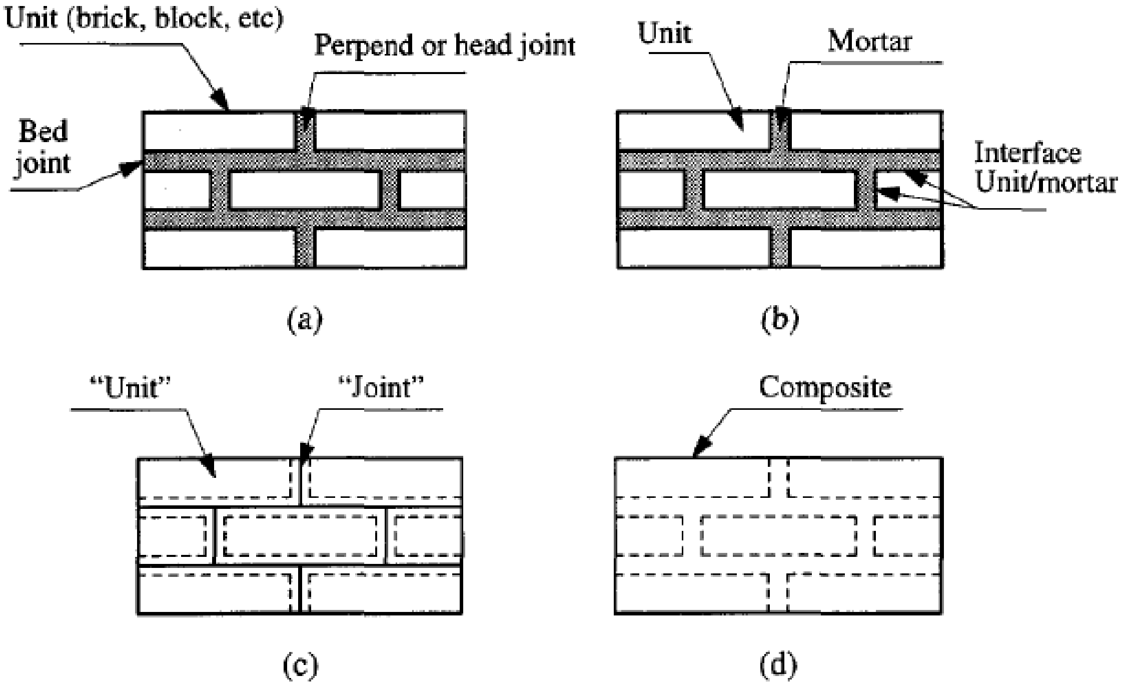

Figure 2-24: Modelling strategies for Masonry structures: a) Masonry sample b)Detailed micro modelling c) simplified micro modelling and d) Macro modelling [9]

The type of modelling used depends on the necessity to study local or global behaviour of masonry structures. Micro modelling consumes a lot of computation resources and time, but has very high accuracy. Macro modelling provides a good balance between accuracy and simplicity due to the less computational memory and time requirements. Simplified micro-modelling ranks between the above two variants.
Apart from modelling techniques, failure criteria is an important input parameter. This describes completely the behaviour of model. Several models have been proposed in the past by researchers to describe the behaviour of masonry. Lourenço et al.(1997)[10] have proposed a composite yield criterion applicable to anisotropic materials under plane stress. It describes material behaviour both in tension and compression regime. However, they are an amalgamation of two different failure types viz. Rankine type criterion for tension which describes a localized process of fracture - cracking and Hill-type criterion for compression which displays a softening and thus a more distributed process - crushing. Using this model, and experimental data, numerical modelling describing masonry shear walls was performed on DIANA, which is a finite element application for structural modelling and analysis. The proposed model fared well in both, tension and compression regimes and hence has been validated. The model as such is suitable for large structures where global behaviour is more critical and is very useful to reduce computational time. But for local failure modes, it should be used with care as this in comparison to discrete modelling approach would have a difference due to the smearing out the cracks. In the absence of effective parameters, a simple continuum model (Total strain Based cracking model) can be used.

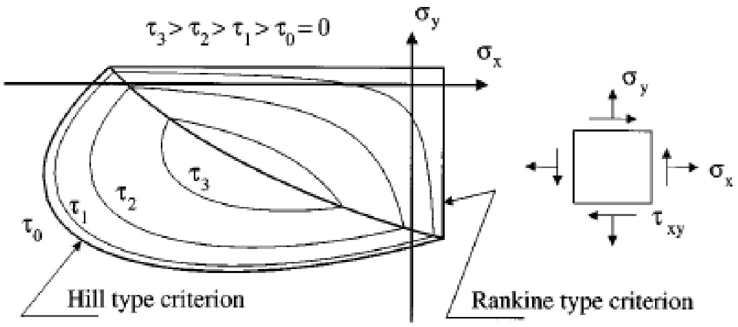

Figure 2-25: Proposed yield criterion for anisotropic elements under plane stress [10]

Another failure model was developed by Lourenço and Rots(1997) that describes all types of failure exhibited by unreinforced masonry. This multisurface interface model or interface cap model has been explained for micro modelling approach, see Figure 2-28 that includes all the possible failure mechanisms of masonry structures as shown in Figure 2-27. The suggested modelling strategy has also been described in figure 2-26 Application of the model to shear wall experiments have produced good match. The model was able to reproduce the complete path of the structures until total degradation without convergence problems, it was also found that the model was mesh insensitive. Nevertheless, the computation effort and time is very high due to micro-modelling.

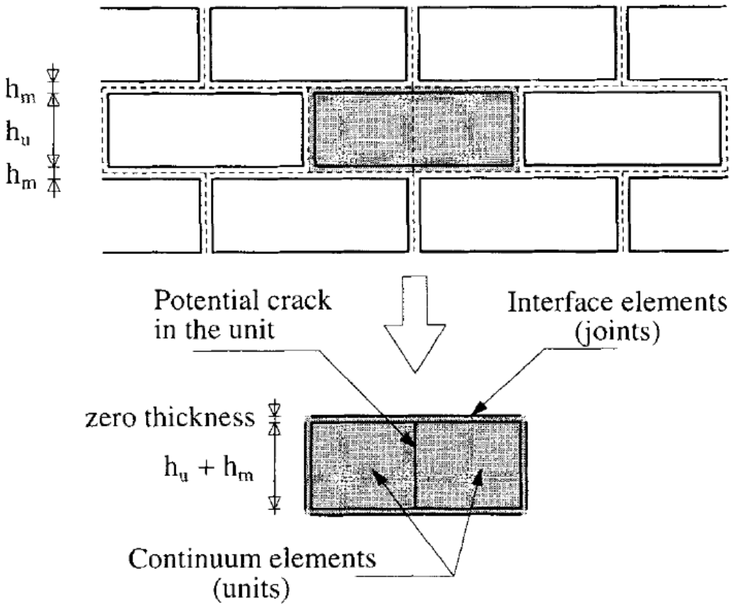

Figure 2-26: Suggested micro-modelling technique

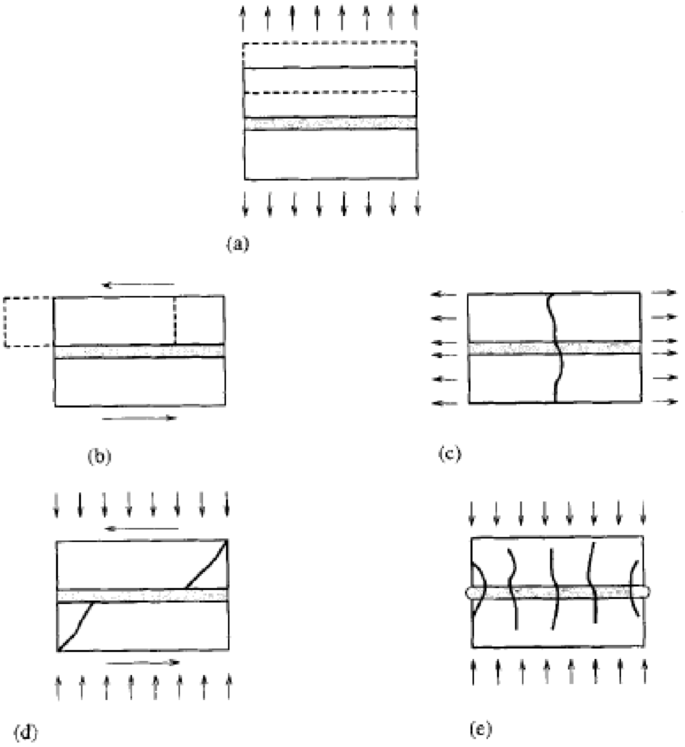

Figure 2-27: Failure Mechanisms of Masonry: (a) Joint Tension Cracking; (b) Joint Slip; (c) Unit Direct Tension Crack; (d) Unit Diagonal Tension Crack; (e) Masonry Crushing

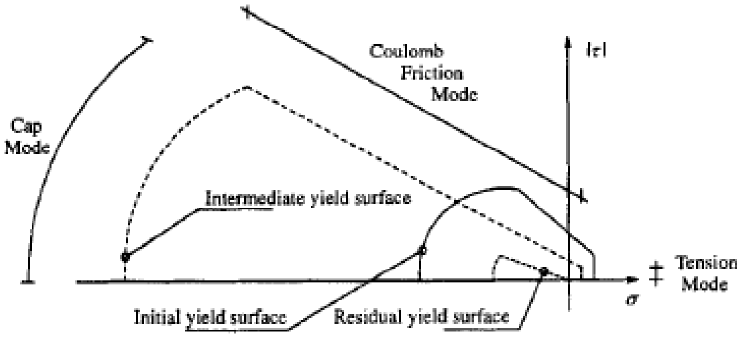

Figure 2-28: Proposed multisurface interface cap model

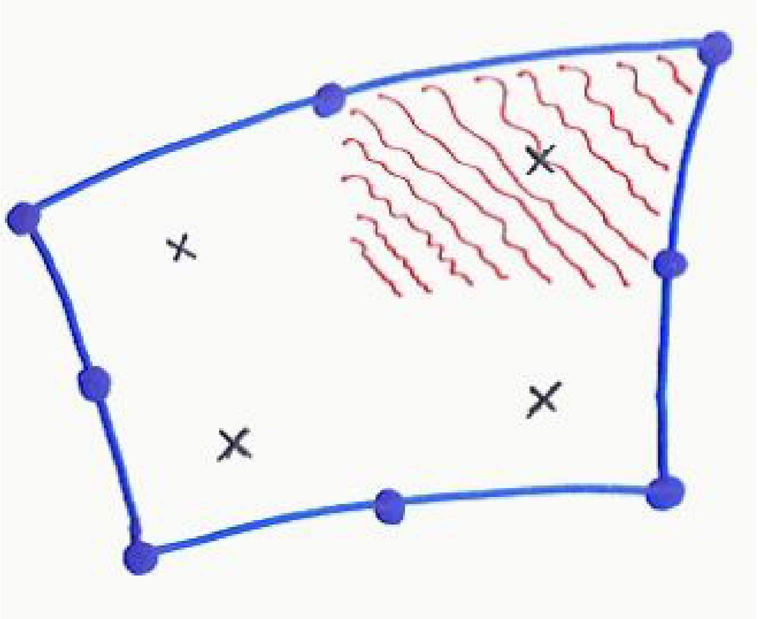

Figure 2-29: Anisotropic continuum crack model

2-6-1 Anisotropic Continuum Model

Lourenço[45] [46] also suggested another type of model, as a development to the previous work of anisotropy for plane stress elements, to apply on shell elements. In this case, the adopted model is an extension of Hill type for compression and Rankine type for tension behaviours. Cracks are smeared over walls and are treated as plastic deformations. The model was validated by a number of experimental and numerical tests and analyses. Since local cracking is not modelled in this case, it is advantageous to model large structures with reduced degrees of freedom compared to micro-modelling. It is also versatile to encourage different tensile and compressive behaviour for different materials. This type of modelling has also been included in the TUDelft curriculum in the course $CIE5148$.

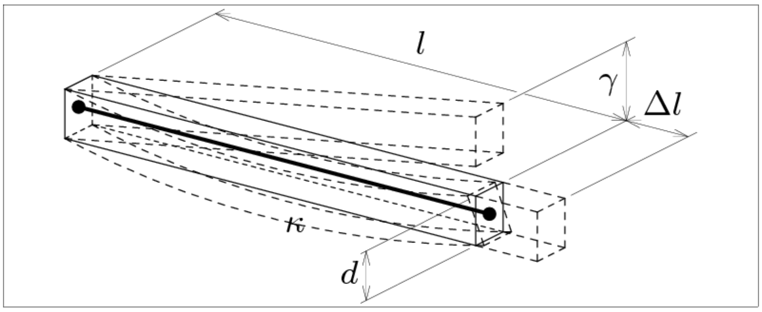

Figure 2-30: Beam Element [11]

2-6-2 Finite Element description

As mentioned before, DIANA 9.6 application is used for structural analysis. Hence, the description of the finite elements as provided by the software is discussed. It is indicated here that u and ϕ denote translational and rotational degrees-of-freedom (DoF) respectively, and the subscripts in the case of ϕ_z indicates the positive direction "*z-axis*" of the element, about which rotation occurs.

Beam Elements

Beam elements are those in which the length dimension "l" is considerably higher than its thickness "d". They can simulate axial deformation Δl, shear deformation γ, curvature κ and torsion. Such an element is shown in figure 2-30. DIANA offers three classes of beams

- Class I: These elements behave in accordance with the classical Bernoulli beam theory and are directly integrated along cross-sections. This element can be used for linear and geometrically non-linear analysis, but is limited in physical non-linearity to stress-strain curves.
- Class II: These are numerically integrated fully and are similar to Class I (refer section 2-6-2) but these elements may also be used for problems involving physical non-linearity of the material.
- Class III: Fully numerically integrated cross-sections which conform to the *Mindlin-Reissner* theory.

For the thesis, class III beam element *CL9BE* is used. It is a $2-D$ curved beam element with 3 nodes and 9 degrees of freedom (DoF) with basic variables being u_x, u_y and ϕ_z. This element is shown below in figure 2-31. The interpolation polynomials for displacements are shown in the equations 2-1.

$$\begin{aligned} u_x(\xi) &= a_0 + a_1(\xi) + a_2(\xi^2) \\ u_y(\xi) &= b_0 + b_1(\xi) + b_2(\xi^2) \\ \phi_z(\xi) &= c_0 + c_1(\xi) + c_2(\xi^2) \end{aligned} \tag{2-1}$$

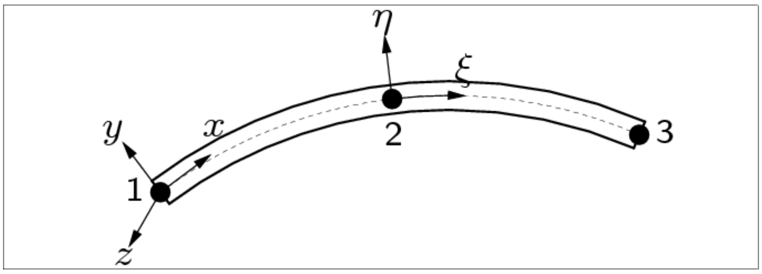

Figure 2-31: Beam Element $CL9BE$[11]

Shell Elements

These elements can further be differentiated into flat and curved shell elements.

Flat Shell Elements These elements are a fusion of plane stress and plate bending elements, but with forces used as variables, instead of Cauchy stresses. Following are the requirements of Flat Shell elements.

- The co-ordinates of the element should all lie in one flat plane
- Thickness "t" should be small with respect to width "b" in the element plane.
- Force loads can act in any direction from perpendicular to the plane to in-plane.
- Moment loads must act in-plane.
- It is assumed that cross-sections remain plane after deformation, however, they do not have to be perpendicular to the element plane.
- Displacement along the thickness direction is constant.
- Numerical integration is performed only in the reference plane.

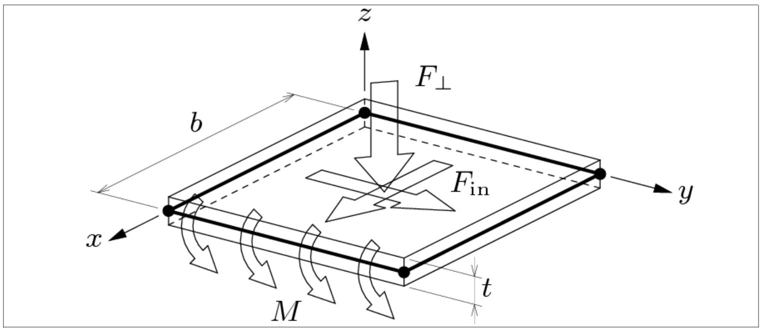

Figure 2-32: Flat Shell element [11]

Curved Shell Elements The curved shell elements are based on iso-parametic degenerated solid approach. However, two types of hypotheses can be selected from, which are:

- Straight normals- Normals of plane sections are straight (plane sections remain plane), but not necessarily normal to the reference surface. Transverse shear behaviour conforms to Mindlin-Reissner theory.
- Zero-normal-stress- This hypothesis assumes that the normal stress component in the normal direction lamina is forced to zero. Element tangent plane is spanned by a lamina basis which relates to a local Cartesian coordinate say (x_1, y_1), which is tangential to the iso-parametric plane(ξ, η) and perpendicular to point z_1.

In-plane lamina strains ε_{xx}, ε_{yy} and γ_{xy} vary linearly , whereas transverse shear strains γ_{xz} and γ_{yz} are forced to be constant, along the thickness direction. Basic degrees of freedom for curved shell elements are u_x, u_y, u_z, ϕ_x, ϕ_y.

When using triangular shell elements, care should be taken to analyse transverse shear as it might lead to "shear locking". This can be avoided by using quadrilateral curved shell elements. For the same reason, only a 2X2 integration $[n_\xi = 2, n_\eta = 2]$ is performed over the area. The default integration in the thickness direction is 3-point Simpson type $[n_\zeta = 3]$, however 2-point Gaussian type can be selected. Schemes greater than 3-point are available and could be used in case of non-linear analyses.

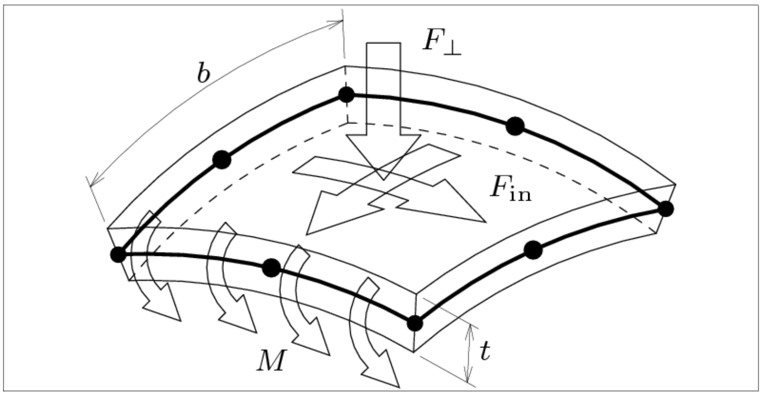

Figure 2-33: Curved Shell quadrilateral element [11]

The curved shell elements used for the project are *CQ40S* and *CT30S*. The former (figure 2-34) is an 8-node quadrilateral curved shell element, based on quadratic interpolation and Gauss integration over the iso-parametric (ξ, η) element area. However, along the thickness(ζ) direction, Gaussian or Simpson integration may be used. The interpolation polynomial for the element is given in equation 2-2. However, the latter one is a 6-node triangular quadratic shell element (figure 2-35) based on area integration, with Gauss or Simpson integration along thickness. The polynomials for translation and rotation are given in equation 2-3.

$$\begin{aligned} u_i(\xi, \eta) &= a_0 + a_1\xi + a_2\eta + a_3\xi\eta + a_4\xi^2 + a_5\eta^2 + a_6\xi^2\eta + a_7\xi\eta^2 \\ \phi_i(\xi, \eta) &= b_0 + b_1\xi + b_2\eta + b_3\xi\eta + b_4\xi^2 + b_5\eta^2 + b_6\xi^2\eta + b_7\xi\eta^2 \end{aligned} \tag{2-2}$$

Direction	Variables				
	ε_{xx}	κ_{xx}	m_{xx}	n_{xx}	q_{xz}
X	Linear				
Y	Quadratic				
Direction	Variables				
	ε_{yy}	κ_{yy}	m_{yy}	n_{yy}	q_{yz}
X	Quadratic				
Y	Linear				

Table 2-1: Stress-strain distribution along element area in ζ lamina

$$
\begin{aligned}
u_i(\xi,\eta) &= a_0 + a_1\xi + a_2\eta + a_3\xi\eta + a_4\xi^2 + a_5\eta^2 \\
\phi_i(\xi,\eta) &= b_0 + b_1\xi + b_2\eta + b_3\xi\eta + b_4\xi^2 + b_5\eta^2
\end{aligned}
\tag{2-3}
$$

Variables which can be sought from curved shell elements are strain ε, curvature κ, moment m, membrane force n and shear force q, their behaviour along different directions are summarized in table 2-1.

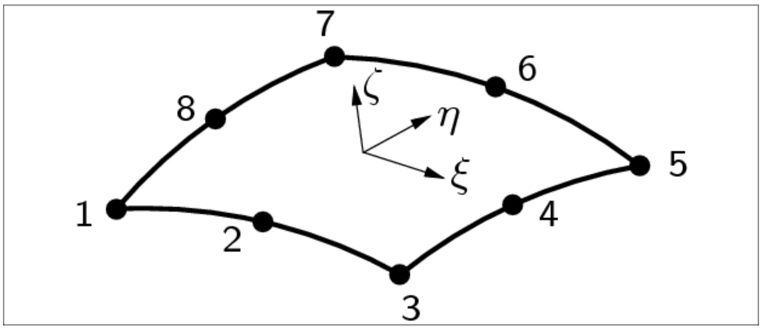

Figure 2-34: Curved Shell element CQ40S [11]

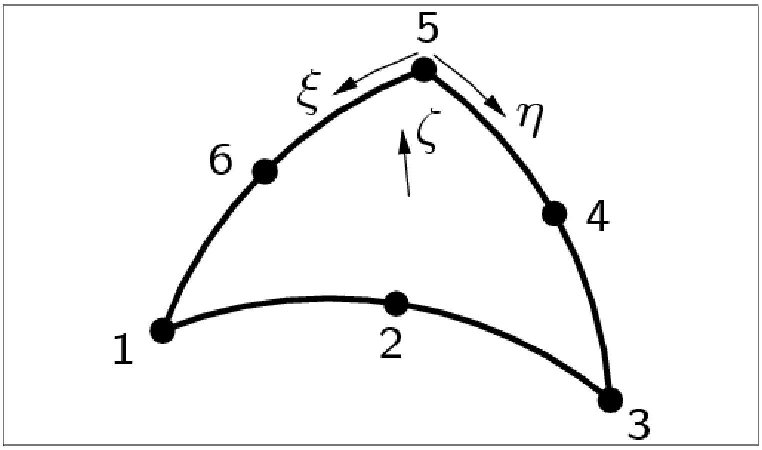

Figure 2-35: Curved Shell triangular element CT30S [11]

Connections

Different connections can be modelled as linear constraints, by the use of *tyings* in DIANA. Dependencies between degrees of freedom can be established which will then simulate physical connections between the desired parts. Adequate care should be exercised to avoid discrepancies between degrees of freedom which will create problems in the stiffness matrices. Constraints between nodes can be established in two ways:

- Single point constraint
- Multi-point constraints

Single point constraints Done by selecting a master node and one or more slave nodes, which naturally means that the solution to the system of equations will solve for master node and then it is copied onto the slave nodes. However, a slave node can neither be a master node in some other tying nor be supported.

Figure 2-36: Tying DoFs: single point [11]

Multi-point constraints In this case, the tying is specified as a connection between a master edge and a slave edge. Edges consist of straight lines and hence it corner nodes or vertices of edges are selected as shown in figure 2-37.

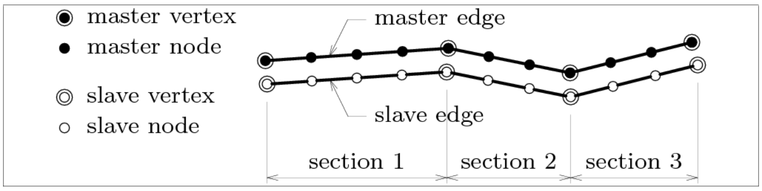

Figure 2-37: Tying DoFs: multi-point [11]

The described two types of connections can be extended to interconnections between two nodes, by which two master nodes can be connected to one slave node as in figure 2-38.

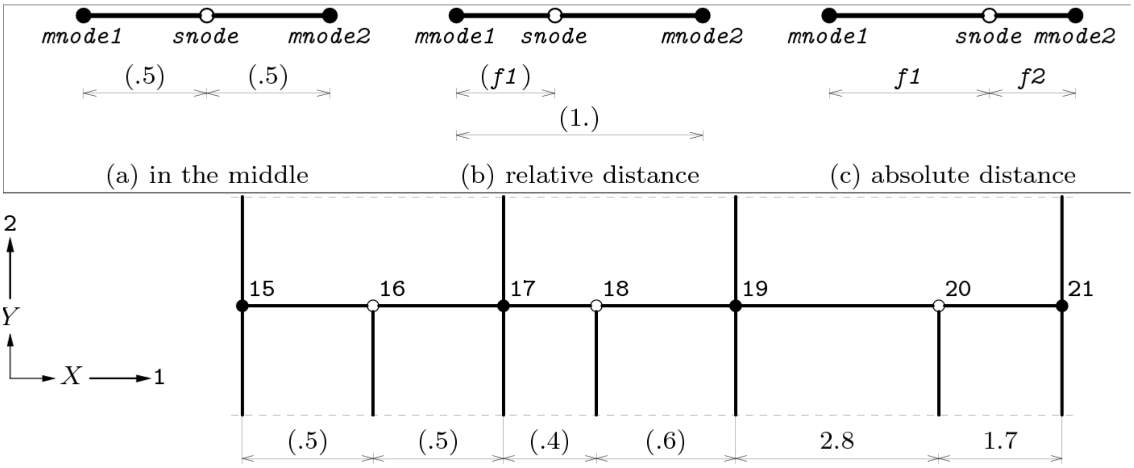

Figure 2-38: Tying DoFs single and multi-point interconnections [11]

2-7 Constitutive model, iteration method and convergence criterion

2-7-1 Constitutive models

Constitutive models available for the macro-modelling of masonry are detailed along with iteration methods and convergence criteria. In smeared cracking of masonry, for the strains and stresses, two main types of constitutive relationships are available in DIANA 9.6[11]. They are -

1. Multi-direction fixed crack model - This model has been used successfully to simulate the behaviour of concrete. In this case, strain decomposition is an initial step by which, total strains are expressed as a sum elastic and cracking strains.

$$\varepsilon = \varepsilon^{e} + \varepsilon^{cr} \tag{2-4}$$

This is advantageous in the case of plasticity behaviour. Further sub-decomposition of crack strain proves favourable to simultaneously model a number of cracks. The fundamental feature of the current model is the assumption that a stress s_i and a strain e_i^{cr} exist in the $n - t$ co-ordinate system, along each crack i.

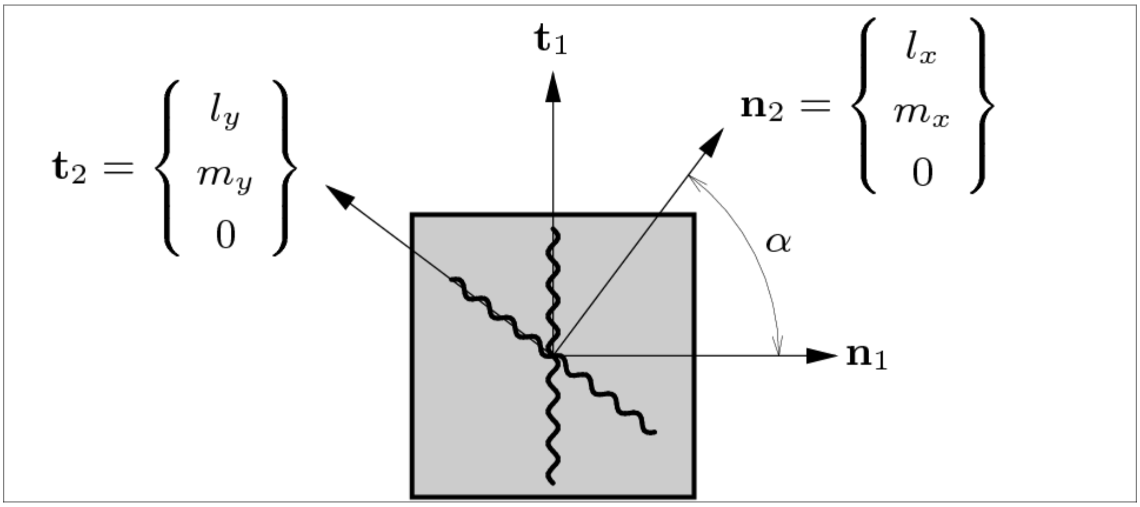

Figure 2-39: Multi-directional fixed crack model[11]

$\mathbf{e}^{cr}$ is the vector assembling crack strain with each crack, which gives,

$$\mathbf{e}^{cr} = [e_1^{cr}, e_2^{cr}, ..., e_i^{cr}, .., e_n^{cr}]^T \tag{2-5}$$

$\mathbf{e}_i^{cr}$ is the crack strain for each crack and is given as,

$$\mathbf{e}_i^{cr} = [\varepsilon_{nn,i}^{cr}, \gamma_{nt,i}^{cr}]^T \tag{2-6}$$

Further the global strain ε^{cr} is related to the strain vector $\mathbf{e}^{cr}$ by the transformation,

$$\begin{aligned} \varepsilon^{cr} &= \mathbf{N}\mathbf{e}^{cr} \\ \text{where, } \mathbf{N} &= [N_1, N_2, .., N_i, .., N_n] \end{aligned} \tag{2-7}$$

$$\text{and for plane strain, } \mathbf{N}_i = \begin{bmatrix} l_x^2 & l_x l_y \\ m_x^2 & m_x m_y \\ 2l_x m_x & l_x m_y + l_y m_x \end{bmatrix} \tag{2-8}$$

$$\begin{aligned} &\mathbf{n}^T = [l_x, m_x, n_x] \text{ is the normalised vector normal to crack plane} \\ &\text{similarly, } s^{cr} = [s_1^{cr}, s_2^{cr}, .., s_i^{cr}, .., s_n^{cr}]^T \text{is the stress vector for each crack.} \end{aligned} \tag{2-9}$$

$\mathbf{s}_i^{cr}$, the crack strain of each crack and is given as,

$$\mathbf{s}_i^{cr} = [\sigma_{nn,i}^{cr}, \tau_{nt,i}^{cr}]^T \tag{2-10}$$

Furthermore the global stress σ is related to the strain vector $\mathbf{s}^{cr}$ by the transformation,

$$\begin{aligned} s^{cr} &= \mathbf{N}^T \sigma \\ &\text{for } \mathbf{N}\text{, refer equation 2-7.} \end{aligned} \tag{2-11}$$

Since, constitutive relation generalise the relation, it could be written as

$$\mathbf{s}^{cr} = \ \mathbf{f}(\mathbf{e}^{cr}) \tag{2-12}$$

The relation (ignoring the dependence between normal and shear stresses), between stress and strain of a crack is given by,

$$\left\{ \begin{array}{c} \sigma_{nn}^{cr} \\ \tau_{nt}^{cr} \end{array} \right\} = \begin{bmatrix} \mathbf{D}_{secant}^{I} & \mathbf{0} \\ \mathbf{0} & \mathrm{D}^{II} \end{bmatrix} + \left\{ \begin{array}{c} \varepsilon_{nn}^{cr} \\ \gamma_{nt}^{cr} \end{array} \right\} \tag{2-13}$$

The secant modulus '$\mathbf{D}_{secant}^{I}$'is derived from the softening relation.

Ultimately, the global stress can be derived from the strain decomposition relation as follows,

$$\begin{aligned} \sigma &= \mathbf{D}\{\varepsilon - \varepsilon^{cr}\} \ldots \text{from equation 2-4} \\ &= \mathbf{D}\{\varepsilon - Ne^{cr}\} \ldots \text{from equation 2-7} \end{aligned} \tag{2-14}$$

With the relation, $s^{cr} = \mathbf{D}_{secant}^{cr} e^{cr}$, it can be further written as

$$\begin{aligned} \sigma &= \mathbf{D}\{\varepsilon - N[\mathbf{D}_{secant}^{cr}]^{-1} N^T \sigma\} \\ &= [\mathrm{D} - \mathbf{D}N[\mathbf{D}_{secant}^{cr} + N^T \mathbf{D} N]^{-1} N^T \mathbf{D}]\varepsilon \end{aligned} \tag{2-15}$$

For example, in a plane stress situation, for a linear-elastic stiffness matrix $\mathbf{D}$, where crack co-ordinate system and the global co-ordinate are the same, with

$$\mathbf{D} = \frac{E}{1 - \nu^2} \begin{bmatrix} 1 & \nu & 0 \\ \nu & 1 & 0 \\ 0 & 0 & \frac{1}{2}(1 - \nu) \end{bmatrix} \tag{2-16}$$

Then, we get the transformation matrix N as follows, and arrive at the final form of the relation as shown in equation 2-17

$$N = \begin{bmatrix} \mathbf{1} & \mathbf{0} \\ \mathbf{0} & \mathbf{0} \\ \mathbf{0} & \mathbf{1} \end{bmatrix} \tag{2-17}$$

$$\begin{Bmatrix} \sigma_{xx} \\ \sigma_{yy} \\ \tau_{xy} \end{Bmatrix} = \begin{bmatrix} \frac{\mu E}{1-\mu v^2} & \frac{\mu v E}{1-\mu v^2} & \mathbf{0} \\ \frac{\mu v E}{1-\mu v^2} & \frac{E}{1-\mu v^2} & \mathbf{0} \\ \mathbf{0} & \mathbf{0} & \frac{\beta E}{2(1+v)} \end{bmatrix} \begin{Bmatrix} \varepsilon_{xx} \\ \varepsilon_{yy} \\ \gamma_{xy} \end{Bmatrix} \tag{2-18}$$

2. Total strain crack models - Under this model also, the constitutive relation is based on total strain, of which stress is a function. Using the orthogonal crack models - two approaches are possible, such as
   - Rotating crack model - In this subtype, the stress-strain relations are evaluated in the principal strain directions. Implemented successfully to simulate reinforced concrete, it is advantageous in a few ways.
   - Fixed crack model - In this model, the stress-strain relationships are based upon a *n,s,t* co-ordinate system, fixed upon cracking. Better displays the physical behaviour of cracking and is hence adopted for the current project.

In this concept, stress is determined in the directions of the crack, i.e. if ε_{xyz} is the strain vector in the co-ordinate system xyz of the element and the corresponding strain increment $\boldsymbol{\Delta}\varepsilon_{xyz}$, then the total strain after time '$\boldsymbol{\Delta t}$' is given by,

$$\begin{gathered} {}^{t+\Delta t}_{i+1}\varepsilon_{xyz} = {}^{t}\,\varepsilon_{xyz} + {}^{t+\Delta t}_{i+1}\,\varepsilon_{xyz} \\ {}^{t+\Delta t}_{i+1}\varepsilon_{nst} = \mathbf{T} \times {}^{t+\Delta t}_{i+1}\,\varepsilon_{xyz} \\ \text{where, } \mathbf{T} \text{ is the strain transformation matrix and} \\ {}^{t+\Delta t}_{i+1}\varepsilon_{nst} \text{ is the strain vector in the local co-ordinate system of the crack.} \end{gathered} \tag{2-19}$$

This point is the main difference between the *rotating* and *fixed* crack models. In the fixed type, the local '*nst*' co-ordinate system is fixed upon cracking, this offers clearer depiction of the cracking concept. In the '*rotating type*'model, the transformation matrix depends on the present strain vector as shown below.

$$\mathbf{T} = \mathbf{T}({}^{t+\Delta t}_{i+1}\varepsilon_{xyz}) \tag{2-20}$$

Furthermore, the strain tensor '**E**' and the rotation matrix '**R**', which contains the eigen-vectors are shown,

$$\begin{gathered} \mathbf{E} = \begin{bmatrix} \varepsilon_{xx} & \varepsilon_{xy} & \varepsilon_{xz} \\ \varepsilon_{yx} & \varepsilon_{yy} & \varepsilon_{yz} \\ \varepsilon_{zx} & \varepsilon_{zy} & \varepsilon_{zz} \end{bmatrix} \\ \mathbf{R} = \begin{bmatrix} n & s & t \end{bmatrix} = \begin{bmatrix} c_{xn} & c_{xs} & c_{xt} \\ c_{yn} & c_{ys} & c_{yt} \\ c_{zn} & c_{zs} & c_{zt} \end{bmatrix} \end{gathered} \tag{2-21}$$

By calculating the direction cosines between axes, the transformation matrix '**T**' is determined. Finally, the constitutive stress-strain relation in the crack local co-ordinate system (*nst*) and global (or element) co-ordinates (*xyz*) are given as -

$$\begin{aligned} {}^{t+\Delta t}_{i+1}\sigma_{nst} &= \sigma({}^{t+\Delta t}_{i+1}\varepsilon_{nst}) \\ {}^{t+\Delta t}_{i+1}\sigma_{xyz} &= \mathbf{T}^T({}^{t+\Delta t}_{i+1}\sigma_{nst}) \end{aligned} \tag{2-22}$$

2-7-2 Stiffness matrix and Iteration methods

Incremental-iterative procedures are those which are employed to achieve equilibrium of external and internal forces and minimize errors produced during the analyses, with the help of stiffness matrix defined by the constitutive relation.
Two types of stiffness matrices can be determined in DIANA,

1. Tangent stiffness - Tangent stiffness matrix '**D**' in the element (global) co-ordinate system, along with the strain transformation matrix '**T**' and tangent stiffness matrix in the crack co-ordinate system is as follows -

   $$\mathbf{D} = \mathbf{T}\mathbf{D}_{tangent}\mathbf{T} \tag{2-23}$$

   This stiffness can be expressed as a matrix made up of 4 sub-matrices as,

   $$\mathbf{D}_{tangent} = \begin{bmatrix} \mathbf{D}_{nn} & \mathbf{D}_{n\theta} \\ \mathbf{D}_{\theta n} & \mathbf{D}_{\theta\theta} \end{bmatrix} \tag{2-24}$$

   where, $\mathbf{D}_{nn}$ gives the stiffness of '*normal*' components of local strain
   where, $\mathbf{D}_{\theta\theta}$ gives the stiffness of '*shear*' components of local strain
   where, $\mathbf{D}_{n\theta}$ and $\mathbf{D}_{\theta n}$ give the stiffness of '*coupled*' components between *normal* and *shear* strains.

   Again, owing to the dependence of stiffness matrix on the constitutive relation, two main divisions are made-

   - Rotational crack model - The major difference in the stiffness matrix in this method is that the sub-matrices representing coupling between normal and shear strains $\mathbf{D}_{\theta n}$ and $\mathbf{D}_{n\theta}$ are zero, and the shear components are directly related to the components of principal stress. This is the direct result of the spin of co-ordinate system of the model.

     $$\mathbf{D}_{\theta\theta} = \begin{bmatrix} \frac{\sigma_1-\sigma_2}{2(\varepsilon_1-\varepsilon_2)} & 0 & 0 \\ 0 & \frac{\sigma_2-\sigma_3}{2(\varepsilon_2-\varepsilon_3)} & 0 \\ 0 & 0 & \frac{\sigma_3-\sigma_1}{2(\varepsilon_3-\varepsilon_1)} \end{bmatrix} \tag{2-25}$$

   - Fixed crack model - In this method, the coupling components are not always zero, but depend on the relation between shear-retention and normal components of strain. $\mathbf{D}_{n\theta}$ is zero, depicting no dependence of normal strain on shear components, so is $\mathbf{D}_{\theta n}$, if shear-retention does not depend on normal strain. Else, in general cases, $\mathbf{D}_{\theta n}$, $\mathbf{D}_{\theta\theta}$ and $\mathbf{D}_{nn}$ are given as-

$$\begin{aligned}
\mathbf{D}_{\theta n} &= \begin{bmatrix} \frac{\partial\sigma_{ns}}{\partial\varepsilon_{nn}} & \frac{\partial\sigma_{ns}}{\partial\varepsilon_{ss}} & \frac{\partial\sigma_{ns}}{\partial\varepsilon_{tt}} \\ \frac{\partial\sigma_{st}}{\partial\varepsilon_{nn}} & \frac{\partial\sigma_{st}}{\partial\varepsilon_{ss}} & \frac{\partial\sigma_{st}}{\partial\varepsilon_{tt}} \\ \frac{\partial\sigma_{tn}}{\partial\varepsilon_{nn}} & \frac{\partial\sigma_{tn}}{\partial\varepsilon_{ss}} & \frac{\partial\sigma_{tn}}{\partial\varepsilon_{tt}} \end{bmatrix} \\
\mathbf{D}_{\theta\theta} &= \begin{bmatrix} \frac{\partial\sigma_{ns}}{\partial\gamma_{ns}} & 0 & 0 \\ \frac{\partial\sigma_{st}}{\partial\gamma_{st}} & 0 & 0 \\ \frac{\partial\sigma_{tn}}{\partial\gamma_{tn}} & 0 & 0 \end{bmatrix} \\
\mathbf{D}_{nn} &= \begin{bmatrix} \frac{\partial\sigma_{nn}}{\partial\varepsilon_{nn}} & \frac{\partial\sigma_{nn}}{\partial\varepsilon_{ss}} & \frac{\partial\sigma_{nn}}{\partial\varepsilon_{tt}} \\ \frac{\partial\sigma_{ss}}{\partial\varepsilon_{nn}} & \frac{\partial\sigma_{ss}}{\partial\varepsilon_{ss}} & \frac{\partial\sigma_{ss}}{\partial\varepsilon_{tt}} \\ \frac{\partial\sigma_{tt}}{\partial\varepsilon_{nn}} & \frac{\partial\sigma_{tt}}{\partial\varepsilon_{ss}} & \frac{\partial\sigma_{tt}}{\partial\varepsilon_{tt}} \end{bmatrix}
\end{aligned} \tag{2-26}$$

2. Secant stiffness - Secant stiffness is followed in accordance with the stiffness of an orthotropic material in the principal co-ordinate system.

$$\mathbf{D}_{secant} = \begin{bmatrix} \bar{E}_1 & 0 & 0 & 0 & 0 & 0 \\ 0 & \bar{E}_2 & 0 & 0 & 0 & 0 \\ 0 & 0 & \bar{E}_3 & 0 & 0 & 0 \\ 0 & 0 & 0 & \bar{G}_{12} & 0 & 0 \\ 0 & 0 & 0 & 0 & \bar{G}_{23} & 0 \\ 0 & 0 & 0 & 0 & 0 & \bar{G}_{31} \end{bmatrix} \tag{2-27}$$

Many iterative procedures are available in DIANA, the important ones are mentioned and the one used is detailed.

- Newton-Raphson method
- Quasi-Newton method
- Linear and constant stiffness method

The action of such procedures on the analysis is best explained using the flowchart in the figure 2-40.

Newton-Raphson iteration is of two types - *regular* and *modified*. The main difference between the two is the calculation of stiffness. A few salient features of the '*regular Newton-Raphson*' iterative procedure are -

- Stiffness matrices are determined at every iteration, though this does not necessitate convergence in the previous step, refer figure 2-41, whereas in the *modified* method, stiffness is determined at the beginning of the increment only. The increment in the displacement vector is based on the previous step as well.

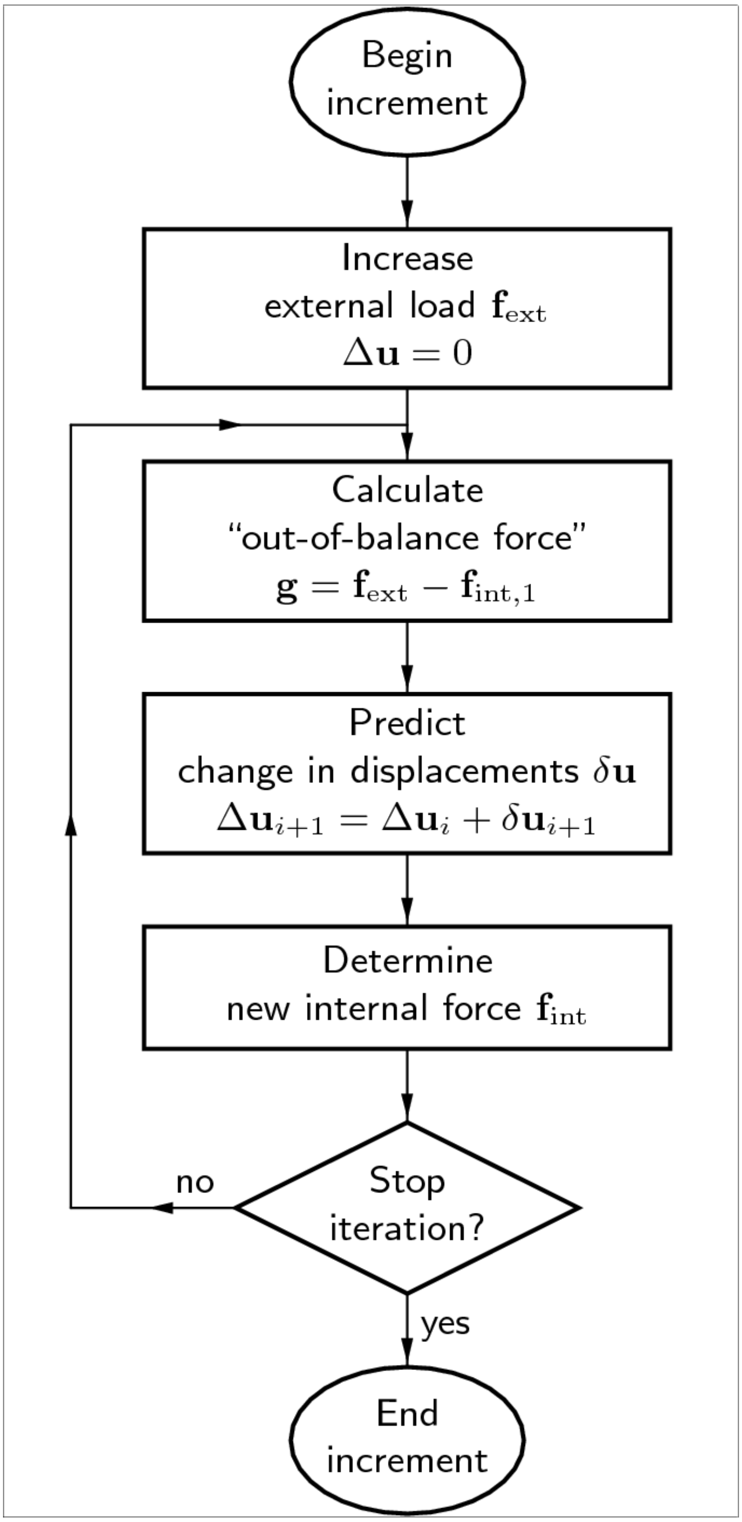

Figure 2-40: Iterative process [11]

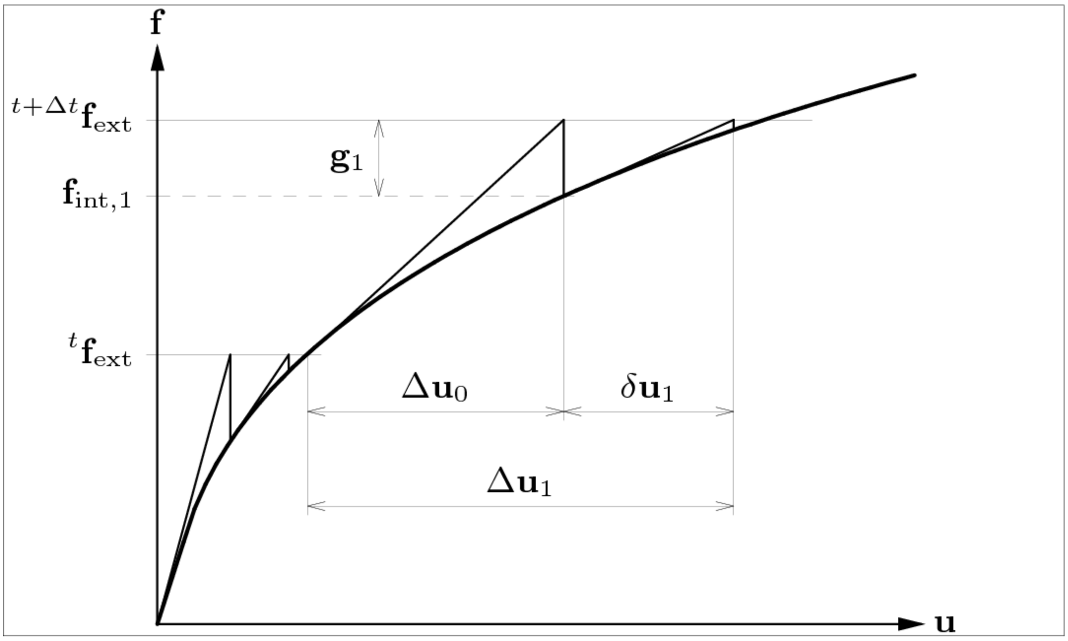

Figure 2-41: Regular Newton-Raphson iteration method [11]

- Time taken to converge in an analysis is less, though each iteration takes long, due to quadratic convergence characteristic.
- Unless correct stiffness matrix is used, divergence may occur easily.

Stiffness matrix for the *Newton-Raphson method* is given by $\mathbf{K}_i$,

$$\mathbf{K}_i = \frac{\partial \mathbf{g}}{\partial \Delta u} \tag{2-28}$$

2-7-3 Non-linear analyses, time integration and convergence

A brief description of the non-linear analysis is presented as determined by the DIANA application.

$$\begin{gathered}
f_{int} = f_{ext}(\text{ with prescibed boundary conditions, say } u_i = u_i^0) \\
(\because \text{ equilibrium of forces acting internally } (f_{int}) \text{ and externally } (f_{ext}) \\
\text{on the structure, where } u_i^0 \text{ is the prescribed boundary condition at } i\text{, say displacement)} \\
f_{int}(u_{past}) = f_{ext}(u_{current}) \text{ where, equilibrium depends on nonlinear displacements} \\
{}^{t+\Delta t}u = {}^{t}\, u + \Delta u \text{ where, equilibrium depends on displacement and time loads} \\
\text{finally, } O_g(\Delta u) = f_{ext}(\Delta u) - f_{int}(\Delta u) \\
\text{where, } O_g \text{ is the residual or out-of-balance force vector.}
\end{gathered} \tag{2-29}$$

Eigenvalue analysis

Eigenvalue analysis or free vibration analysis is performed to understand the natural modes of vibration characteristic of the structure. Free vibration is a condition in which external force is absent. Natural frequency of a structure can be calculated as shown below.
Assuming single degree of freedom, for a structure of mass *'M'*, stiffness *'K'*, displacement vector *'x(t)'* and external force *'F(t)'*, with predefined initial (at $t = 0$) displacement ($x(0) = x_o$) and velocity ($\dot{x}(0) = v_o$), the equation of motion can be written as-

$$\begin{aligned} M\ddot{x(t)} + Kx(t) &= F(t), \\ \ddot{x(t)} &= \frac{d^2x}{dt^2} \end{aligned} \tag{2-30}$$

If *F(t) = 0*, then the equation becomes a homogeneous differential equation.

$$M\ddot{x(t)} + Kx(t) = F(t) = 0 \tag{2-31}$$

The general solution to such a second order homogeneous differential equation is given by

$$x(t) = \sum_{n=1}^{2} X_n exp^{\pm i\omega_n t} = \overrightarrow{x} = \hat{x} \tag{2-32}$$

Applying 2-32 in 2-31, we get,

$$\begin{aligned} (-M{\omega_n}^2 + K)\overrightarrow{x} &= 0 \\ M{\omega_n}^2 &= K \\ \omega_n &= \pm\sqrt{\frac{K}{M}} \end{aligned} \tag{2-33}$$

The entity 'ω_n' is called the **natural frequency** measured in radians/second, '$\pm i\omega_n'$ are called the **eigenvalues** and '$\overrightarrow{x}$' is called the **eigen vector**. Expanding the general solution from equation 2-32, we get,

$$\begin{aligned} x(t) &= x_o \cos(\omega_n t) + \frac{v_o}{\omega_n}\sin(\omega_n t) \\ &= A_o \cos(\omega_n t - \phi_o) \end{aligned} \tag{2-34}$$

$$\begin{aligned} \text{where } A_o &= \sqrt{{x_o}^2 + (\frac{v_o}{\omega_n})^2} \text{ denotes } \textbf{Amplitude} \\ \text{and, } \phi_o &= \arctan\left(\frac{v_o}{x_o\omega_n}\right) \text{ denotes } \textbf{Initial Phase} \end{aligned} \tag{2-35}$$

The same concept is extended to structures with multiple degrees of freedom, also taking into consideration damping if applicable, then the number of equations increase drastically and becomes cumbersome to solve by hand. Mass *'M'*, Stiffness *'K'* and displacement vector *'x(t)'* will be replaced by mass matrices *'**[M]**'*, stiffness matrices *'**[K]**'* and displacement

tensors'*[**W(x,t)**'* of order $n * n$, where n is the number of degrees of freedom of the structure. For larger structures, higher computation and memory requirements are necessary and hence computer application are made use of.
For structures with multiple modes and degrees of freedom, it is not feasible to analyse all modes. Hence, effective mass participation factor (EMPF) is used. EMPF is a measure of the energy contained in that particular mode. It depends on the direction and magnitude of vibration and the available mass undergoing vibration in that particular direction. From the free vibration analysis of the model, the important modes analysed based on highest EMPF in each direction are discussed in the following tables.

Non-linear dynamic analysis

Transient Dynamic Analyses can be performed using DIANA and the analysis can be presented as follows:

$$\begin{gathered} Mu\ddot{(t)} + Cu\dot{(t)} + f_{int}(\mathrm{u}, \dot{\mathbf{u}}, \boldsymbol{\varepsilon}, \boldsymbol{\sigma}, \boldsymbol{t}, \dots) = f_{ext}(t), \\ u\ddot{(t)} = \frac{d^2u}{dt^2}; u\dot{(t)} = \frac{du}{dt} \\ \text{for linear analysis, } f_{int} = K \times u(t) \\ \text{for non-linear analyses, } f_{int} = \int B^T \sigma \end{gathered} \tag{2-36}$$

However, on the application of base excitation, the equations of motion can be presented as shown -

$$\begin{bmatrix} M_{ii} & M_{ib} \\ M_{bi} & M_{bb} \end{bmatrix} \begin{Bmatrix} \ddot{u}_i^{(a)} \\ \ddot{u}_b^{(a)} \end{Bmatrix} + \begin{bmatrix} C_{ii} & C_{ib} \\ C_{bi} & C_{bb} \end{bmatrix} \begin{Bmatrix} \dot{u}_i^{(a)} \\ \dot{u}_b^{(a)} \end{Bmatrix} + \begin{bmatrix} K_{ii} & K_{ib} \\ K_{bi} & K_{bb} \end{bmatrix} \begin{Bmatrix} u_i^{(a)} \\ u_b^{(a)} \end{Bmatrix} = \begin{Bmatrix} 0 \\ f_b \end{Bmatrix} \tag{2-37}$$

Here u_i represents internal movements and u_b represents applied base movements. Considering only the unknown internal movements, the above equation 2-37 can be simplified as -

$$M_{ii}\ddot{u}_i^{(a)} + C_{ii}\dot{u}_i^{(a)} + K_{ii}u_i^{(a)} = -M_{ib}\ddot{u}_b^{(a)} - C_{ib}\dot{u}_b^{(a)} - K_{ib}u_b^{(a)} = \hat{f}_i \tag{2-38}$$

Here, $\hat{f}_i$ signifies the *equivalent dynamic forces*. This way, the relative response, say $u^{(r)}$, is found by deducting the base movements from the absolute ones $u^{(a)}$. Such a second-order differential equation can be computed using suitable schemes.

Convergence criterion and Time Integration

Convergence represents the completion of a particular step or iteration in an analysis, or if the analysis results are adequate it can be used to terminate the analysis by limiting it to a number of iterations and/or steps.

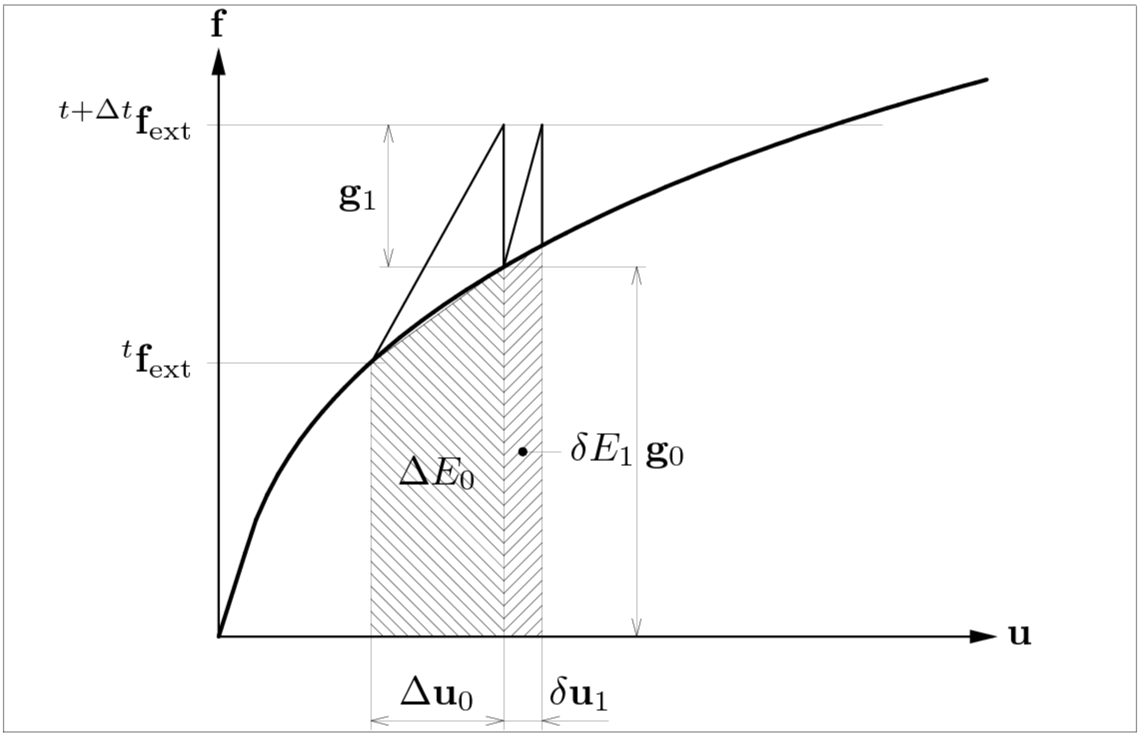

Figure 2-42: Energy criterion for convergence [11]

Energy norm is used for the analysis and is indicated, with reference to the figure 2-42. It is important to note that the choice of norm and convergence criterion is highly dependent on the type of analysis being carried out. To this end, strict criterion has to be adopted for complex analyses like the softening behaviour.

This norm is constituted by *internal forces* (ΔE_0) and *relative displacements* (δE_1). Note that internal forces (Δu_0 and δu_1) are used instead of out-of-balance forces (g_0 and g_1). Convergence is achieved using a ratio -

$$\text{Energy ratio for convergence norm } = \left| \frac{\delta u_1^T (f_{int,i+1} + f_{int,i})}{\Delta u_0^T (f_{int,1} + f_{int,0})} \right| \tag{2-39}$$

The time integration scheme used in the non-linear time history analyses is the *Newmark* method. It is an *implicit time integration* scheme, which means, it takes into consideration both the preceding time steps as well as the next one to compute the solution. This means higher computation, but it also poses an advantage of being numerically stable, proving convenient to choose between big and small step sizes, but still achieve convergence. Other examples for such a time integration scheme are *Backward Euler, Hilber-Hughes-Taylor* methods. This kind of scheme involves an extra step of computation for solution-

$$M\ddot{u}(t+\Delta t) + C\dot{u}(t+\Delta t) + f_{int}(\mathrm{u}, \dot{\mathbf{u}}, \varepsilon, \sigma, \boldsymbol{t}, \dots)(t+\Delta t) = f_{ext}(t+\Delta t) \tag{2-40}$$

Explicit time integration involves computing of the past time steps to arrive at the solution for the next one. Though less time consuming, it is not suitable for a precise analyses. Some of the methods following such a scheme are *central difference, Runge-Kutta* methods.

2-7-4 Physical behaviour and Numerical modelling of URM with flexible Diaphragms

Numerical modelling of masonry, either as a single shear or flexure wall consisting of single and/or double- wythe, or simple masonry buildings has been carried out from very long ago. Some of these are Dvorkin and Bathe(1984)[47],Tomazevic et al.(1987)[32], D.P.Abrams(1992)[48], Gambarotta and Lagomarsino(1997)[49], Pegon and Anthoine[50] Paquette and Bruneau(2003)[36], Milani et al.(2006)[51][52] Griffith et. al(2007)[53], Derakshan et al.(2013)[30]. However, very limited data is available on the behaviour of timber diaphragms.

Studies on the behaviour of timber diaphragms are limited. Itani and Cheung(1984)[12] performed non-linear modelling of sheathed floor diaphragm by considering two panel nailed sheathing diaphragm. It was divided into three parts- nail joints, beams and sheathing membrane. In the numerical analysis, beams and sheathing membrane were modelled as *elastic* beam and plane stress (4 node quadrilateral) elements respectively, whereas the nonlinearity was imposed on the "joint element" which was essentially a series of spring-pairs which are mutually perpendicular to each other (axial and shear springs). Using stiffness method, the joint element stiffness is formulated.

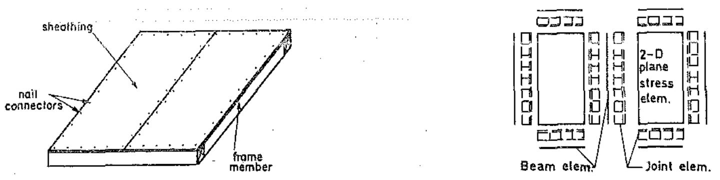

Figure 2-43: Physical and Numerical Representation adapted from [12]

Chui et al.(1998)[13] developed a FEM model for nailed wood joints under reversed cyclic loads. They investigated that joint strength increases when frequency of loading increases. They have observed that small diameter fasteners like nails, rivets, bolts can fail in a ductile matter, and that they undergo non-linear hysteresis effects under cyclic loading. The details of the FEM model are as shown in figure 2-44. They modelled three important aspects- nail, wood and the frictional behaviour between them. Successively, the nail was modelled as a 3 node beam element, load-embedding characteristics of wood using spring elements, friction between wood and nail by link elements.

Patton-Mallory et al.(1997)[54] studied a numerical model of bolted wood connections. They developed a constitutive non-linear 3D model and a numerical model to study the behaviour of a bolted connection loaded parallel to the grain.

Peralta et al.(2004)[14] studied four retrofit methods on wood diaphragms of pre-1950's URM buildings, experimentally and analytically. In the experimental study, the diaphragm was made up of $2x10$ joists spaced at $406mm$ centre-to-centre. The joists were supported at their ends by support frames. An additional gravity support was added at mid-span. Refer figures 2-47 and 2-48. In the numerical modelling prepared on *ABAQUS(2003)*, nonlinearity was assigned only to fasteners, whereas friction and mechanical contact between

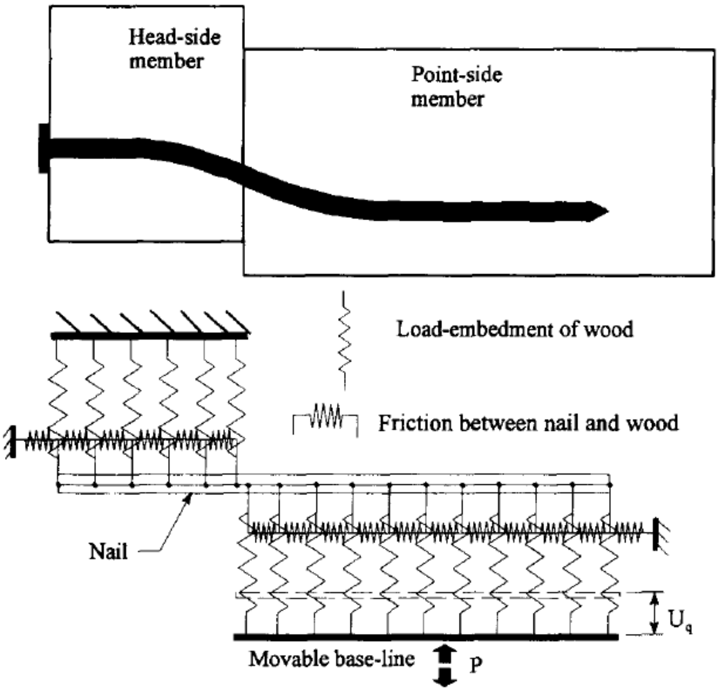

Figure 2-44: FEM model developed by Chui et al.[13]

surfaces were neglected. The wood specimens along with the joint were modelled as follows. Beam joists as 2-node linear Timoshenko beam element, sheathing boards as 8-node rectangular plane-stress element (quadratic interpolation was also used for accuracy) and nails as a system of two non-linear mutually perpendicular springs. Peralta et al.(2004)[14] studied the lateral in-plane behaviour of timber diaphragms according to different design guidelines formulated by the American *Federal Emergency Management Agency(FEMA)* and found that the allowable design lateral load Z_{FEMA} according to FEMA356 is nearly twice as much as that according to FEMA273.
Anderson and Bertero(2004)[55] performed experimental testing and numerical modelling on the seismic behaviour of tilt-up wall building. Numerical model was prepared and analysed on SAP2000. Non-linearity was incorporated into connections between wood joists, purlins and the roof diaphragm.
Similarly Tissell and Elliot(2004)[55] also made a detailed experimental study on different sizes and dimensions of plywood diaphragms for the *Engineered Wood Association*.

A few available research studies consisting of URM structures with flexible diaphragms were referred.
Tianyi Yi[56] performed numerical modelling of an URM structure with flexible diaphragms. It was assumed that rigid diaphragms act as a hinge support to the flexure walls, and hence, wooden diaphragm being flexible in nature, act as a “spring support”. The researcher also insists a few points regarding timber diaphragms and its improper connections.

- Timber diaphragms, being flexible in nature, act as a spring support to the out-of-

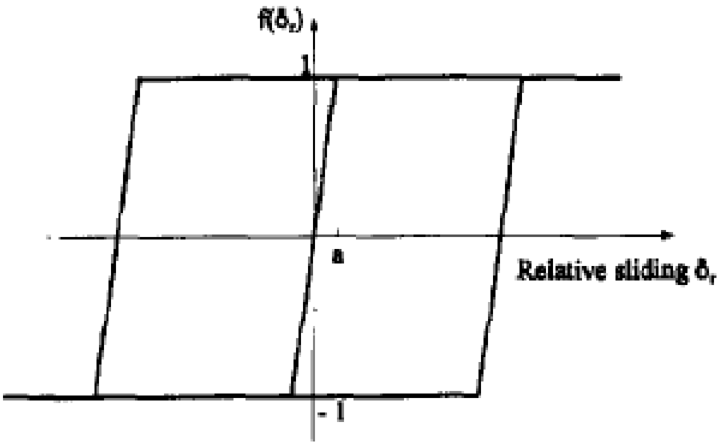

Figure 2-45: Wood-nail friction model[13]

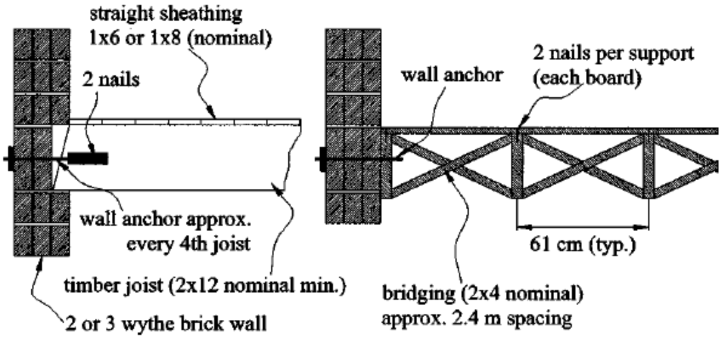

Figure 2-46: Wall-diaphragm connection adapted from[14]

plane wall, whereas rigid diaphragms act as hinge support.

- Improper connection between out-of-plane walls and timber diaphragms can lead to *"Pounding"* of diaphragm onto the walls, which will lead to cracks in the flexure walls.
- Weak connections can also cause the timber diaphragm to slip-off its supports.
- Wood diaphragms have large deformation capacity and high strength relative to its mass.
- It is observed that failure of wood diaphragms are rare, however, improper connections are the critical points which lead to failure.

Aaron Wilson(2012)[16] also studied seismic in-plane behaviour of flexible wood diaphragms in URM buildings. After investigating the different configurations of timber diaphragms in existing literature, he sought to establish a *Standard Diaphragm*, refer figures **??** and 2-49. He tested three different configurations of timber diaphragms experimentally.

- Nail connection test - indicated that connections in already existing URM structures possess very low capacity of stiffness, strength and deformation.

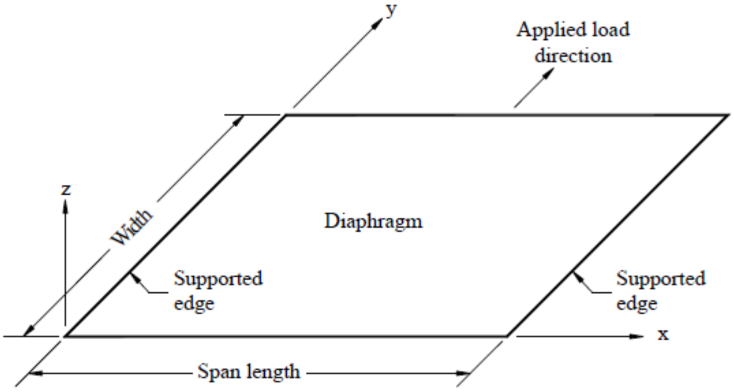

Figure 2-47: Experimental set up[15]

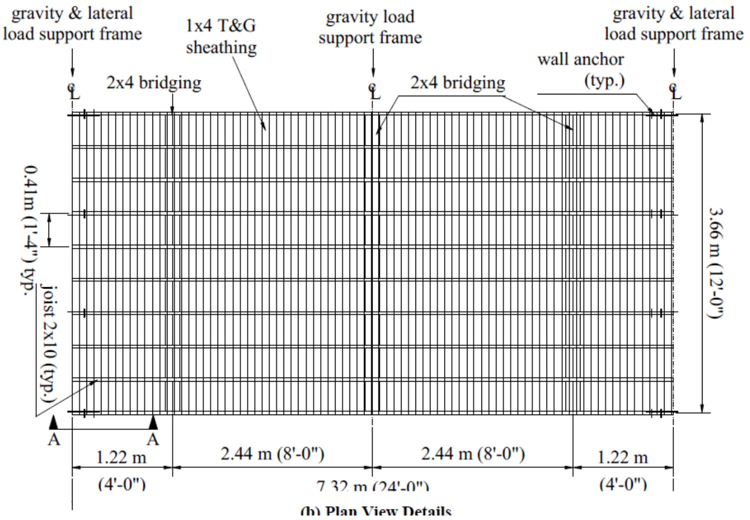

Figure 2-48: Experimental set up[15]

- Small scale diaphragm test - showed that friction between floor boards is negligible.
- Full-scale diaphragm test - confirmed the high flexibility and orthotropic behaviour of floor diaphragms.

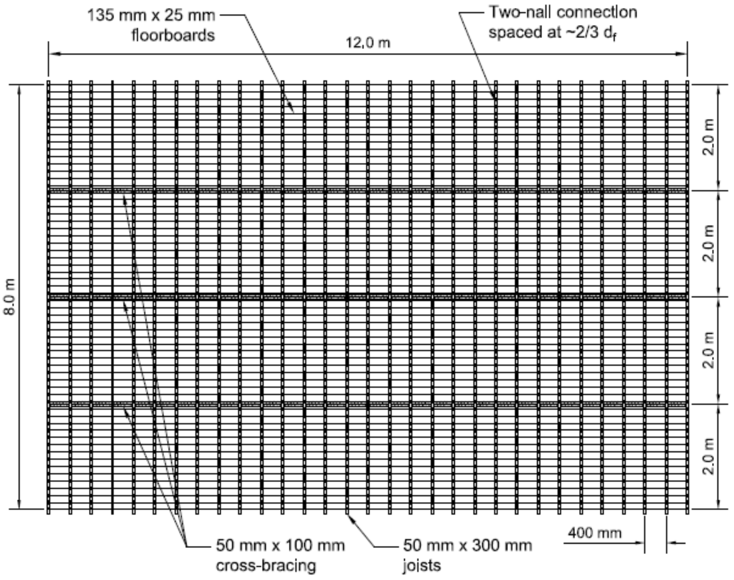

Parameter	Value	Parameter	Value
Diaphragm dimensions (m)	12.0 × 8.0	Joist spacing, ℓ (mm)	400
Floorboard thickness, t_f (mm)	25	Cross-bracing thickness, t_b	50
Floorboard width, d_f (mm)	135	Cross-bracing depth, d_b	100
Joist thickness, t_j (mm)	50	Cross-bracing spacing (m)	2.0
Joist depth, d_j (mm)	300	Timber elastic modulus, E (GPa)	10.0

Figure 2-49: Standard Diaphragm Details[16]

Also, finite element model of timber diaphragm was prepared using SAP2000 software and validated against the experimental data for monotonic and cyclic response of timber diaphragm. The following are specifications for which the models were tested.

- Symmetrical and rectangular diaphragms were tested under uniformly distributed lateral loads.
- Continuously spanning floorboards
- Theoretical non-linear load-slip behaviour characteristics of the nail connection.

As discussed before in 2-7-4, non-linearity was assigned only to the fasteners, in this case, nails. Numerical modelling was also similar to those used by Peralta(2004)[14]. Floorboards, joists and cross-bracings were modelled, as elastic frame elements, at their true centre-line. Each floor-board to joist nail connection was modelled using a non-linear link element, they were coupled to the floorboards using rigid frame elements at an adequate spacing of nail couples, as shown in figure 2-50

Further, the link element described to simulate nail connection behaviour is shown in figure 2-51. Moreover, each degree of freedom is explained in the table **??** DoFs $U1$ is fixed so as to prevent elongation or compression of nail, whereas $R2$ and $R3$ are fixed to prevent relative rotation between joists and floorboards, $R1$ which is a torsional rotation is

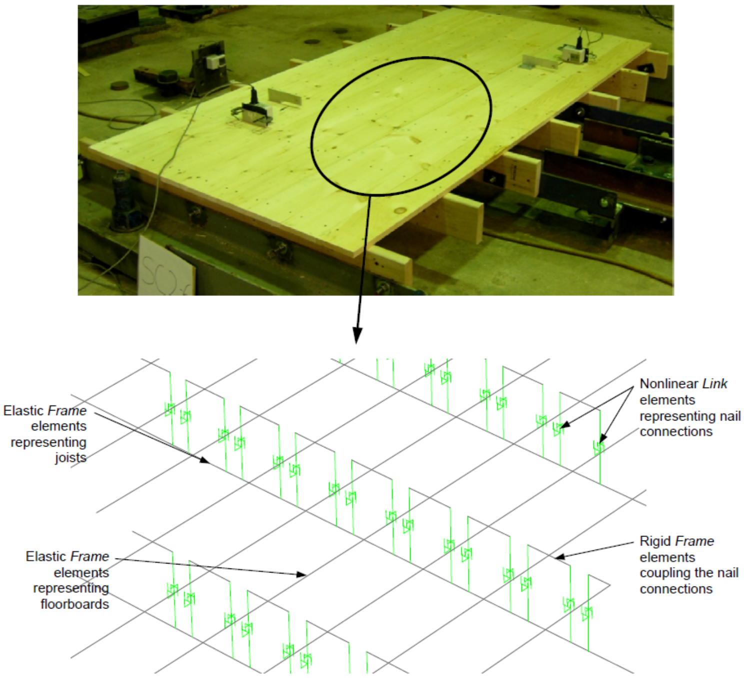

Figure 2-50: Physical Model to Mechanical representation[16]

Degree of Freedom	Condition
U1	Fixed
U2	Nail-slip data
U3	Nail-slip data
R1	Free
R2	Fixed
R3	Fixed

Table 2-2: Degrees of freedom of link element with respect to figure 2-51

free. $U2$ and $U3$ are assigned experimental monotonic and hysteresis behaviour obtained beforehand.

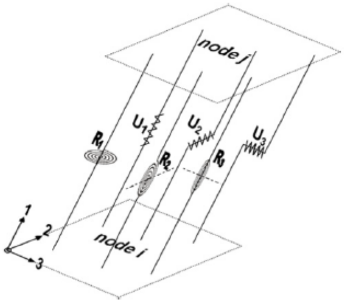

Figure 2-51: Nail Connection using Link element[16]

Chapter 3

Case study description: Detached masonry building

3-1 Modelling of type T3a building - An Overview

To numerically model any structure and to analyse it accurately, a disciplined methodology has to be followed in order to input correct parameters, material properties, physical dimensions and failure criteria. Furthermore, when a complete structure has to be modelled, there exists number of connections between walls, diaphragms, openings. Care should be taken to model these components as failing to do so will give rise to number of errors and convergence issues. The modelling discipline is shown below in figure 3-1.

The structural model will be built along this discipline. The detailed emphasis on each step and sub-step from the physical structure towards the final working numerical model is presented in this chapter.

3-1-1 General overview of the Structure

In this section, an overview of the structure selected for the study is analysed.

There are many types and configurations of masonry houses around Groningen. Analysing each one of them is impractical, cumbersome and time-consuming. However, general topologies have been identified, which is a rough approximation of different kinds of houses found in the area.

The one going to be used in this project is a detached house or a villa. Among the different typologies, this is named T3a. The characteristics of this typology of houses are that more than 50 percent of these kind of houses were built after 1960. Most of these houses

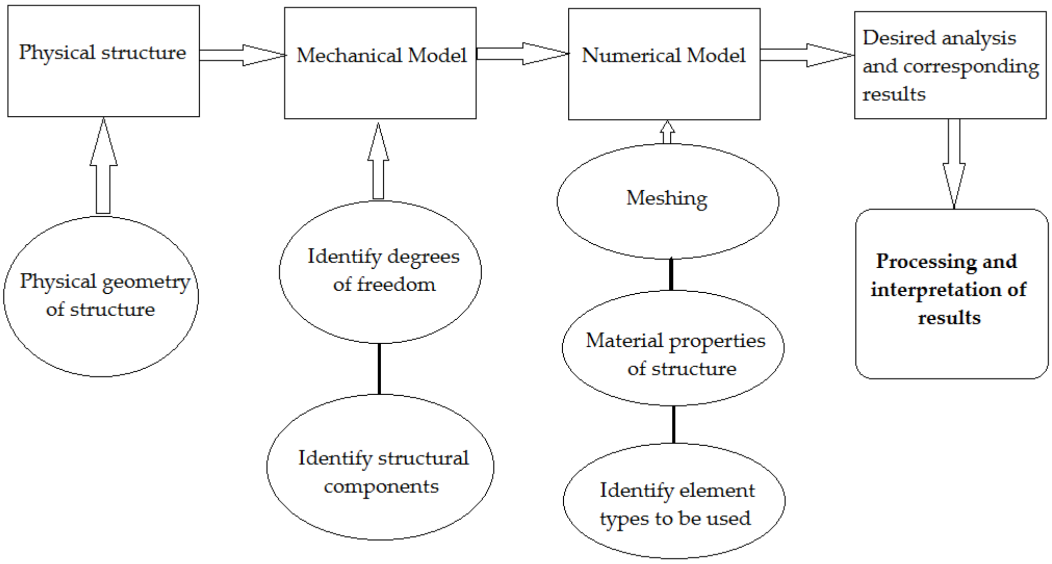

Figure 3-1: Numerical Modelling of Structures - path to be followed

have wooden flooring. The structure has two storeys, has an asymmetric plan layout. The building plan is shown below.

3-1-2 Physical details of the Structure

The detached house is made up of single wythe 230mm unreinforced brick masonry wall. The flooring is made of timber. Superficial details are available regarding the timber diaphragms as provided by ARUP in figure 3-3, however reference is made to important researchers who have studied timber diaphragms in depth, both through testing and numerical modelling. The building has openings of different geometry on all of its walls. Lintels have been assumed to be made of a course of brick masonry itself.

The masonry wall is supported on its footings and is assumed to be a fixed connection to the ground. However, the flooring of the ground storey is not modelled, since its contribution cannot be properly justified without considering soil interaction, since it is in direct contact with soil underneath. Hence, not much emphasis is laid on the sub-structure in this project.

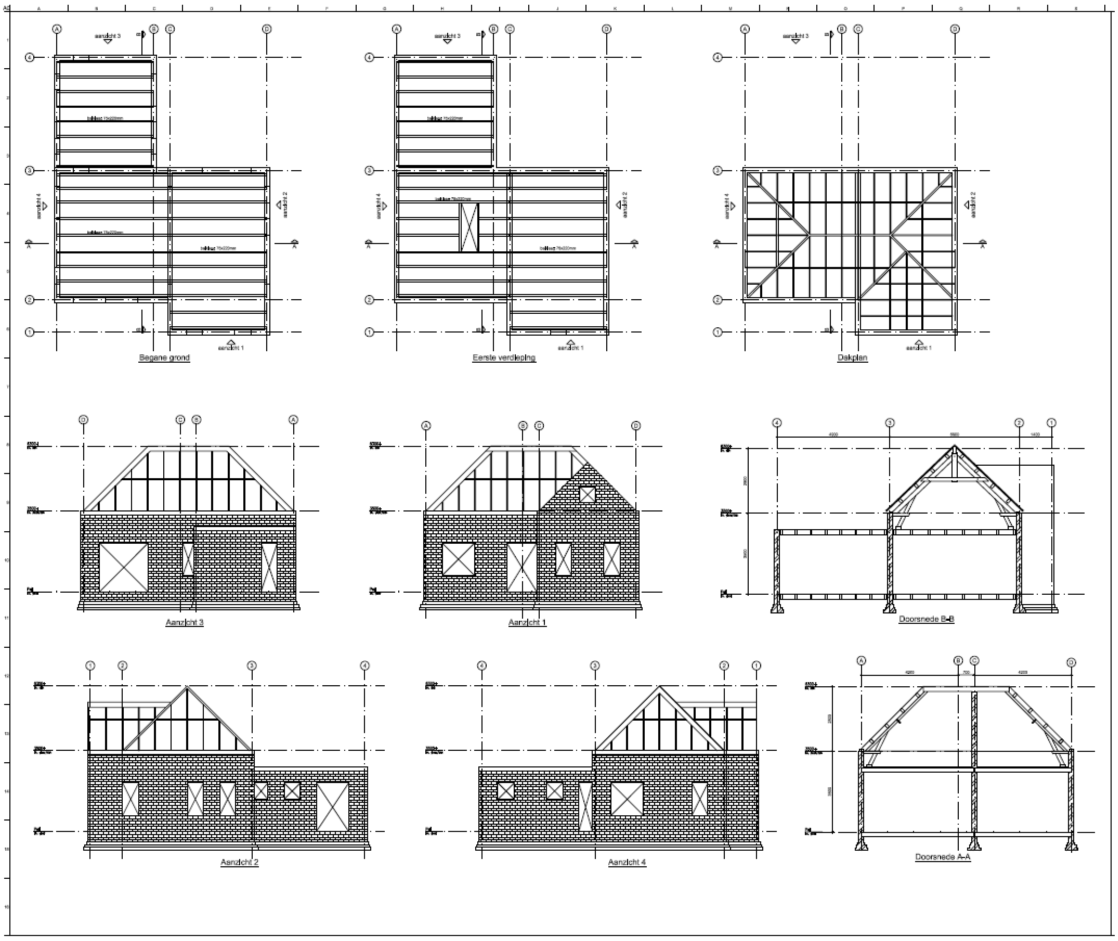

Figure 3-2: Plan for the type T3a building

3-2 General Guidelines for Numerical Modelling of Masonry

Lourenço(2002) has suggested a few good practices with respect to numerical modelling of historic masonry structures, which is extended to general masonry modelling in this project.

- $3D$ idealization of geometry is very time-consuming. Using $8 - node$ bricks with just one element over the wall thickness produces meaningless results.
- Shell elements can be used, but analysis of stress-states along its thickness could be difficult. Also, large thickness of elements gives improper and inaccurate responses.
- Increasing the size and details of a model might lead to loss of clarity of the model.
- Usage of $2D$ model instead of $3D$ model, unless necessary.
- Avoid using shell elements for analysis of global behaviour of a structure.
- Modelling of structural details could be useful than modelling large structures.

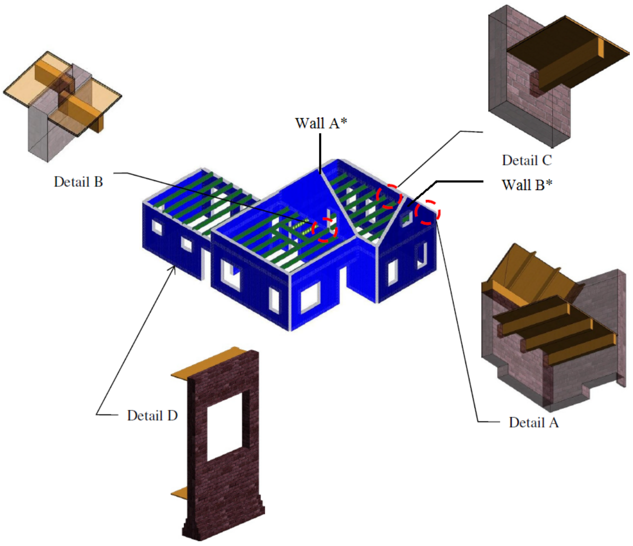

Figure 3-3: Timber diaphragm details provided by ARUP

- Non-linear analysis of is the most powerful method to track the complete response of the structure from elastic range through cracking, crushing upto complete failure.
- Non-linearity can be of two types- Physical and geometrical, which correspond to physical non-linearity in the material and local buckling instabilities, respectively.
- Limit analyses (or plastic analysis) can estimate the failure load, but it is difficult to select an adequate mechanism for a set load combination.
- Though elastic analyses give a rough idea of the behaviour of a structure, it is not practical since masonry does not obey Hooke's law.
- Serviceability limit state is reached during the gradual evolution of cracking, and hence in ULS, tension zones should be modelled carefully.

3-3 Idealization of geometry and structural behaviour

After carefully reviewing all available past and current literature, the modelling strategy is discussed here. The representative masonry wall-timber diaphragm connection assumed in this work, is shown in figure 3-4

- Owing to the size of the *T3a* building, global behaviour is more relevant, which means anisotropic continuum modelling or macro-modelling is adopted.
- Walls are modelled using flat shell and curved shell elements to capture both shear and flexure wall behaviours.

- The bottom end of walls runs down till the foundation level, where a footing holds the wall in place, for which case, the walls are assumed to be fixed to the foundation.
- The timber beam-wall connection is represented by tyings, in which all translations are curtailed.
- The timber flooring is assumed to be made up of timber joists, timber sheath and fasteners to connect the two. In the modelling, however, the timber sheathing is attached to the beam by rigid connection of nodes, representing nail fastenings. This is an assumption, to avoid any relative displacements between timber beam and the timber sheathing.

The following is described graphically in figure 3-5 where a clear transition from physicality to mechanical to numerical model can be observed. Here, only the most important connections are described.

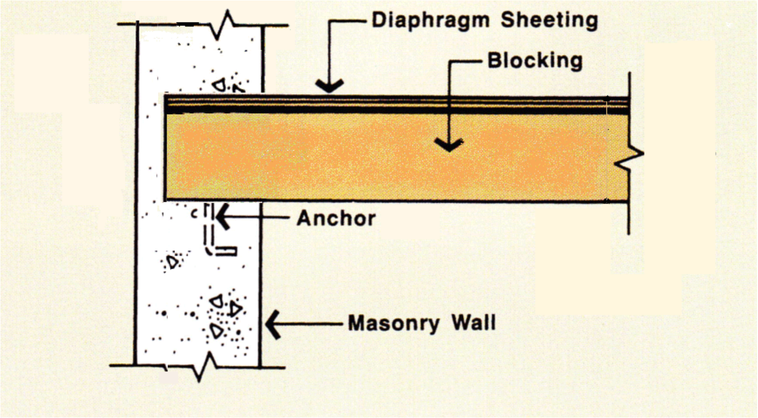

Figure 3-4: Representative masonry wall-timber diaphragm connection

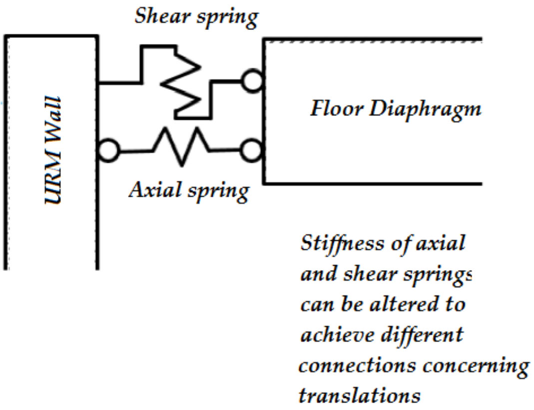

Figure 3-5: Mechanical model of representative wall-diaphragm connection

3-4 Choice of elements for modelling

The behaviour of the several components of a masonry structure is studied, and this governs the choice of elements which can best describe the behaviour of the constituent parts, which in turn contributes to the global mechanism. Keeping that in mind, the following choices are made, as shown in table 3-1.

Part	Finite Elements	Dimensions(mm)	Average mesh size(mm)
URM walls	Flat shell or curved shell (in linear and quadratic order)	Thickness $= 230$	200
Timber beams	Class III-Beam element	$75X220$	200
Timber floor slab	Flat shell or curved shell (in linear and quadratic order)	Thickness $= 25$	200

Table 3-1: Finite element details

Chapter 4

Model and setup for analyses

4-1 Curved Shell Model

A finite element continuum macro-model is prepared to study the response of the structure to different types of loading inputs. Masonry walls and timber floor slab are modelled as curved shell elements *CQ40S*, and beams using *CL9BE*.

4-1-1 Connections

1. *Foundation* - Walls are connected to the ground using node-wise fixed connections, which simulates the foundation. This is shown in the figure 4-1

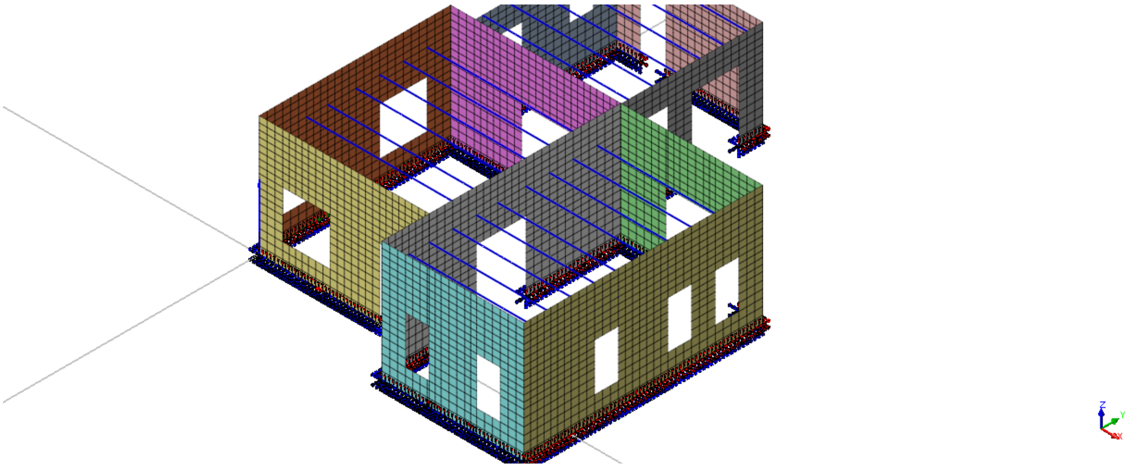

Figure 4-1: Fixed foundation of the structure

2. *Between walls* - Between adjacent walls, common nodes are used in the corner vertices which make sure there is continuity of walls. Refer figure 4-2, the red lines show the

free edges. Absence of red lines means that continuity is maintained or there are no free edges.

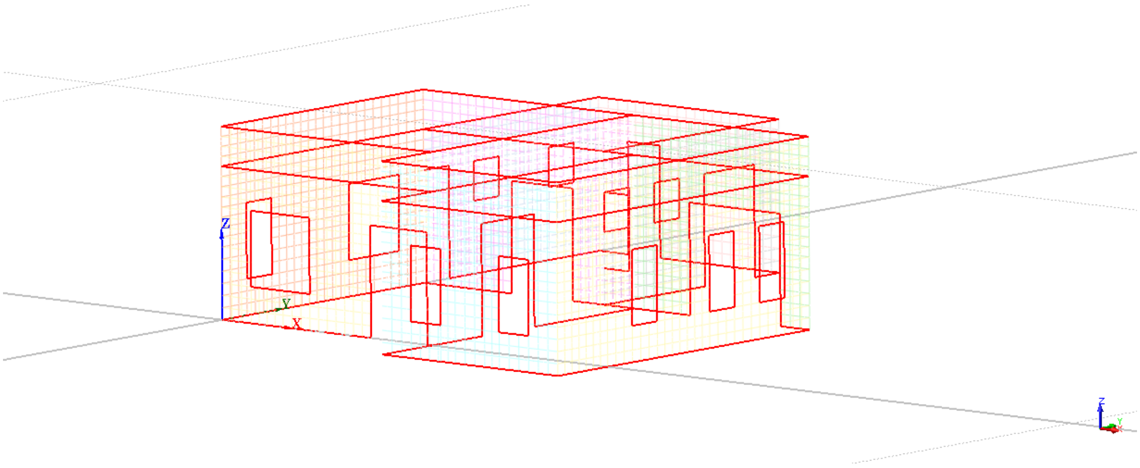

Figure 4-2: Continuity of adjacent walls and free edges

3. *Timber Diaphragm* -

   - Wall-Beam Ends - Fixity conditions between masonry walls and timber beams are either of Fixed or Pinned type. According to the available connection details of this typology as shown in figure 4-6, the beam ends are fixed . However, beams are allowed to undergo rotation in reality. This is one of the important aspects in this thesis and will be dealt with in detail in the subsequent sections. Referring to figure 4-3, the difference in connections is in the usage of, coincident nodes in the previous case and, link elements (shown in red) at every beam end in the latter case, in between beam ends and walls.

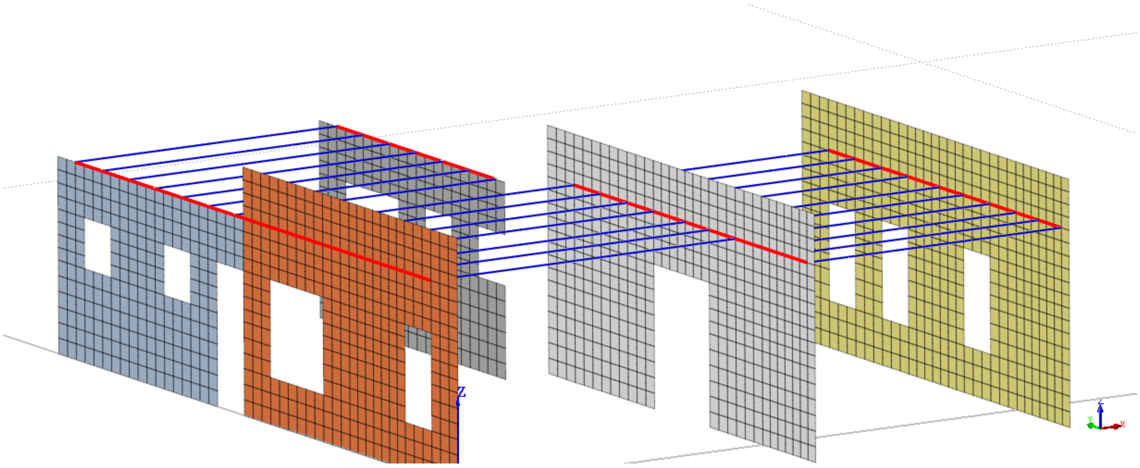

Figure 4-3: Wall-Beam End connections

   - Beam Slab Connection - Timber slabs are attached to the beam ends through coincident nodes. However, the timber slabs are not connected to masonry walls at any point. This is shown in figure 4-4. Colour coding is as follows - Grey in between Blue = Floor Slabs, Blue = Beams, Red Lines = Free edges

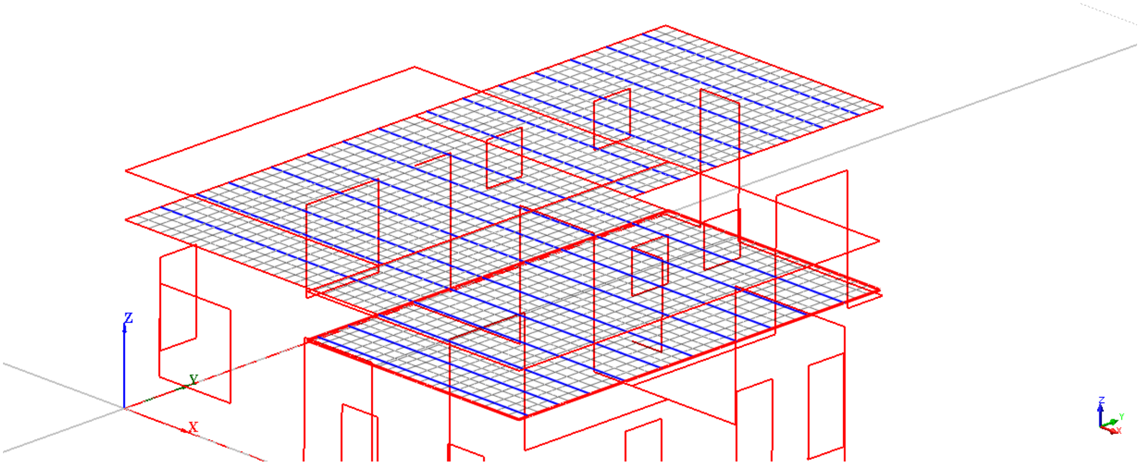

Figure 4-4: Beam Slab Wall connections

4-1-2 Material and Geometric Properties

The typology of the structure under consideration has an asymmetric building layout, refer figure 3-2. This house is built using clay brick masonry and timber components. The material properties for these materials, as suggested by ARUP, are as follows

Material Property		Masonry	Timber
Density	(kg/m^3)	1900	600
	$(N/mm^3/g)$	$1.9 * 10^{-9}$	$6 * 10^{-10}$
Young's Modulus	(MPa)	4410	6000
	(N/mm^2)	4410	6000
Poisson's Ratio		0.25	0.10
Dimension		2D	1D, 2D

Table 4-1: Material Properties

4-1-3 Loading

The loading used here is made of 3 cases. Load combination used for the elastic linear analysis is

$$F_{total} = SW + SDL + 0.24LL \tag{4-1}$$

1. *Gravity or Self Weight - SW* - This load as an effect of gravity ($g = 9810\ mm/s^2$) is derived from the material and geometrical properties of sections, refer table 4-1. The self weight, therefore, naturally differs for different materials and their corresponding section and acts in the negative Z axis according to the model.

2. *Standard Dead Load - SDL* - As its name suggests, it is the standard dead load on the floor slab and this is defined as a face pressure on the floor slabs with a value of 2.5 kPa, i.e $2.5 * 10^{-3}\ N/mm^2$.

3. *Live Loads - LL* - This is the factored live load to be taken into consideration in the loading conditions. This is also applied as a face pressure with a value of 1.75 kPa or $1.75 * 10^{-3}\ N/mm^2$ and a factor of 0.24.

The weight calculations of the structure derived by input of material properties matches numerical calculations by hand. For simplification purposes, roof structure and walls A^* and B^* will not be included in the analysis, refer figure 4-6.

The prepared model is shown in figure 4-5. To begin with, the model will possess numerous issues with respect to stiffness matrices and convergence due to hanging nodes, free edges, improper meshing etc. After numerous iterations and realizing the best methods to model, a stable and accurate model is presented.

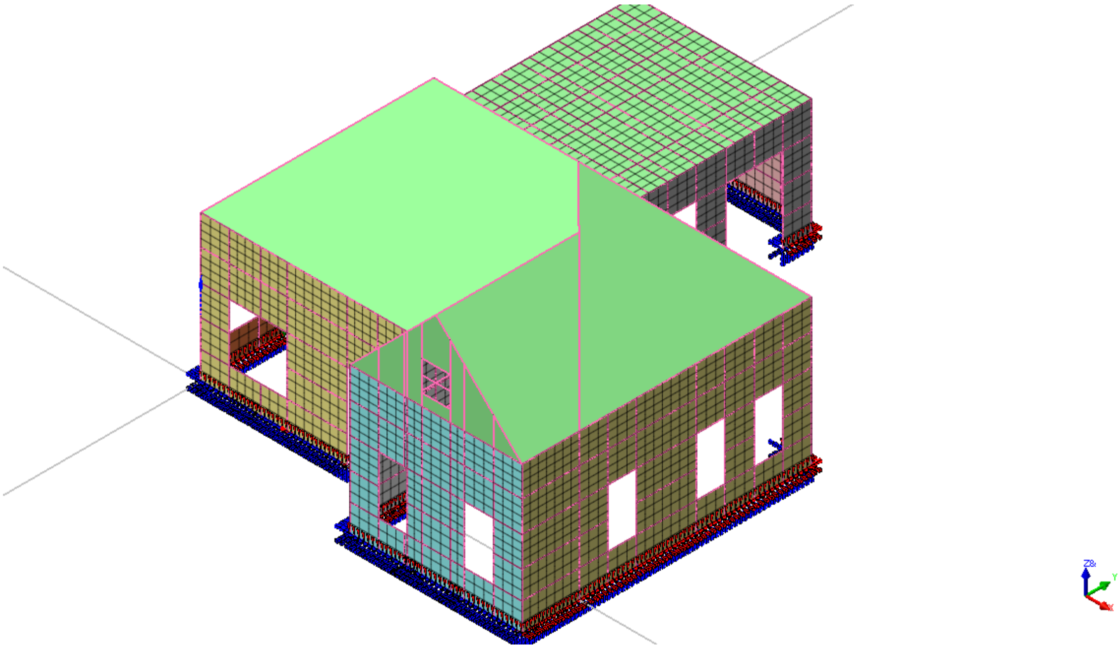

Figure 4-5: Finite Element Model of the structure

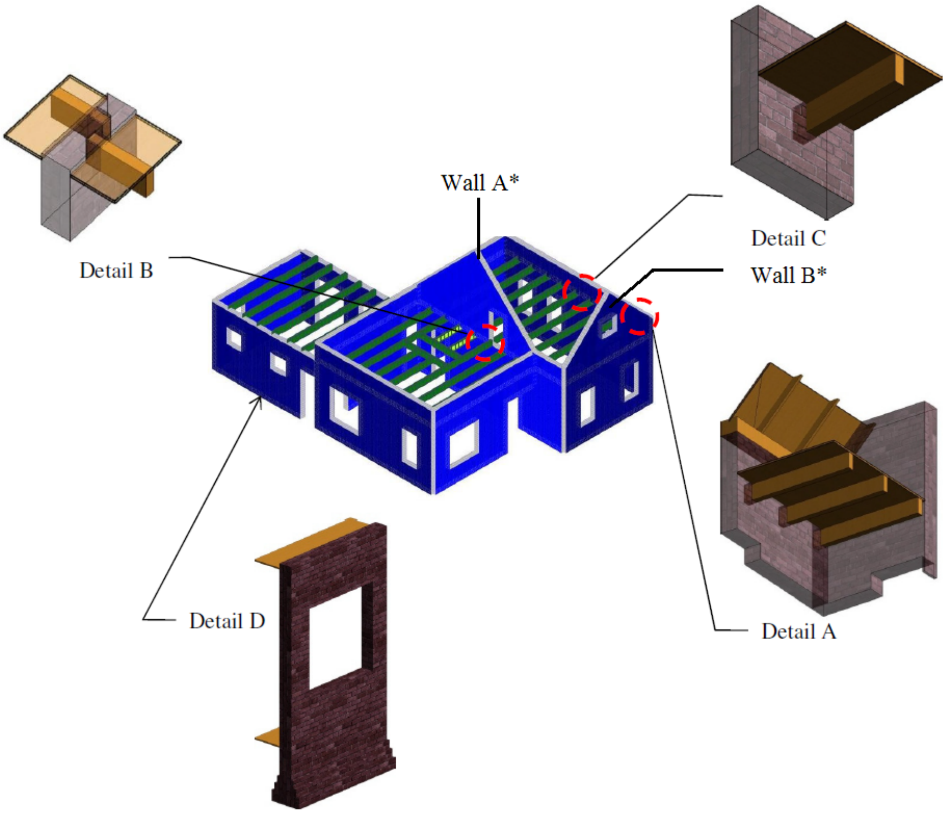

Figure 4-6: Timber beam end connections

4-2 Linear Elastic Analyses

It is always important to check a finite element model by performing a linear static analysis. Such an analysis shows the general deformation of the structure under the elastic theory. This signifies the relationship between the structural parts and it becomes easy to identify modelling errors. For simplification, roof is excluded in the model, however it will be included in the weight calculations of the non-linear analyses which is analysed in further sections.

4-2-1 Linear Elastic Analysis - Beam Ends Fixed - Case 1

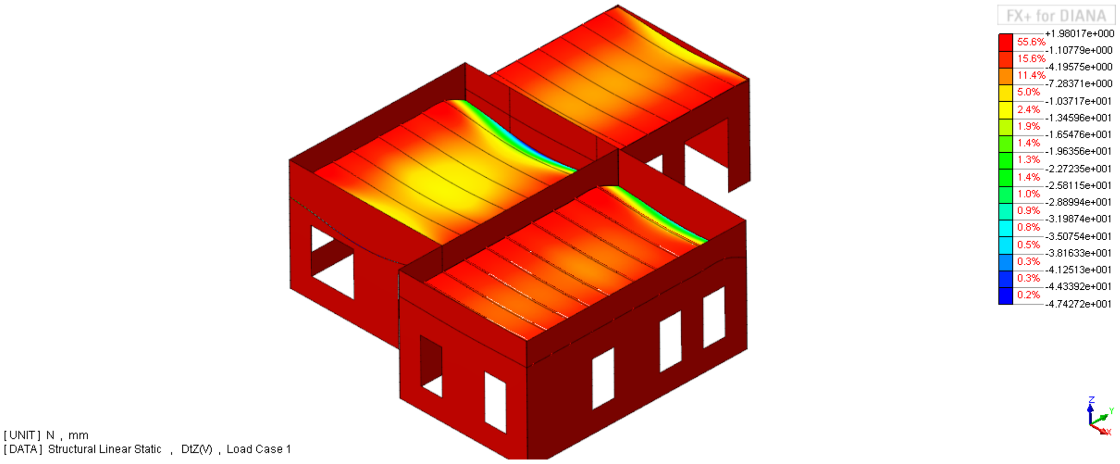

Figure 4-7: Linear Elastic Analyses Result - Beam Ends Fixed

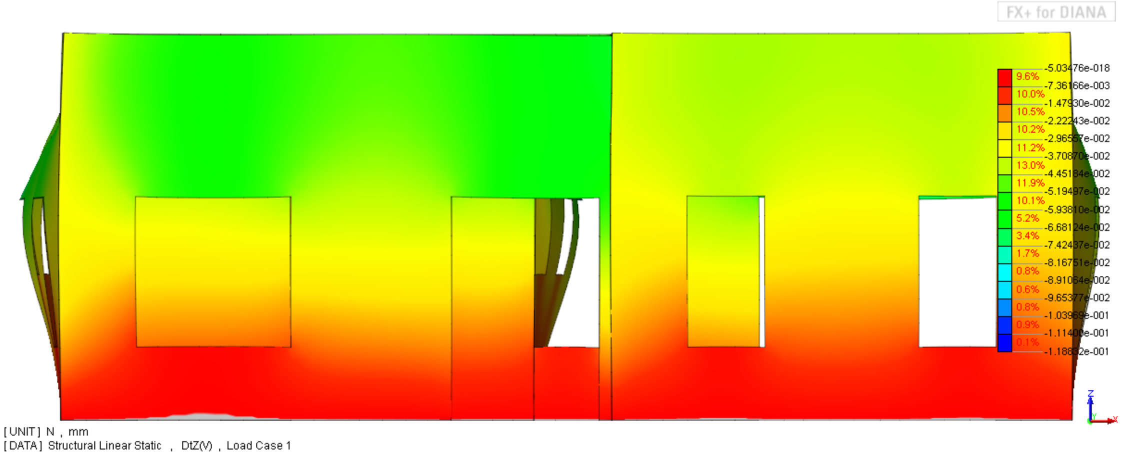

Figure 4-8: Linear Elastic Analyses Result-Wall behaviour - Beam Ends Fixed

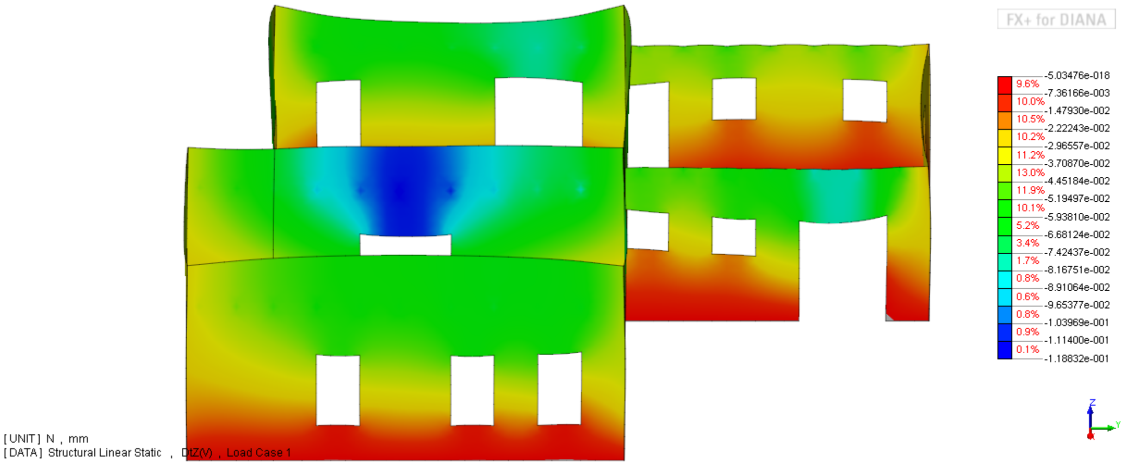

Figure 4-9: Linear Elastic Analyses Result-Wall behaviour - Beam Ends Fixed

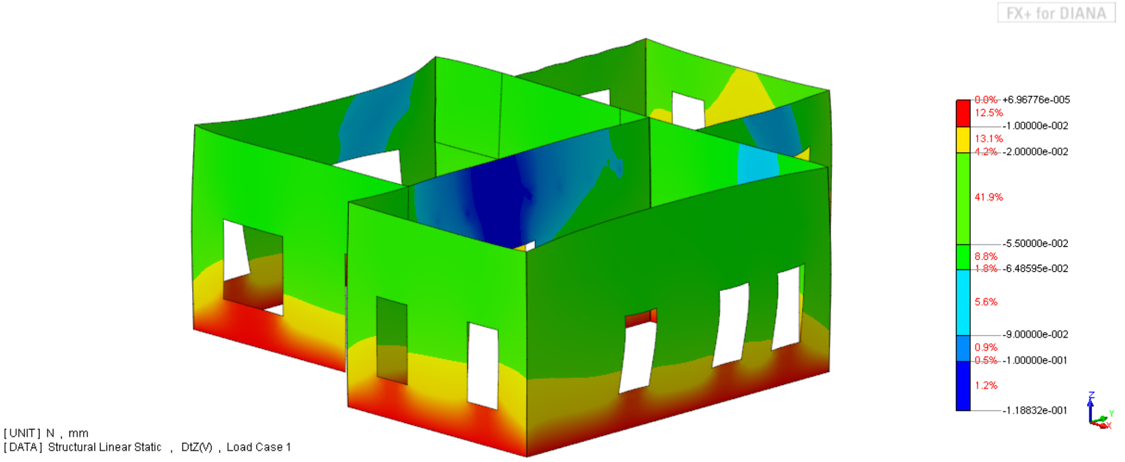

Figure 4-10: Linear Elastic Analyses Result-Wall behaviour - Beam Ends Fixed

The results of the linear static analysis is shown in figure 4-7. Floor Slabs show sagging which verify diaphragm action. Beam ends show least deformation after wall foundation. Figures 4-8, 4-9, 4-10 shows the behaviour of only the walls (beams and floor slabs hidden). It is observed that the wall systems bulge, higher displacement is observed around openings, and the general behaviour is depicted satisfactorily. The response of the timber diaphragm made up of beams and timber floor slab is shown in figure 4-11, grey area representing upward displacement and the red area showing displacements between $+0.1$ to -0.1 mm. It is observed that the beams simulate the fixed end conditions. The diaphragm system can be seen hogging at the free ends, beam ends show negligible displacement and confirming that the modelling is accurate.

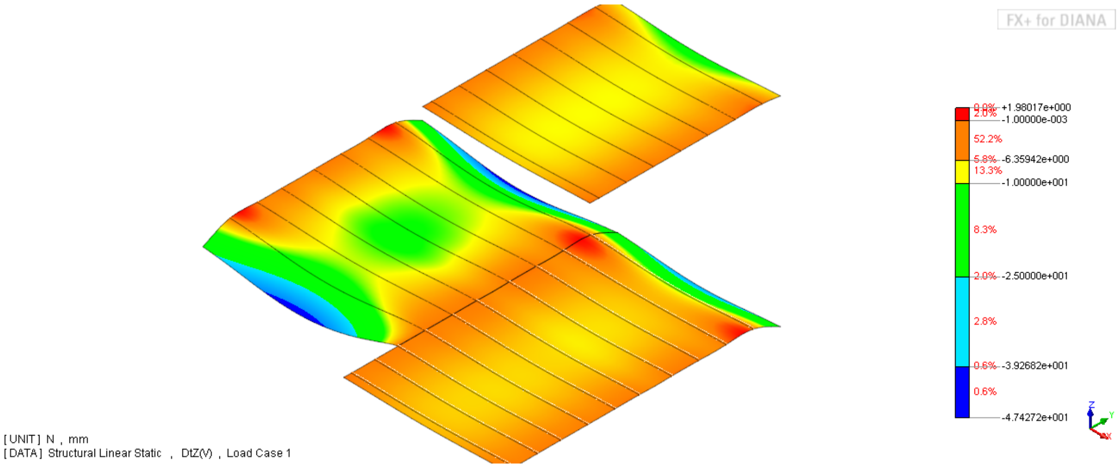

Figure 4-11: Linear Elastic Analyses Result- Timber Diaphragm system - Fixed Beam Ends

4-2-2 Linear Elastic Analysis - Beam Ends Pinned - Case 2

This section shows the linear elastic check for a similar model as described in the previous section. However, the difference is that the beam ends are simulated to be pinned in this case. *Link Elements* are used to connect the masonry walls to the beam ends. The advantage in using link elements is that the user can manipulate the degrees of freedom between nodes of two different elements which are intended to be connected, in this case - *shell and beam elements*. The floor system is similar to the previous case.

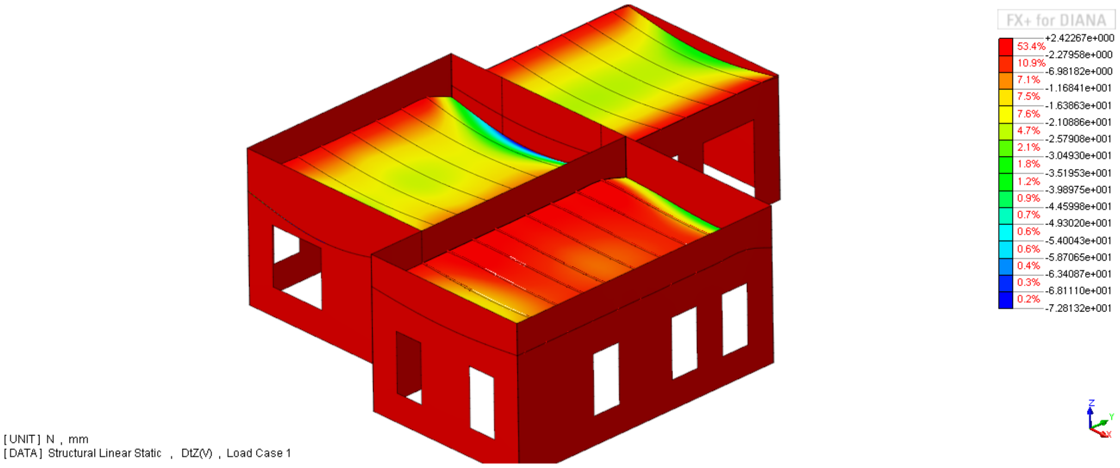

Figure 4-12: Linear Elastic Analyses Result - Beam Ends Pinned

The behaviour of walls slightly differs with respect to the previous case, refer figures 4-8, 4-9, 4-10. Figures 4-13, 4-14, 4-15 show the behaviour for the case of beam ends pinned. The timber diaphragm exhibits a different behaviour compared to the fixed end, which is expected, as shown in figure 4-16. The beam ends rotate more freely showing higher displacement of timber diaphragm system.

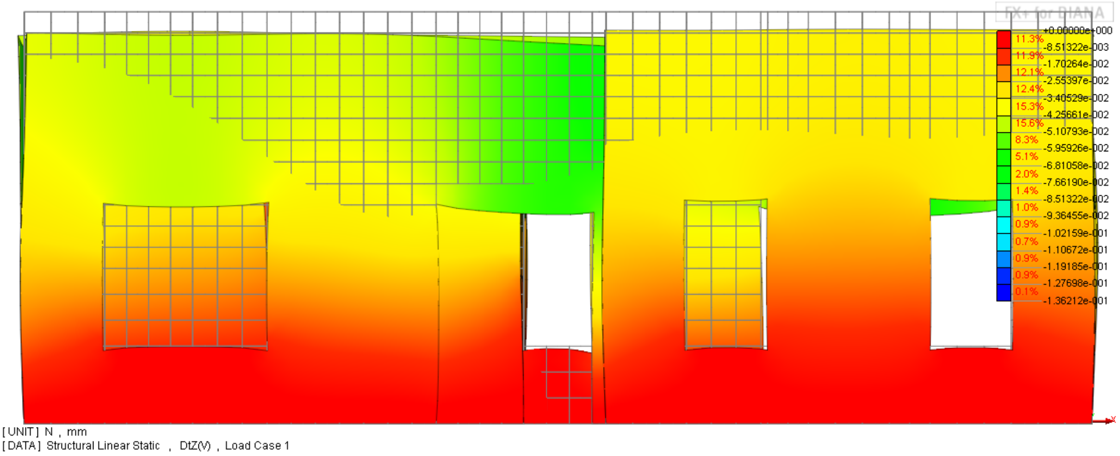

Figure 4-13: Linear Elastic Analyses Result - Walls - Pinned Beam Ends

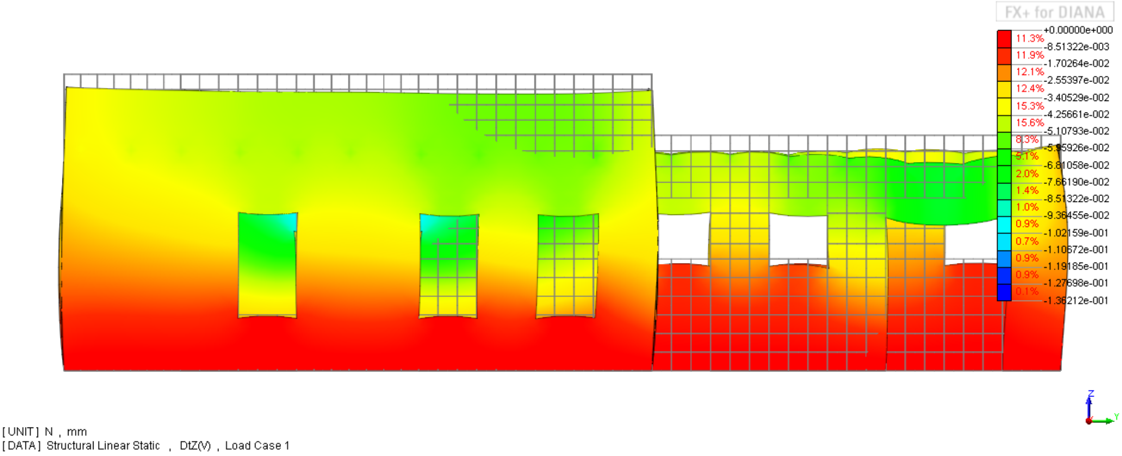

Figure 4-14: Linear Elastic Analyses Result - Walls - Pinned Beam Ends

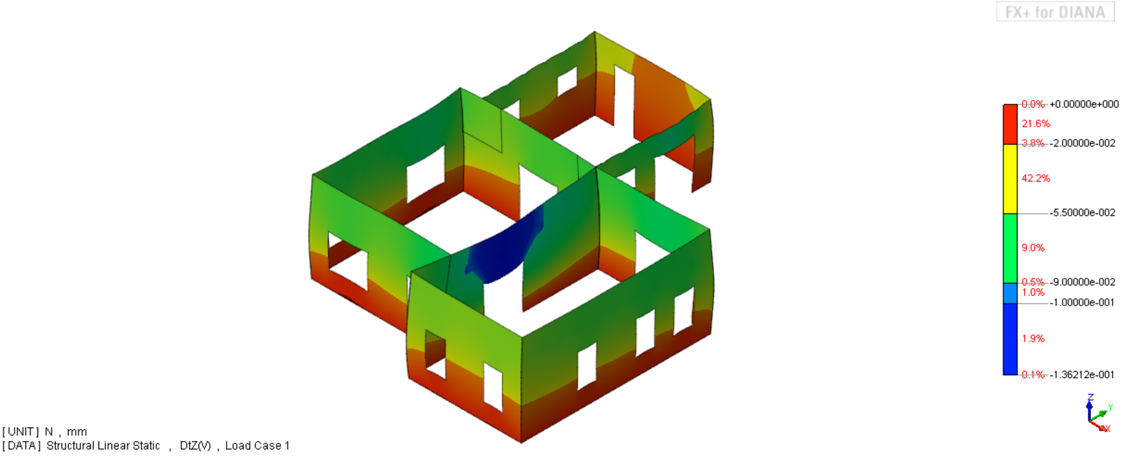

Figure 4-15: Linear Elastic Analyses Result - Walls - Pinned Beam Ends

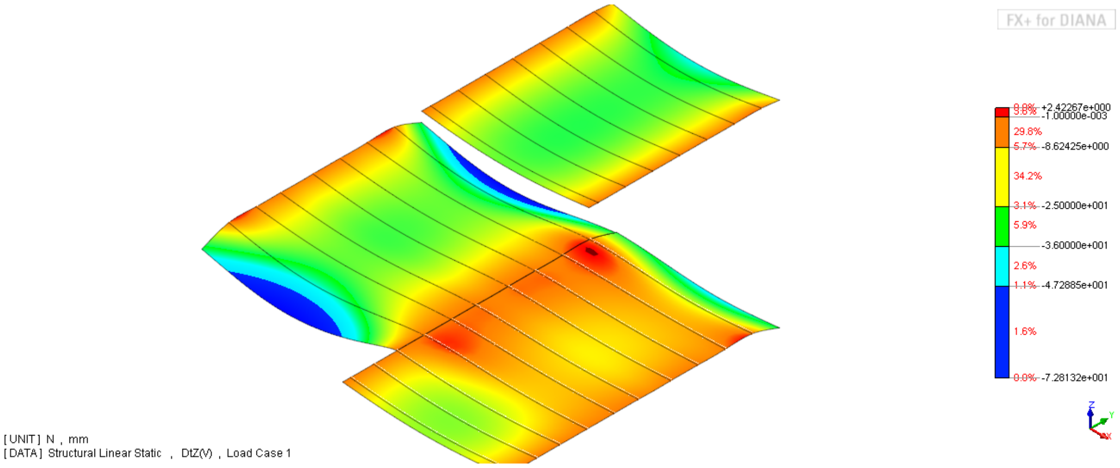

Figure 4-16: Linear Elastic Analyses Result - Timber Diaphragm system - Pinned Beam Ends

4-2-3 Inference from Linear Elastic Analyses

The main differences between the two models as analysed are as follows

1. Beam Behaviour - The beams behave very differently according to their boundary conditions. This can be seen in figures 4-17 and 4-18. Fixed end beams show less rotation and hence less deformation.
2. Wall System - Wall system in case 1, with help from the beams, undergoes convex curvature displaying higher stiffness in comparison with case 2, which show bulging and concavity. Also, the deformation is higher in case 2. This can be clearly seen by comparing figures 4-10 and 4-15.
3. Timber Diaphragm - This system behaves similarly in both the cases. However, as is the case, deformation is higher in case 2. Deformation pattern is also similar in both cases. Refer figures 4-11 and 4-16.

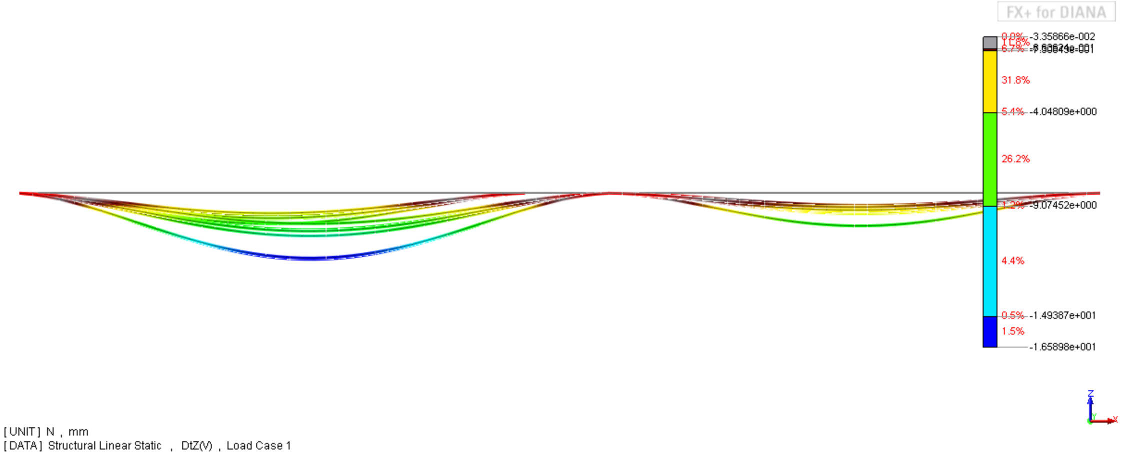

Figure 4-17: Linear Elastic Analyses Result - Fixed Beam Ends

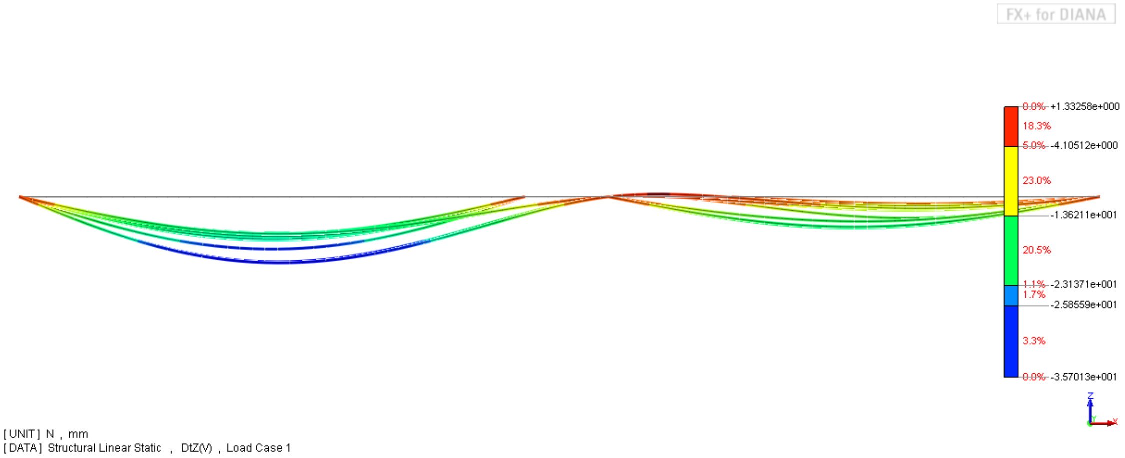

Figure 4-18: Linear Elastic Analyses Result - Pinned Beam Ends

4-3 Eigenvalue Analyses - Results

Eigenvalue analysis was performed on both the cases, as discussed in elastic linear analyses, and the first 50 natural frequencies were determined. Structural stiffness being different for both cases (i.e. different beam end conditions) can be seen in the eigenvalue response.

Direction	Mode Number	Frequency(Hz)	Effective mass participation (%)
X-direction	8	18.476	13.827
	10	18.871	13.100
	22	26.160	10.847
Y-direction	5	16.555	3.986
	6	18.015	9.394
	8	18.476	4.541
Z-direction	17	23.356	0.580
	20	25.132	0.872
	Higher significant effective mass participation percentage not found		

Table 4-2: Structural Eigenvalue response - Case 1 - Beam ends *fixed*

Direction	Mode Number	Frequency(Hz)	Effective mass participation (%)
X-direction	18	18.423	23.167
	29	26.080	11.667
Y-direction	9	13.902	6.696
	16	18.014	9.341
	18	18.423	5.838
Z-direction	15	17.588	1.040
	Higher significant effective mass participation percentage not found		

Table 4-3: Structural Eigenvalue response - Case 2 - Beam ends *pinned*

Generally, the modes in which higher than 80% of the effective mass is involved, is used as the most significant mode. However, the mode shapes for the highest EMPF for X and Y direction for both cases are shown in figures 4-19 and 4-20. Response for the other direction has been omitted as the EMPF was found to be negligible, refer tables 4-2 and 4-3.

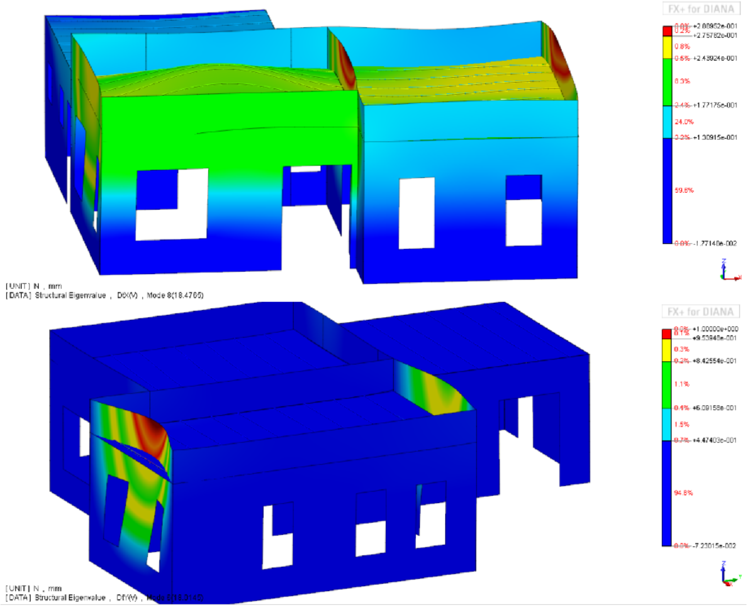

Figure 4-19: Eigenmode with highest mass participation in X and Y directions - Case 1

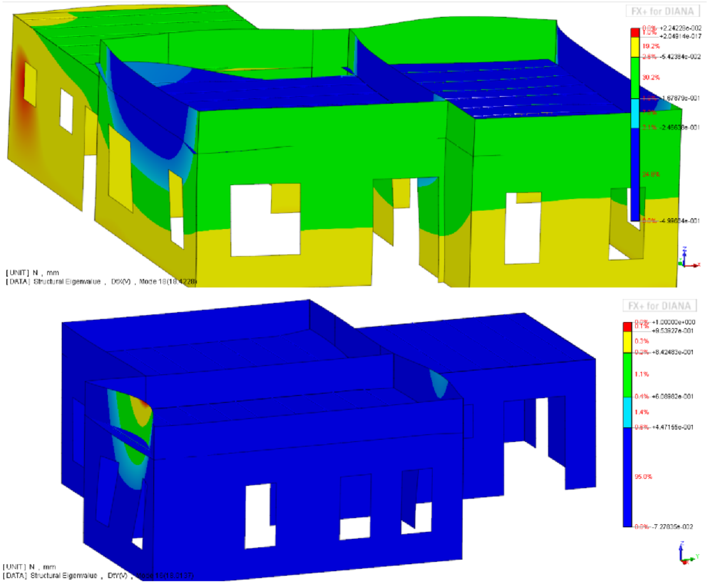

Figure 4-20: Eigenmode with highest mass participation in X and Y directions - Case 2

4-4 Non-Linear Time History Analyses - The Setup

It is understood widely that a detailed study of such a structure necessitates non-linear analyses. Some of the important seismic analyses carried out on masonry specimens using shake tables and real or factored earthquake signals are discussed earlier in section 2-4. To carry out similar tests on computational models, it is inevitable to use non-linear analyses, because of its accuracy and detail in the response. This will naturally help us understand the seismic behaviour of the structure better. Accordingly, an earthquake record of acceleration v/s time is input using base excitation, and its results are studied. In this regard, time-history data is applied parallel to each direction axis of the structure. So, base excitation is input along X, Y and Z directions separately and their results are studied accordingly.
The model is similar to the one described in section 4-1 with some minor modifications to suit the non-linear regime, which are detailed below.

4-4-1 Finite Element Modelling and Connections

There are no changes with respect to the model being used for the non-linear analyses, including connections, as described in section 4-1-1. The mesh quality can be determined by looking at the aspect ratio of elements, as shown in figure 4-21. An aspect ratio reaching 1 implies that the elements approach a square, and it can be observed that about 94.5% of the elements have an aspect ratio > 0.90. It is important to note that all non-linearity has been concentrated into masonry, as sufficient detail regarding timber material was unavailable. Hence, masonry is the material of focus in this analysis. To increase accuracy and detail of the analysis, $3 * 3 * 5$ numerical integration is used for shell elements simulating masonry.

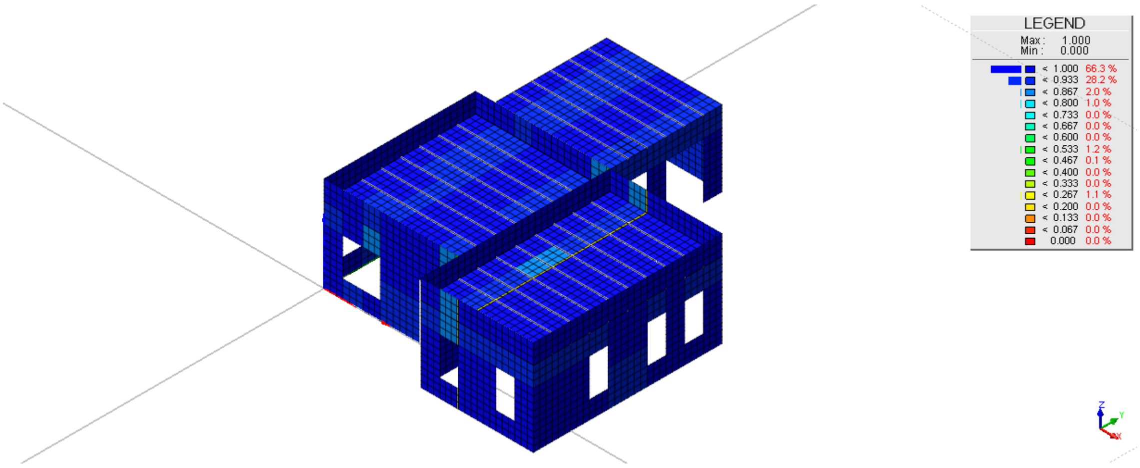

Figure 4-21: Mesh quality - Aspect ratio of elements

4-4-2 Material Properties

Masonry Properties	
Property	Value (Units)
Material class	Concrete
Density	$1.9 * 10^{-9}$ $(N/mm^3/g)$
Young's modulus	4410 (N/mm^2)
Poisson's ratio	0.25
Decrease in Poisson's ratio	None
Constitutive model	Fixed stress-strain
Total Strain Crack model	Fixed
Tensile softening	Exponential
Tensile strength (f_t)	0.10 (N/mm^2)
Mode-I fracture energy (G_f^I)	0.015 (N/mm)
Lateral influence on cracking	None
Compression behaviour	Parabolic
Lateral influence on compression	None
Compression strength (f_c)	6.30 (N/mm^2)
Compression fracture energy (G_c)	43.4 (N/mm)
Rayleigh damping mass co-efficient (a)	4.036 $(1/s)$
Rayleigh damping spring co-efficient (b)	$1.13 * 10^{-4}$ (s)
Shear retention type	Damage based

Table 4-4: Non-linear material properties of masonry

Non-linearity is confined to masonry and hence, applied to masonry only. The timber beams and floor behave elastically. The following table enlists the material properties and modifications used for the non-linear analyses.
The constitutive model used in the analysis is the total strain crack model, in which, the stress at any point in the material is derived as a function of its strain. Under this concept, two types of crack models can be used as discussed before namely, *rotating crack* and *fixed crack*. In these analyses, the fixed crack model is selected.

4-4-3 Loading

Loading for this analysis is of two types-

1. *Static Loads* - These loads are similar to the ones discussed in section 4-1-3. However, the loading is differently applied here.
    - Gravity load is removed so as to not interfere with earthquake loading. However they are modelled as volume loads since cracking is confined only to masonry.
    - All imposed loads on the floor slabs have been calculated and converted to point loads at beam ends following flow of load from floor to beam to beam supports

in eventuality. The calculations for these loads are shown in appendix. It is to be noted that these loads were applied as first load set for all dynamic analyses as well in order to prevent cracking due to these loads.

- Roof structure is not included as indicated before. However, the weights of two masonry walls A^* and B^*, that have been excluded in the model due to the reason that they are sure to fail first as the maximum displacement will occur at the highest points in the structure, are included in the volume loads for the walls directly below them.

2. *Time based earthquake load* - This load is applied by base excitation coupled with acceleration due to gravity ($g = 9810\ mm/s^2$) in the desired direction of excitation. The earthquake load applied to each analysis will be shown, graphically, accordingly. Two sets of time-history were given to be used as input. The two signals are shown below in figures 4-22 and 4-23. One is encouraged to view the detailed tabular format given in the appendix.

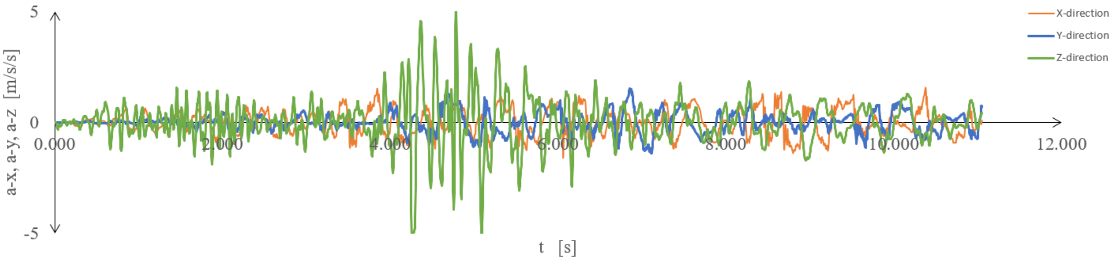

Figure 4-22: Time history inputs - Record 1 - Along all 3 axes

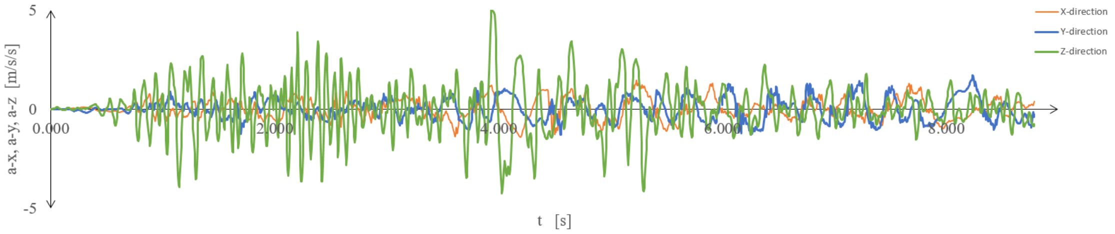

Figure 4-23: Time history inputs - Record 2 - Along all 3 axes

4-4-4 Expected failure pattern

After studying through various literature and theory on the behaviour of masonry buildings, it is important for an engineer to be able to predict, based on his knowledge, the general behaviour of any given structure under seismic loads. Such expected failure patterns are described below for the current structure. Since it is a rectangle box-type structure, failure could be attributed to either a single or multiple mechanisms.

1. Early structural collapse - This type of failure will occur as an effect of loss of/missing connections between walls. However, it is ensured that the connections between walls are continuous and is discussed in section 4-1-1 and figure 4-2.

2. In-plane walls - These walls, which are parallel to the direction of the applied seismic load, may undergo the typical failure patterns like the diagonal or stair type cracking and/or rocking behaviour along with sliding behaviour if overburden load is relatively less, as described in section 2-3-1. Such walls are labelled in the figure **??** below.

3. Flexure walls - These walls are perpendicular to the direction of seismic loading in the structure. Typically, they form a yield pattern as discussed in section 2-3-2.

4. Failure due to low capacity - This is one of most recurring causes of seismic failure in masonry structures. Parts of the masonry structure which are susceptible to such a failure are the openings- such as windows and doors. So, it may follow that the walls with the openings are prone to failure, irrespective of whether they are shear or flexure walls. Also, in the current structure prone to earthquake forces, it is difficult to pin point to the exact mechanism of failure, but can be anticipated by continuously studying the development and growth of cracks, principal strains and stresses.

4-4-5 Percentage by area of openings in walls

The table below describes the percentage by area of openings- inclusive of doors and windows, in each of the walls. It is to be read in reference with the figure **??**. It is to be noted that walls $IP1$ and $IP2$, have equal areas but different openings, which is similar to the pairs $IP4$ and $IP5$, $OP2$ and $OP4$ and $OP3$ and $OP5$.

In-plane walls	Percentage of openings	Out-of-plane walls	Percentage of openings
IP1	26.65%	OP1	14.65%
IP2	21.61%	OP2	17.90%
IP3	12.92%	OP3	12.10%
IP4	13.08%	OP4	28.40%
IP5	30.02%	OP5	11.69%

Table 4-5: Walls and their percentage openings

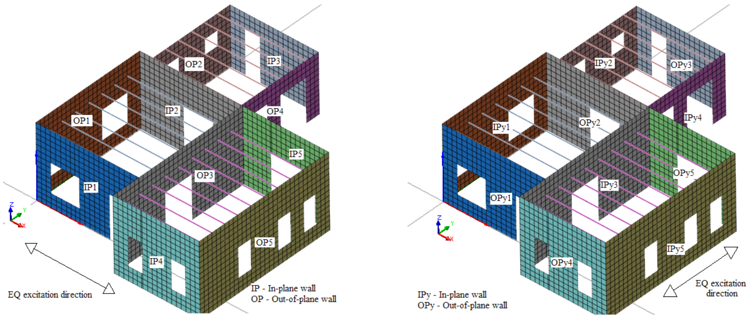

Figure 4-24: Wall type and nomenclature with respect to earthquake excitation in X-direction and Y-direction

Under seismic loading, the walls of a masonry structure play a major role in re-distribution of forces by box behaviour. The force flows firstly through in-plane walls and then onto diaphragms which in turn activates the out-of-plane walls. However, the presence of openings can undermine its capacity for the flow of forces. Hence, it is important to calculate the percentage of openings to gauge its significance under seismic loading. Here, the walls $IP5$ and $IP1$ have the highest percentage of openings. However, $IP1$ has two openings on the same wall which further reduces its resistant capacity. Similarly, $OP4$ also consists of two such openings. Generally, cracking and/or damage would occur at such weak points.

Chapter 5

Non-linear analyses

In this chapter, the non-linear time history analyses (NLTHA) are discussed in detail. In reality, earthquake forces do not act exactly along the primary axes of the structure, but such an assumption is made to understand the behaviour along three primary axes of the model (structure). Similarly, to simplify the analyses, a few assumptions have been made. These have been discussed before, however, a recap is given to make certain things clear before the analyses are performed.

Assumptions

1. Roof structure and two walls (A*,B*) have not been included in the model, however, the weight of the walls has been included in static loading (volume loads), on the walls directly below. This is done to avoid the obvious failure of these particular walls, since there at the highest level in terms of height.

2. All imposed static loads, such as SDL and LL, have been converted by calculation to point loads at beam ends, eventually acting on the walls which act as supports. This is done to avoid initial failure of timber diaphragm system, since it is modelled as an elastic material.

3. Following from the previous point, non-linearity (e.g. - cracking, Rayleigh damping, etc.) is confined to masonry only (to maintain focus on masonry), and hence its weight is modelled as volume loads.

4. Non-linear time-history analyses are strictly directional. Time-history data is input using base excitation(combined with $g = 1980\ mm/s^2$) and energy norm is used for convergence.

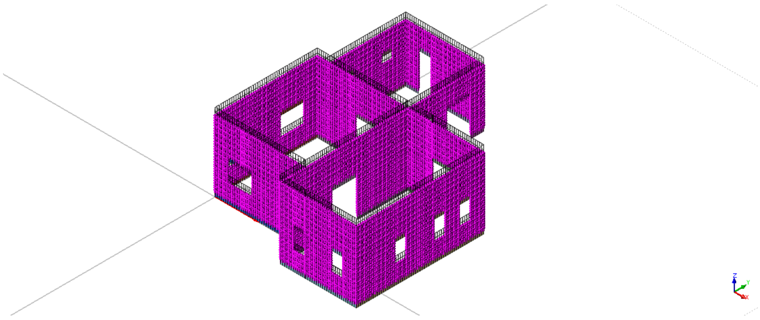

Figure 5-1: Non-linear analysis - Static volume loads - Input

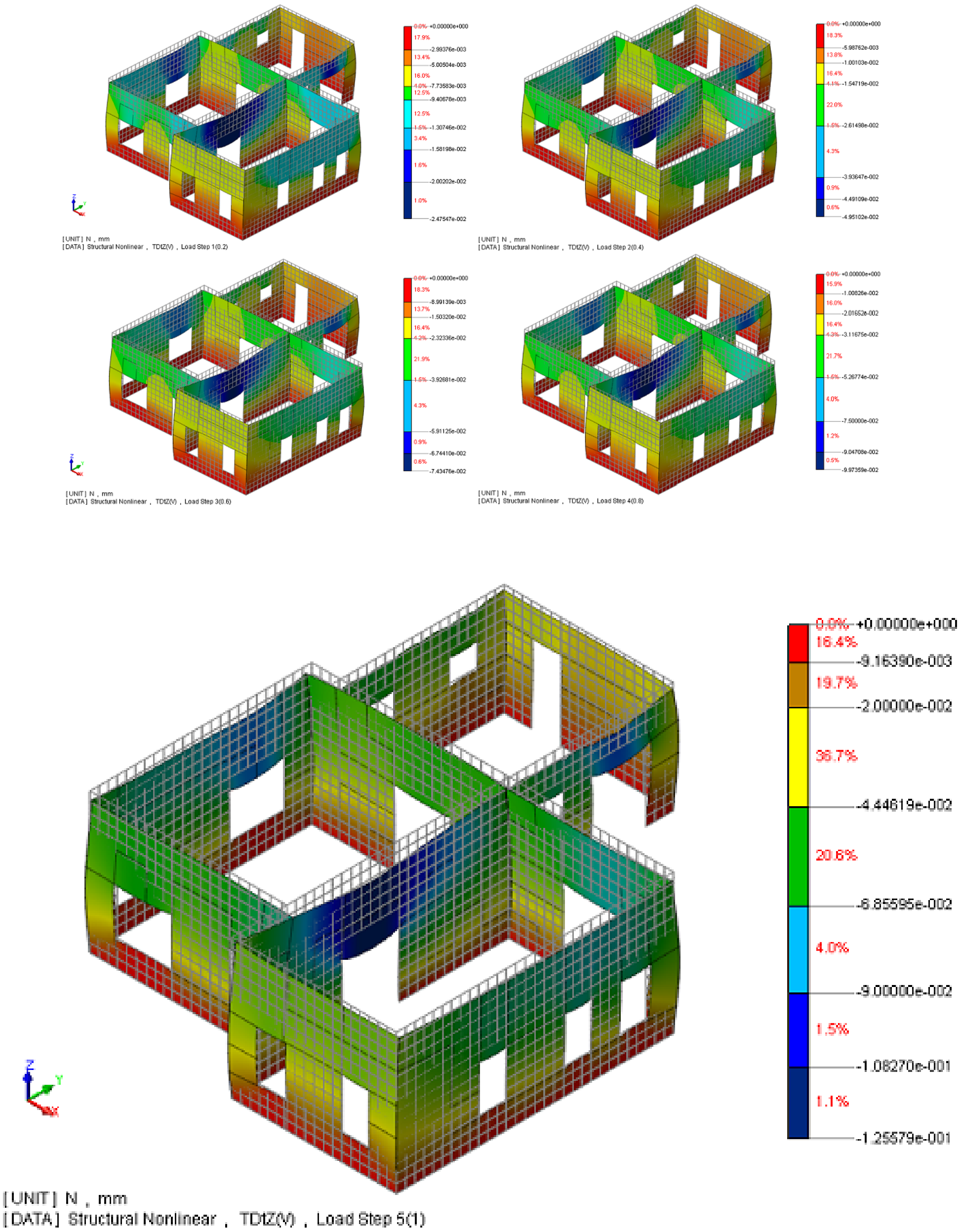

Figure 5-2: Non-linear analysis - Static loads - 5 steps - Load factor 0.20

Non-linear analysis - static loads

The static loads are applied in the initial 5 load steps, with a load factor 0.20. This is the same in all the non-linear analyses, since the static loading is the same, refer figure 5-1 and is hence presented at the beginning of this section. Results are similar to the elastic analysis except that all loads act on the shell elements only, refer figure 5-2.

5-1 Analysis along X-direction

To understand the seismic behaviour of the structure, it is important to determine its behaviour using scaling of the input signal. The idea behind analysing using different levels of scaling (in ascending order) is to find the least level of time history input that does not induce any significant damage leading to failure of the structure. Since the values given are already in acceleration units, it is not required to further multiply the applied load with acceleration due to gravity. However, the time history values are given with respect to $0.16g$. However, the signal along Z-direction is the only one conforming to $0.5g$. Furthermore, the signals along X and Y direction conform to $0.16g$. The maximum value for surface motion under foundation beams available in time history input with a scaling to $0.16g$ along X-direction is 1.57234 m/s^2.

This value corresponds to Shindo number 4 of the Japan Meteorological Agency (JMA) scale and approximately to the intensity V-VII of Mercalli Scale. According to the JMA, seismic activity of this level results in shaking of residential buildings, with slight damage and appearance of small cracks.

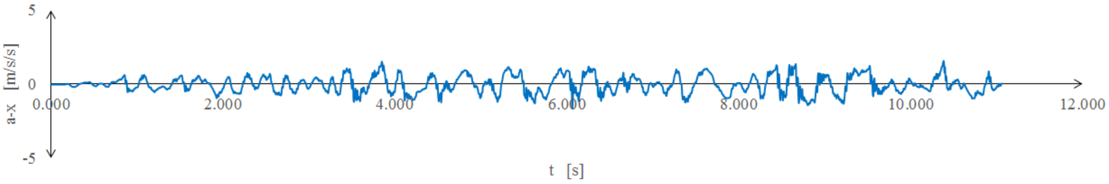

Figure 5-3: Time history input - Record 1 - Along X-axis, scaled to $0.16g$

By calculating the ultimate crack strain in the global structure, it is possible to understand the crack phases. In these analyses, exponential tensile softening is assumed, and hence the corresponding ultimate crack strain is given by the following equation. However, the crack is considered to be in the fully open stage when $\varepsilon_{nn}^{cr} > 2 \times \varepsilon_{nn.ult}^{cr}$.

$$
\begin{aligned}
\varepsilon^{cr}_{nn.ult} &= \frac{G^I_f}{f_t * h} \\
\varepsilon^{cr}_{nn.ult.min} &= \frac{f_t}{E}
\end{aligned}
$$

$$
\begin{gathered}
\text{where, } \varepsilon^{cr}_{nn.ult} \text{ is the ultimate strain in masonry} \\
G^I_f \text{ is the mode-I fracture energy} \\
f_t \text{ is the tensile strength} \\
h \text{ is the crack bandwidth} \\
\varepsilon^{cr}_{nn.ult.min} \text{ is the minimum ultimate strain in masonry} \\
E \text{ is the Young's modulus of masonry}
\end{gathered}
\tag{5-1}
$$

Similarly, for compression regime, parabolic softening is assumed. In this case, the ultimate compressive strain is calculated differently. $\alpha_{c/3}$ is the strain at which one-third of the maximum compressive strength is reached. α_c is the strain at which maximum strength is reached. However, the ultimate crack strain in compression after the material has undergone softening is given by α_u. The following equation gives the idea of these different strains -

$$
\begin{gathered}
\alpha_{c/3} = -\frac{1}{3}\frac{f_c}{E} \\
\alpha_c = -\frac{5}{3}\frac{f_c}{E} = 5\alpha_{c/3} \\
\alpha_u = \alpha_c - \frac{3}{2}\frac{G_c}{h * f_c} \\
\text{where, } f_c \text{ is the maximum compressive strength of masonry} \\
E \text{ is the Young's modulus of masonry} \\
G_c \text{ is the compressive fracture energy of masonry} \\
h \text{ is the characteristic element length}
\end{gathered}
\tag{5-2}
$$

According to the current modelling strategy, an approximate mesh width of $200mm$ is used, i.e. $h \approx 200mm$. From the table 4-4, we can calculate the ultimate tensile and compressive strains that the masonry can withstand. The values are

$$
\varepsilon^{cr}_{nn.ult} = 1.50 * 10^{-3} \text{ , } \varepsilon^{cr}_{nn.ult.min} = 2.268 * 10^{-5} \text{ and } \alpha_u = -54.05 * 10^{-3} \tag{5-3}
$$

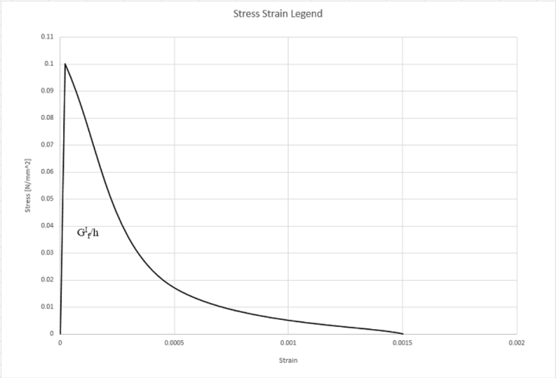

Figure 5-4: Stress-strain legend for cracking strain

These values conform to the notion that the compressive fracture energy are approximately higher than 50 times the tensile fracture energy.

5-1-1 NLTHA - X direction - $0.16g$

Input

The input signal is shown above in the figure 5-3. However, for an input of $0.16g$, the values were input as is. Time steps are of $0.01(s)$ applied in 1200 steps totalling to $12s$. Also, 50 iterations per time step was input to achieve convergence with an energy tolerance of $1 * 10^{-4}$. The seismic response of the floor slabs are depicted in the following subsection. For the same, the three different floor slabs are named as shown in the figure 5-5. In this analysis, two configurations of the beam ends are studied. First, the model with pinned end beams at first storey were studied, followed by the model with fixed end beams.

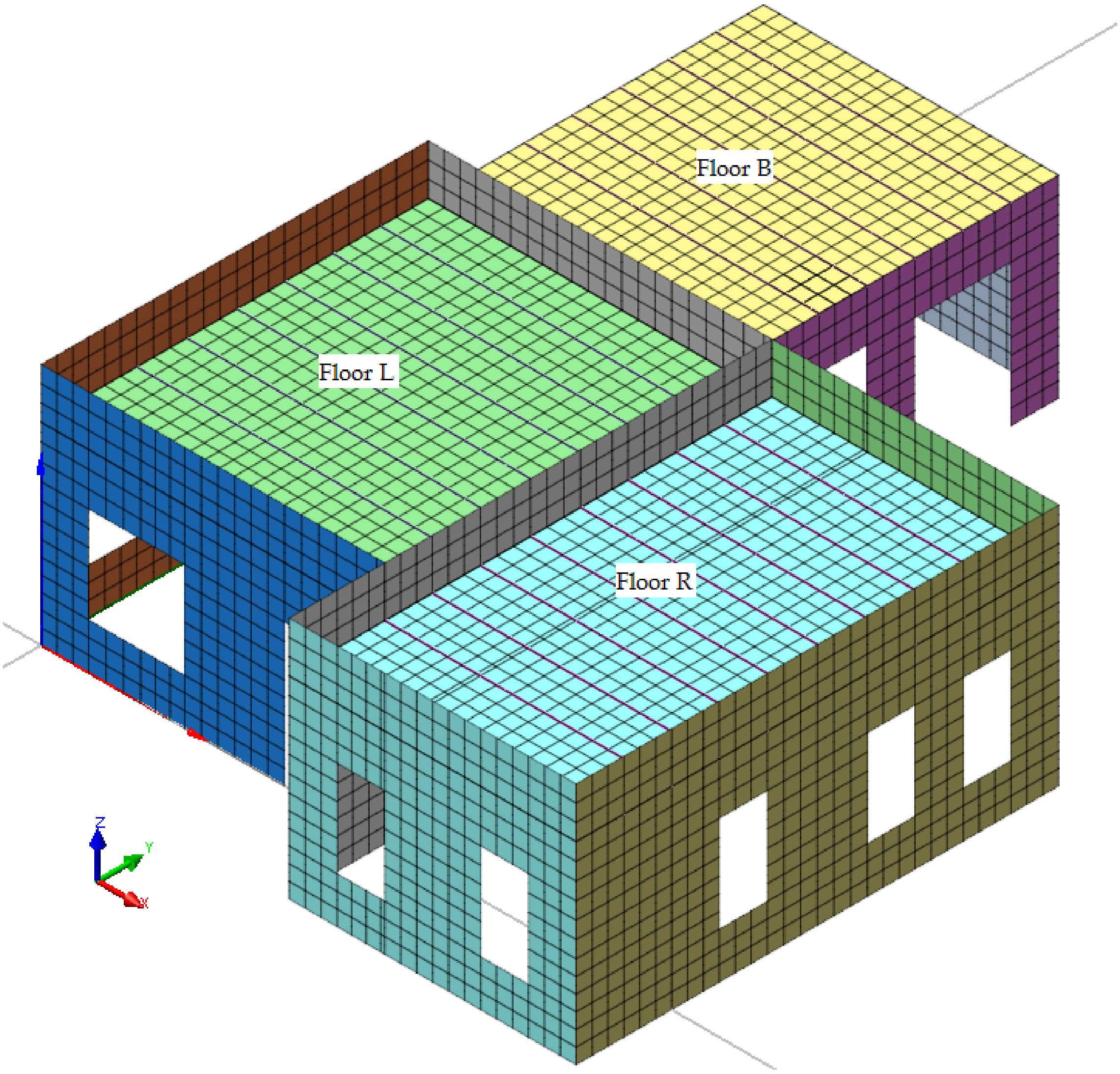

Figure 5-5: Floor Slab Nomenclature

Results

1. Pinned end beams at first floor level

   This is an uni-directional analysis along X-direction. Though the analysis is continued until time of $11.15s$ at which point divergence occurred, the last step at which convergence is achieved successfully is at $11.10s$. However. the last time step according to the input given is $11.05s$, according to which, the highest relative displacements recorded for the Floor slabs L, R and B are $\pm 0.25mm$, $\pm 0.25mm$ and $\pm 0.18mm$ respectively.

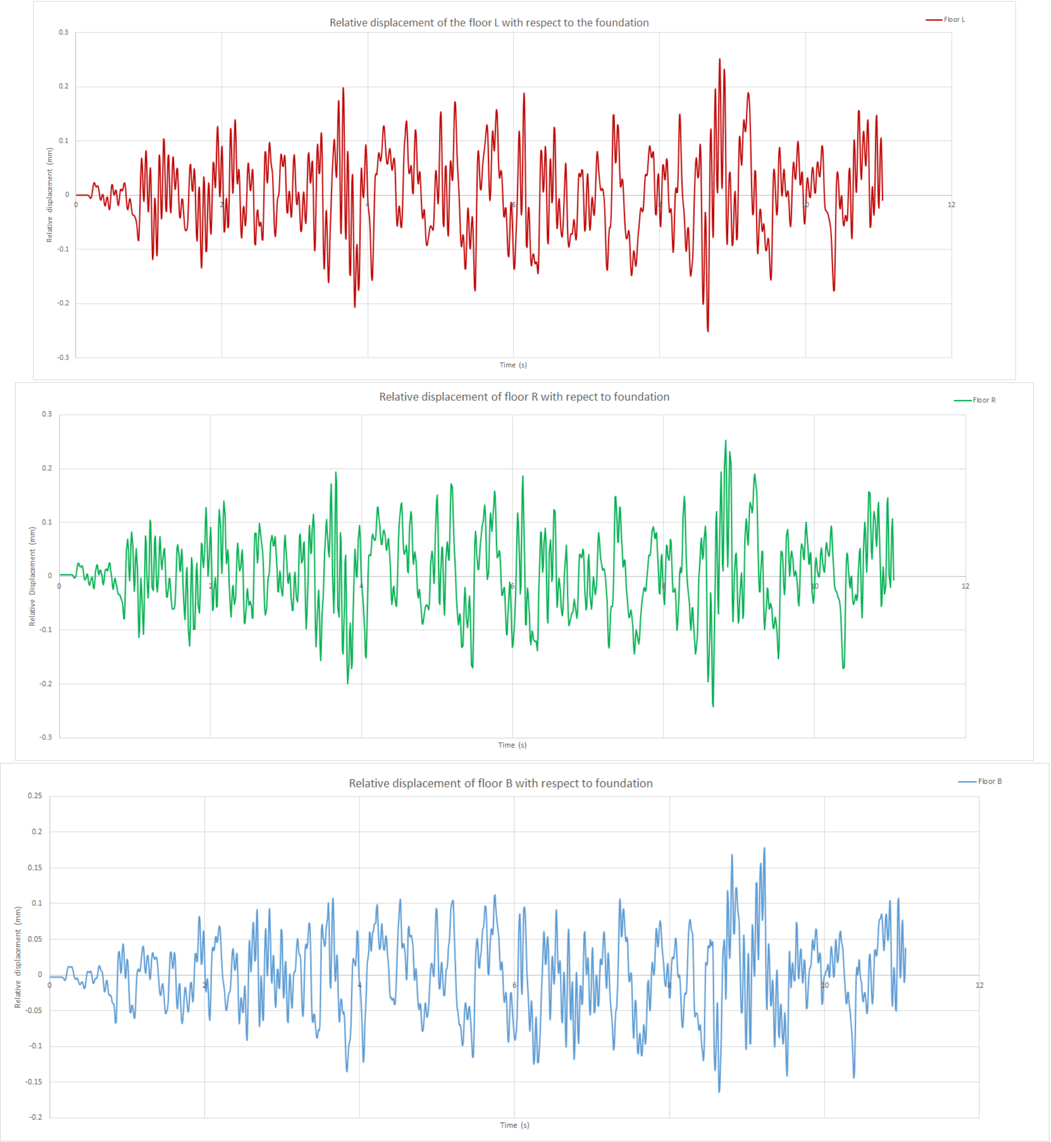

Figure 5-6: Relative displacement of the floors L,R and B with reference to foundation

By studying these hysteresis curves, the relationship between the drift of the structure at the first floor level and the base shear force acting at the level of foundation can be understood. The slabs L and R behave similarly displaying, ±0.25mm of drift at base shear of -127 and $+113$ kN. However, the floor B displays -0.165 to 0.177mm of drift at base shear of -127 to 114 kN. It can be observed that the drift in this case is lesser for the same base shear force, than the previous two floors.

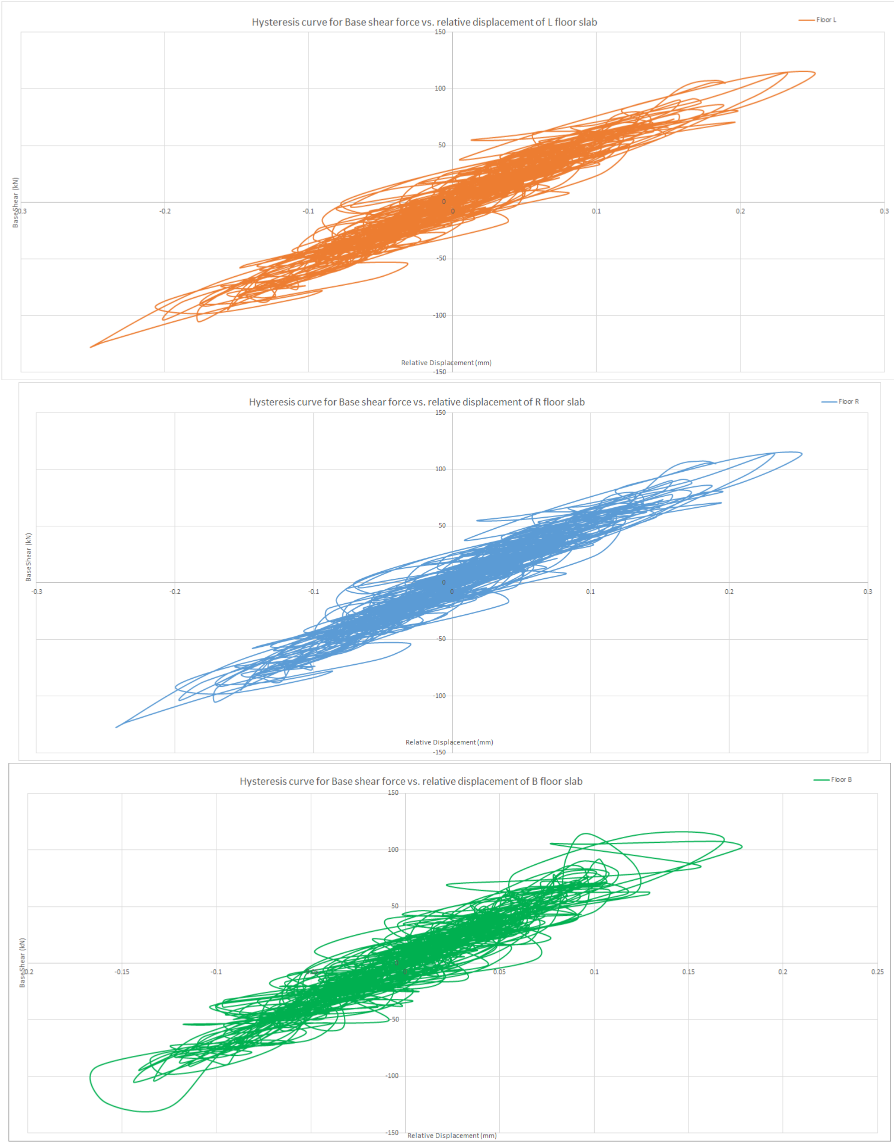

Figure 5-7: Hysteresis curves for base shear vs. relative displacement of the floors L,R and B relative to foundation

2. Fixed end beams at first floor level

The same analysis carried out on the structure with the difference being the fixed beam ends. General behaviour of the structure is studied by observing the displacement plots, refer figure 5-8. Again the convergence is achieved easily until the end of the time-history input i.e. time step of 11.05*s*. Up to this time step, the highest displacements (in mm) observed for the floor slabs L, R and B were 0.248 to -0.246, 0.25 to -0.24 and 0.165 to -0.15 occurring between $8.60 - 8.90$s respectively.

Figure 5-8: Relative displacement of the floors L,R and B with reference to foundation

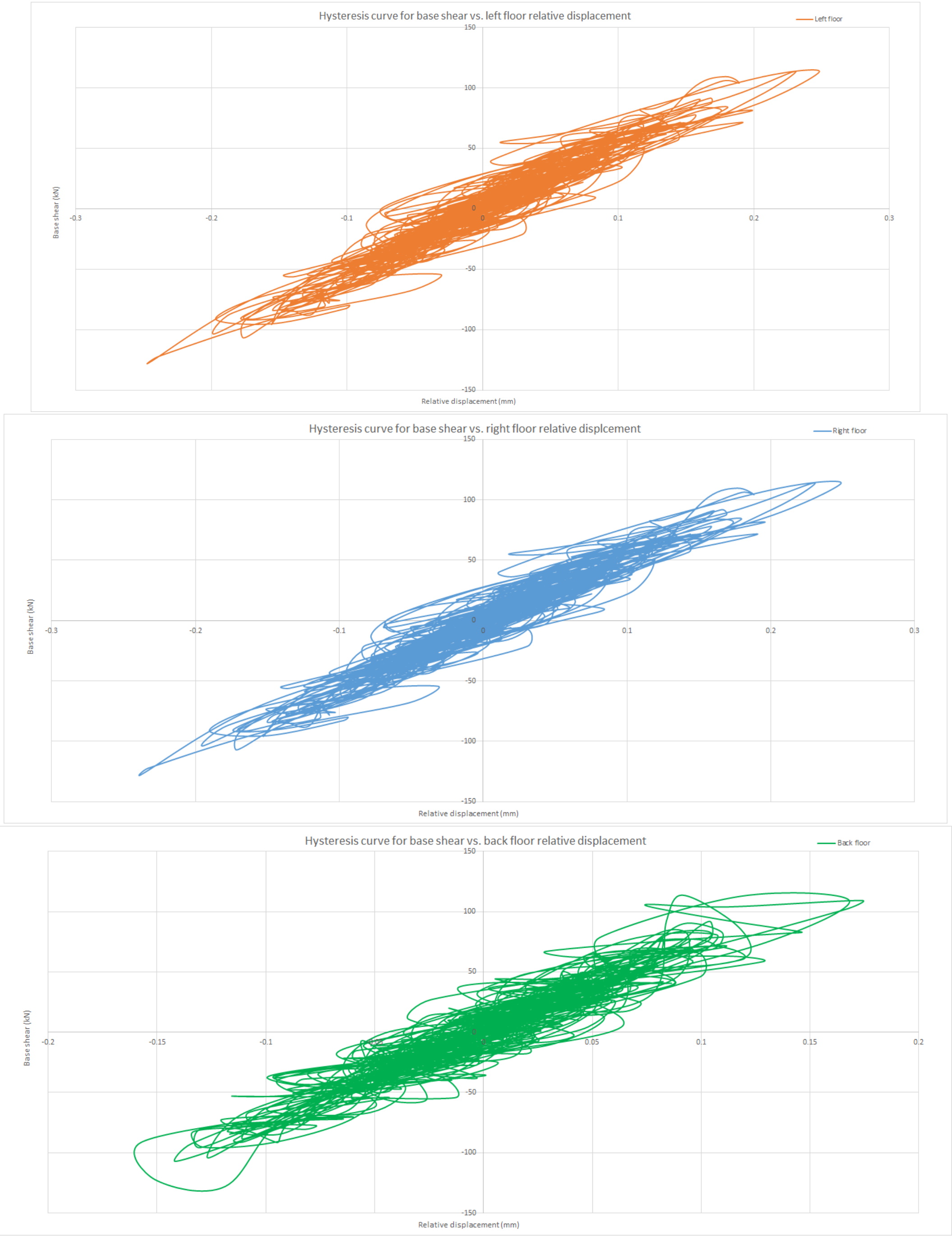

Figure 5-9: Hysteresis curves for base shear vs. relative displacement of the floors L,R and B with reference to foundation

The hysteresis curve is also plotted with base shear force versus relative drift for each of the floors and the maximum base shear force is -128 to $113\ kN$.

It is interesting to observe the order of displacement between the two cases shown in figures 5-6 and 5-8. In both the cases, floor L and R show close similarities and floor

R shows lesser displacement. The hysteresis curves do not display much difference when compared with the varying beam end cases. But, the difference is more evident when the crack strains are compared. However, no failure can be observed and that can be attributed to - input signal being weak since it is scaled to $0.16g$ and very low crack strains.

5-1-2 NLTHA - X direction - $0.25g$

Input

The input signal is shown below in the figure 5-10. The previous analysis is repeated with a stronger signal. First, the model with pinned end beams at first storey are studied, followed by the model with fixed end beams.

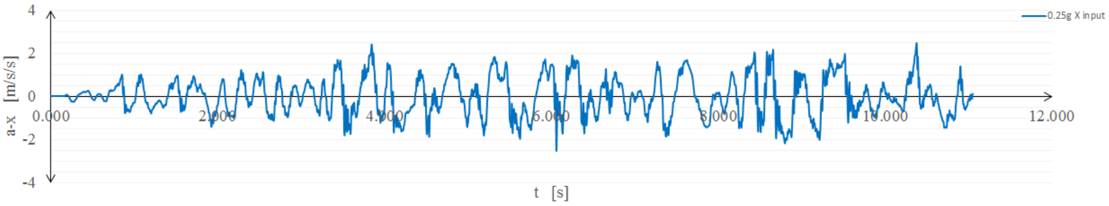

Figure 5-10: Time history input - Record 1 - Along X-axis, scaled to $0.25g$

Results

1. Pinned end beams at first floor level

   This is an uni-directional analysis along X-direction. Though the analysis is continued until time of $11.15s$ at which point divergence occurred, the last step at which convergence is achieved successfully is at $11.10s$. However, the last time step according to the input given is $11.05s$, according to which, the highest relative displacements recorded for the Floor slabs L, R and B are (read in mm) -0.423 to $+0.443$, -0.408 to 0.438 and -0.282 to 0.290 respectively. The highest negative displacements occur at $8.66s$ for left and right floors and the same for positive maximum occurs at 9.22. However, the positive maximum and the highest negative displacement for the back floor occurs at $8.65s$ and $9.23s$ respectively.

   By studying the hysteresis curves, the relationship between the drift of the structure at the first floor level and the base shear force acting at the level of foundation can be understood. The highest displacements occur at base shear forces of -205 and $+184$ kN. It can be observed that the drift in the case of back floor is lesser than that of the previous two floors, however for the same base shear force.

Figure 5-11: Relative displacement of the floors L,R and B with reference to foundation

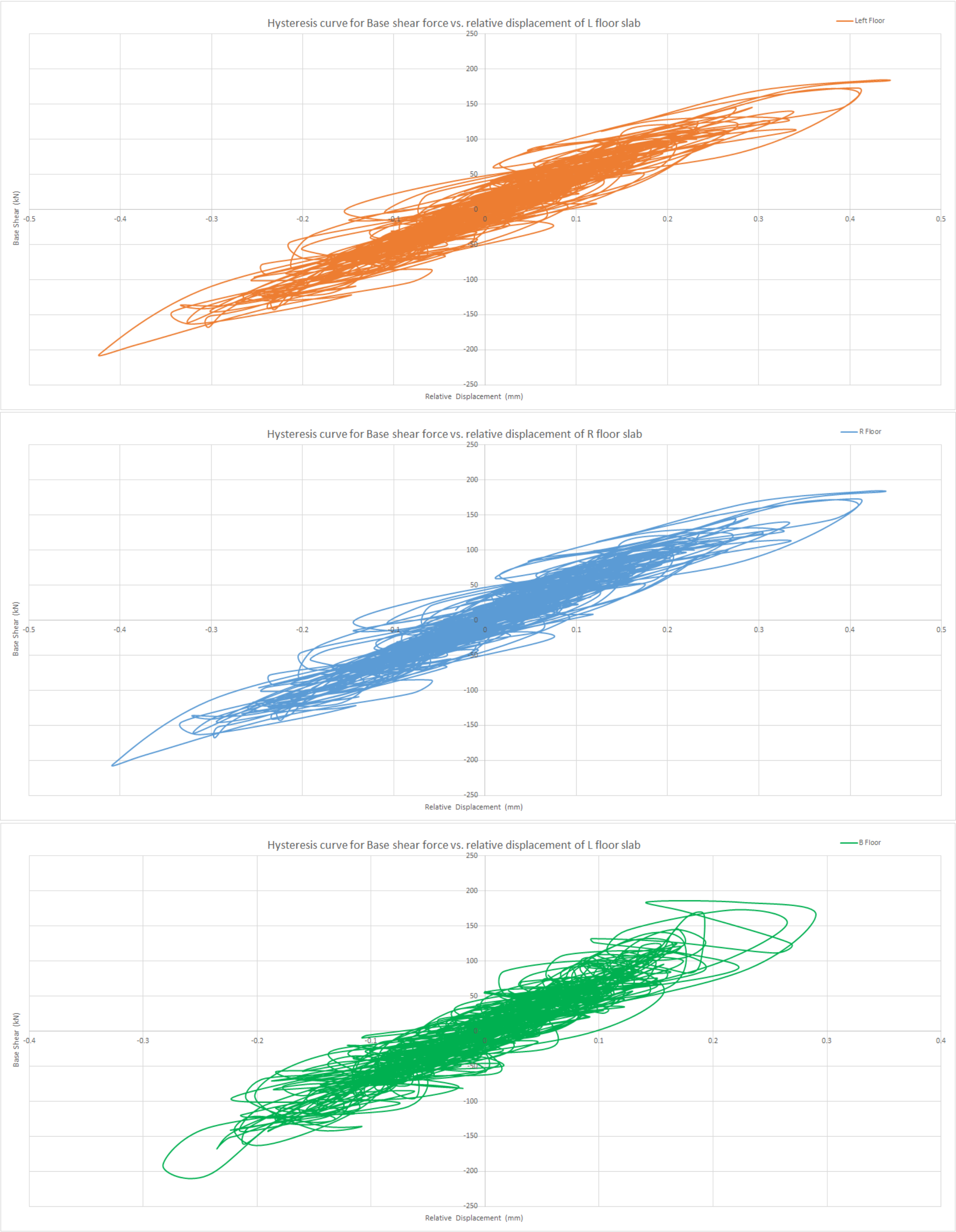

Figure 5-12: Hysteresis curves for base shear vs. relative displacement of the floors L,R and B relative to foundation

2. Fixed end beams at first floor level

The model with fixed beam ends is now analysed with the same input shown in figure 5-10. Again the convergence is achieved easily until the end of the time-history input i.e. time step of 11.05*s*. Up to this time step, the highest displacements (in *mm*) observed for the floor slabs L, R and B were -0.406 to $+0.423$, -0.393 to $+0.416$ and -0.271 to 0.284 respectively.

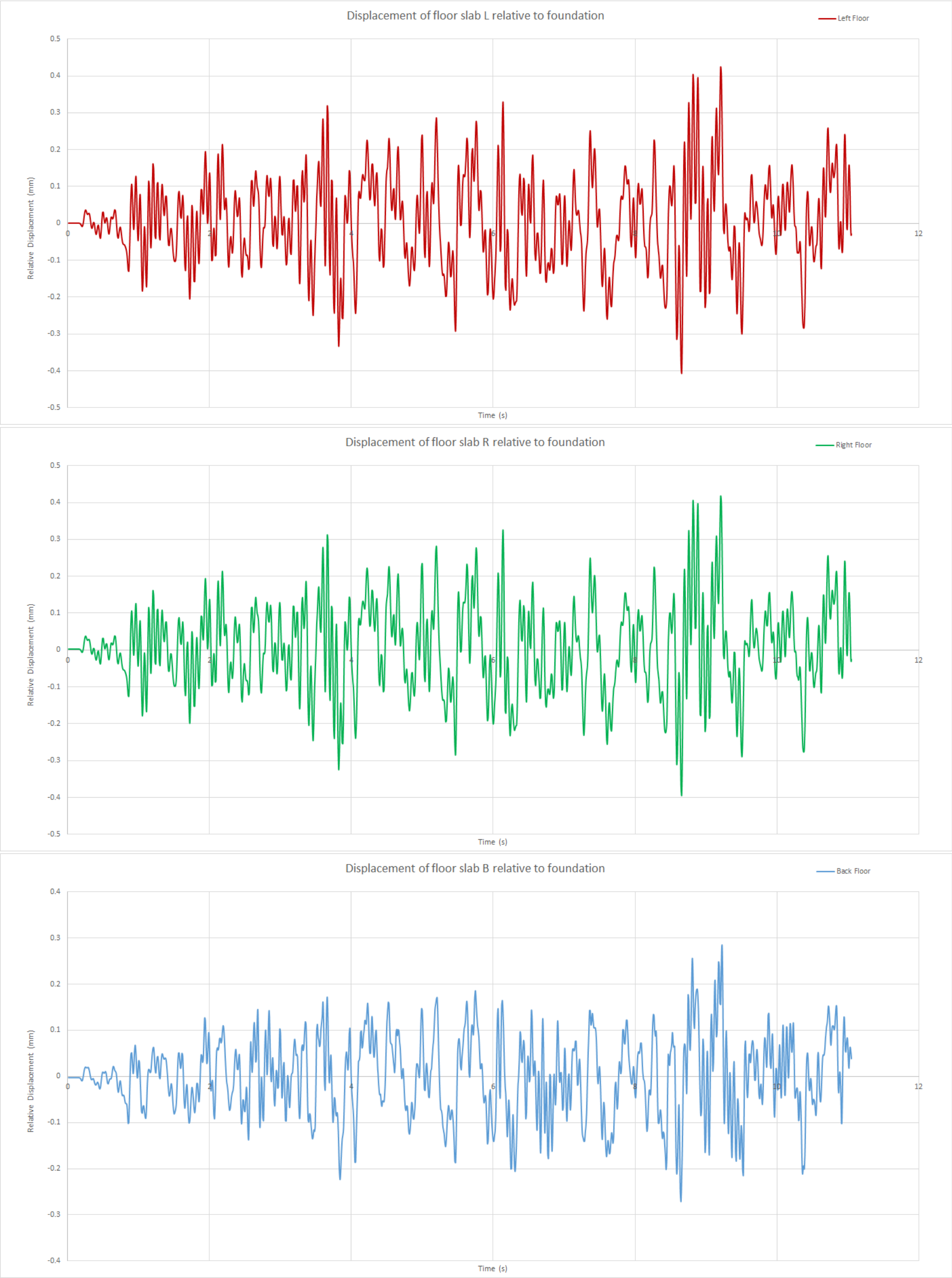

Figure 5-13: Relative displacement of the floors L,R and B with reference to foundation

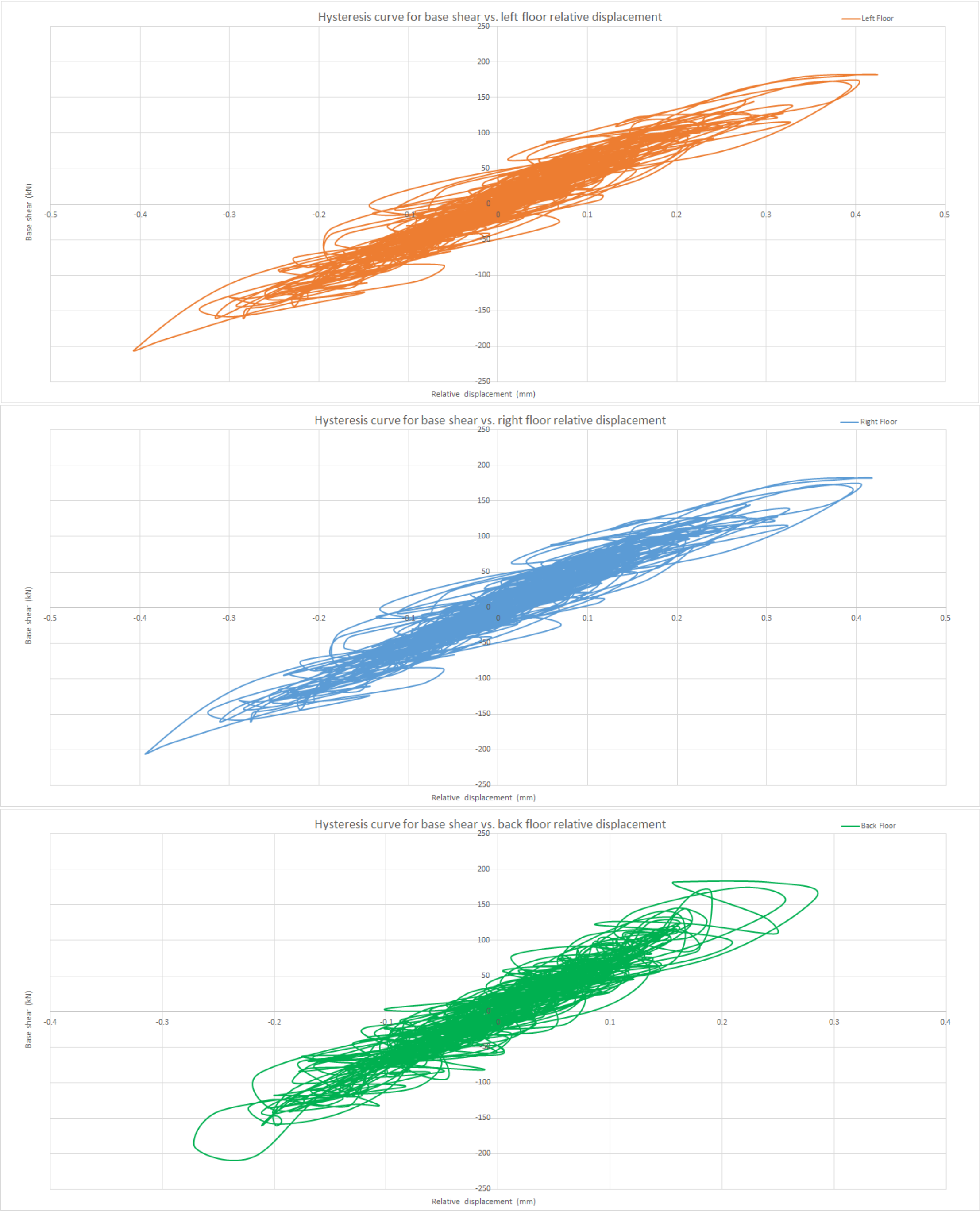

Figure 5-14: Hysteresis curves for base shear vs. relative displacement of the floors L,R and B with reference to foundation

The hysteresis curves show the relationship of the relative drift of the floors with base shear force. The highest negative and positive base shear force for $0.25g$ input is $-204kN$ and $+182kN$. It can be seen by comparing the hysteresis curves that the left and right floors follow quite a similar path whereas the back floor can be seen moving across back and forth of the centre along an imaginary trend line drawn for these hysteresis curves.

It is interesting to observe the order of displacement between the two cases shown in figures 5-11 and 5-13. In both the cases, floor L and R show close similarities and floor R shows lesser displacement. The hysteresis curves do not display much difference when compared with the varying beam end cases. However, there is a faint difference in time instants at which the back floor achieves maximum of both positive and negative displacements when compared to that of left and right floors which appear to be in sync - the highest positive displacement for the left and right floors occur at $9.21s$ and the highest negative displacement for the same occurs at $8.66s$. This is slightly different for the back floor for which maximum in both directions occurs at $8.65s$ and $9.23s$.

5-1-3 NLTHA - X direction - $0.50g$

Input

The input signal is shown in the figure 5-15. However, for an input of $0.50g$, the values were scaled accordingly. A scaling of $0.5g$ means that the highest acceleration is close to $5m/s^2$. Time steps are of $0.01(s)$ applied in $0.01(1000) + 0.005(250)$ steps totalling to $11.25s$. Also, 50 iterations per time step was input to achieve convergence with an energy tolerance of $1 * 10^{-4}$. The seismic response of the floor slabs are depicted in the following subsection. In this analysis, two configurations of the beam ends are studied. First, the model with pinned end beams at first story were studied, followed by the model with fixed end beams.

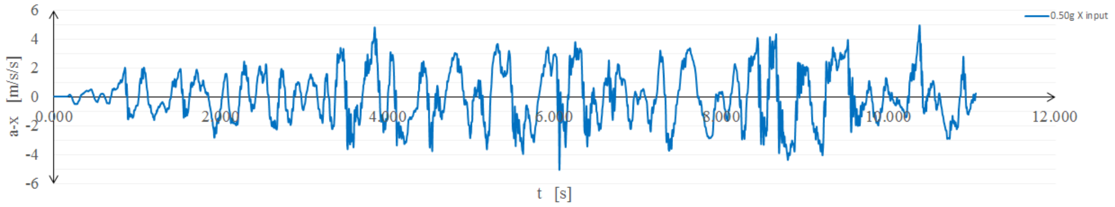

Figure 5-15: Time history input - Record 1 - Along X-axis, scaled to $0.50g$

Results

1. Pinned end beams at first floor level

   This is an uni-directional analysis along X-direction. Owing to the strong scaling of the input signal the analysis achieved convergence till $4.58s$, ultimately diverging at $4.71s$. All the steps in between showed no convergence even after 50 iterations. The highest relative displacements recorded for the floor slabs L, R and B are (in mm) -1.143 to $+1.130$, -1.094 to 1.134 and -0.936 to 0.650 respectively.

   By studying the following hysteresis curves, the relationship between the drift of the structure at the first floor level and the base shear force acting at the level of foundation can be understood. The maximum base shear force that was recorded in the analysis is equal to -334 to 248 kN. There is a repeating pattern in the left and right floor slabs behaving similarly whereas the back floor follows the two. This can evidently be seen from the displacement plots by comparing the time instants at which different floors show corresponding maximum drifts.

Figure 5-16: Relative displacement of the floors L,R and B with reference to foundation

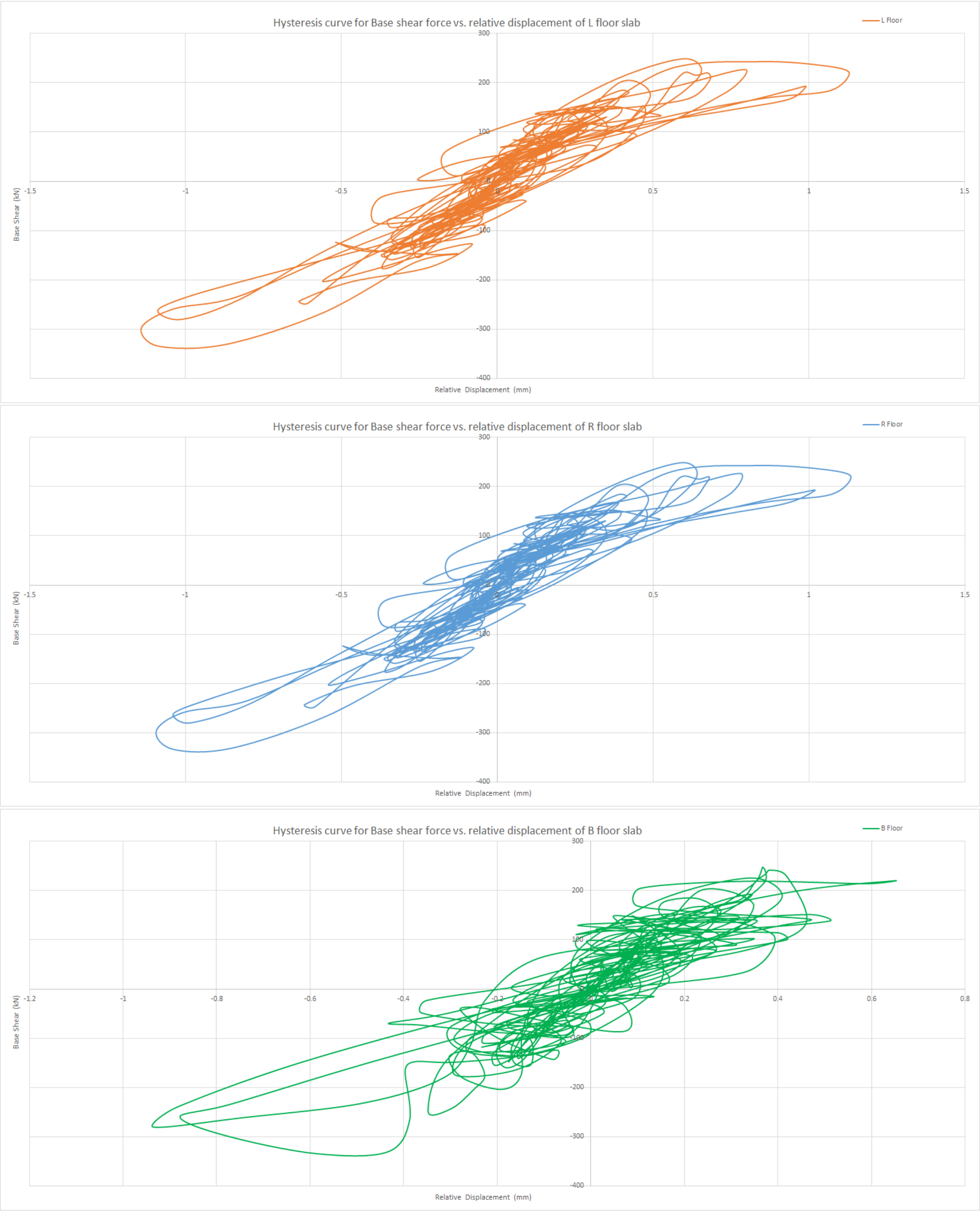

Figure 5-17: Hysteresis curves for base shear vs. relative displacement of the floors L,R and B relative to foundation

2. Fixed end beams at first floor level

Figure 5-18: Relative displacement of the floors L,R and B with reference to foundation

Similar to the previous case, the analysis is repeated with the same input signal but a different model with fixed beam end type. Since the input signal is quite strong with a scaling of $0.5g$, the last successfully converged step occurred at $5.25s$ or time step 530. However, the analysis is allowed to continue and divergence occurred at step 534 or $5.29s$. The maximum relative displacements ranged in the negative and positive directions for the left, right and back floor as follows (in mm)- -1.029 to $+0.937$, -0.980 to $+0.924$ and -0.838 to $+0.529$, respectively. However, towards the end of the analysis where convergence was not achieved completely for certain steps (including the steps upto and including divergence) show higher displacements of the range (in mm) -1.60 to $+1.93$, -1.533 to $+1.95$ and -0.496 to $+0.619$ respectively for the left, right and back floors.

The hysteresis curves for the analysis is shown below in figure 5-19. The maximum base shear force recorded during this analysis is -338 to $+274$ kN. Following the pattern from all the previous analyses, even in this case, the back floor shows lesser magnitude of drift than the left and right floors. Comparing the displacement responses for the different beam end cases, it can be seen that the fixed end beam type model undergoes divergence at a later stage at 5.29s which is longer by 0.58s when compared to the model with pinned end type beams. This is a significant point of difference showing higher durability for the latter model.

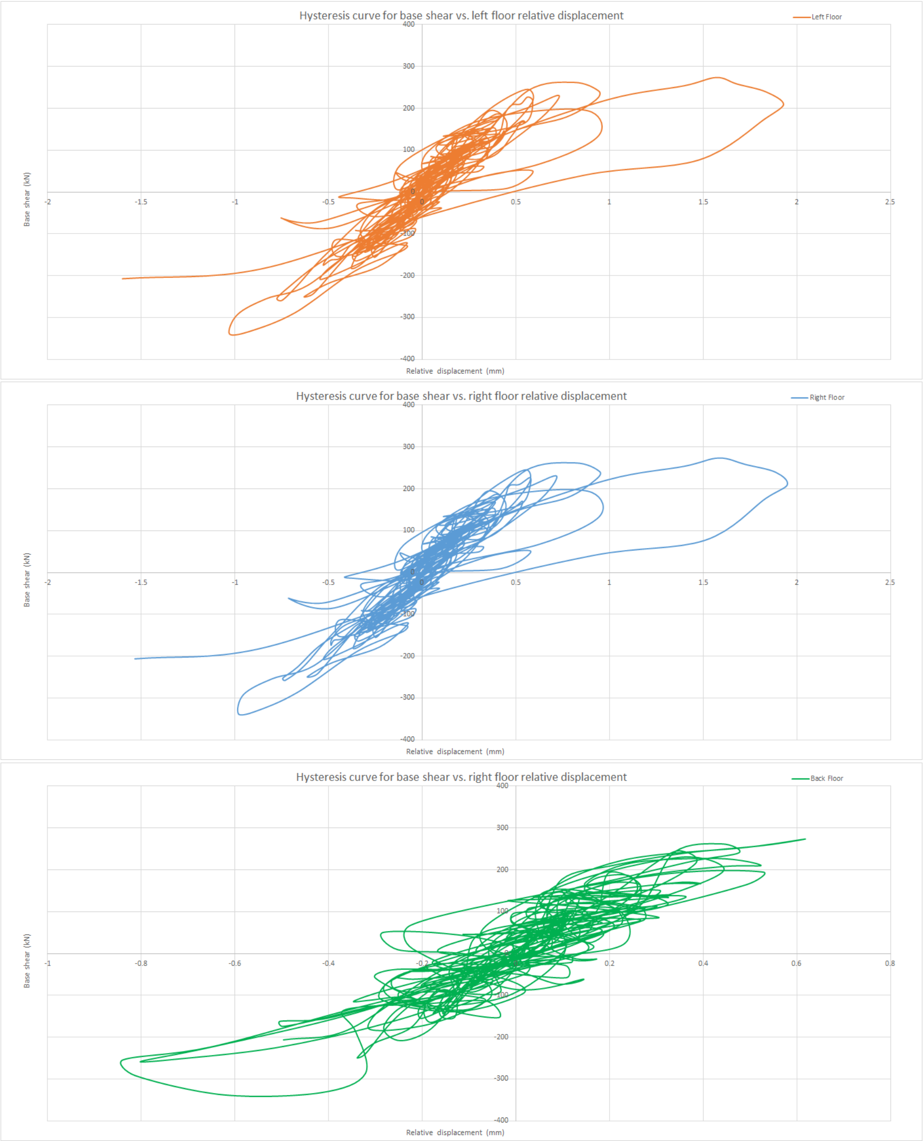

Figure 5-19: Hysteresis curves for base shear vs. relative displacement of the floors L,R and B with reference to foundation

5-1-4 Inferences

1. It is observed that the seismic input signal scaling of $0.16g$ and $0.25g$ induce no significant cracking in the structure. Though cracking is observed, they are dynamic in nature which means they are under initiation stage yet. This is true for both kinds of beam end connections i.e. both pinned end beams and fixed end beams.

2. With respect to the higher scaling of $0.50g$, first plastic cracks (that are in the stabilised stage) occur at time step of $4.42s$ in the case of the model with pinned end beams. From this point on through to the step where divergence occurs, 15 steps can be identified where convergence is not reached even after 50 iterations. However, it is to be noted that there is gradual increase in number of plastic cracks which results in the degeneration of the structure culminating finally at $4.71s$ due to occurrence of divergence.

3. With regard to the model with fixed beam ends, first plastic cracks occur at time step of $4.04s$. It is also important to note that from this point, 30 steps can be identified where convergence is not reached even after 50 iterations. However, the analysis is allowed to continue. It is interesting to note two points of interest here though, that the first plastic crack appears at time of $4.04s$ which is $0.40s$ earlier in comparison to the model with pinned beam ends and divergence occurs at time step of $5.31s$ i.e. $0.60s$ later than that for the former type of model.

5-2 Analysis along Y-direction

5-2-1 NLTHA - Y direction - $0.16g$

Input

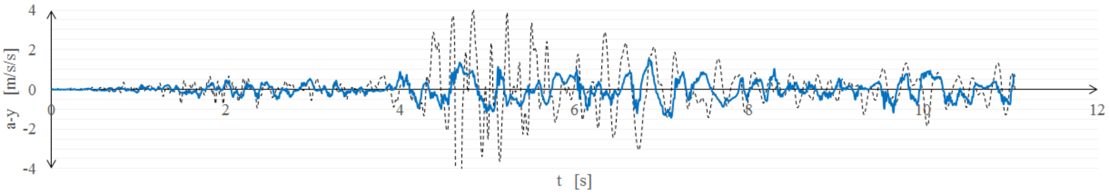

Figure 5-20: Time history input - Record 1 - Along Y-axis, scaled to $0.16g$

In this analysis, the given time history record is input directly without any scaling. However, the record is scaled to $0.16g$ acceleration. By observing the inputs in figure 5-21, one can identify that for the signal corresponding to X-axis (blue curve), there are many more peaks and higher acceleration values compared to that along Y-axis (red curve). This pattern reflects as well on the response of the structure. In the values for Y-axis, the average values over the entire time-line is about half compared to that of values along X-axis.

Hence, the input along Y-axis is a weaker signal and it follows that it causes lesser damage to the structure.

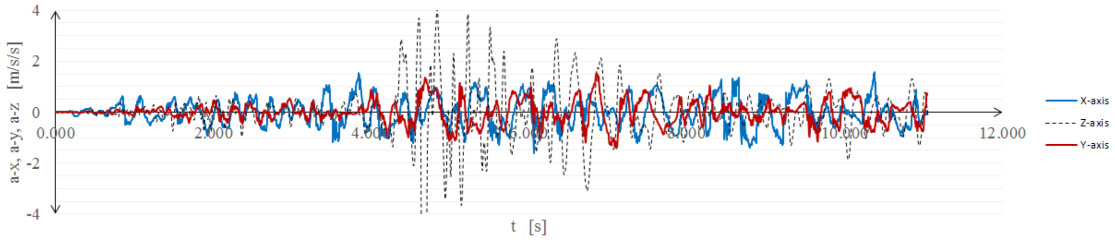

Figure 5-21: Time history input - Record 1 - Along X,Y and Z-axis

Results

1. Pinned end beams at first floor level

The beam ends in the structure in this analysis are pinned type. The displacement curves are shown below in figure 5-22. Maximum values as displayed by the left, right and back floors are -0.0432 to $+0.0350$ mm, -0.0389 to $+0.0423$ mm and -0.0357 to $+0.0400$ mm respectively. It can be observed that the left and right floors show similar net displacements upto the end of the time history input. The maximum crack strain at the mid layer of wall elements is $4.65 * 10^{-5}$ which is 3% of the calculated ultimate crack strain. There is no damage upto the end of the time history input which is the final step of the analysis.

Figure 5-22: Relative displacement of the floors L,R and B with reference to foundation

The hysteresis curves show the relationship between base shear force and displacement of all the floors. The maximum base shear forces that are recorded are -113 and $+102$ kN. This is the response until the end of time history input.

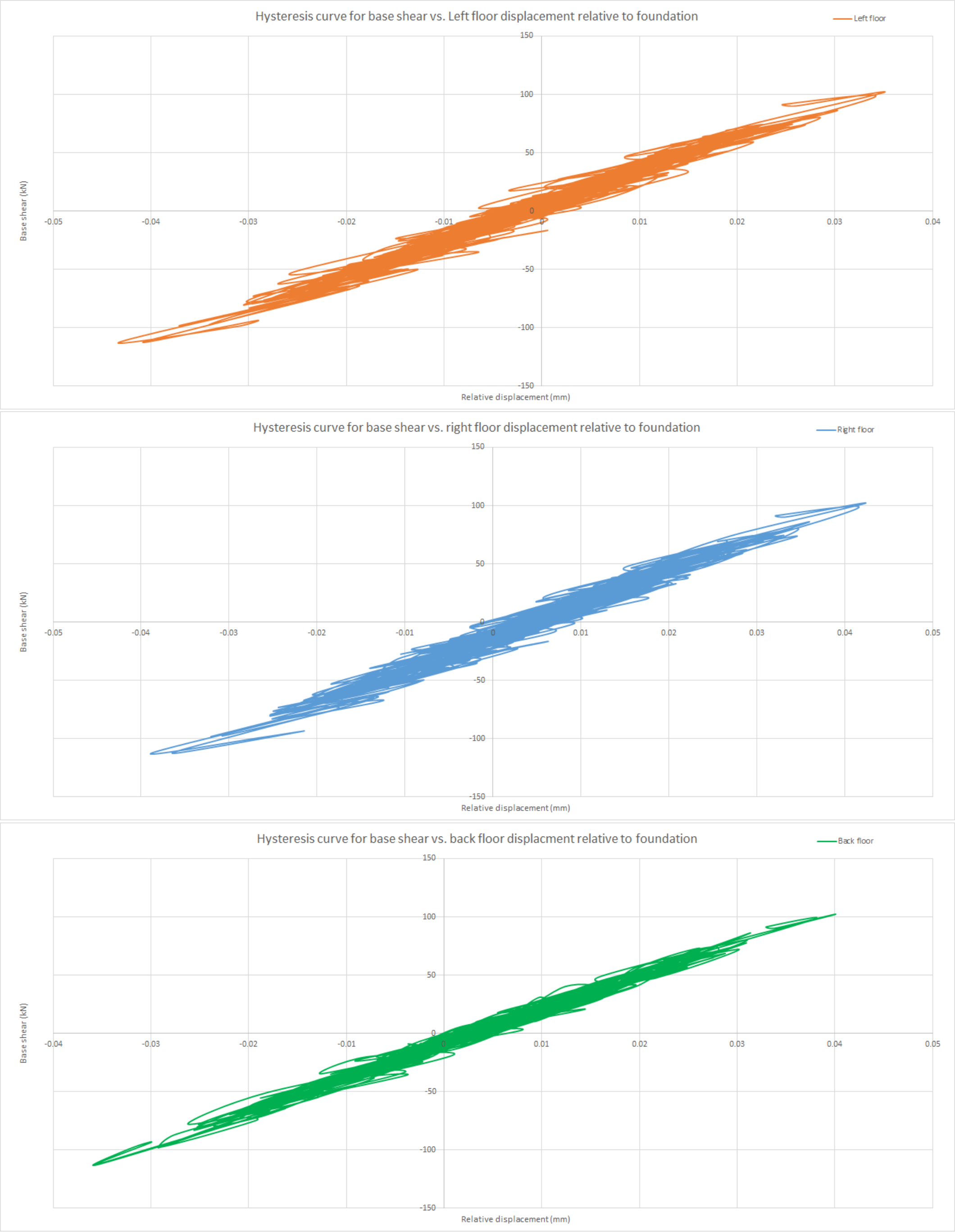

Figure 5-23: Hysteresis curve for base shear vs. relative displacement of the floors L,R and B with reference to foundation

2. <u>Fixed end beams at first floor level</u>

   The analysis is repeated for the model consisting of timber beam ends fixed. This is done by merging beam end nodes with wall nodes. The results are similar to the previous one with pinned type beam ends, however, the results are discussed below.

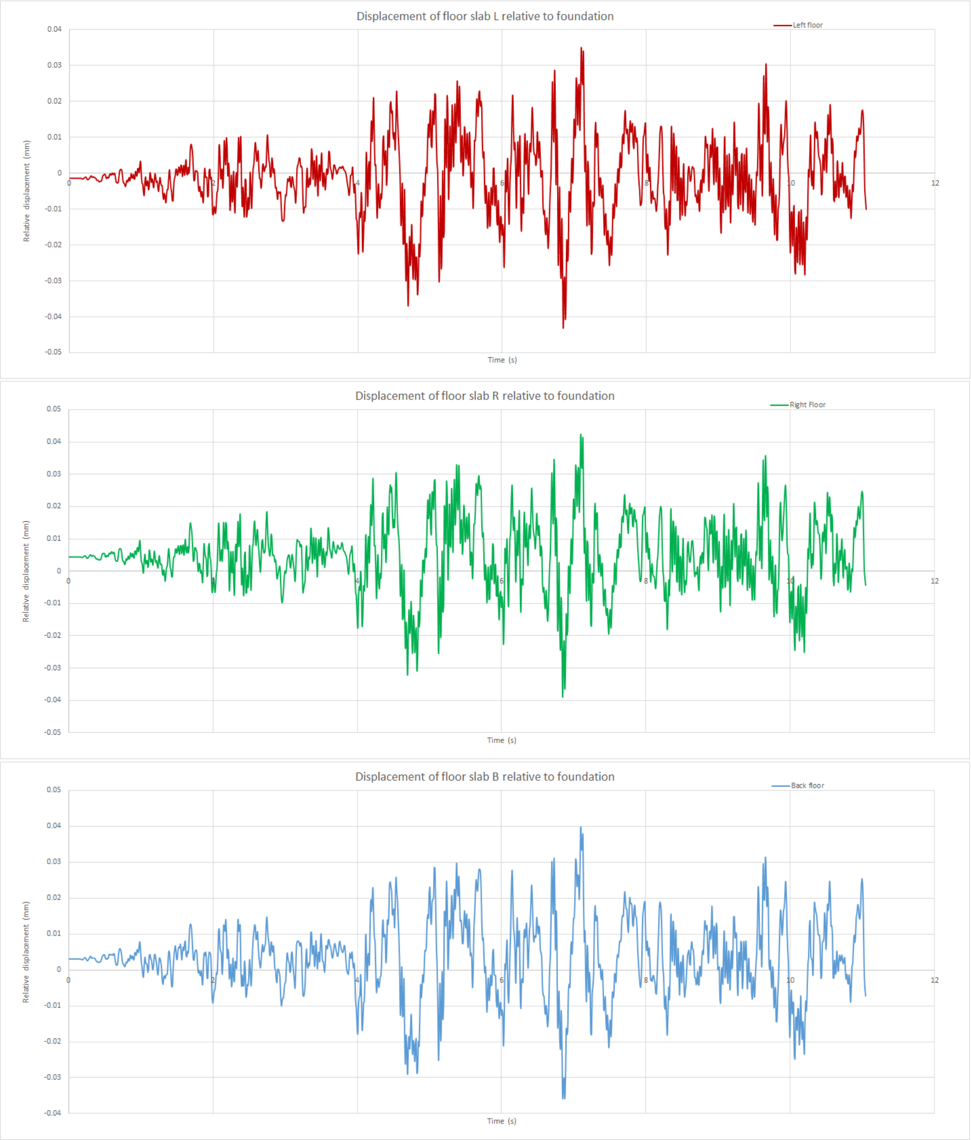

Figure 5-24: Relative displacement of the floors L,R and B with reference to foundation

The figure 5-24 shows the displacement response of the floors with respect to the foundation of the structure. The maximum floor displacement (in mm) for L, R and B floors are -0.0432 to $+0.0349$, -0.039 to $+0.0424$ and -0.0358 to $+0.0397$ respectively. In this regime, it can be seen that the right floor undergoes highest net displacement. These values are the maximum for the time history input. Maximum relative displacements for the left and right floors occur at time instant of $6.85s$ for the negative Y direction and $+7.10s$ in the positive Y-direction. However, for the back floor, the maximum displacement in the negative Y-direction occurs at 6.88*s* though the maximum displacement in the positive direction occurs at 7.10*s*, which is the same for the left and right floors.

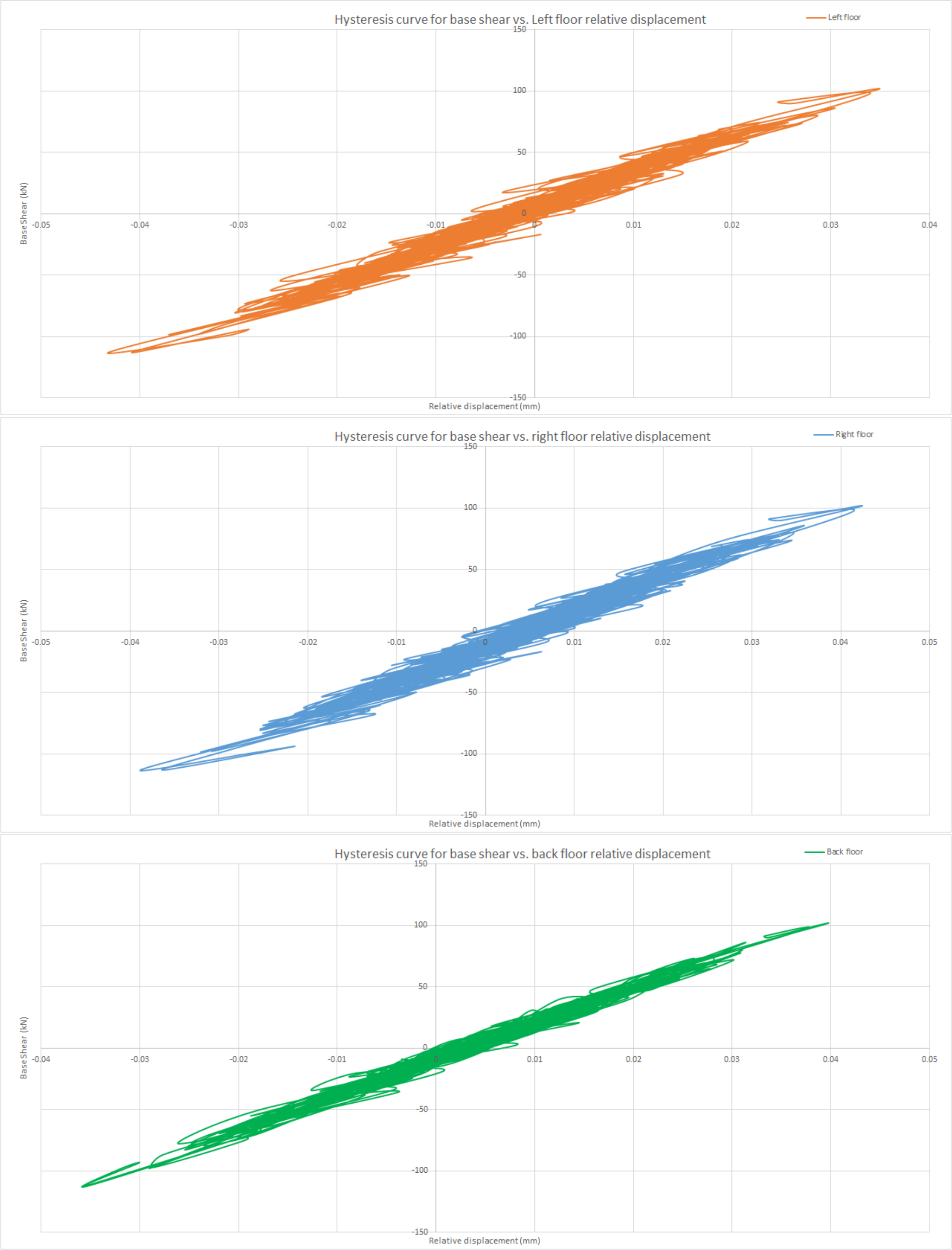

Figure 5-25: Hysteresis curve for base shear vs. relative displacement of the floors L,R and B with reference to foundation

The hysteresis curve shows base shear force plotted against relative displacement of the floors, showing the maximum base shear force at maximum displacements. For the time history input, the maximum base shear forces recorded are -113 to $+102$ kN. It can be observed that the difference in the maximum crack strain at the end of time history input (at time step 1110) between the two cases of beam ends fixed and pinned is very low. The influence of beam ends is not significantly different. The crack strain values of the model using fixed beam ends is minutely higher by a unit of $0.05 * 10^{-5}$, which is quite a negligible value.

5-2-2 NLTHA - Y direction - $0.25g$

Input

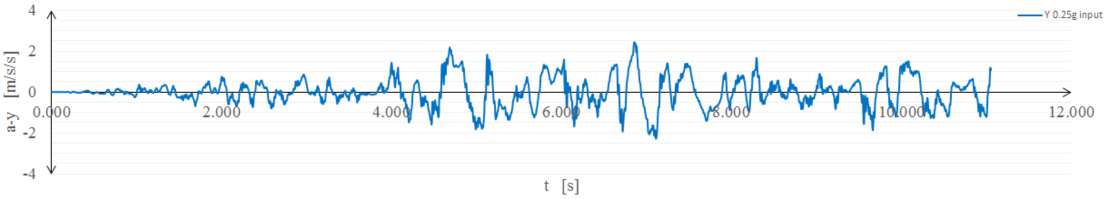

Figure 5-26: Time history input - Record 1 - Along Y-axis, scaled to $0.25g$

In this analysis, the given time history record is accordingly scaled. However, the record is scaled to $0.25g$ acceleration as in the previous case for signal along X-direction. This means that the maximum acceleration present in the input signal is equal to 2.45 m/s^2. The analysis is performed with the signal input along the Y-direction. The results are presented as follows.

Results

1. Pinned end beams at first floor level

   The beam ends in the structure in this analysis are pinned type. The displacement curves are shown below in figure 5-27. Maximum values of relative displacement in the negative and positive Y-direction as displayed by the left, right and back floors are -0.071 to $+0.048$ mm, -0.066 to $+0.057$ mm and -0.058 to $+0.061$ mm respectively. This analysis could not continue until the last step of history due to the following reasons - the last converged step is at time 10.79s or step 1163. However, the analysis was allowed to continue further, where convergence was not achieved for any step (except for step 1172 or time 10.83s) and finally diverged at step 1182 or 10.88 s.

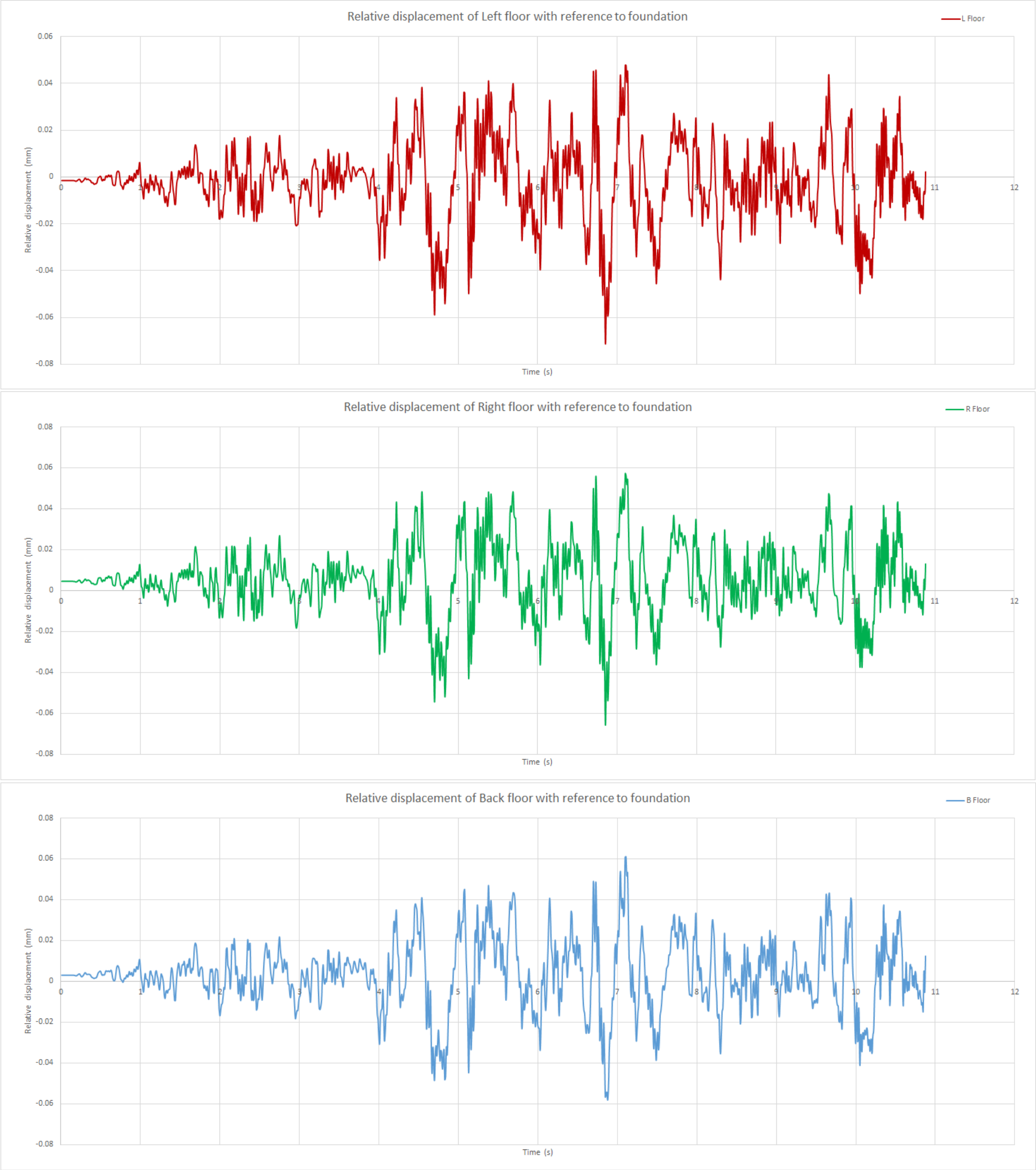

Figure 5-27: Relative displacement of the floors L,R and B with reference to foundation

The hysteresis curves show the relationship between base shear force and displacement of all the floors. The maximum base shear forces that are recorded are -183 and $+159$ kN. This is the response until the end of time history input. Even along the Y-direction, the back floor achieves maximum displacements at different time instants than the left and right floors, this can be observed by looking at the displacements plots for different floors. This is achieved by the left and right floors at 6.85 and 7.1 s whereas for the back floor, the same is achieved at 6.88 and 7.11 s.

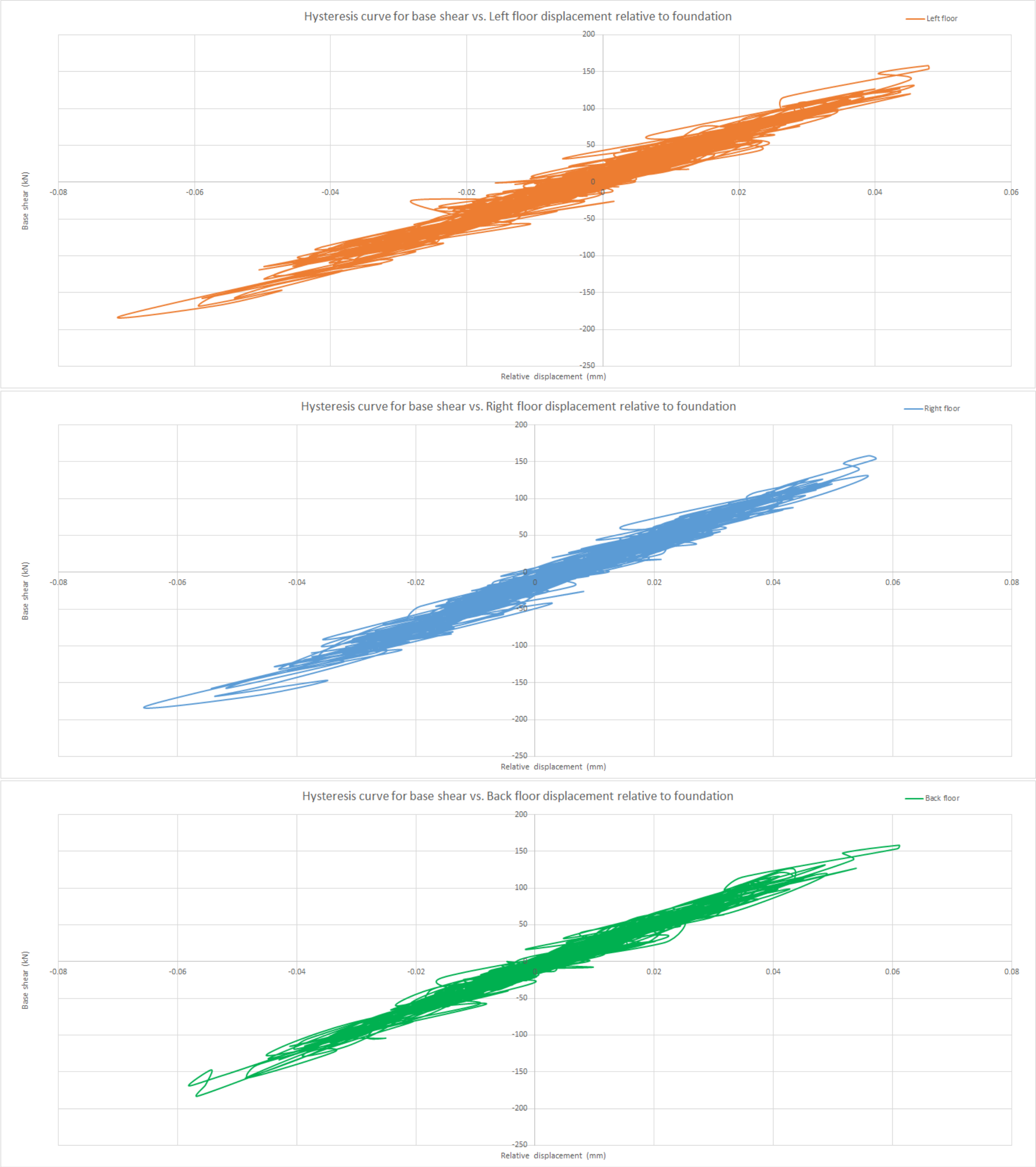

Figure 5-28: Hysteresis curve for base shear vs. relative displacement of the floors L,R and B with reference to foundation

2. Fixed end beams at first floor level

   The analysis is repeated for the model consisting of timber beam ends fixed. This is done by merging beam end nodes with wall nodes. Similar input scaled to $0.25g$ is input for the corresponding model and analysed for seismic displacements along Y-direction.

   The maximum floor displacement for L, R and B floors are -0.0713 to $+0.0474$ mm,

-0.0713 to $+0.0474$ mm and -0.0582 to $+0.0604$ mm respectively. In this regime, it can be seen that the right floor undergoes highest net displacement. These values are the maximum for the time history input. This occurs within time interval of $6.85 - 7.20$s. The last converged step is at time $8.82s$ or step 887. However, the analysis was allowed to continue further, where convergence was not achieved for a number of steps from time $8.60s$ to $8.82s$.

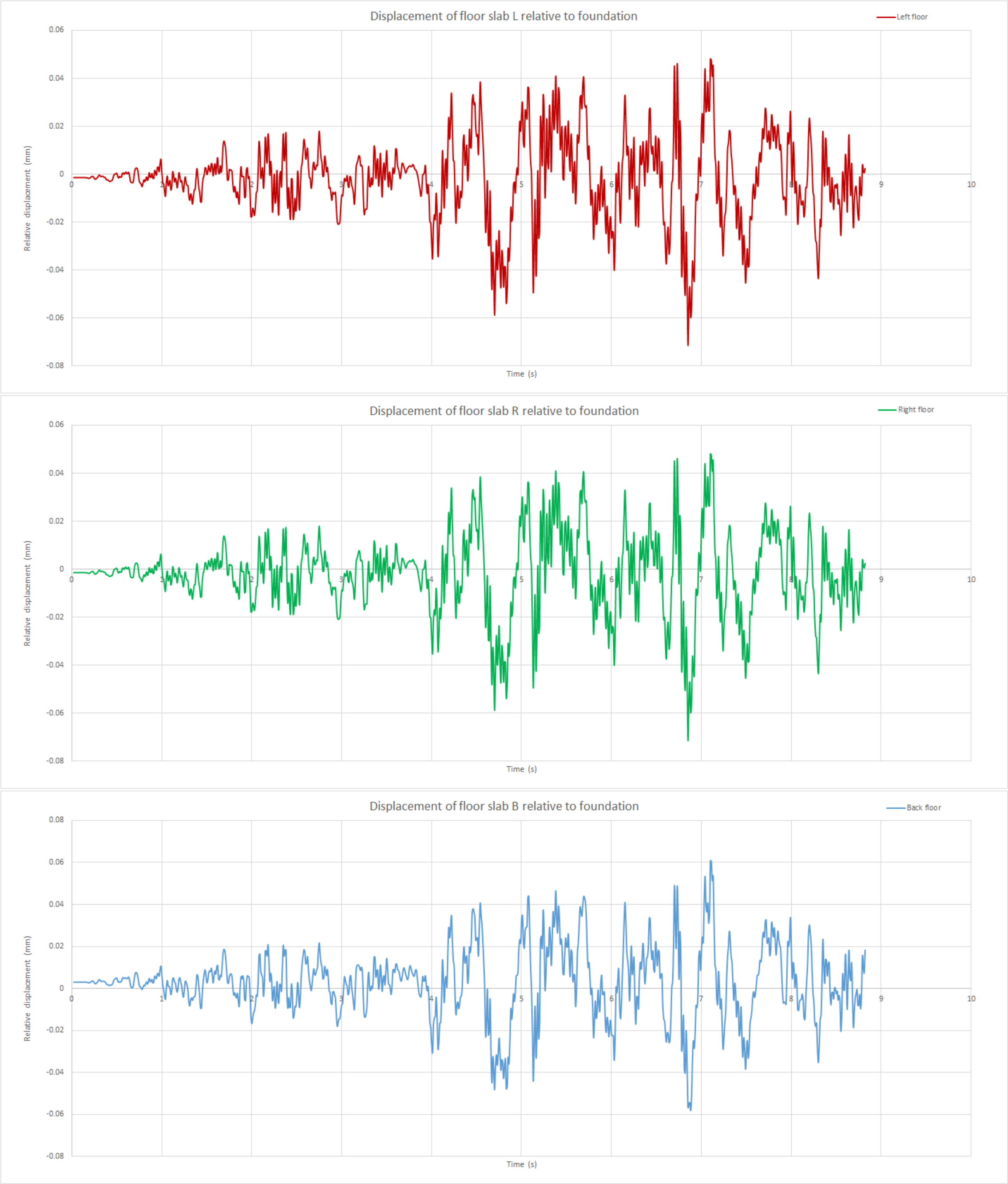

Figure 5-29: Relative displacement of the floors L,R and B with reference to foundation

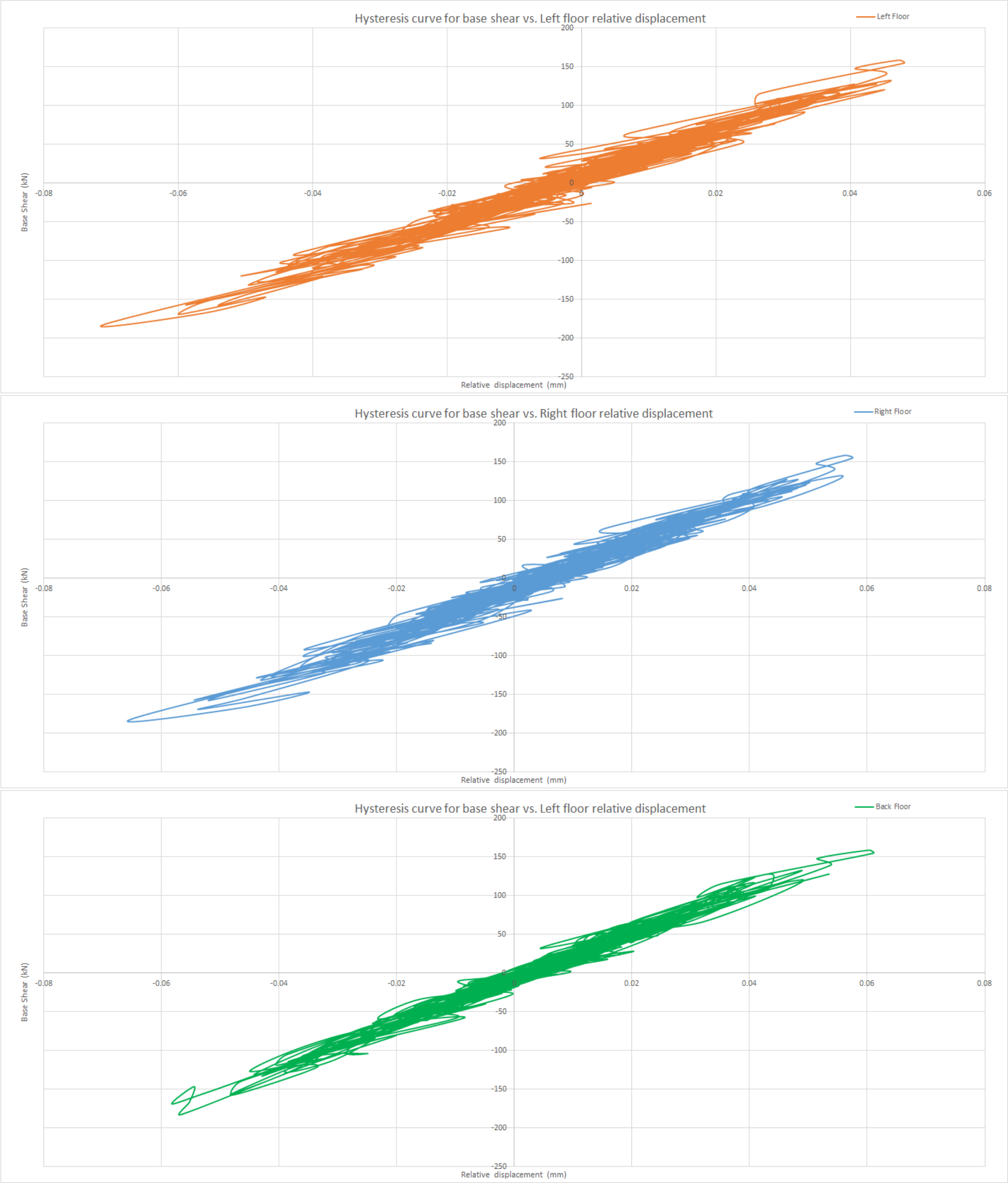

Figure 5-30: Hysteresis curve for base shear vs. relative displacement of the floors L,R and B with reference to foundation

The hysteresis curve shows base shear force plotted against relative displacement of the floors, showing the maximum base shear force at maximum displacements. For the time history input, the maximum base shear forces recorded are −183 to +158 kN. It can be observed that the difference in the maximum crack strain at the end of time history input (at time step 1110) between the two cases of beam ends fixed and pinned is very low. The influence of beam ends is not significantly different.

The crack strain values of the model using fixed beam ends is minutely higher by a unit of $0.05 * 10^{-5}$, which is quite a negligible value. It is interesting to note that the model with fixed beam ends undergoes divergence much earlier than that compared to the former case with pinned beam ends by a big difference of $2.08s$. Also, this is a significant departure when compared to the analysis along X-direction, for the same scaling, i.e. $0.25g$, of the input signal.

5-2-3 NLTHA - Y direction - $0.50g$

Input

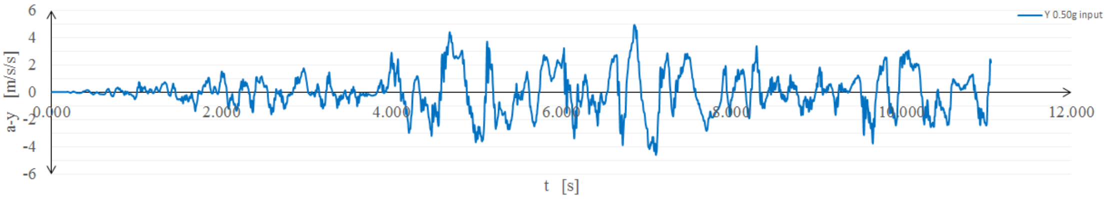

Figure 5-31: Time history input - Record 1 - Along Y-axis, scaled to $0.50g$

In this analysis, the given time history record is input accordingly after proper scaling to $0.50g$ acceleration. This scaling means that the highest value of acceleration in the input signal is equal to $4.95 - 5\ m/s^2$. This is the highest scaling applied to the input signal. It is expected that the model will not be able to withstand such a strong input and hence will undergo divergence much earlier than the previous analyses. However, the results are presented below.

Results

1. <u>Pinned end beams at first floor level</u>

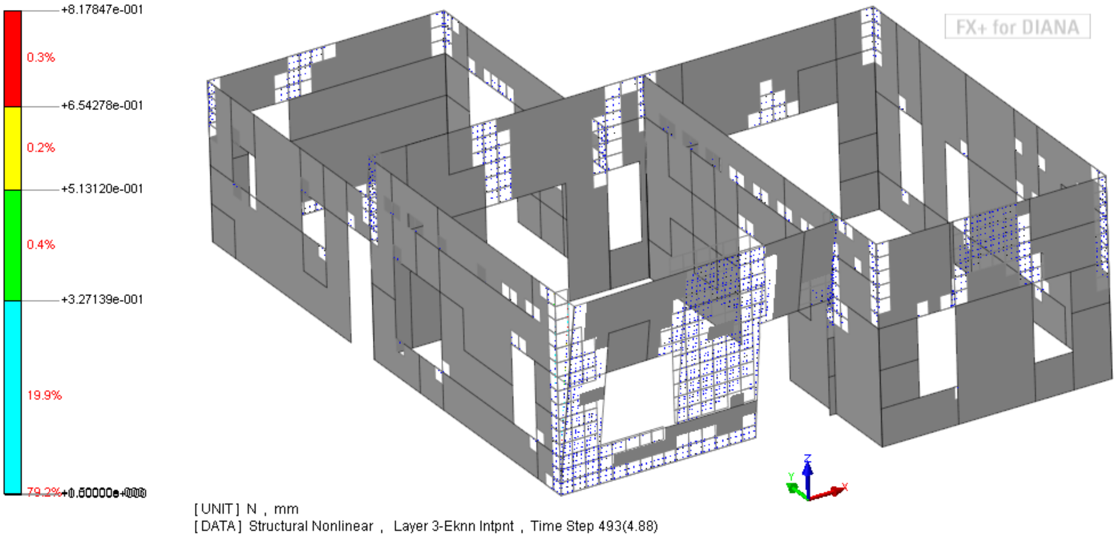

Figure 5-32: Crack strain at layer 3 of walls under $0.50g$ signal

The beam ends in the structure in this analysis are of pinned type. Maximum relative displacement values in the negative and positive Y-direction as displayed by the left, right and back floors are -0.0572 to $+0.0712$ mm, -0.0573 to $+0.0837$ mm and -0.0690 to $+0.0810$ mm respectively. These values are recorded before the analysis failed to achieve convergence. The last successfully converged step was step 493 at $4.88s$, however, divergence occurred at step 494 or $4.89s$. Although, the maximum relative displacements are given above, the maximum negative relative drift recorded (in mm) was -0.112, -0.096 and -0.110 for left, right and back floors respectively. The hysteresis curves show the relationship between base shear force and displacement of all the floors. The maximum base shear forces that are recorded are -286 and $+218$ kN. This is the response recorded before the divergence occurred.

Figure 5-33: Relative displacement of the floors L,R and B with reference to foundation

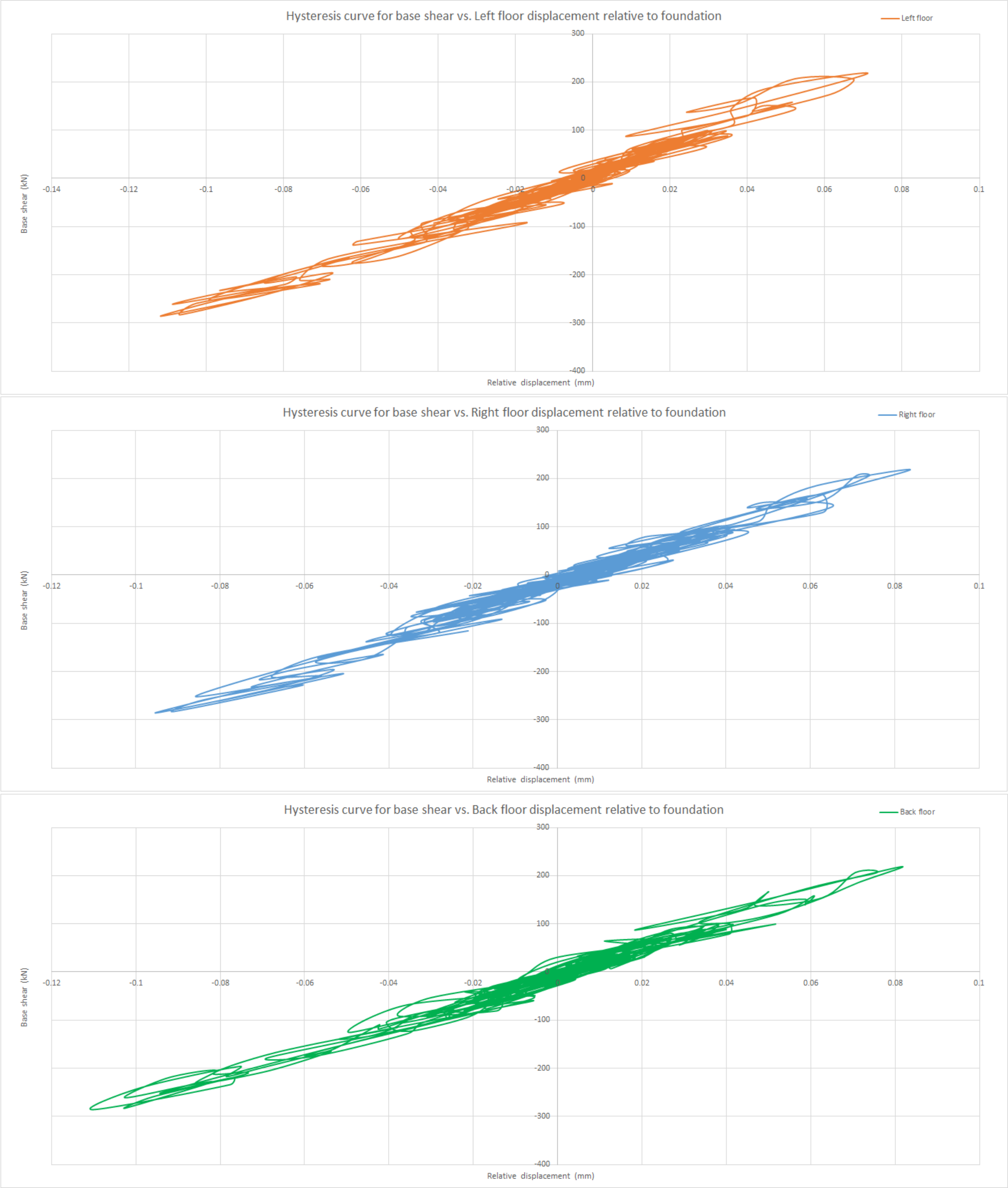

Figure 5-34: Hysteresis curve for base shear vs. relative displacement of the floors L,R and B with reference to foundation

The highest drift in the negative Y-direction occurred at 4.70*s*, as given below. Nevertheless, the significant point to be noted here is that this drift occurred for all floors simultaneously. This shows that the connection between these floor parts are still well in place, unlike in certain previous cases where the back floor was seen to attain the maximum drift after the left and right floors i.e. with considerable lag.

2. Fixed end beams at first floor level

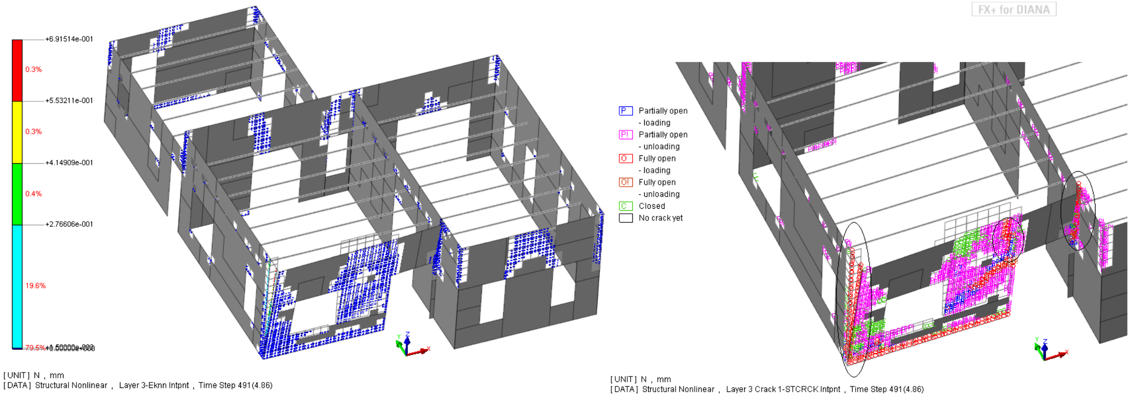

Figure 5-35: Crack strain and crack status at layer 3 of walls under $0.50g$ signal

The analysis is repeated for the model consisting of fixed timber beam ends. This is done by merging beam end nodes with wall nodes. The results are similar to the previous one with pinned type beam ends and is discussed below. The figure 5-36 shows the displacement response of the floors with respect to the foundation of the structure. The maximum floor displacement for L, R and B floors are -0.0688 to $+0.0704$ mm, -0.0576 to $+0.0828$ mm and -0.0692 to $+0.0821$ mm respectively. In this analysis, the last successfully converged step was at $4.86s$ or step 491, also, divergence occurred at step 492 or at $4.87s$. This is very similar to the former case of pinned beam ends, without significant difference in time at which divergence occurred.

Figure 5-36: Relative displacement of the floors L,R and B with reference to foundation

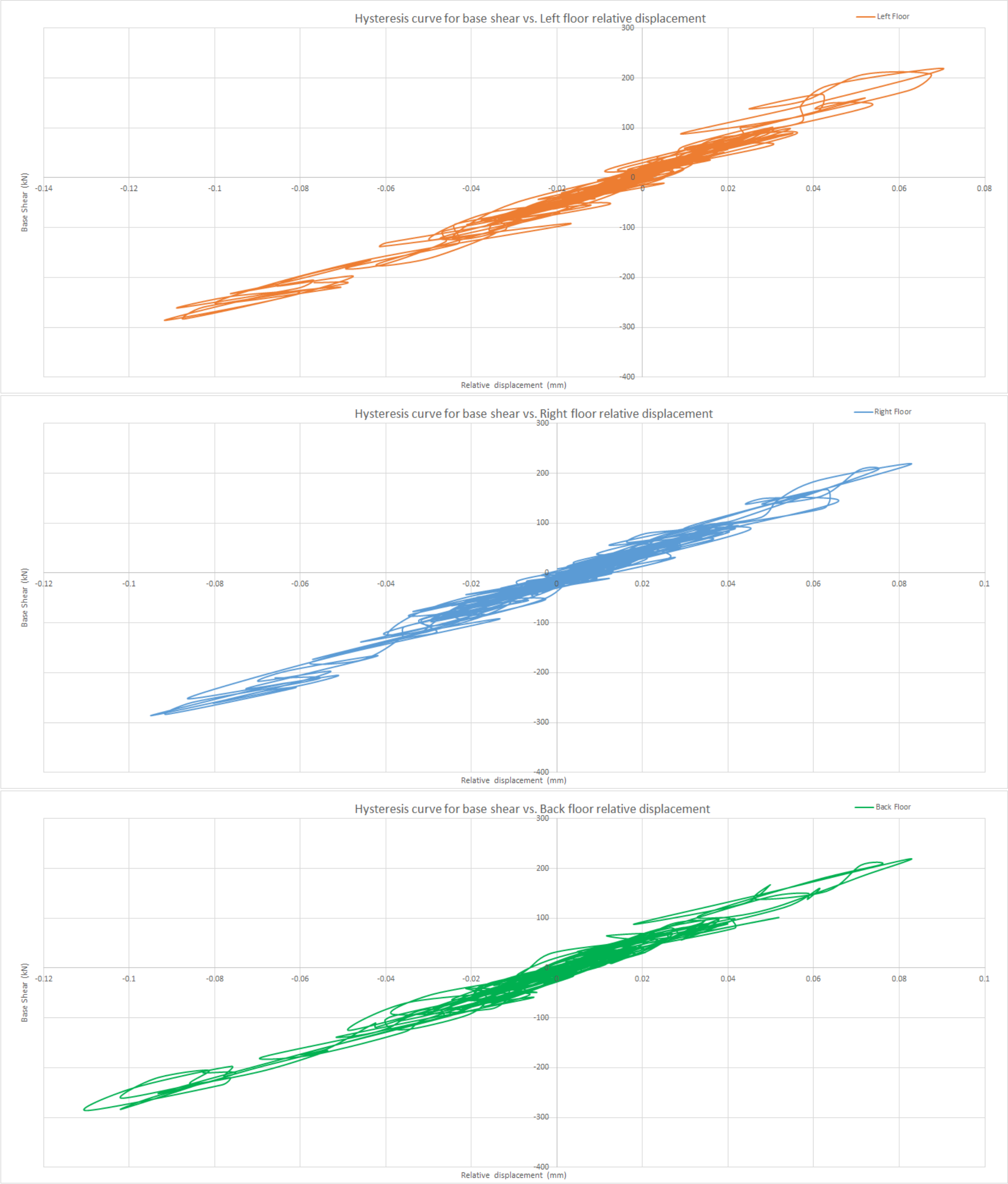

Figure 5-37: Hysteresis curve for base shear vs. relative displacement of the floors L,R and B with reference to foundation

The hysteresis curve shows base shear force plotted against relative displacement of the floors, showing the maximum base shear force at maximum displacements. For the time history input, the maximum base shear forces recorded are −285 to 218 kN. The influence of beam ends is not significantly different.

5-2-4 Inferences

1. It is observed that the seismic input signal scaling of 0.16*g* and 0.25*g* induce no significant cracking in the structure even for the analyses along Y-axis. Though cracking is observed, they are minute in strain which means they are under initiation stage yet. This is true for both kinds of beam end connections i.e. both pinned end beams and fixed end beams.

2. With respect to the higher scaling of 0.50*g*, first plastic cracks (that are in the stabilised stage) occur at time step of 4.42*s* in the case of the model with pinned end beams. From this point on through to the step where divergence occurs, 15 steps can be identified where convergence is not reached even after 50 iterations. However, it is to be noted that there is gradual increase in number of plastic cracks which results in the degeneration of the structure culminating finally at 4.71*s* due to occurrence of divergence.

3. With regard to the model with fixed beam ends, first plastic cracks occur at time step of 4.04*s*. It is also important to note that from this point, 30 steps can be identified where convergence is not reached even after 50 iterations. However, the analysis is allowed to continue. It is interesting to note two points of interest here though, that the first plastic crack appears at time of 4.04*s* which is 0.40*s* earlier in comparison to the model with pinned beam ends and divergence occurs at time step of 5.31*s* i.e. 0.60*s* later than that for the former type of model.

5-3 Analysis of structure including roof

All the previous analyses were carried out on the structure without modelling the roof. However, it was decided to be included to understand its influence on the global response of the structure. However, due to lack of reliable data, the roof part is modelled only partially. Also, the input scaled to 0.16*g*, 0.25*g* and 0.50*g* has been used for the subsequent analyses, which are uni-directional in nature. Accordingly, the model was input with time-history input along X and Y axis of the structure. The model used for these analyses is shown in figure. Two walls on the first storey *A** and *B**, refer 4-6, have been included as well. As they are triangular in shape, choosing quadrilateral elements to model the walls will eventually give rise to non-uniform meshing (haphazard element sizes). To avoid this disadvantage, meshing of these walls as well as the timber roofing is carried out using *CT30S*, which is a six-node triangular quadratic curved shell element and is based on area integration. The model is shown below in figure 5-38. Also, the time steps are analysed using different steps from here on. Time history input is given in 0.01*s* for the first 1000 steps and then time history is input in 0.005*s* for the next 250 steps.

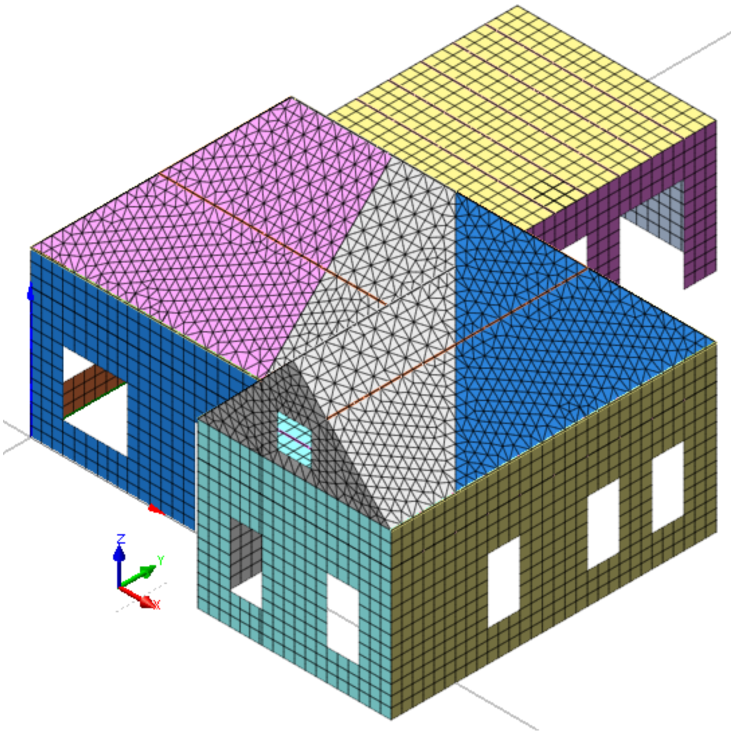

Figure 5-38: Model with roof used for the subsequent analyses

5-3-1 NLTHA with roof - X direction - $0.16g$

The following analyses are carried out using the given 0.16g and higher scaling input, since it has been observed that lower scaling input signal does not induce any serious damage. Hence, the analyses is carried out with higher scaling. The results are discussed as follows.

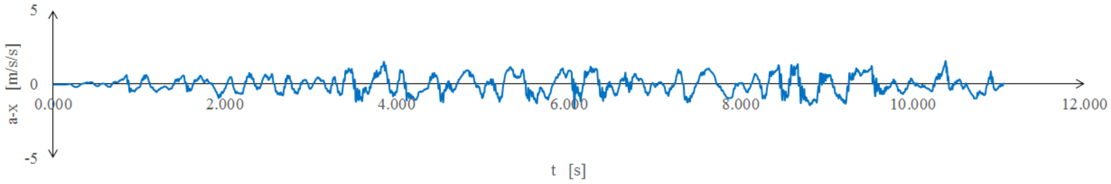

Figure 5-39: Time history input - Record 1 - Along X-axis, scaled to $0.16g$

Results

1. Pinned end beams at first floor level
   The relative displacement of the floors are displayed in the displacement curves below. The drift values for this analysis is visibly higher to the previous one within the time-input regime. The following are the maximum displacement values for the floors L, R and B are -0.224 and $+0.245$ mm, -0.219 and $+0.247$ mm and -0.175 and $+0.183$

mm, respectively. The maximum negative displacements for the left and right floors occur at time 8.66 s whereas the maximum positives occur at 8.82 s, however the same for the back floor occurs at 8.65 s and 8.81 s. The last converged step and the last step of the time history input is at step 1215.

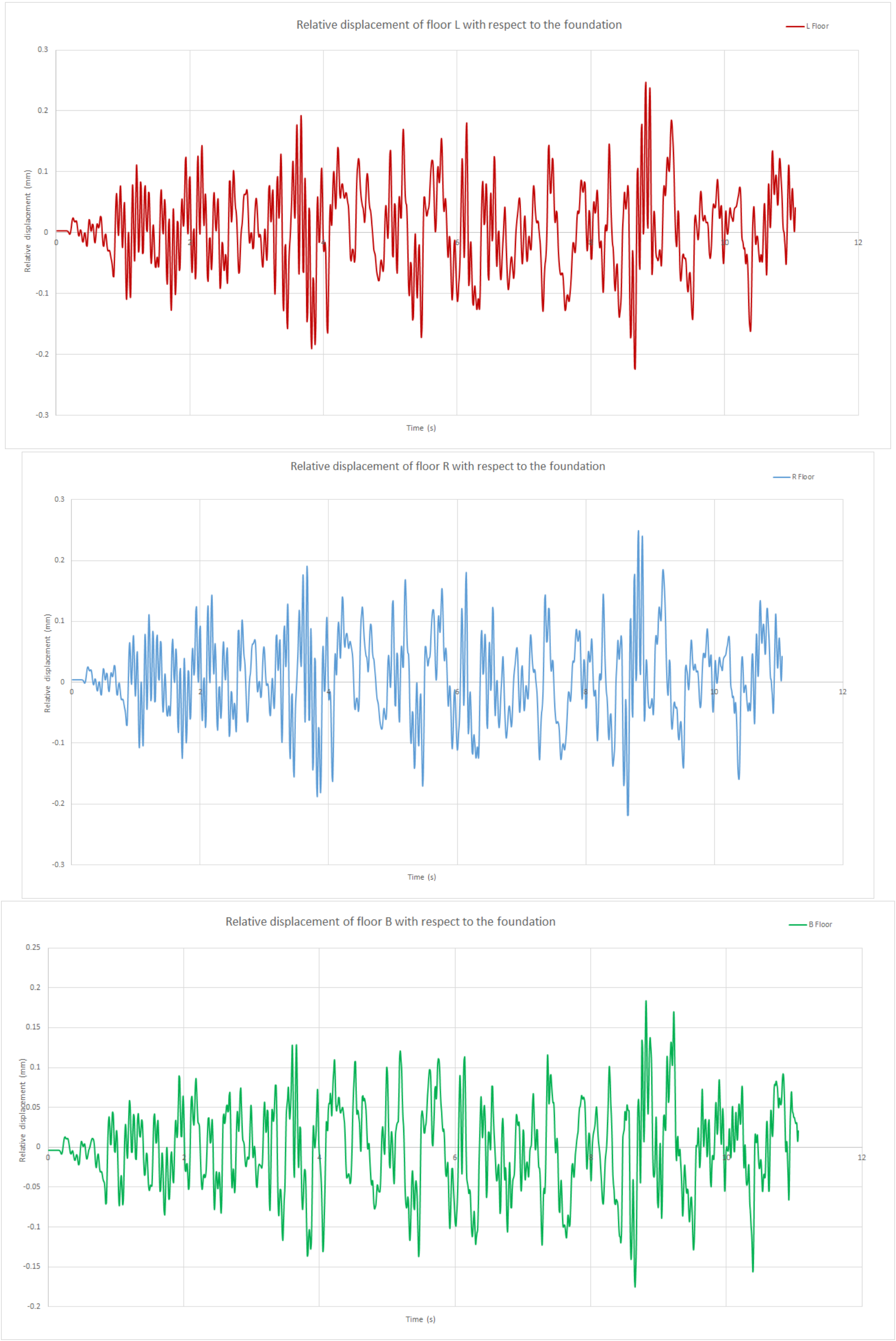

Figure 5-40: Relative displacement of the floors L,R and B with reference to foundation

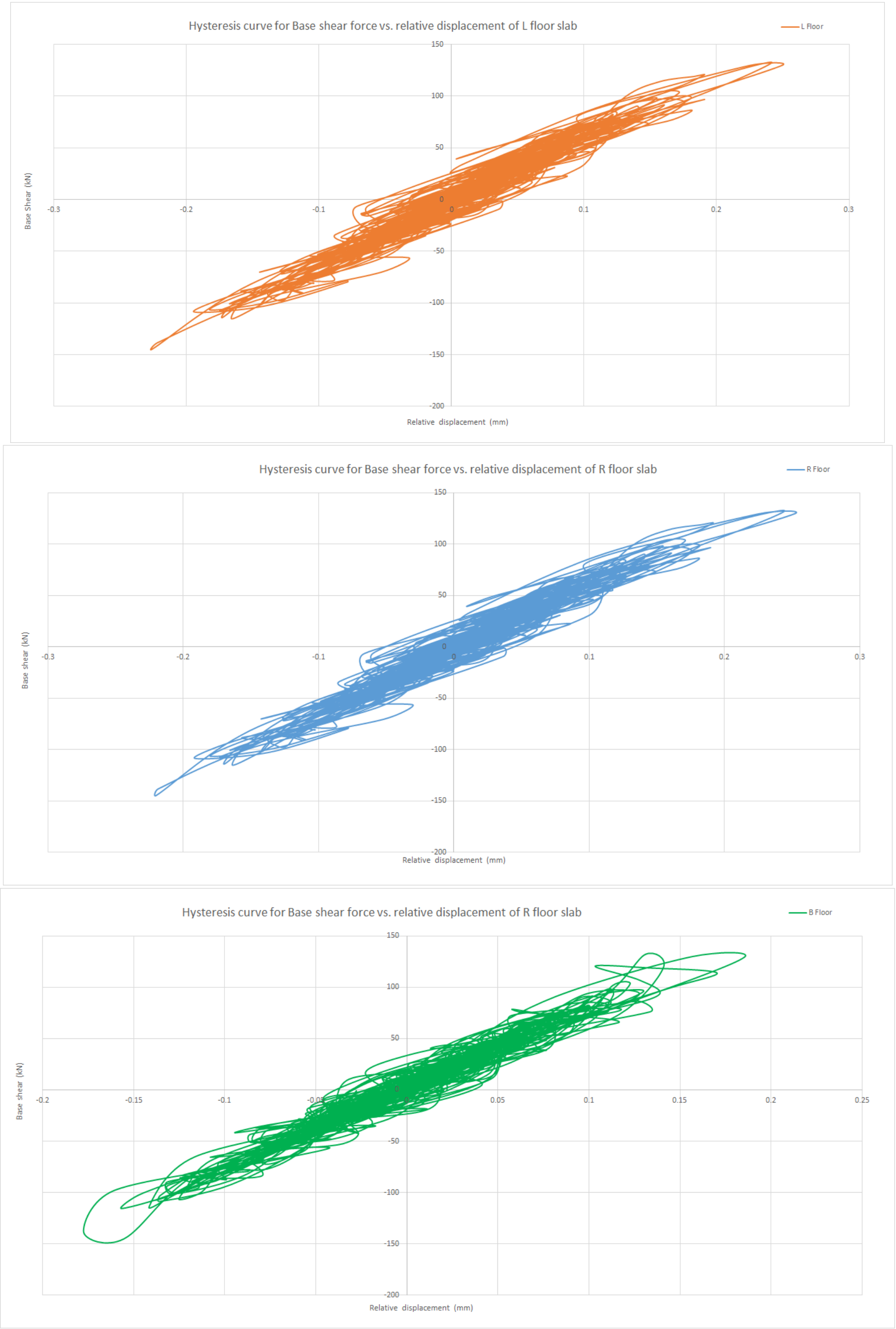

Figure 5-41: Hysteresis curve for base shear vs. relative displacement of the floors L,R and B with reference to foundation

At the last time-history input step which was converged without any error (i.e at time step 1215), the crack strain in this analysis was found to be $1.33 * 10^{-4}$. This suggests that no extensive cracking can be observed and that the cracks are still in the initiation stage. These values are very low compared to $1.5 * 10^{-3}$ which is the calculated ultimate crack strain. The figure 5-42 shows the crack pattern and crack status at the last step of time history input (step 1215). The plotted hysteresis curves shows the relationship between base shear force and the floor relative displacement. The maximum base shear forces recorded are -145 to $+130$ kN. This range is for the regime of time history input.

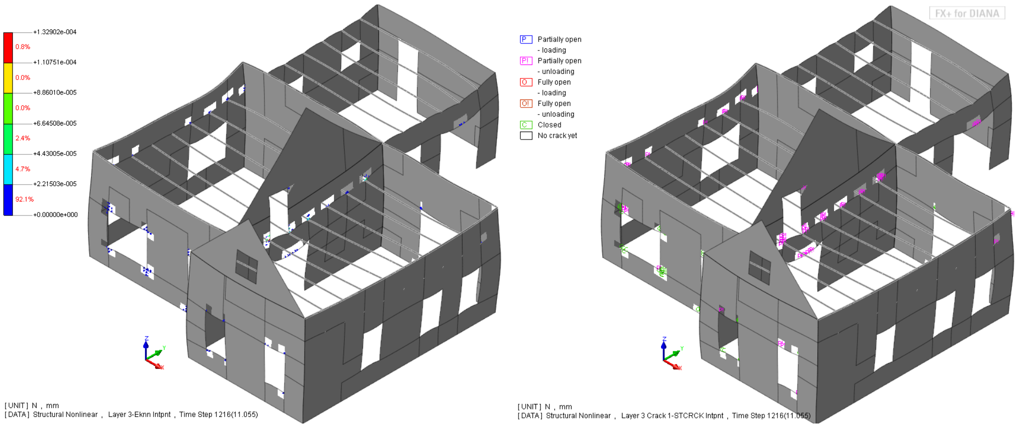

Figure 5-42: Crack strains and crack status at step 1216

2. <u>Fixed end beams at first floor level</u>
   Similarly, the model with the beam ends fixed, are analysed with $0.5g$ input along X-direction of the structure. The relative displacement of the floors are displayed in the displacement curves below. The maximum displacement values for the floors L, R and B are -0.224 and $+0.243$ mm, -0.218 and $+0.245$ mm and -0.168 and $+0.182$ mm, respectively. The maximum negative displacements for the left and right floors occur at time 8.66 s whereas the maximum positives occur at 8.82 s, however the same for the back floor occurs at 8.65 s and 8.81 s. The values are similar to the ones observed for the case of pinned beam ends. The last converged step and the last step of the time history input is at step 1216.

At the last time-history input step which was converged without any error (i.e at time step 1216), the crack strain in this analysis was found to be $1.33 * 10^{-4}$. This suggests that no extensive cracking can be observed and that the cracks are still in the initiation stage in the time history regime. These values are very low compared to $1.5 * 10^{-3}$ which is the calculated ultimate crack strain. The figure 5-45 shows the cracking status of the structure at the last time history step.

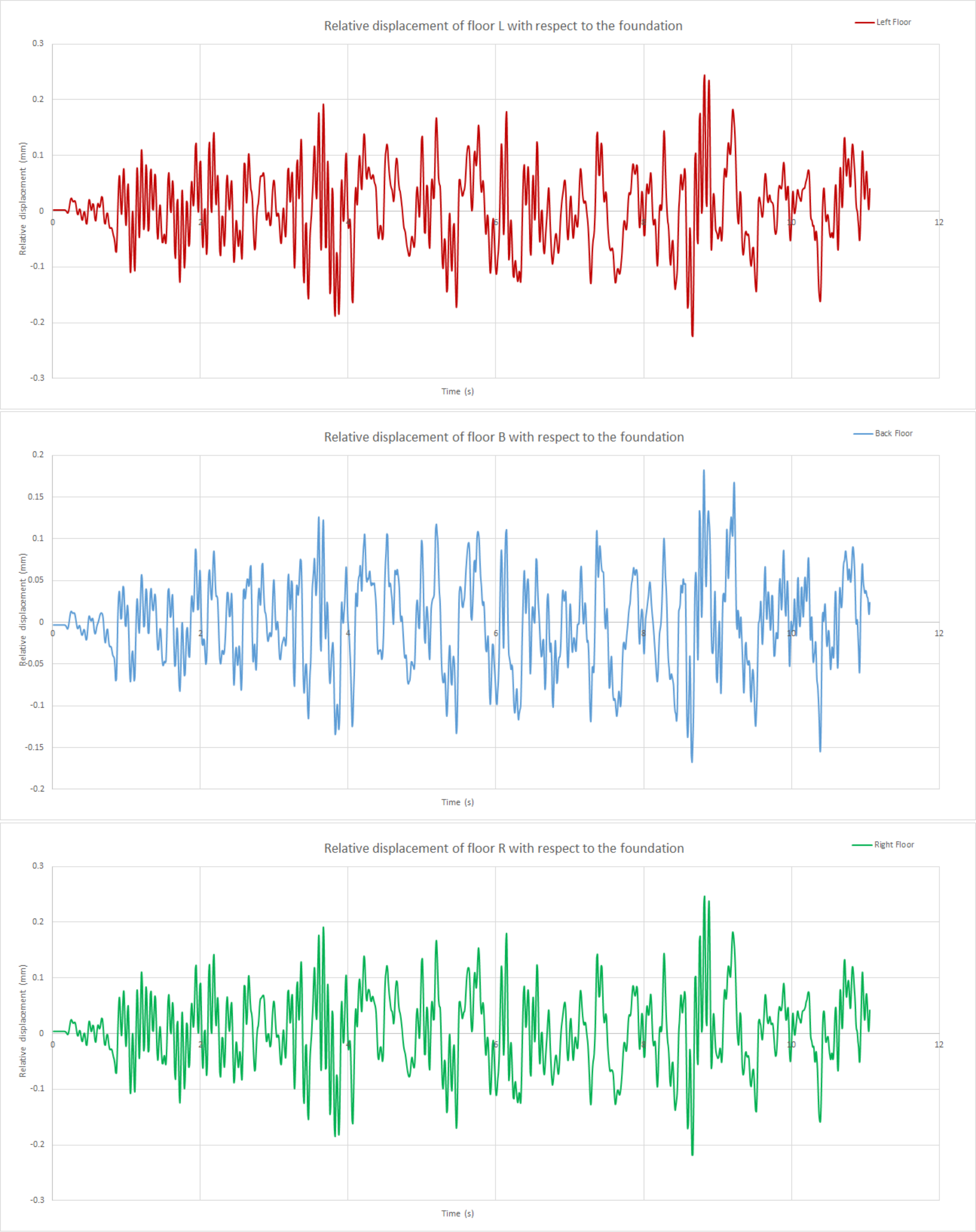

Figure 5-43: Relative displacement of the floors L,R and B with reference to foundation

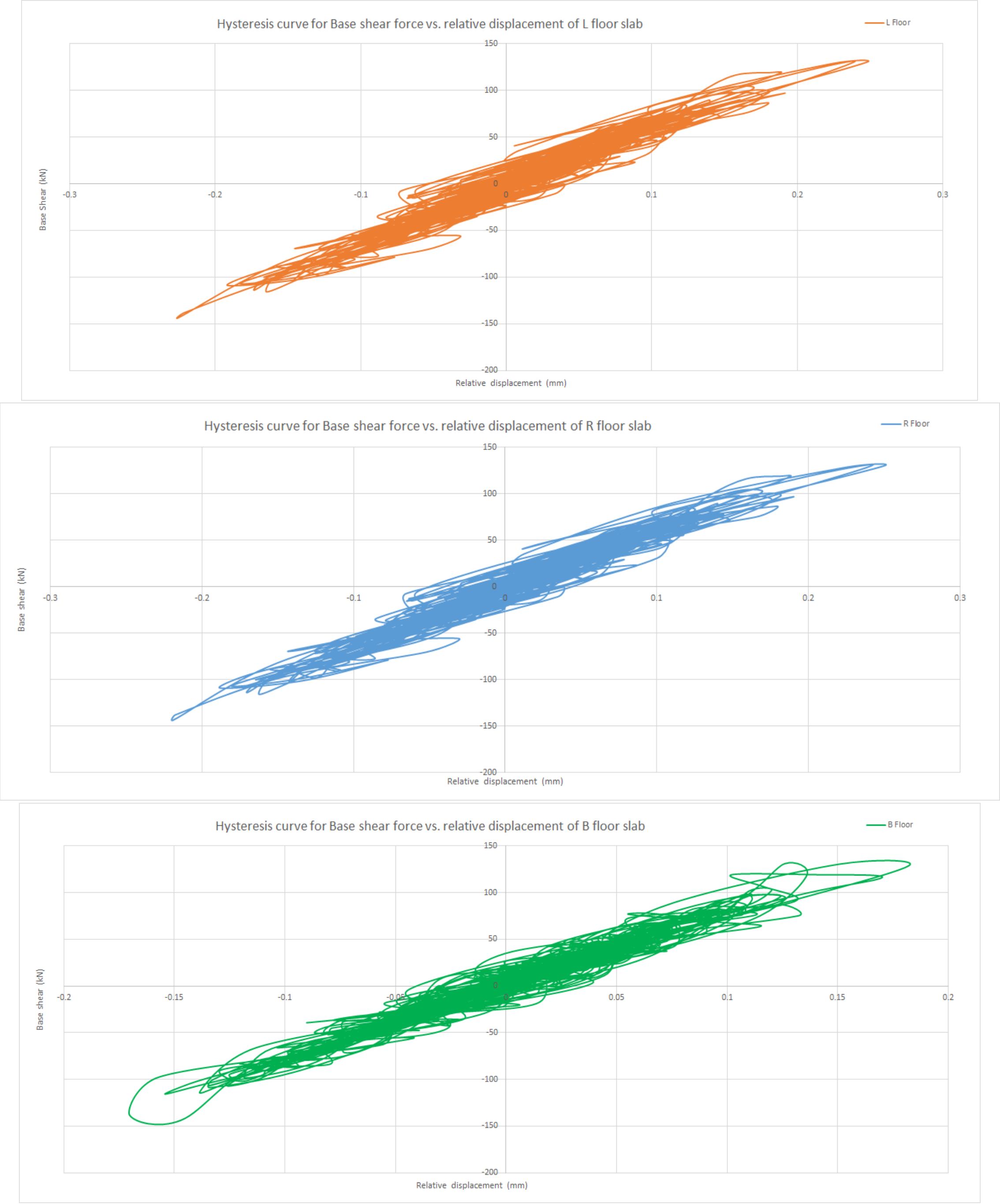

Figure 5-44: Hysteresis curve for base shear vs. relative displacement of the floors L,R and B with reference to foundation

The plotted hysteresis curves shows the relationship between base shear force and the floor relative displacement. The maximum base shear forces recorded are -143 to $+129$ kN. This range is for the regime of time history input.

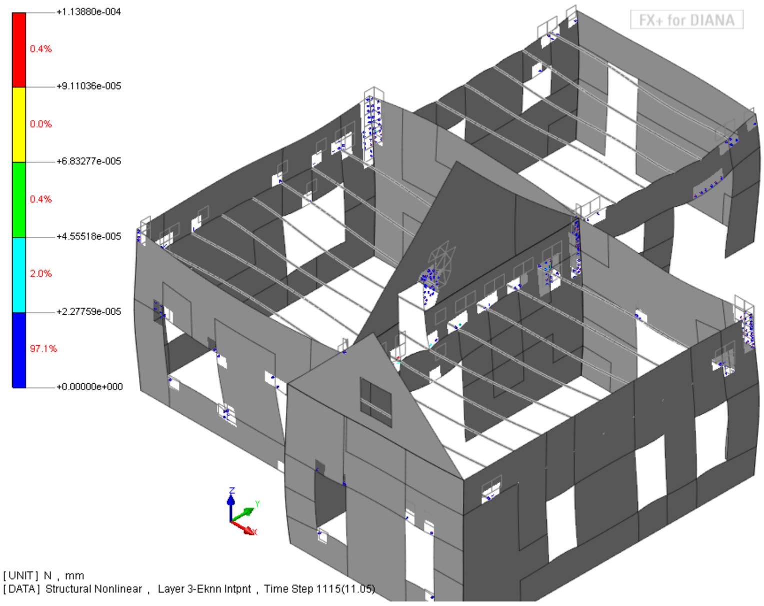

Figure 5-45: Crack pattern at step 1215

5-3-2 NLTHA with roof - X direction - $0.25g$

The model is now subjected to a stronger scaling of the time history input of $0.25g$. The input signal for this analysis is shown in figure 5-46. As was seen in the previous case, the structure did not undergo any damage through intensive cracking, and hence, the analyses is carried out with higher scaling. The results are discussed as follows.

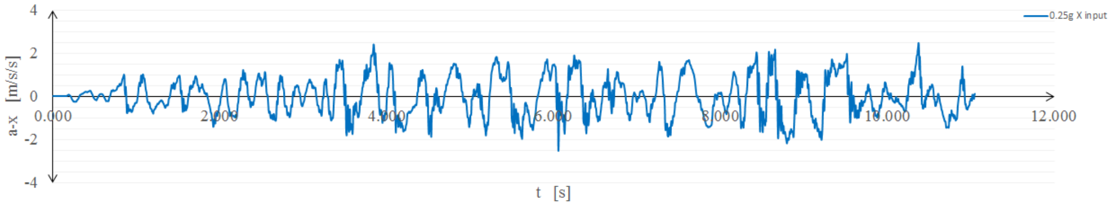

Figure 5-46: Time history input - Record 1 - Along X-axis, scaled to $0.25g$

Results

1. Pinned end beams at first floor level
   The relative displacement of the floors are displayed in the displacement curves below. The drift values for this analysis is visibly higher to the previous one within the time-input regime. The following are the maximum displacement values for the floors L, R and B are −0.368 to +0.424 mm, −0.358 to +0.427 mm and −0.279 to +0.289 mm, respectively. The maximum negative displacements for the left and right floors occur at time 8.66 s whereas the maximum positives occur at 8.82 s, however the same for the back floor occurs at 8.65 s and 8.81 s. The values are ten times higher than that

observed in the previous cases. The last converged step and the last step of the time history input is at step 1216.

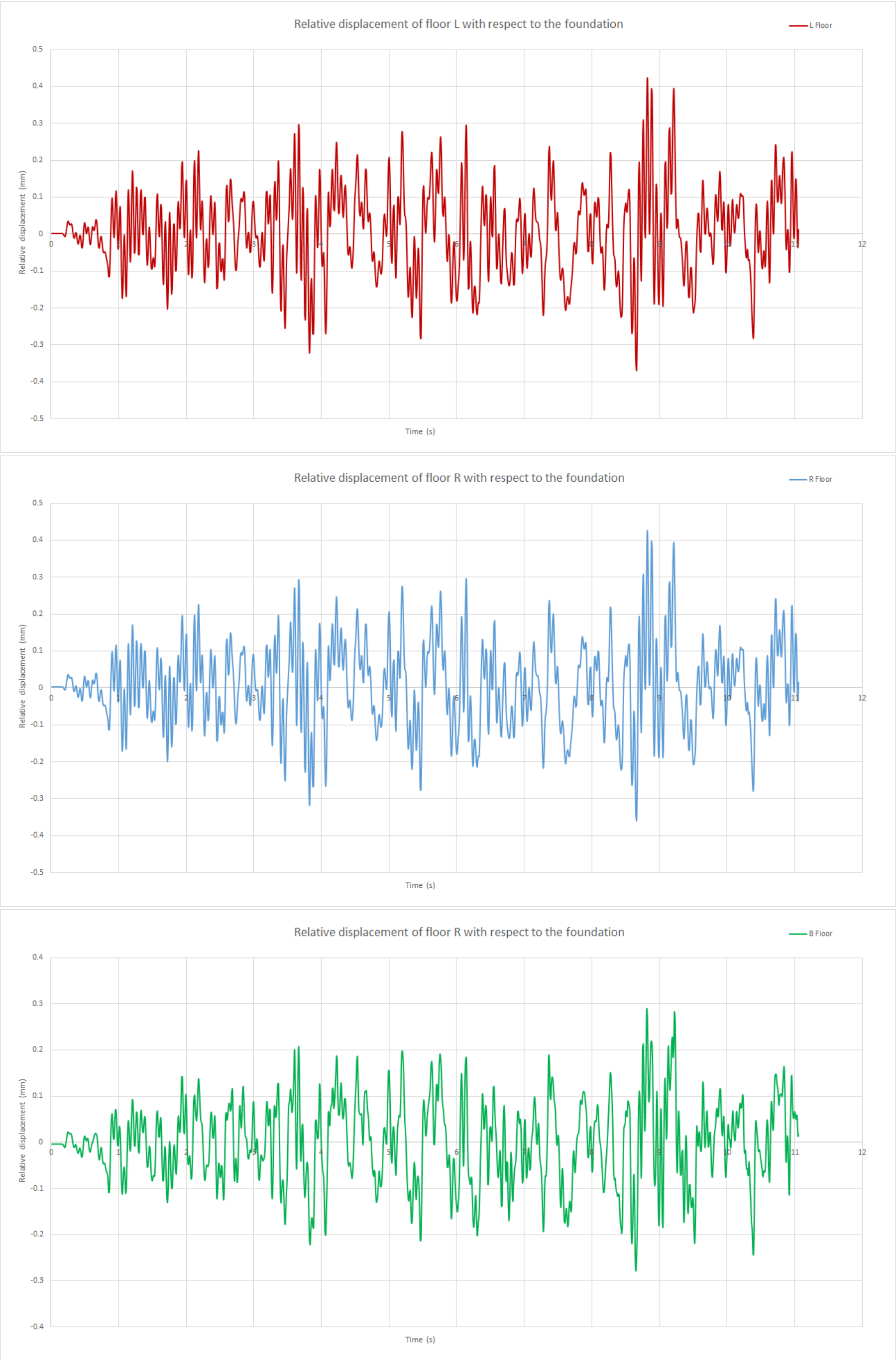

Figure 5-47: Relative displacement of the floors L,R and B with reference to foundation

At the last time-history input step which was converged without any error (i.e at time step 1215), the crack strain in this analysis was found to be $1.555 * 10^{-4}$. This suggests that no extensive cracking can be observed and that the cracks are still in the initiation stage. These values are very low compared to $1.5 * 10^{-3}$ which is the calculated ultimate crack strain. The figure 5-42 shows the difference in crack pattern at the end of time history input (step 1215). However, there is a faint increase in the cracking strains compared to the previous case of $0.16g$ signal.

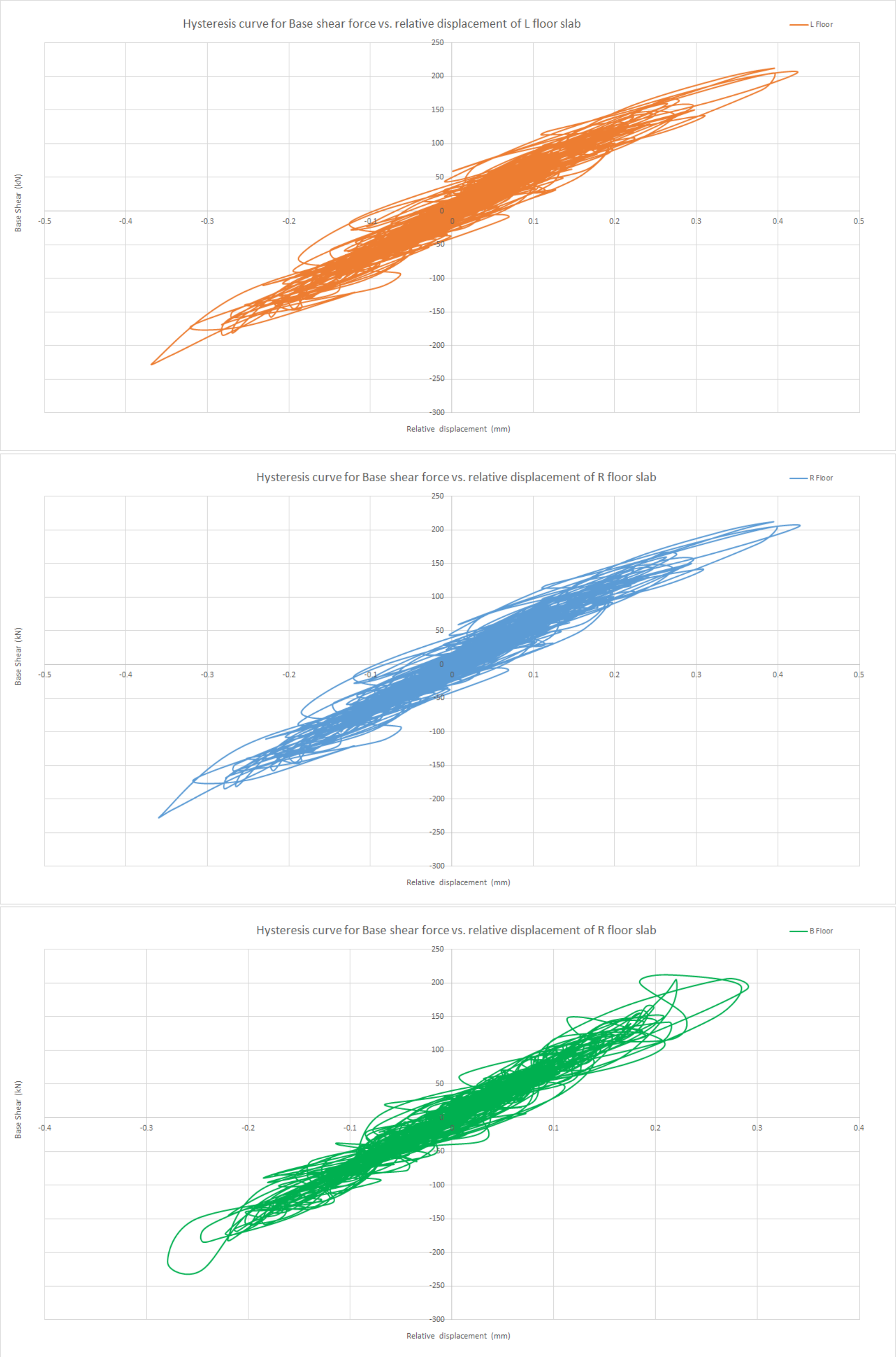

Figure 5-48: Hysteresis curve for base shear vs. relative displacement of the floors L,R and B with reference to foundation

The plotted hysteresis curves shows the relationship between base shear force and the floor relative displacement. The maximum base shear forces recorded are -226 to $+213$ kN. This range is for the regime of time history input.

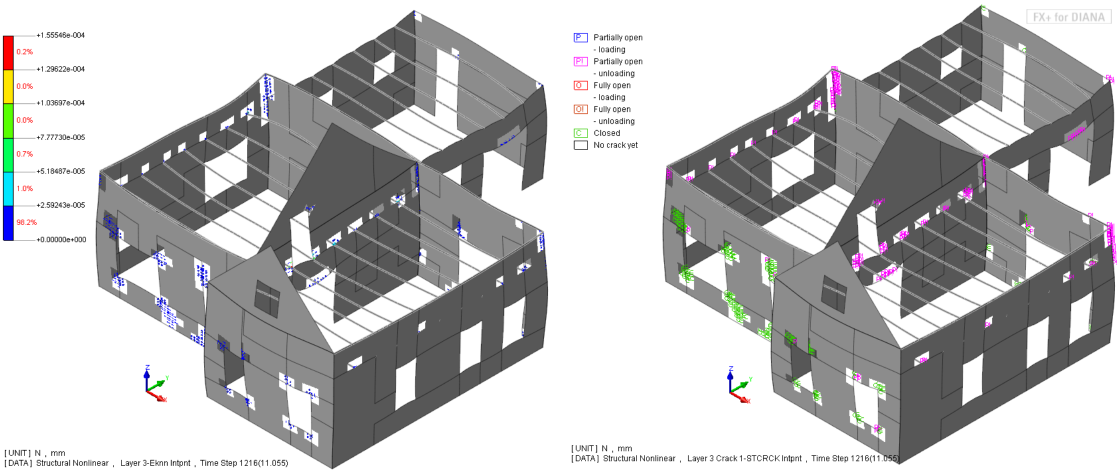

Figure 5-49: Crack strains and crack status at steps 1216

2. Fixed end beams at first floor level
   Similarly, the model with the beam ends fixed, are analysed with $0.25g$ input along X-direction of the structure. The relative displacement of the floors are displayed in the displacement curves below. The maximum displacement values for the floors L, R and B are -0.368 to $+0.425$ mm, -0.358 to $+0.428$ mm and -0.269 to $+0.289$ mm, respectively. The maximum displacement occurs between time periods 8.6 to 8.9 s, except for the back floor where the positive maximum occurs at $9.22s$. Such a behaviour shows that the back floor is lagging behind the two former ones. The values are similar to the ones observed for the case of pinned beam ends. The last converged step and the last step of the time history input is at step 1216, however the analysis was allowed to continue up to time step 1241.

At the last time-history input step which was converged without any error (i.e at time step 1216), the crack strain in this analysis was found to be $1.47 * 10^{-4}$. This suggests that no extensive cracking can be observed and that the cracks are still in the initiation stage in the time history regime. These values are very low compared to $1.5 * 10^{-3}$ which is the calculated ultimate crack strain. The figure 5-45 shows the difference in the cracking of the structure firstly within the time history range (upto time step 1216).

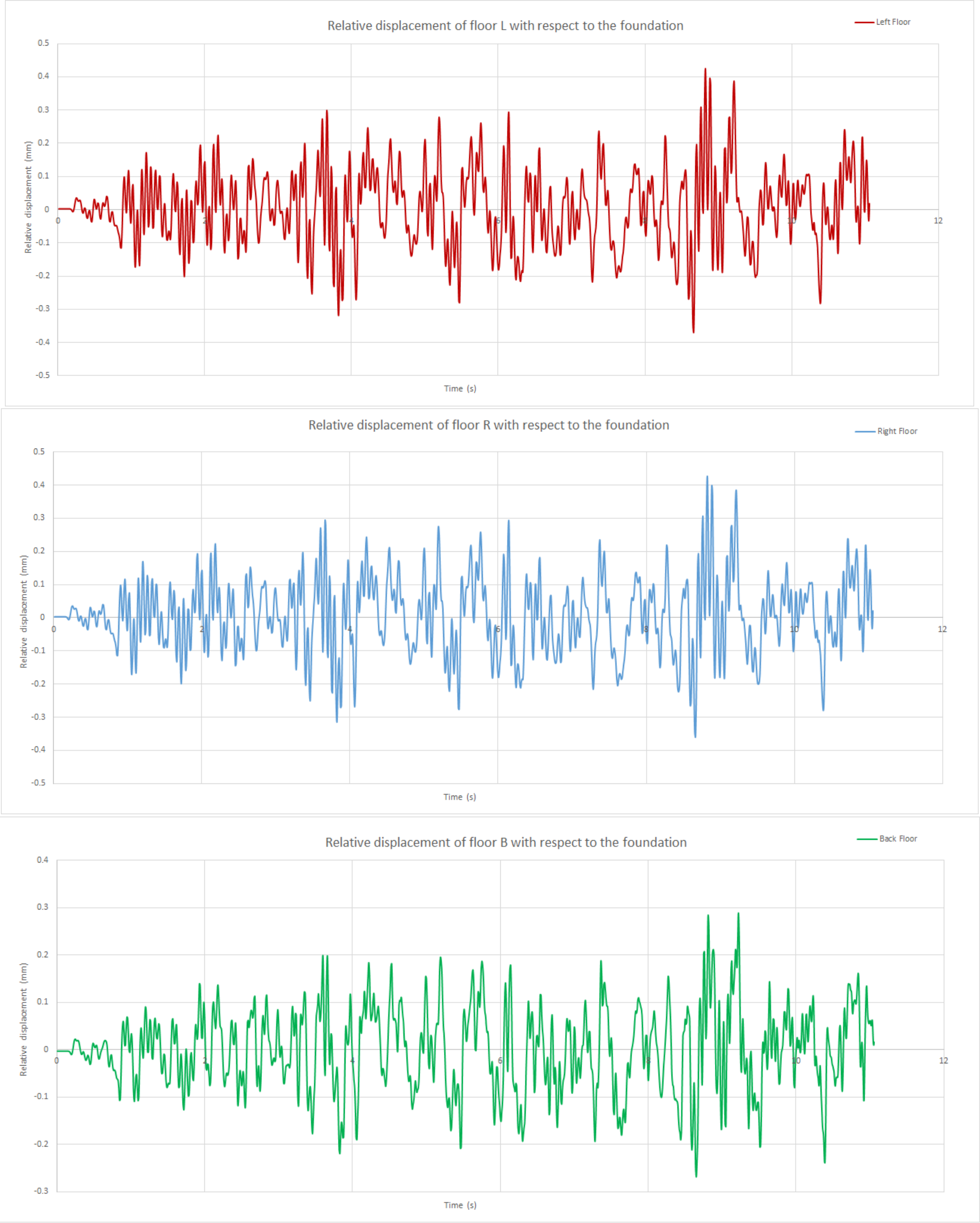

Figure 5-50: Relative displacement of the floors L,R and B with reference to foundation

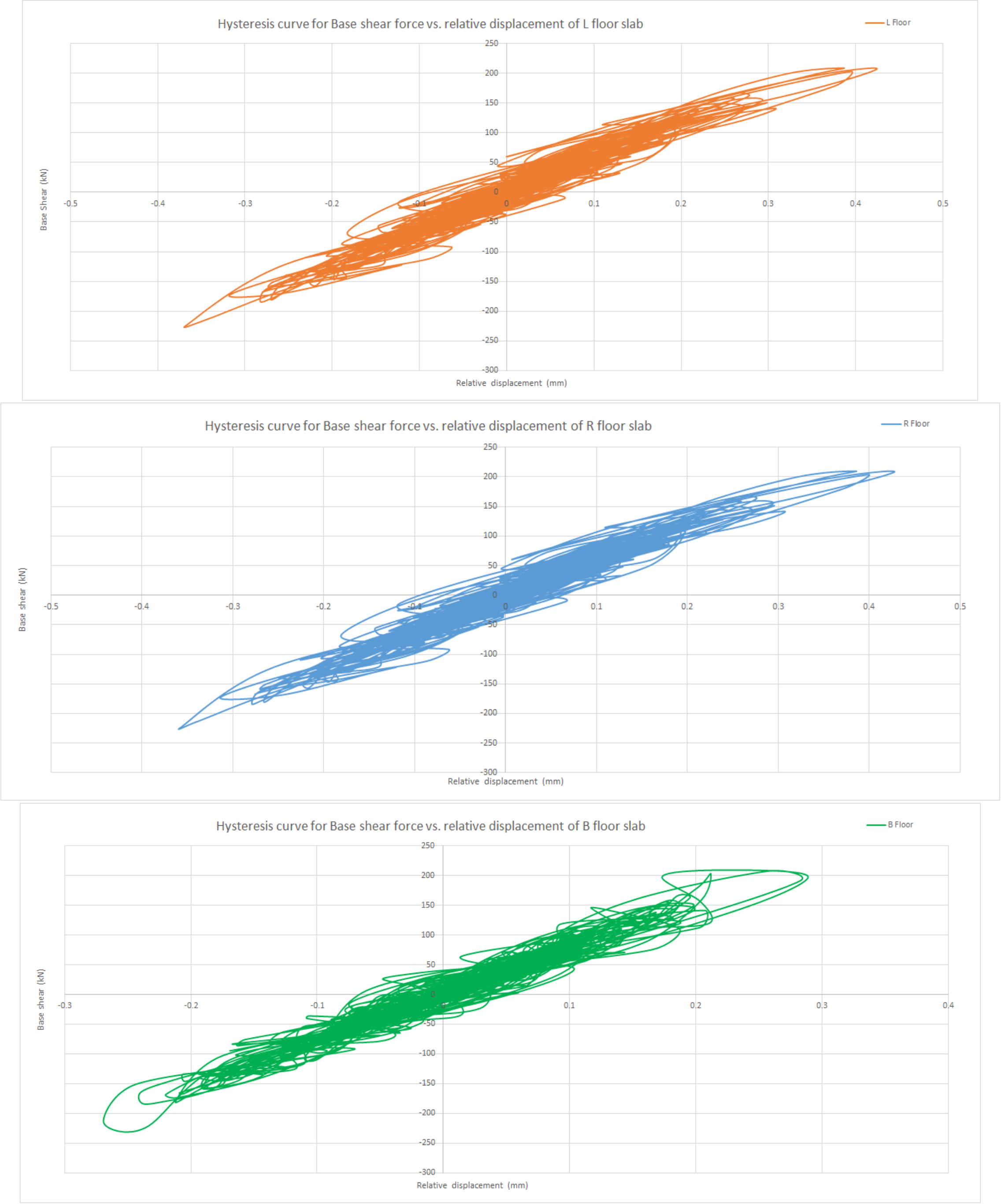

Figure 5-51: Hysteresis curve for base shear vs. relative displacement of the floors L,R and B with reference to foundation

The plotted hysteresis curves shows the relationship between base shear force and the floor relative displacement. The maximum base shear forces recorded are −225 to +210 kN. This range is for the regime of time history input.

Figure 5-52: Crack pattern at step 1216

5-3-3 NLTHA with roof - X direction - $0.50g$

The following analysis is carried out using the time history input scaled to 0.50g. The input signal is shown in figure 5-53. At this scaling, the maximum acceleration is 4.98 m/s^2. This value is very high with respect to earthquake signal and corresponds to the strongest of earthquakes. The results are discussed as follows.

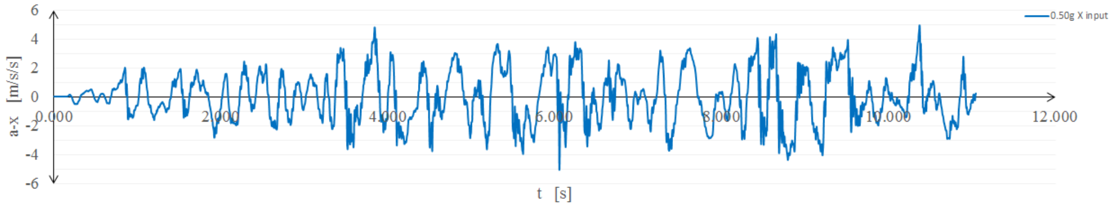

Figure 5-53: Time history input - Record 1 - Along X-axis, scaled to $0.50g$

Results

1. <u>Pinned end beams at first floor level</u>
   The relative displacement of the floors are displayed in the displacement curves below. The drift values for this analysis is visibly higher to the previous one within the time-input regime. The following are the maximum displacement values for the floors L, R and B are -1.806 and $+1.178$ mm, -1.782 and $+1.148$ mm and -1.581 and $+1.194$ mm, respectively. The maximum negative displacements for the left and right floor occurs at time 6.3 s and at 6.33 s for the back floor whereas the maximum positives occur at 6.38 s for left floor and back floor, but for the right floor it occurs at 5.61 s. Since the time history input given here has very high values of acceleration, the analyses reached divergence at time step of 6.49s.

At the last step where convergence was achieved without any error (i.e at time step 656), the crack strain in this analysis was found to be $10.49 * 10^{-3}$. This suggests the formation of extensive cracking since these values are higher than $1.5 * 10^{-3}$ which is the calculated ultimate crack strain. The figure 5-56 shows the difference in crack pattern at the last converged time step of 654 at time 6.49s. It can be observed from the crack status in the figure 5-56 that the wall junctions have cracked extensively. However, out-of-plane walls are the highest affected with cracks which are fully open and in the stabilisation stage which means that the cracks are fully formed and are giving rise to new cracks.

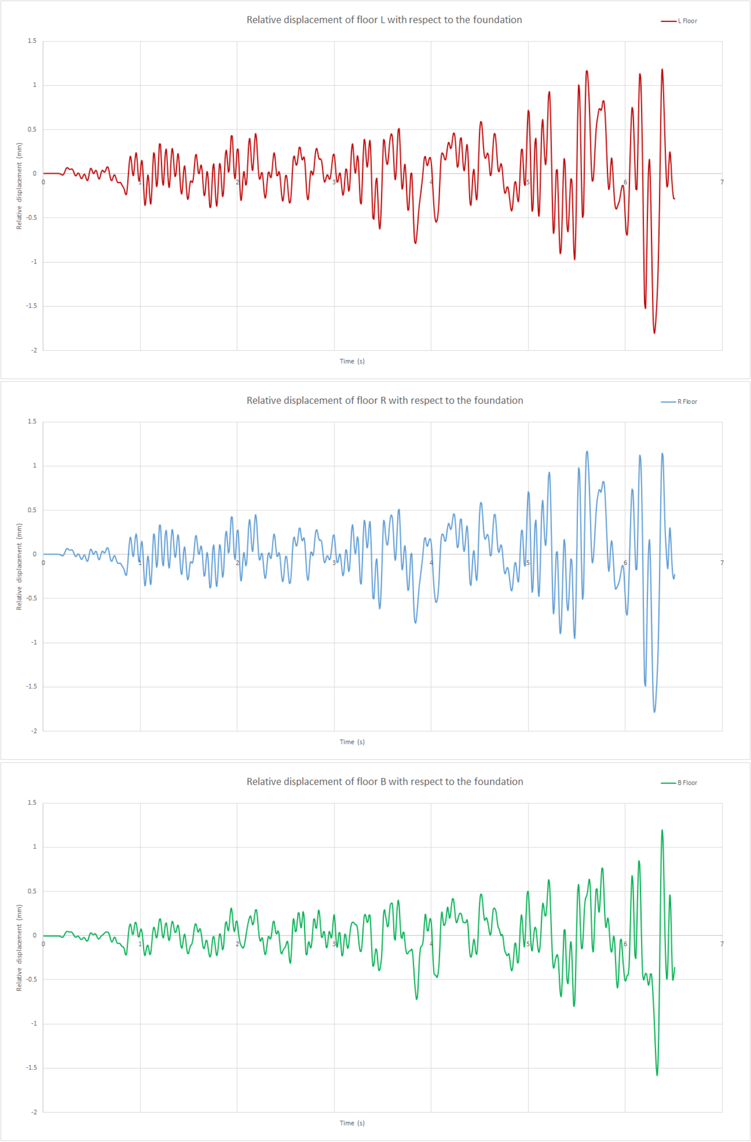

Figure 5-54: Relative displacement of the floors L,R and B with reference to foundation

Figure 5-55: Hysteresis curve for base shear vs. relative displacement of the floors L,R and B with reference to foundation

The plotted hysteresis curves shows the relationship between base shear force and the floor relative displacement. The maximum base shear forces recorded are −371 to +416 kN. This range is for the regime of time history input which achieved convergence.

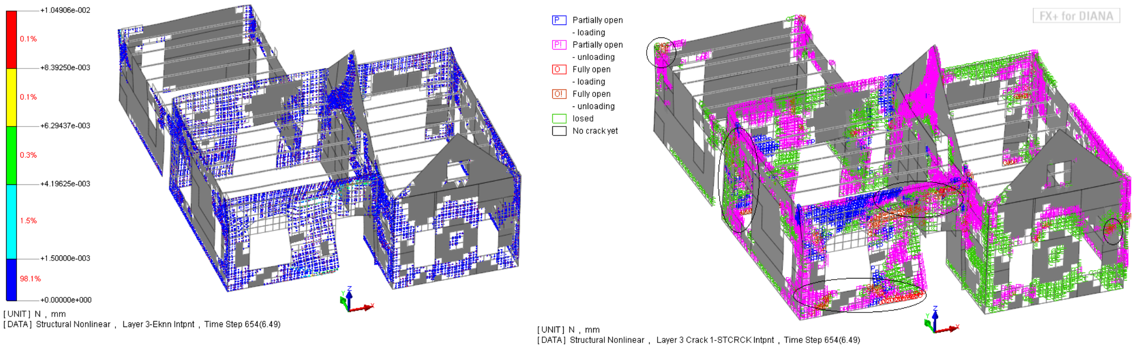

Figure 5-56: Crack pattern at last converged step at 6.49 s

2. <u>Fixed end beams at first floor level</u>

Similarly, the model with the beam ends fixed, are analysed with $0.5g$ input along X-direction of the structure. The relative displacement of the floors are displayed in the displacement curves below. The maximum relative displacement values for the floors L, R and B are -1.490 to $+1.160$ mm, -1.473 to $+1.162$ mm and -0.595 to $+1.00$ mm, respectively. The maximum negative displacement for all floors occurs at time 6.28 s whereas the maximum positive displacement for left and right floors occurs at 6.15 s, except for the back floor which reaches its maximum relative positive displacement at 5.76 s . The values are similar to the ones observed for the case of pinned beam ends. Owing to the high values of acceleration, divergence occurred at 6.99s. It is interesting to note that for the same signal the model with fixed beam end type shows convergence for an extra 0.46 s when compared to that with the pinned end type.

At the last step where convergence was achieved without any error (i.e at time step 702 or 6.97s), the crack strain in this analysis was found to be $48.50 * 10^{-3}$. This suggests the formation of extensive cracking since these values are higher than $1.5 * 10^{-3}$ which is the calculated ultimate crack strain. The figure 5-59 shows the difference in crack pattern at the last converged time step of 702 at time 6.97s. It can be observed from the crack status in the figure 5-60 that the wall junctions have cracked extensively. However, out-of-plane walls are the highest affected with cracks which are fully open (O! in red) and in the stabilisation stage which means that the cracks are fully formed and are giving rise to new cracks.

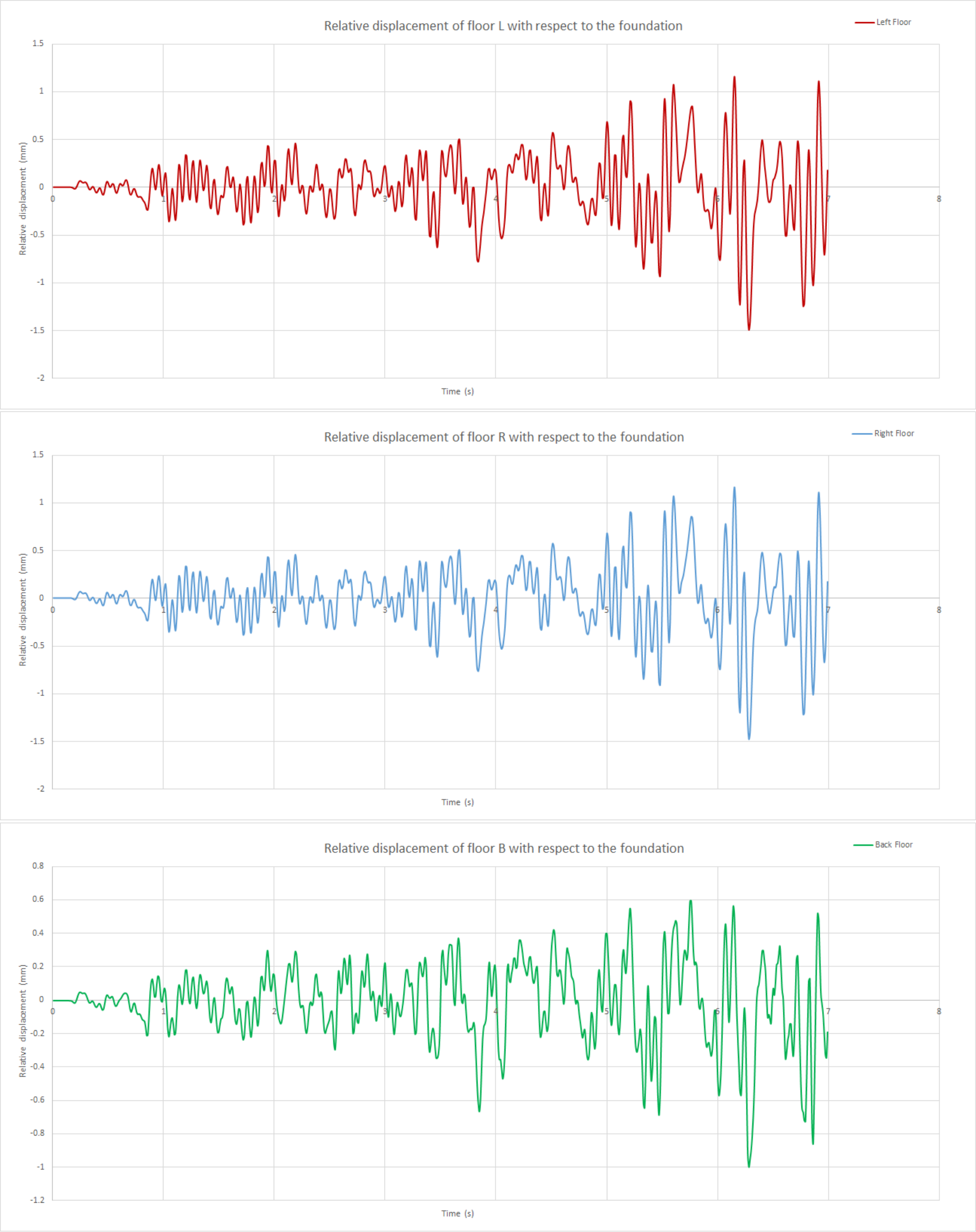

Figure 5-57: Relative displacement of the floors L,R and B with reference to foundation

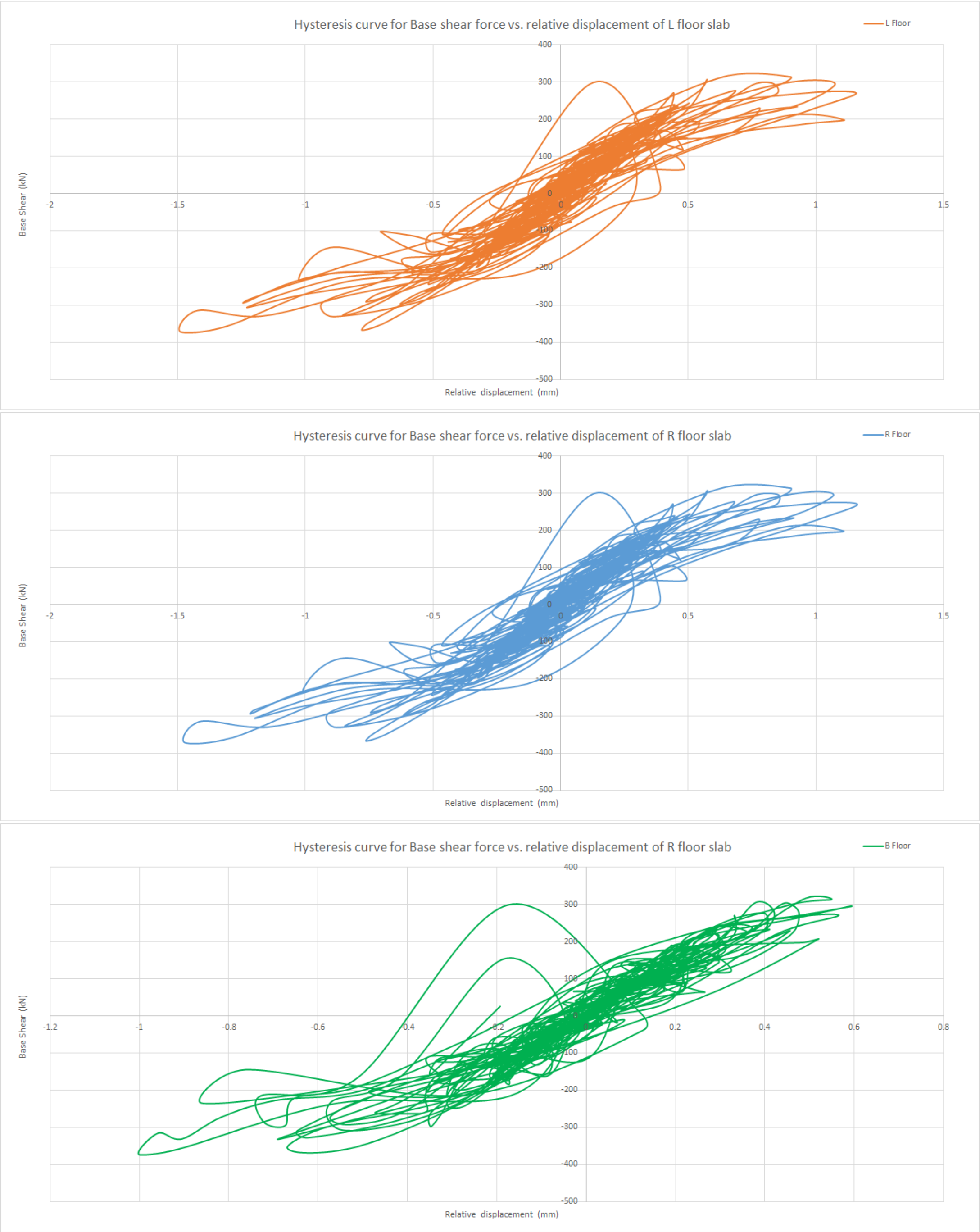

Figure 5-58: Hysteresis curve for base shear vs. relative displacement of the floors L,R and B with reference to foundation

The plotted hysteresis curves shows the relationship between base shear force and the floor relative displacement. The maximum base shear forces recorded are -372 to $+317$ kN. This range is for the regime of time history input.

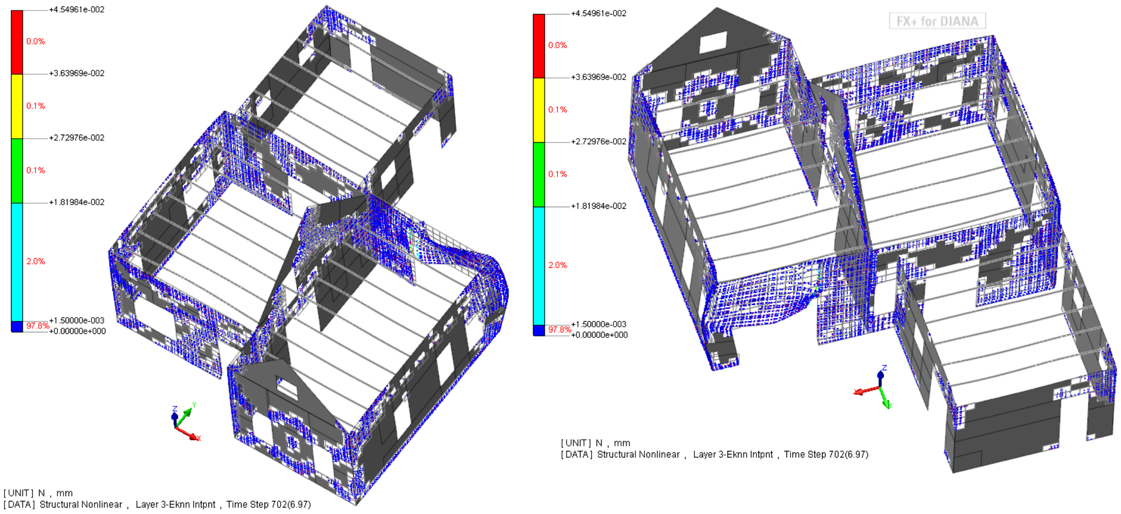

Figure 5-59: Crack pattern at last converged step at 6.97 s

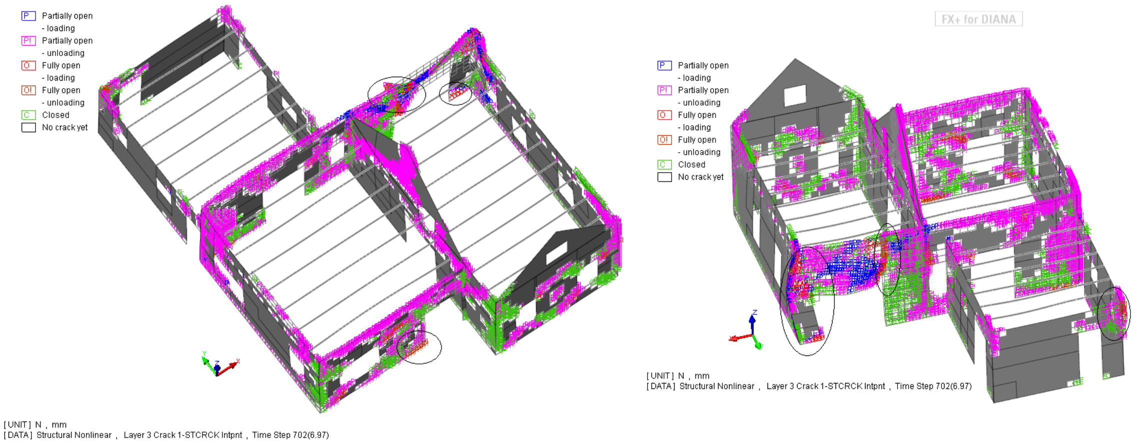

Figure 5-60: Crack pattern at last converged step at 6.97 s

5-3-4 NLTHA with roof - Y direction - $0.16g$

The model with roof is now analysed along Y-direction using the relevant Y-direction $0.16g$ time history input. As described before, the model is improved to account for parts of the roof - two walls and timber roofing and underlying timber beams. Again, non-linearity is concentrated to masonry and hence timber parts are modelled only with linear elastic behaviour. However, it was not possible to model inclined beams as it was rejected as a conflict by the program at the beginning of the analyses. It is understood that the given input signal along Y-direction is not as strong compared to that of X-direction. Accordingly, the results will be similarly affected with crack strains and displacements. The results are presented below.

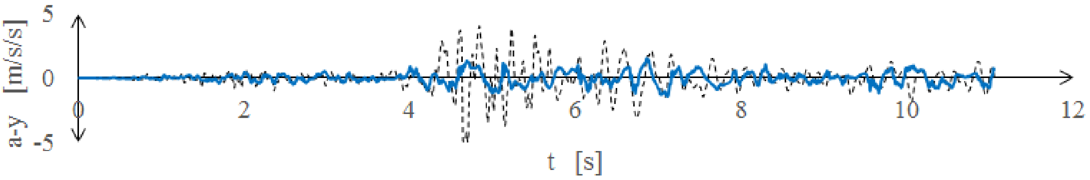

Figure 5-61: Time history input - Record 1 - Along Y-axis, scaled to $0.16g$

Results

1. Pinned end beams at first floor level
   The relative displacement of the floors are displayed in the displacement curves below. The drift values for this analysis is visibly higher to the previous one within the time-input regime. The following are the maximum displacement values for the floors L, R and B are -0.054 to $+0.039$ mm, -0.053 to $+0.047$ mm and -0.039 to $+0.037$ mm, respectively. All these maximum negative displacements occurs at time 6.87 whereas the maximum positives occur at 7.11 s. The last converged step and the last step of the time history input is at step 1216.

   From observing the analysis along X-direction, it can be seen that the displacement in the current case is approximately one fourth of that found in the former case.

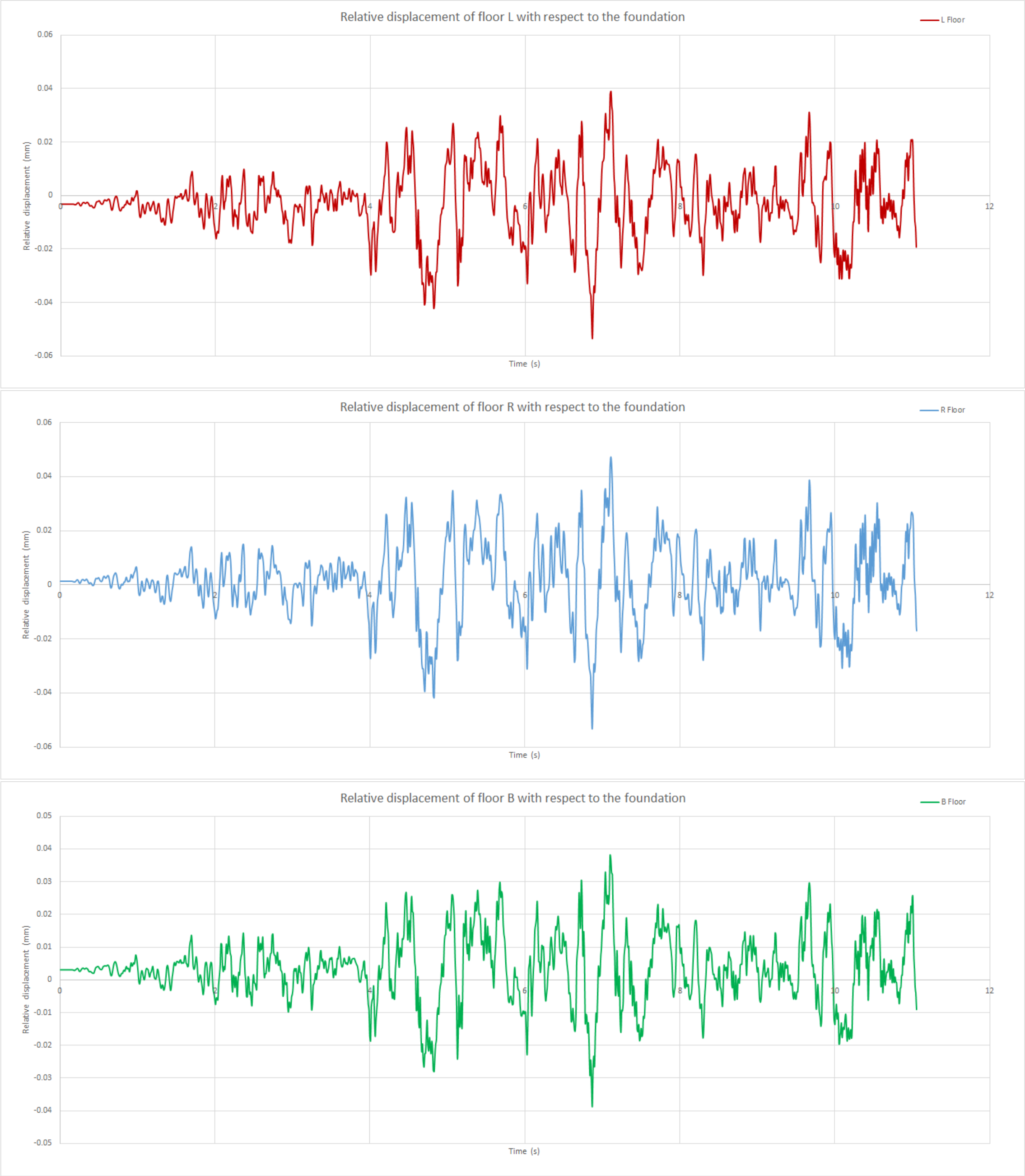

Figure 5-62: Relative displacement of the floors L,R and B with reference to foundation

At the last time-history input step which was converged without any error (i.e at time step 1216), the crack strain in this analysis was found to be $1.666 * 10^{-4}$. This suggests that no extensive cracking can be observed and that the cracks are still in the initiation stage. These values are very low compared to $1.5 * 10^{-3}$ which is the calculated ultimate crack strain, hence of not much importance.

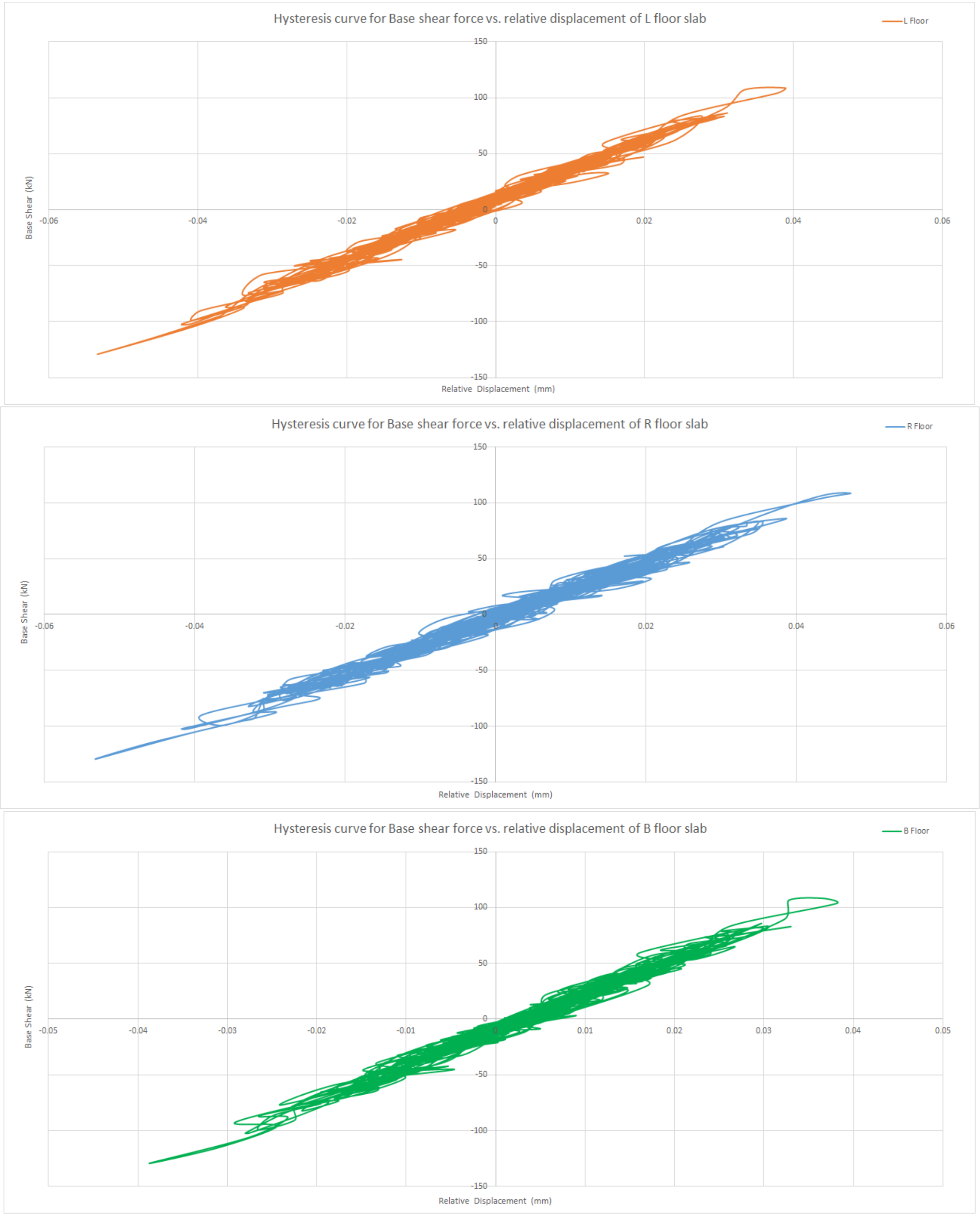

Figure 5-63: Hysteresis curve for base shear vs. relative displacement of the floors L,R and B with reference to foundation

The plotted hysteresis curves shows the relationship between base shear force and the floor relative displacement. The maximum base shear forces recorded are -129 to $+108$ kN. This range is for the regime of time history input.

2. Fixed end beams at first floor level

The relative displacement of the floors are displayed in the displacement curves below. The drift values for this analysis is visibly higher to the previous one within the time-input regime. The following are the maximum displacement values for the floors L, R and B are -0.053 to $+0.039$ mm, -0.053 to $+0.048$ mm and -0.039 to $+0.036$ mm, respectively. All these maximum negative displacements occurs at time 6.87 whereas the maximum positives occur at 7.11 s. The last converged step of importance and the last step of the time history input is at step 1216.

It is interesting to see that the analysis along Y-direction yields smaller displacements, as well as the non-existence of any effect on the displacement due to the use of different beam end type in the structure.

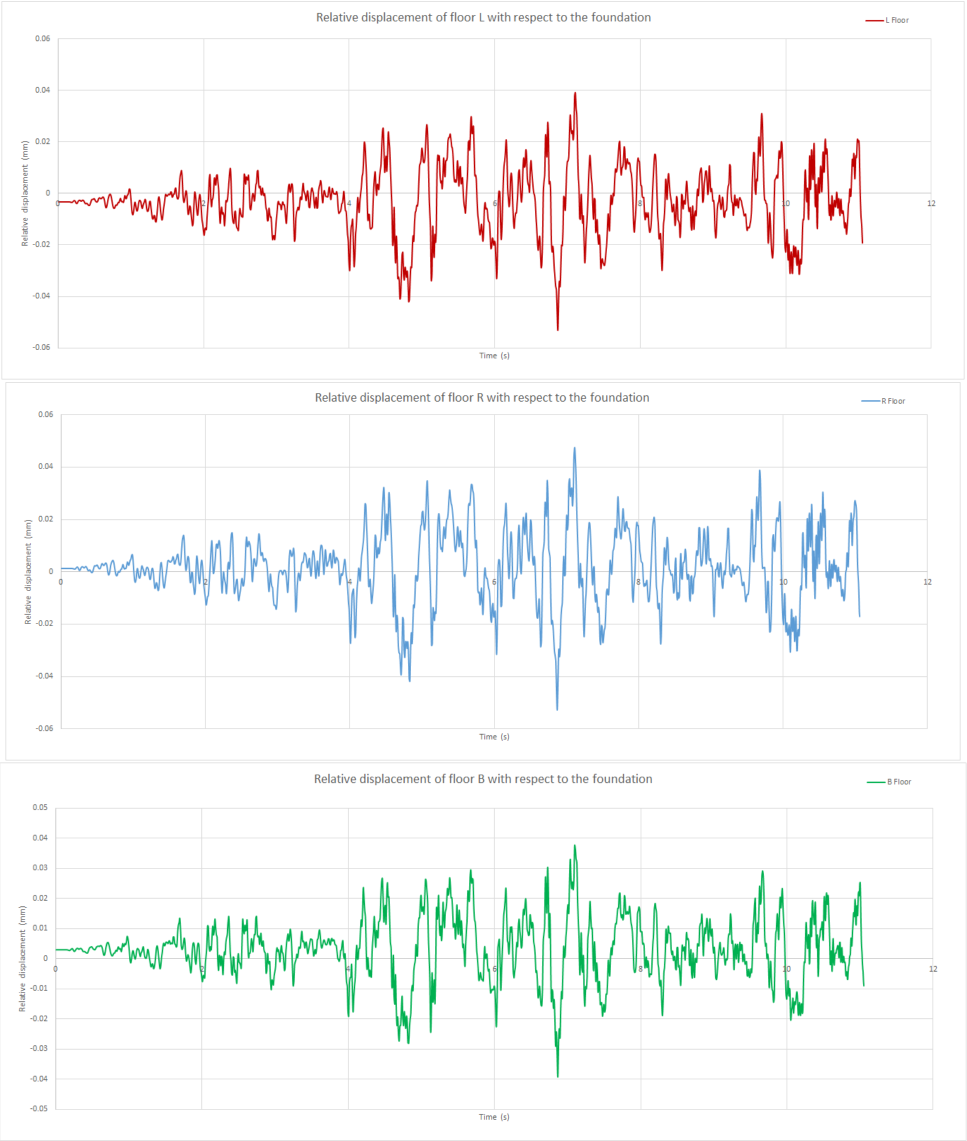

Figure 5-64: Relative displacement of the floors L,R and B with reference to foundation

At the last time-history input step which was converged without any error (i.e at time step 1216), the crack strain in this analysis was found to be $1.670 * 10^{-4}$. This suggests that no extensive cracking can be observed and that the cracks are still in the initiation stage. These values are very low compared to $1.5 * 10^{-3}$ which is the calculated ultimate crack strain, hence not of much importance.

The plotted hysteresis curves shows the relationship between base shear force and the floor relative displacement. The maximum base shear forces recorded are -129 to $+109$ kN. This range is for the regime of time history input.

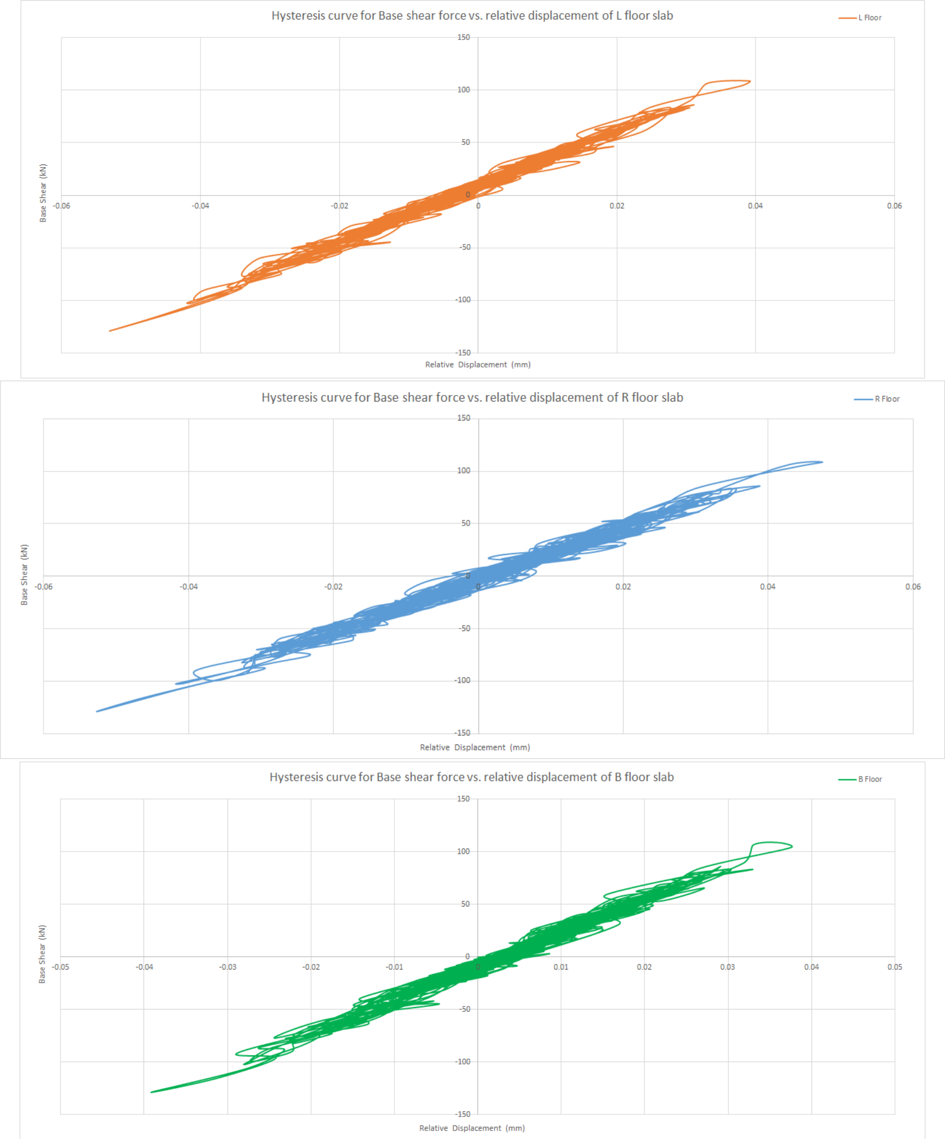

Figure 5-65: Hysteresis curve for base shear vs. relative displacement of the floors L,R and B with reference to foundation

5-3-5 NLTHA with roof - Y direction - $0.25g$

The model with roof is now analysed along Y-direction using the relevant Y-direction $0.25g$ time history input. As described before, the model is improved to account for parts of the roof - two walls and timber roofing and underlying timber beams. Again, non-linearity is concentrated to masonry and hence timber parts are modelled only with linear elastic behaviour. However, it was not possible to model inclined beams as it was rejected as a conflict by the program at the beginning of the analyses. It is understood that the given input signal along Y-direction is not as strong compared to that of X-direction. Accordingly, the results will be similarly affected with crack strains and displacements. The results are presented below.

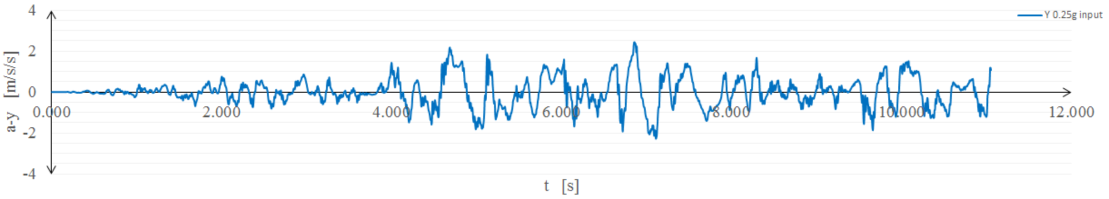

Figure 5-66: Time history input - Record 1 - Along Y-axis, scaled to $0.25g$

Results

1. Pinned end beams at first floor level
   The relative displacement of the floors are displayed in the displacement curves below. The drift values for this analysis is visibly higher to the previous one within the time-input regime. The following are the maximum displacement values for the floors L, R and B are -0.085 to $+0.065$ mm, -0.088 to $+0.075$ mm and -0.065 to $+0.059$ mm, respectively. All these maximum negative displacements occurs at time 6.87 whereas the maximum positives occur at 7.11 s. The last converged step of importance and the last step of the time history input is at step 1216.

   From observing the analysis along X-direction, it can be seen that the displacement in the current case is approximately one fourth of that found in the former case. At the last time-history input step which was converged without any error (i.e at time step 1216), the crack strain in this analysis was found to be $2.079 * 10^{-4}$. This suggests that no extensive cracking can be observed and that the cracks are still in the initiation stage. These values are very low compared to $1.5 * 10^{-3}$ which is the calculated ultimate crack strain.

Figure 5-67: Relative displacement of the floors L,R and B with reference to foundation

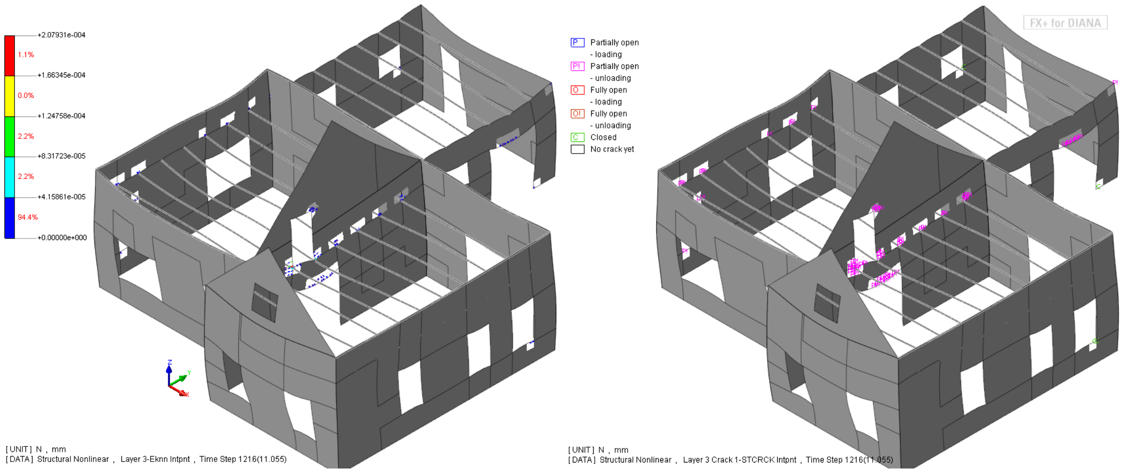

Figure 5-68: Crack pattern and element status at step 1216

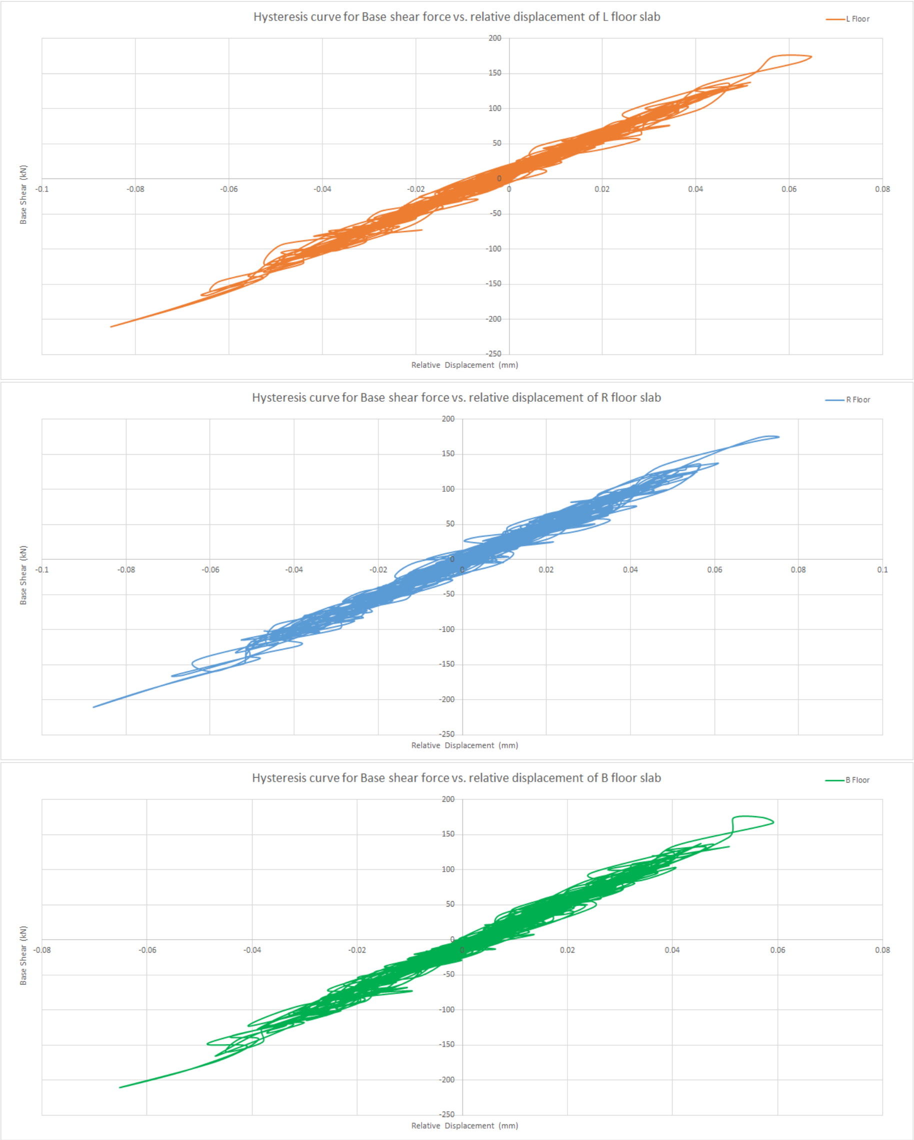

Figure 5-69: Hysteresis curve for base shear vs. relative displacement of the floors L,R and B with reference to foundation

The plotted hysteresis curves shows the relationship between base shear force and the floor relative displacement. The maximum base shear forces recorded are -210 to $+175$ kN. This range is for the regime of time history input.

2. Fixed end beams at first floor level
The relative displacement of the floors are displayed in the displacement curves below. The drift values for this analysis is visibly higher to the previous one within the time-input regime. The following are the maximum displacement values for the floors L, R and B are -0.085 to $+0.065$ mm, -0.087 to $+0.076$ mm and -0.066 to $+0.056$ mm, respectively. All these maximum negative displacements occurs at time 6.87 whereas the maximum positives occur at 7.11 s. The last converged step and the last step of

the time history input is at step 1216.

It is interesting to see that the analysis along Y-direction yields smaller displacements, as well as the non-existence of any effect on the displacement due to the use of different beam end type in the structure.

Figure 5-70: Relative displacement of the floors L,R and B with reference to foundation

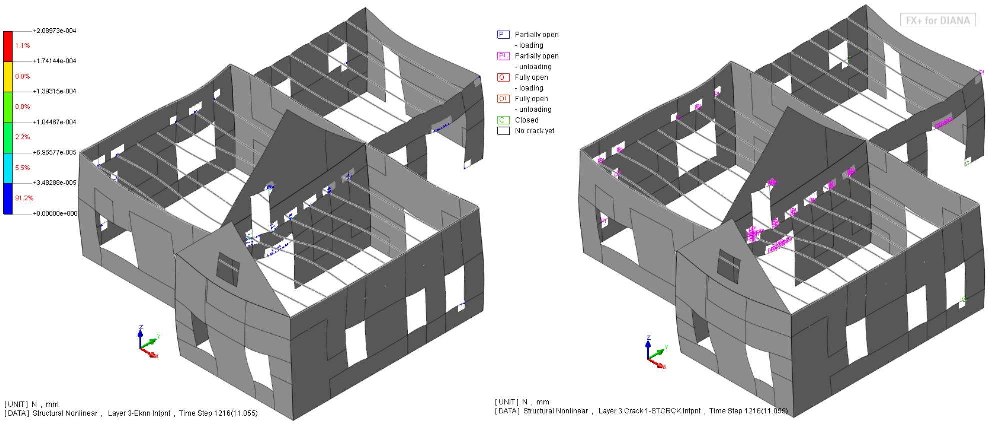

Figure 5-71: Crack pattern and element status at step 1216

At the last time-history input step which was converged without any error (i.e at time step 1216), the crack strain in this analysis was found to be $2.090 * 10^{-4}$. This suggests that no extensive cracking can be observed and that the cracks are still in the initiation stage. These values are very low compared to $1.5 * 10^{-3}$ which is the calculated ultimate crack strain.

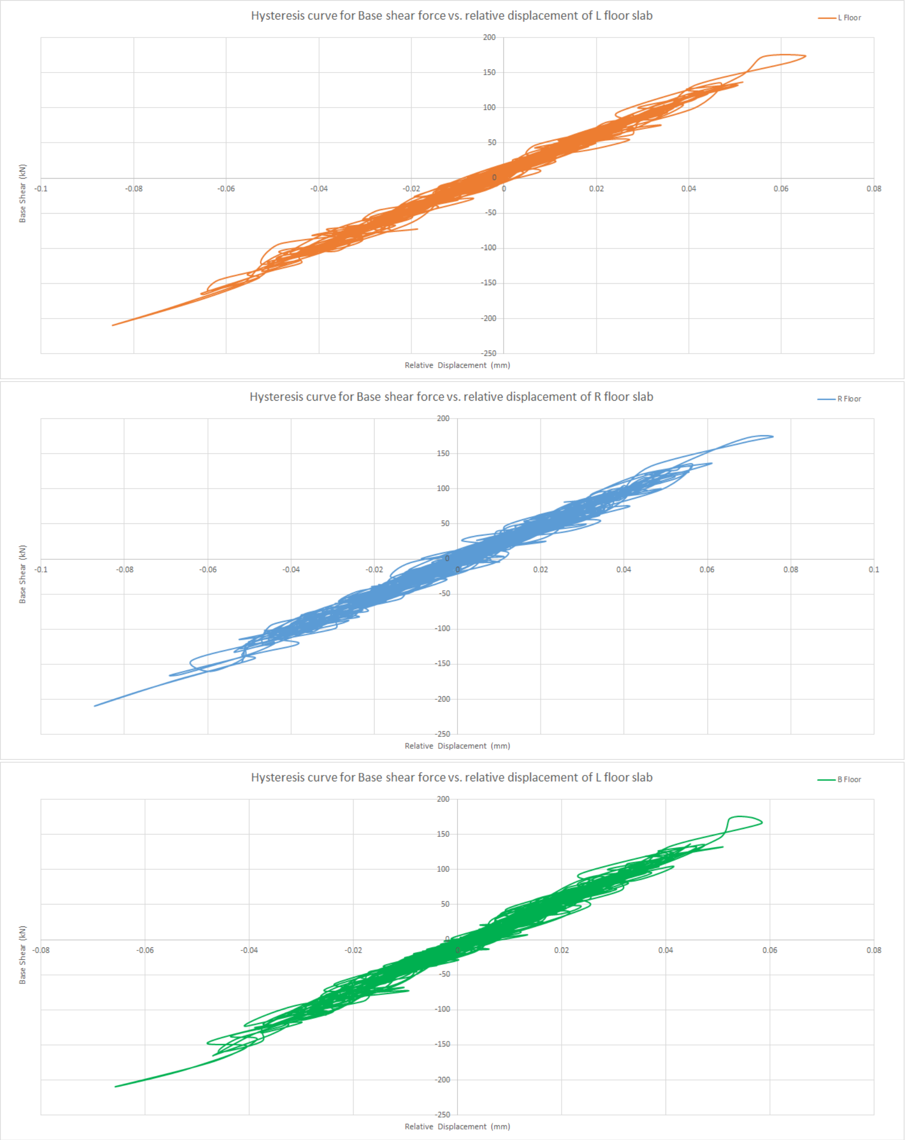

Figure 5-72: Hysteresis curve for base shear vs. relative displacement of the floors L,R and B with reference to foundation

The plotted hysteresis curves shows the relationship between base shear force and the floor relative displacement. The maximum base shear forces recorded are -210 to $+175$ kN. This range is for the regime of time history input.

5-3-6 NLTHA with roof - Y direction - $0.50g$

The model with roof is now analysed along Y-direction using the relevant Y-direction $0.50g$ time history input. This means that the maximum acceleration is equal to 4.98 m/s^2. Such a strong earthquake occurs rarely, but is strong enough to induce damage to the structure.

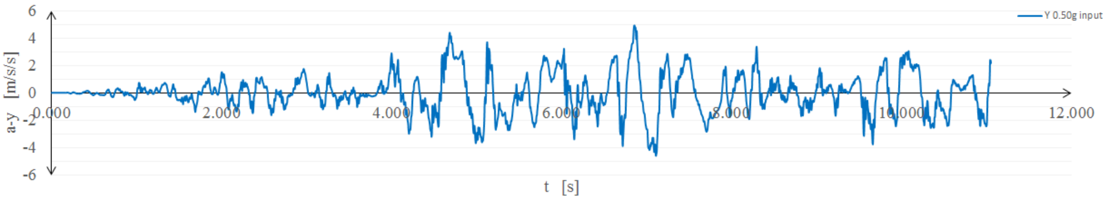

Figure 5-73: Time history input - Record 1 - Along Y-axis, scaled to $0.50g$

Results

1. <u>Pinned end beams at first floor level</u>
   The relative displacement of the floors are displayed in the displacement curves below. The drift values for this analysis is visibly higher to the previous one within the time-input regime. The following are the maximum displacement values for the floors L, R and B are -0.132 to $+0.109$ mm, -0.146 to $+0.110$ mm and -0.096 to $+0.109$ mm, respectively. All these maximum negative displacements occurs at time 4.83s whereas the maximum positives occur at 5.68s for the left and right floor, whereas the same for back floor occurs at 5.69s. The last converged step is at 6.33s or time step 638 with relative displacements of $+0.046\ mm$, $+0.052\ mm$ and $+0.040\ mm$ for floors L, R and B respectively.

   At the last time-history input step which was converged without any error (i.e at time step 638), the crack strain in this analysis was found to be $1.146 * 10^{-2}$. This suggests that extensive cracking can be observed and that the cracks are in the initiation stage. These values are very low compared to $1.5 * 10^{-3}$ which is the calculated ultimate crack strain.

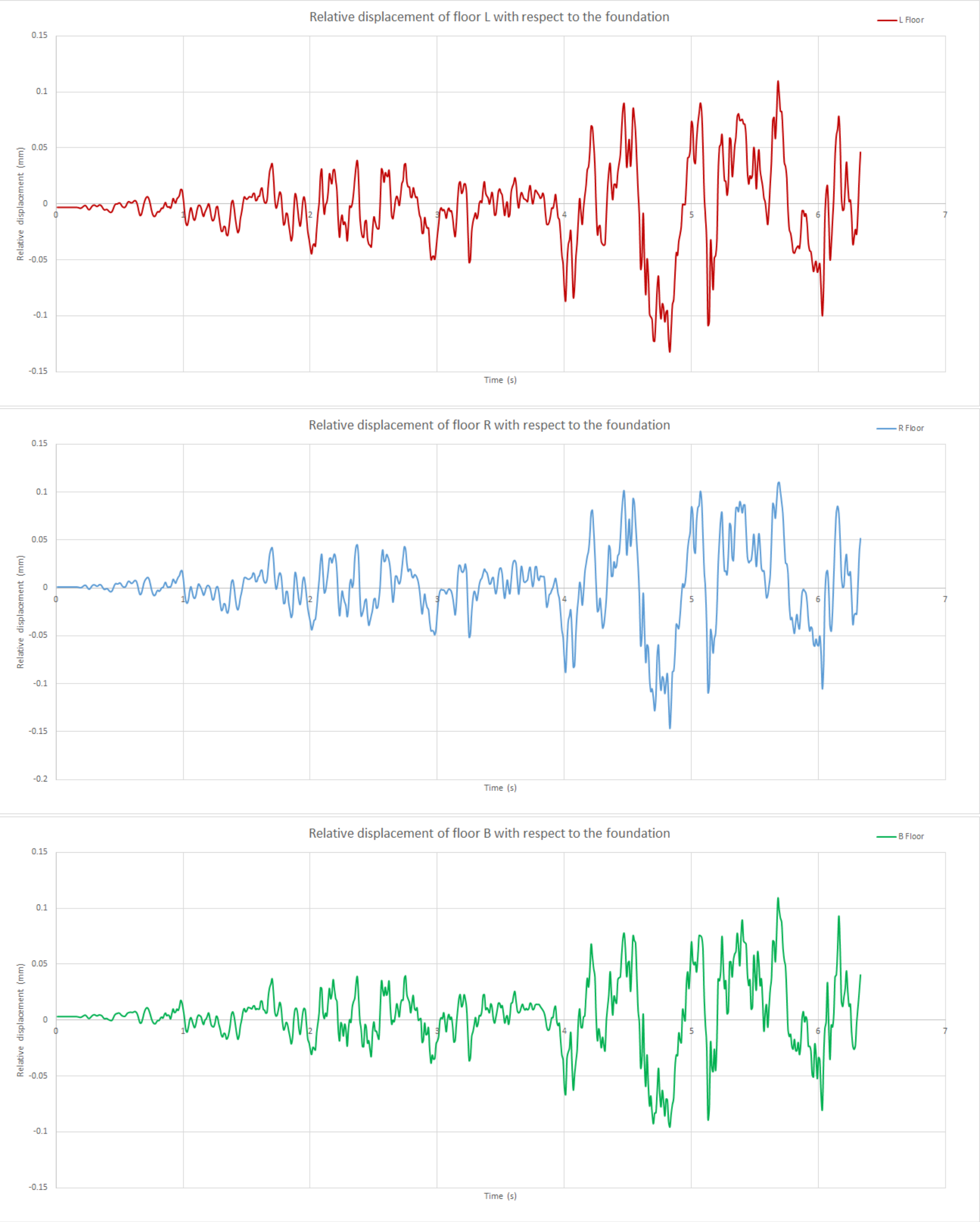

Figure 5-74: Relative displacement of the floors L,R and B with reference to foundation

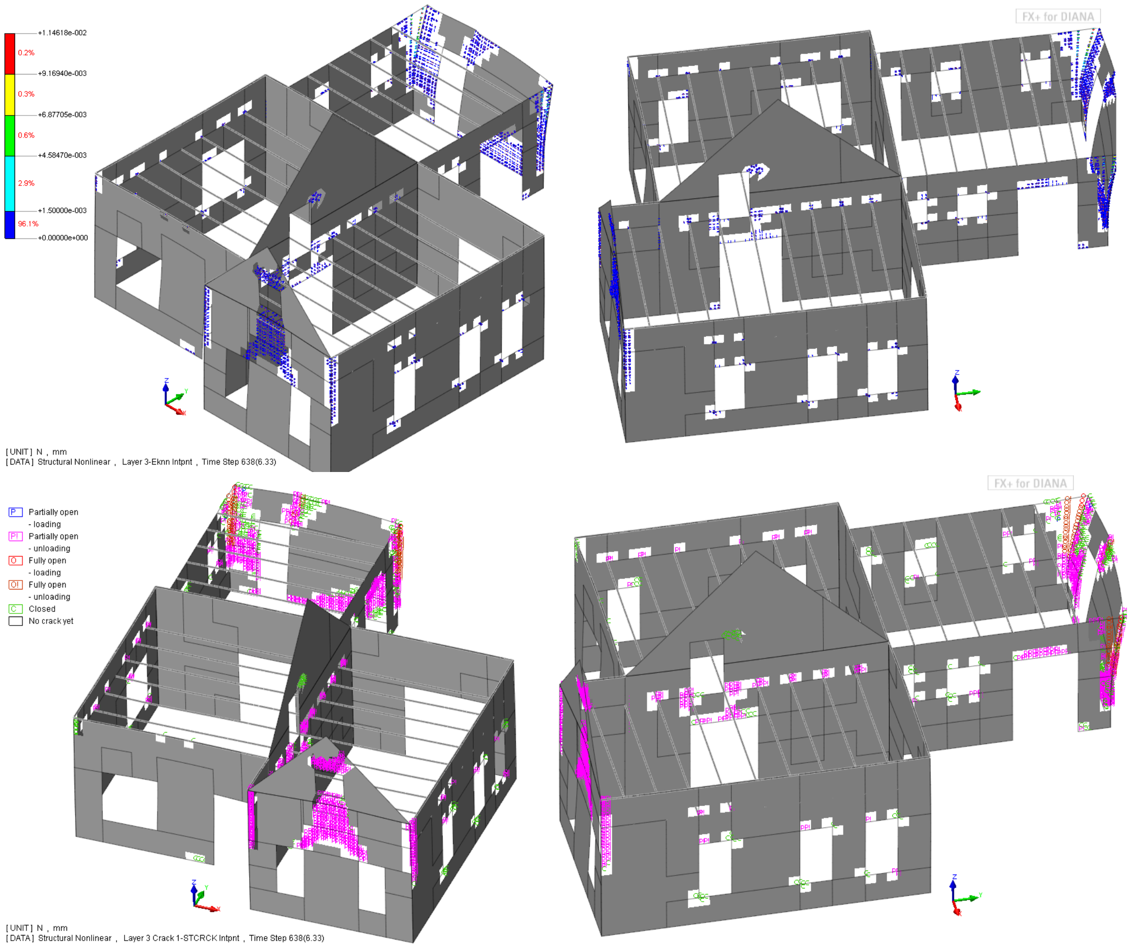

Figure 5-75: Crack pattern and element status at final converged step 638

The plotted hysteresis curves shows the relationship between base shear force and the floor relative displacement. The maximum base shear forces recorded are -334 to $+276$ kN. This range is for the regime of time history input for which convergence was achieved.

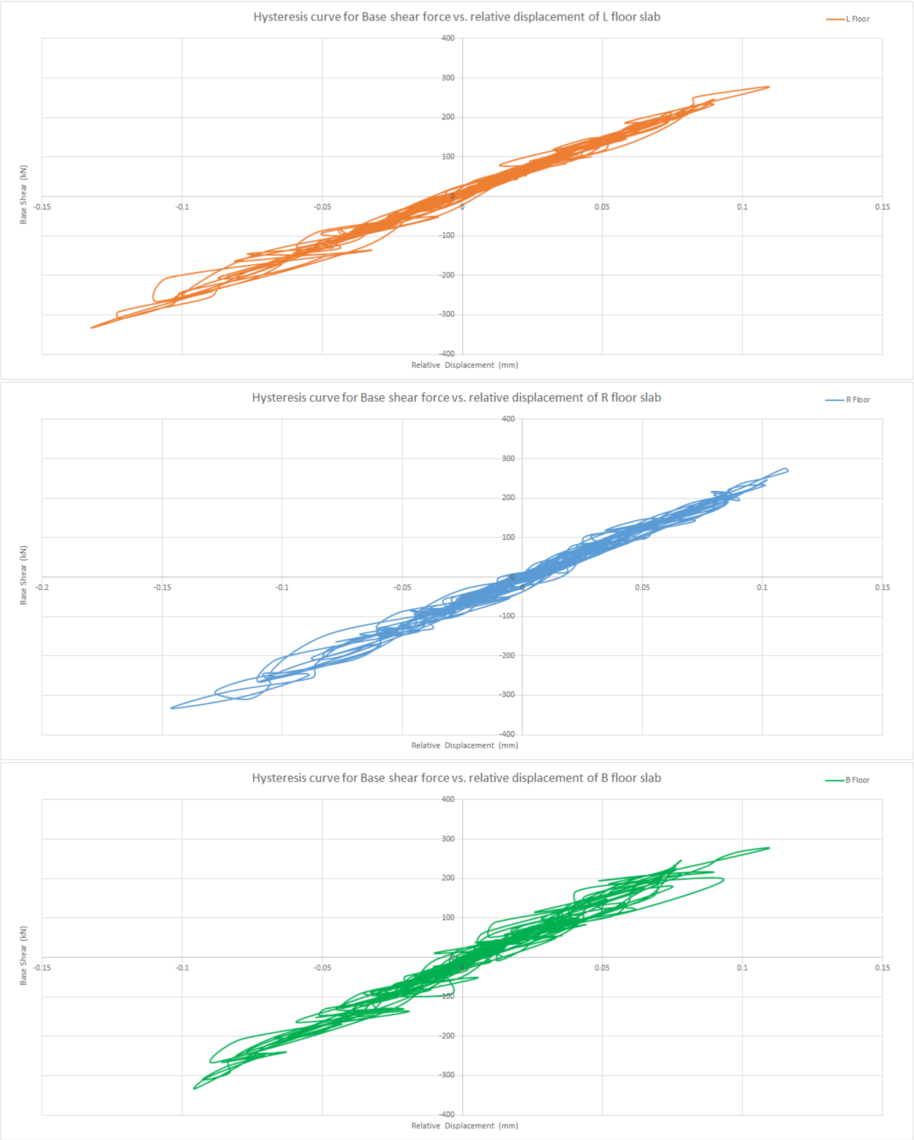

Figure 5-76: Hysteresis curve for base shear vs. relative displacement of the floors L,R and B with reference to foundation

2. <u>Fixed end beams at first floor level</u>
   The relative displacement of the floors are displayed in the displacement curves below. The drift values for this analysis is visibly higher to the previous one with respect to the time-input regime. The following are the maximum displacement values for the floors L, R and B are -0.133 to $+0.109$ mm, -0.146 to $+0.110$ mm and -0.097 to $+0.108$ mm, respectively. All these maximum negative displacements occurs at time 4.83 s whereas the maximum positives occur at 5.68 s for the left and back floors, whereas for the right floor it occurs at 5.69 s. The last converged step of importance and the last step of this analysis is at time of 6.46 s which is at step 651 with relative drifts (in mm) of $+0.007$, 0.010 and 0.031 for left, right and back floors respectively.

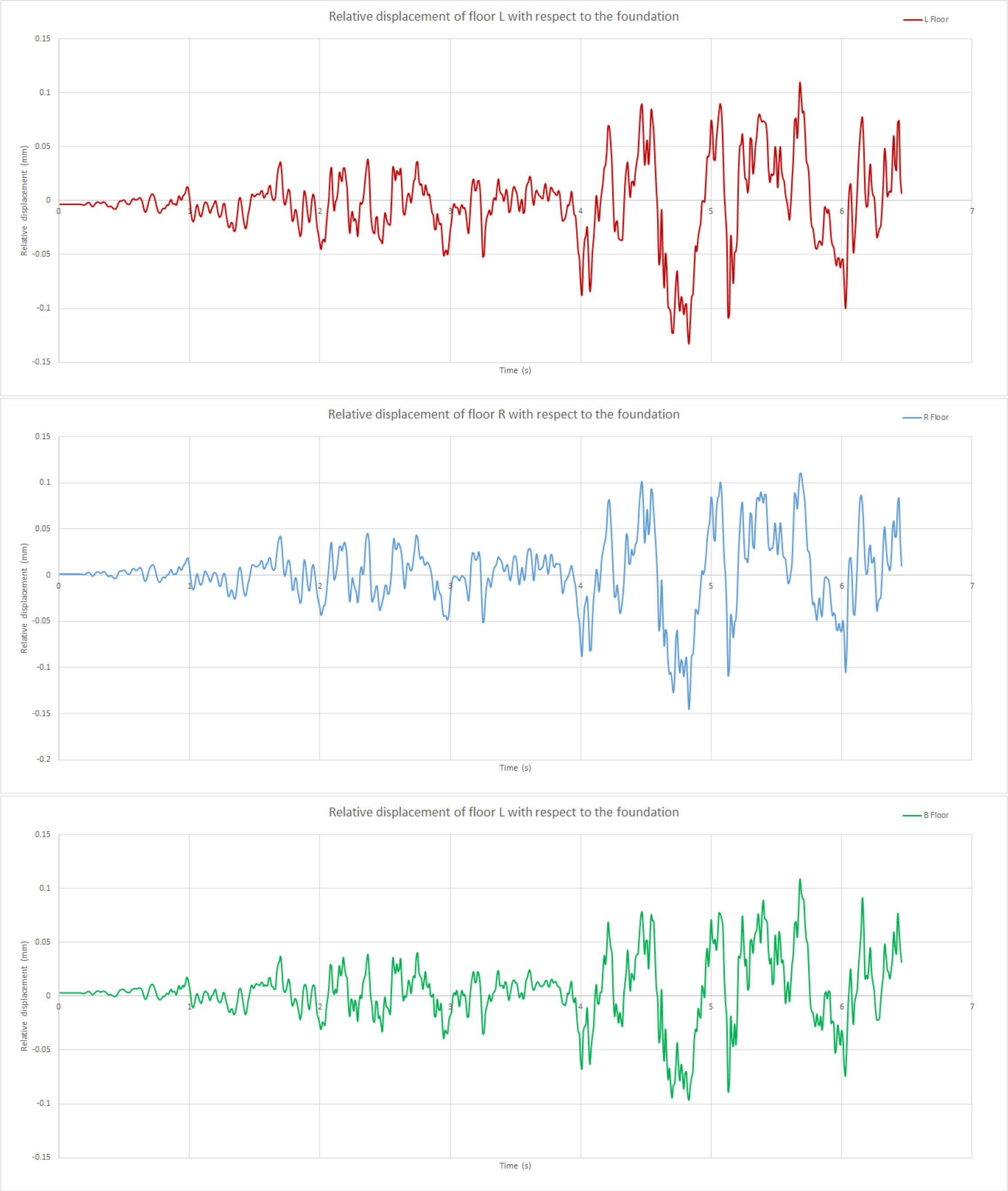

Figure 5-77: Relative displacement of the floors L,R and B with reference to foundation

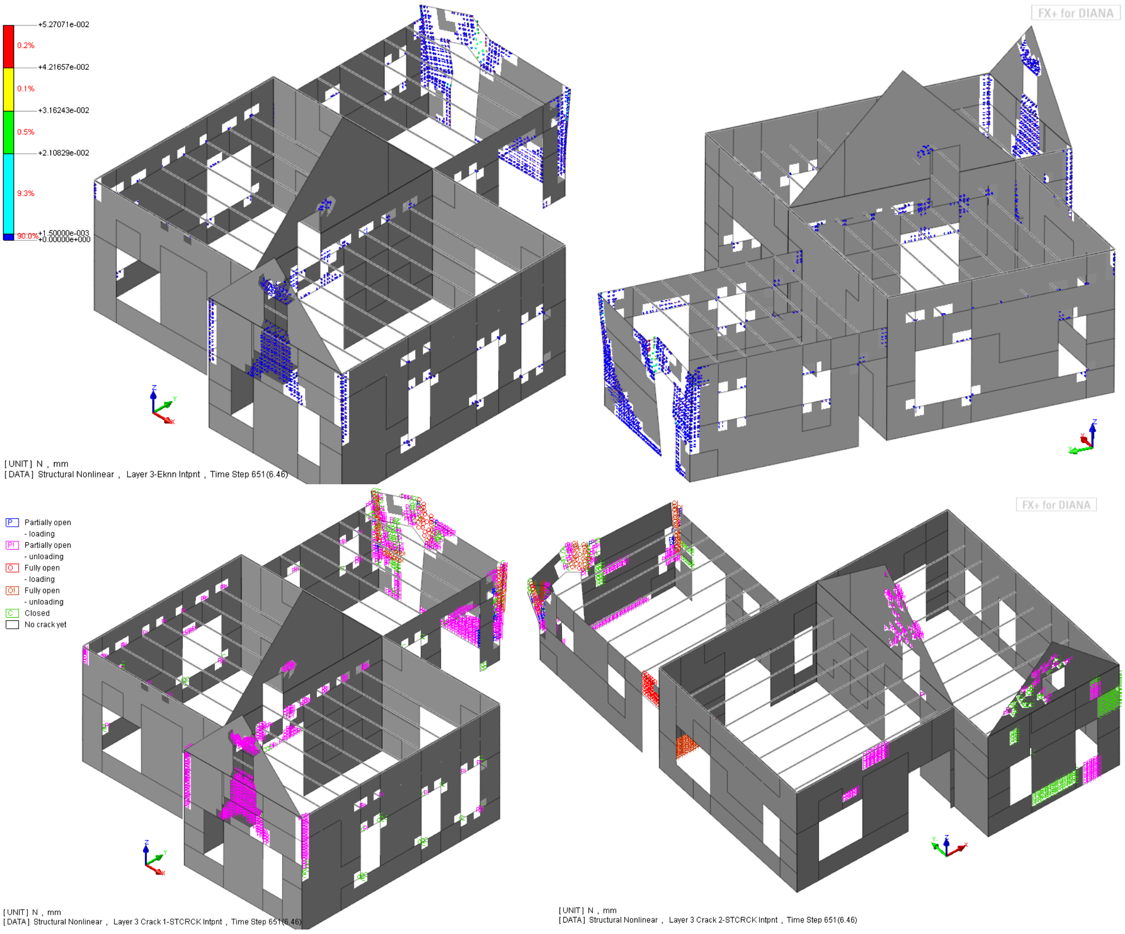

Figure 5-78: Crack pattern and element status at final converged step 651

It is interesting to see that the analysis shows convergence upto different points with respect to beam end connections. For the model with fixed beam type connections, divergence occurs after 0.13 s as that compared to the pinned type, for the same signal.

At the last time-history input step which was converged without any error (i.e at time step 651), the maximum crack strain in this analysis was found to be $5.271 * 10^{-2}$. This suggests that extensive cracking can be observed and that the cracks greater than $1.5 * 10^{-3}$ which is the calculated ultimate crack strain.

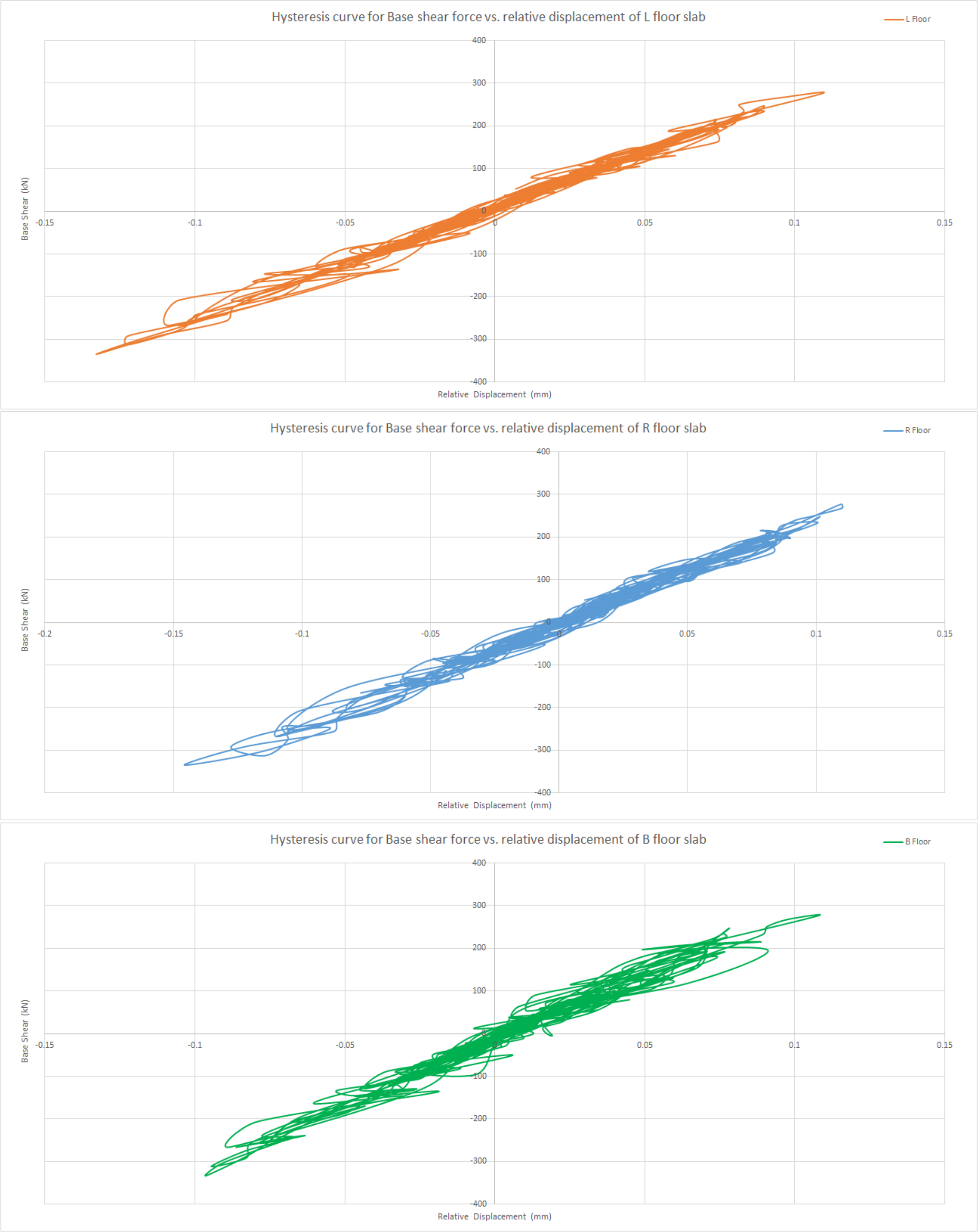

Figure 5-79: Hysteresis curve for base shear vs. relative displacement of the floors L,R and B with reference to foundation

The plotted hysteresis curves shows the relationship between base shear force and the floor relative displacement. The maximum base shear forces recorded are −334 to +277 kN. This range is for the converged regime of time history input. These values are similar to that compared to the pinned type connections.

5-4 Non-linear mass proportional pushover analysis of the structure

The structure is analysed using mass proportional pushover method where it is loaded laterally in monotonic load steps using gravity load. Accordingly, the structure is analysed in four directions- positive X direction, negative X direction, positive Y direction and negative Y direction. This analysis is also extended to the two variations of beam fixity conditions- pinned beam ends and fixed beam ends. The results are presented below. To improve the convergence and to get a clear peak response, arc length control and line search criteria have been used. The load is input in units of $0.01g$ in 200 steps. However, general response after the load factor $0.7g$ for X-direction and $0.8g$ for Y-direction was in the form of a hysteresis loop which has been omitted due to non-converging results.

5-4-1 Pushover in positive X-direction

1. Pinned end beams at first floor level

   The gravity load is applied in the positive X-direction for the model with pinned type beam ends. The results depict the capacity curve with base shear force plotted against relative floor displacement. The results plotted are limited to the maximum gravity load steps for which convergence has been achieved successfully. For the current analysis, this is achieved at load factor of $0.6g$. The corresponding maximum base shear force is 412.72 kN and the relative displacement (in mm) for the left, right and back floors are 1.126, 1.124 and 0.96 respectively. However, the analysis was continued further which resulted in a "plateau", where increase in loading does not correspond to increase in base shear, however, the relative displacement (in mm) increases upto 1.64, 1.63 and 1.60 for left, right and back floors respectively. At this point, the recorded base shear is 391 kN. The first cracks appear at a load factor of $0.417g$ (load step 48) where a maximum crack strain of $1.59 * 10^{-3}$ is recorded. The location of these cracks are at the beam ends and corners of openings- windows and doors. The cracks occur at the left top and right bottom corners of all openings. After this step, the cracking increases extensively and at the load step 118, it reaches a value of $1.78 * 10^{-2}$ which is higher than the calculated ultimate crack strain of $1.5 * 10^{-3}$. It is to be noted that these values of crack strains are extracted from layer 3 (mid layer) of 5 designated to curved shell element representing masonry, which means the outer layers on either side undergo higher cracking.

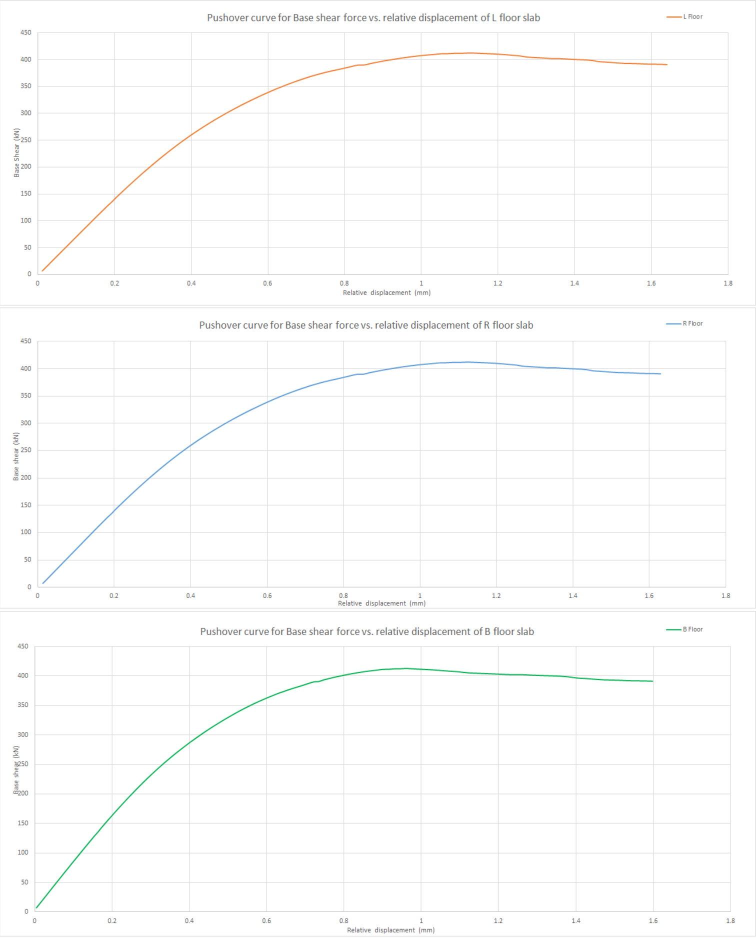

Figure 5-80: Pushover curves for base shear vs. relative displacement of the floors L,R and B with reference to foundation

2. Fixed end beams at first floor level

The exercise is repeated for the model with fixed type beam ends. The results depict the capacity curve with base shear force plotted against relative floor displacement. The results plotted are limited to the maximum gravity load steps for which convergence has been achieved successfully. For the current analysis, this is achieved at load factor of $0.62g$. The corresponding maximum base shear force is 416 kN and the relative displacement (in mm) for the left, right and back floors are 1.130, 1.128 and 0.892 respectively. However, the analysis was continued further which resulted in a "plateau", where increase in loading does not correspond to increase in base shear, however, the relative displacement (in mm) increases upto 1.714, 1.702 and 1.435 for left, right and back floors respectively. At this point, the recorded base shear is 397.5 kN. The first cracks appear at a load factor of $0.435g$ (load step 50) where a maximum crack strain of $1.59 * 10^{-3}$ is recorded. The location of these cracks are similar to the previous case. The cracks occur at the left top and right bottom corners of all openings. After this step, the cracking increases extensively and at the load step

121 at load factor of $0.589g$, it reaches a value of $1.843 * 10^{-2}$ which is higher than the calculated ultimate crack strain of $1.5 * 10^{-3}$. It is to be noted that these values of crack strains are extracted from layer 3 (mid layer) of 5 designated to curved shell element representing masonry, which means the outer layers on either side undergo higher cracking.

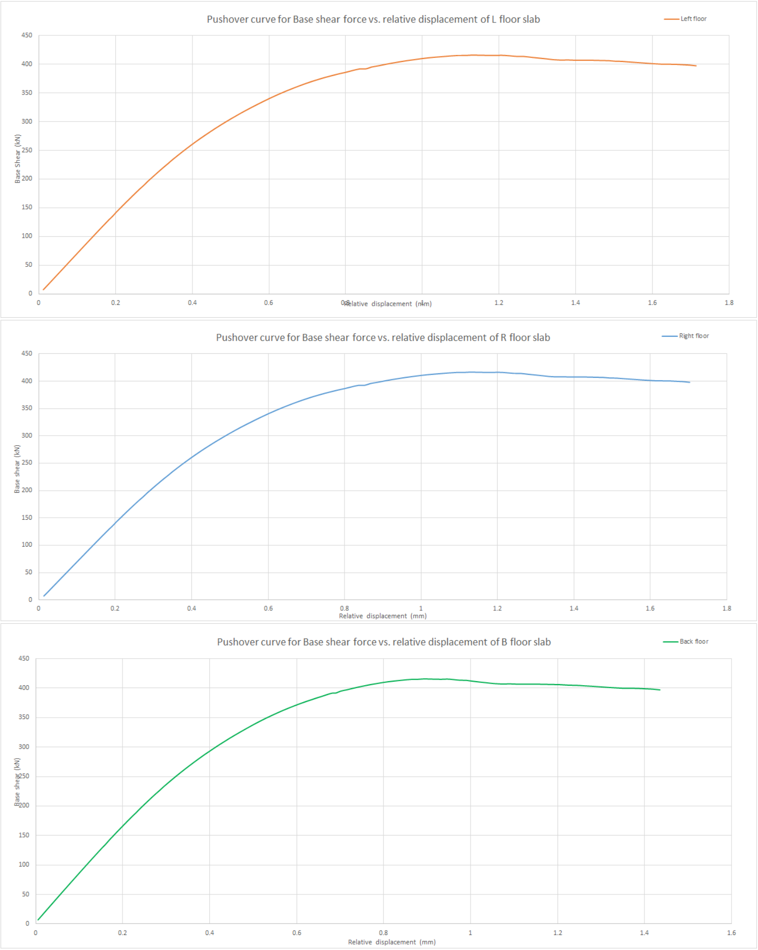

Figure 5-81: Pushover curves for base shear vs. relative displacement of the floors L,R and B with reference to foundation

5-4-2 Pushover in negative X-direction

1. <u>Pinned end beams at first floor</u>
   This analysis is similar to the previous case with the gravity load applied, but in the negative X-direction for the model with pinned type beam ends. The results depict the capacity curve with base shear force plotted against relative floor displacement. The results plotted are limited to the maximum gravity load steps for which convergence has been achieved successfully.

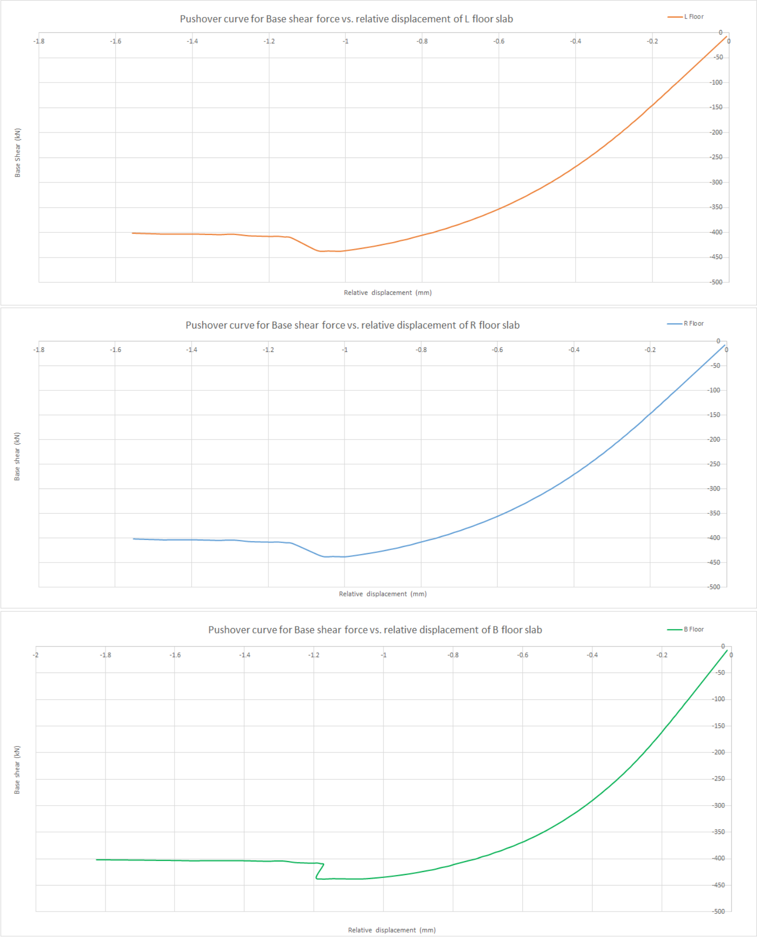

Figure 5-82: Pushover curves for base shear vs. relative displacement of the floors L,R and B with reference to foundation

In this case, the maximum load factor with successful convergence was $0.65g$ at load step 89. The corresponding maximum base shear force is -437.93 kN and the relative displacement (in mm) for the left, right and back floors are -1.065, -1.513 and -1.177 respectively. But when the analysis was continued further, it resulted in a "plateau", where increase in loading does not correspond to increase in base shear, in contrast a slight decrease in base shear is observed, however, the relative displacement (in mm) increases upto -1.557, -1.553 and -1.826 for left, right and back floors respectively at base shear force of -401.55 kN. Extensive cracking begins at a load factor of $0.462g$ (load step 53) where a maximum crack strain of $1.074 * 10^{-3}$ is recorded. The location of these cracks are at the beam ends, junctions of walls and corners of openings- windows and doors. The cracks occur at the right top and left bottom corners of all openings which is the exact opposite of the pattern observed for the pushover for positive X-direction. Furthermore, the cracking increases and at load step 86 in which the maximum load factor is applied, it reaches a value of $3.856 * 10^{-3}$ which is higher than double the calculated ultimate crack strain of $1.5 * 10^{-3}$. Between load steps 90 to 94, highest percentage of the structure has undergone cracking with maximum crack strain reading $6.1 * 10^{-3}$. Even though the analysis is continued, the cracks continue to stabilise, with a few cracks closing up and others widening to achieve higher crack strains. Damage is mostly concentrated in the form of diagonal cracks around openings in the in-plane walls, however in the case of out-of-plane walls, damage is restricted to the wall base and junctions.

2. Fixed end beams at first floor level

   The exercise is repeated for the model with fixed type beam ends. The results are plotted below in figure 5-83 and are limited to the maximum gravity load steps for which convergence has been achieved successfully.

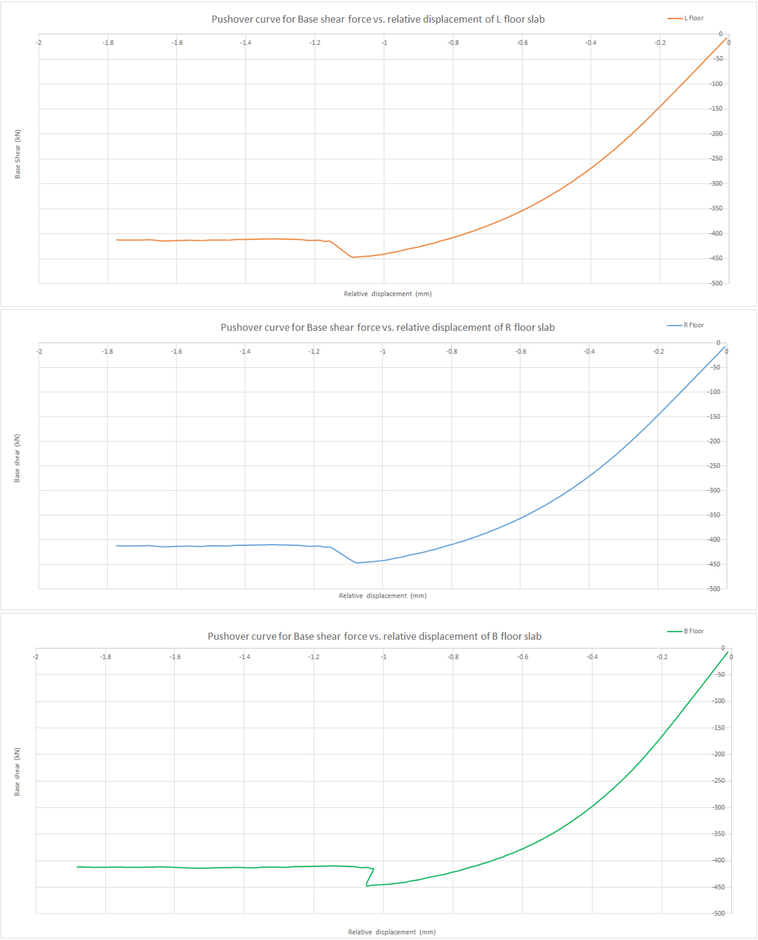

Figure 5-83: Pushover curves for base shear vs. relative displacement of the floors L,R and B with reference to foundation

For the current analysis, the maximum load factor is $0.66g$ at load step 88. The corresponding maximum base shear force is 416 kN and the relative displacement (in mm) for the left, right and back floors are -1.060, -1.046 and -1.010 respectively. However, the analysis was continued further which resulted in a relatively flat response, where increase in loading does not correspond to increase in base shear, however, the relative displacement (in mm) increases upto -1.774, -1.774 and -1.881 for left, right and back floors respectively. At this point, the recorded base shear is -412 kN.It is important to note that furthermore only the back floor shows higher displacement upto -2.050 mm, whereas the other two floors show lesser displacement. The first cracks appear at a load factor of $0.51g$ (load step 59) where a maximum crack strain of $1.5 * 10^{-3}$ is recorded. The location of these cracks are similar to the previous case of model with pinned beam end. After this step, the cracking increases extensively and at load step 92 at load factor of $0.613g$,extensive cracking begins. At this point, the two front in-plane walls are highly cracked with diagonal cracks running through most of the walls and continuing towards corners from the wall base to the top end of the walls. Out-of-plane walls are cracked only near wall junctions in the top parts.

5-4-3 Pushover in positive Y-direction

1. Pinned end beams at first floor level

Now the direction along which the gravity loading is input is changed to Y-direction. This is firstly analysed for the pinned end type beams. For the current analysis, the maximum gravity load applied is a factor of $0.54g$ at load step 61. The corresponding maximum base shear force is 363 kN and the relative displacement (in mm) for the left, right and back floors are 0.142, 0.153 and 0.129 respectively. These are the maximum drift values for the three floors in this analysis. No plateau was observed for the pushover analysis along positive Y-direction. Instead, when the analysis was let to continue, both base shear force and drift values decreased. The important contrast observed here is that the maximum crack strain observed is $7.83 * 10^{-4}$ which is lesser than the calculated ultimate crack strain. At this point, only the out-of-plane wall in the extended back part of the structure shows signs of cracking.

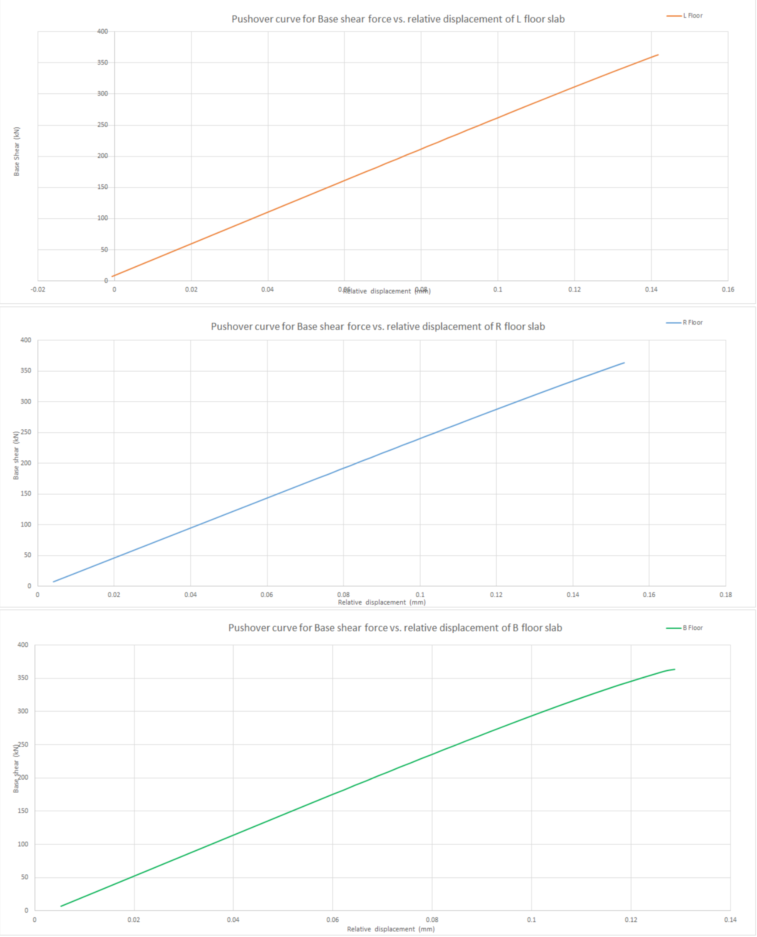

Figure 5-84: Pushover curves for base shear vs. relative displacement of the floors L,R and B with reference to foundation

2. Fixed end beams at first floor level

In this analysis, the model used is the one with the beam ends fixed. For the current analysis, the maximum gravity load applied is a factor of $0.54g$ at load step 61, which is very similar to the previous case. The corresponding maximum base shear force is 364 kN and the relative displacement (in mm) for the left, right and back floors are 0.142, 0.154 and 0.129 respectively. These are the maximum drift values for the three floors in this analysis. Again, no plateau was observed for the pushover analysis along positive Y-direction. Instead, when the analysis was let to continue, both base shear force and drift values decreased. Also, due to poor convergence, the last successful step of this analysis was load step 62 at which the base shear force recorded was 216 kN. However, the highest crack strain observed in layer 3 was $7.66 * 10^{-4}$ at step 61. This value is similar to that achieved for the analysis with pinned beam ends, however it is slightly less.

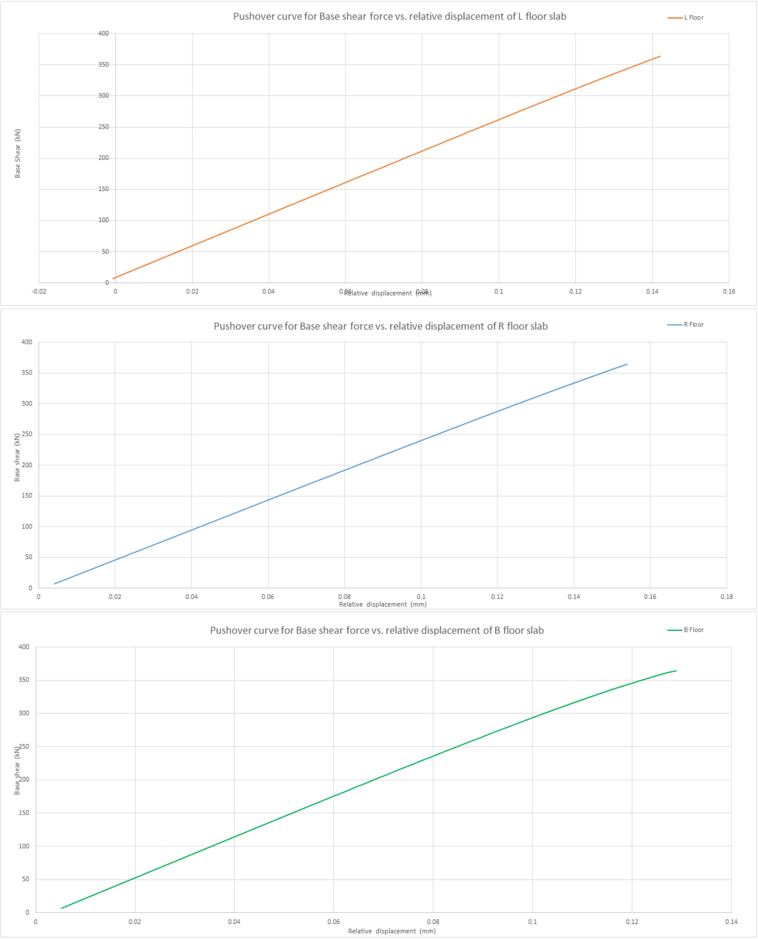

Figure 5-85: Pushover curves for base shear vs. relative displacement of the floors L,R and B with reference to foundation

5-4-4 Pushover in negative Y-direction

1. Pinned end beams at first floor level

In this analysis, the gravity loading is input along the negative Y-direction for the model with pinned type beam ends. For the current analysis, the maximum gravity load applied is a factor of $0.74g$ at load step 85. The corresponding maximum base shear force is $-497\ kN$ and the relative displacement (in mm) for the left, right and back floors are -0.217, -0.223 and -0.163 respectively. These are the maximum drift values for the three floors in this analysis. No plateau was observed for the pushover analysis along positive Y-direction. Instead, when the analysis was let to continue, both base shear force and drift values decreased. The important point to be observed here is, though the applied loading is $0.74g$, the maximum crack strain observed is $6.21 * 10^{-4}$ which is lesser than the calculated ultimate crack strain. At this point, only the out-of-plane walls - in the extended back part of the structure and the front walls of the structure show signs of crack development mostly at the bottom and top levels

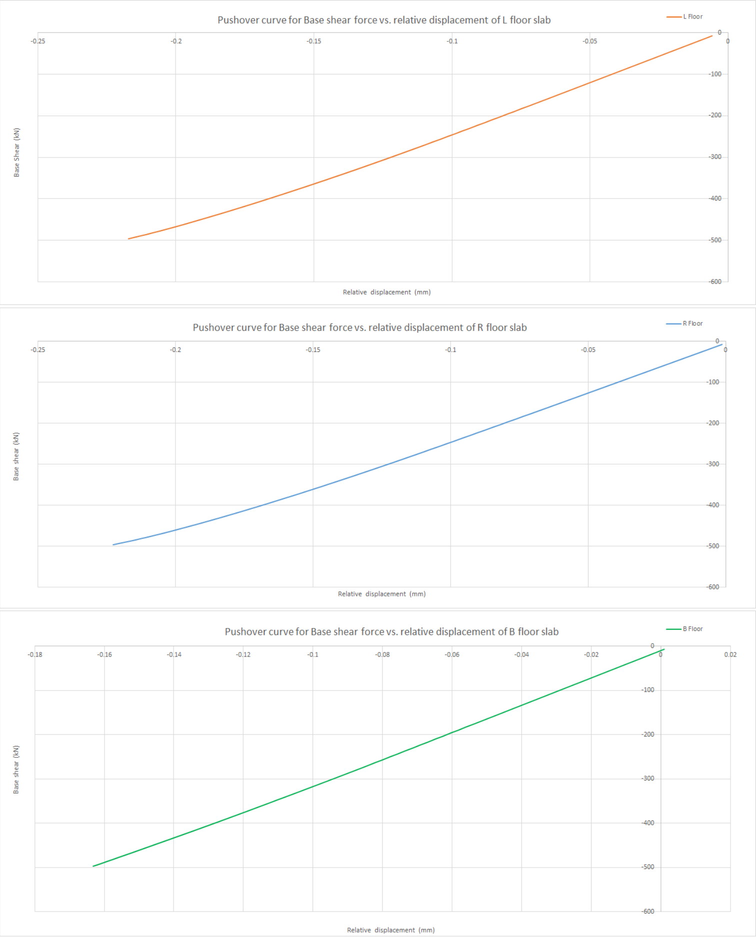

Figure 5-86: Pushover curves for base shear vs. relative displacement of the floors L,R and B with reference to foundation

2. Fixed end beams at first floor level

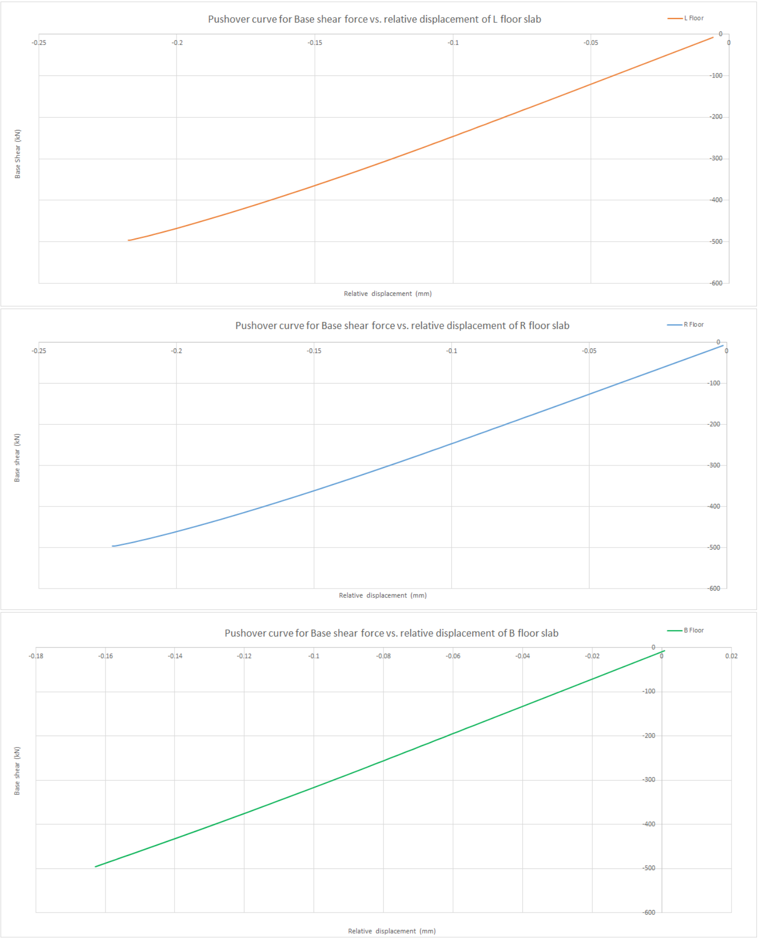

Figure 5-87: Pushover curves for base shear vs. relative displacement of the floors L,R and B with reference to foundation

In this analysis, the model used is the one with the beam ends fixed, with the gravity loading applied along the negative Y-direction. For the current analysis, the maximum gravity load applied is a factor of $0.733g$ at load step 86, which is very similar to the previous case. The corresponding maximum base shear force is -496 kN and the relative displacement (in mm) for the left, right and back floors are -0.218, -0.223 and -0.163 respectively. These are the maximum drift values for the three floors in this analysis. Again, no plateau was observed for the pushover analysis along negative Y-direction. Instead, when the analysis was let to continue, both base shear force and drift values decreased. However, the highest crack strain observed in layer 3 was $1.60 * 10^{-3}$ at step 86. This maximum crack strain value was derived from the wall layer 1 of the model, however layer 3 shows a lesser value of $7.33 * 10^{-4}$. Similar to the previous case, only the out-of plane walls in the back and front part of the structure are affected by out-of-plane bending. In-plane walls show scarcely any sign of cracking. Though there is no extensive cracking observed in the analysis along Y-direction, the results for all the different cases are consistent.

Chapter 6

Results, Conclusion and Discussion

The scientific inferences are the most important part of a research project. It details the salient points observed during the research. It is also a measure of how the objective of the project and its adequacy is realised. To that effect, it also summarises the understanding of the project and its outcome by the researcher. Depending on this, many improvements can be worked upon, which will, eventually, add more quality to the body of work taken up. It also gives the researcher an opportunity to interpret and critique his own work. Following this idea, the final summary and understanding of the current project is dealt with in the following section.

6-1 Results of Non-linear time history analyses

In this section, all the non-linear time history analyses (NLTHA) carried out on the finite element model of the detached type villa (T3a) has been summarised. All the analyses carried out are uni-directional in nature, meaning that the time-history data is input only along one direction of the model and its response studied. In total, 14 such analyses were carried out, with variation in the direction of seismic input, its scaling levels, type of beam end connections and finally, the inclusion of the roof part of the structure. It is to be noted that the results obtained are specific to the model and associated analyses. Non-linearity is limited only to masonry, with the other materials assumed as linear elastic. The following table 6-1 describes these different analyses carried out on the initial model without roof. It shows the different scaling levels of the input signal, direction of seismic excitation, acceleration values for different analyses and their corresponding displacement response, using which the principal strains, crack strains etc. are computed along with the corresponding base shear force values found from the analyses. It is to be noted that these values relate only to the time-history input regime i.e upto time step where convergence was successfully achieved, but the path to divergence is also closely followed to understand if the divergence is valid. Further the table 6-2 gives the summary of results relating to the final model inclusive of the roof part.

6-1-1 Summary of NLTHAs without roof part

Nonlinear time history analyses										
Model type	Direction of input signal	Scaling of input signal	Type of beam end connection	Max. acceleration (m/s^2)	Maximum floor relative displacement (mm)	Crack strains ($*10^{-5}$)	Principal stress (N/mm^2)	Principal strain ($*10^{-5}$)	Base Shear (kN)	Cracking stage
Without Roof	X-direction	$0.16g$	Pinned	-1.616	-0.097 to $+0.098$	4.285	0.1070	5.164	-50.81 to $+45.61$	Crack initiation
			Fixed		-0.097 to $+0.098$	4.50	0.1073	5.273	-51.28 to $+45.52$	Crack initiation
		$0.25g$	Pinned	-2.525	-0.198 to $+0.199$	4.753	0.1083	5.832	-101.81 to $+91.48$	Crack initiation
			Fixed		-0.196 to $+0.196$	5.096	0.1087	5.771	-102.48 to $+91.0$	Crack initiation
		$0.5g$	Pinned	-5.05	-0.25 to $+0.25$	**884.34**	**0.215**	**513.50**	-127.34 to $+114.41$	Stabilised cracking
			Fixed		-0.248 to $+0.246$	**1253.45**	**0.159**	**774.25**	-127.78 to $+113.07$	Stabilised cracking
	Y-direction	$0.25g$	Pinned	2.457	-0.0345 to $+0.0344$	206.8	0.0231	5881.0	-91.25 to $+80.74$	Local cracking
			Fixed		-0.0345 to $+0.0345$	4.58	0.1022	5.230	-91.33 to $+80.64$	Crack initiation
		$0.5g$	Pinned	4.914	-0.0432 to $+0.0432$	**441.54**	**0.123**	**206.20**	-112.68 to $+101.82$	Stabilised cracking
			Fixed		-0.0432 to $+0.0424$	**44853.3**	**0.117**	**233.75**	$-112.78$to $+101.70$	Stabilised cracking

Table 6-1: Summary of NLTHA without roof

The given input signal complies to the level of $0.16g$ acceleration, for both X and Y directions. The maximum acceleration in the signal occurs at $6.06s$ for X-direction and at $6.855s$ for Y-direction with values - -1.616 and $+1.523$ respectively in m/s^2. However, this signal proved not to inflict any serious damage on the structure. Hence, it was scaled to $0.25g$ and $0.50g$ for further analyses.

The above analyses were carried out on the model without the second storey (roof part). The crack strain, principal stress and strain values for the $0.16g$ signal are very low and hence can be neglected for both directions.

Irrespective of the input signal, the general flow of the analyses is as follows.

1. Static Loads are applied in steps of 0.2 for 5 steps.

2. Seismic signal is input using base excitation from step 6 in steps of 0.01 times 1000 and then in steps of 0.005 for the remaining 210 steps. The total time period of the signal is $11.05s$.

3. The first cracks appear at the beam ends, then the corners of openings begin to crack, and further it depends on the specific analysis.

For the $0.25g$ signal along the X-direction, no significant damage was observed. Similar behaviour was observed in the analyses along Y-direction for fixed type beam end connections. However, for the model with pinned type beam ends and seismic signal along Y-direction, local cracking was observed in the form of pier action and base shearing only on the front wall.
The last scaling of the signal to $0.50g$ is strong enough to induce visible damage which is detrimental to the structure. Though the whole structure will not collapse, it will affect several walls and cracking is widespread.

6-1-2 Summary of NLTHAs inclusive of roof part

Nonlinear time history analyses										
Model type	Direction of input signal	Scaling of input signal	Type of beam end connection	Max. acceleration (m/s^2)	Maximum floor relative displacement (mm)	Crack strains $(*10^{-3})$	Principal stress (N/mm^2)	Principal strain $(*10^{-3})$	Base Shear (kN)	Cracking stage
With Roof	X-direction	$0.16g$	Pinned	-1.616	-0.224 to $+0.247$ L,R	0.133	0.118	0.118	-145.0 to $+130$	Crack initiation
			Fixed		-0.224 to $+0.245$ L, R	0.112	0.114	0.122	-143.5 to $+129.3$	Crack initiation
		$0.25g$	Pinned	-2.525	-0.368 to $+0.427$ L, R	0.155	0.0925	0.110	-226 to $+213$	Crack initiation
			Fixed		-0.368 to $+0.428$ L, R	0.147	0.103	0.108	-225 to $+210$	Crack initiation
		$0.50g$	Pinned	-5.050	-1.806 to $+1.194$ L, B	**10.49**	**0.852**	**16.41**	-371 to $+416$	Severely cracked
			Fixed		-1.490 to $+1.162$ L, R	**29.70**	**0.557**	**41.45**	-372 to $+317$	Severly cracked
	Y-direction	$0.16g$	Pinned	1.523	-0.054 to $+0.047$ L, R	0.1610	0.025	0.0136	-129 to $+108$	Crack initiation
			Fixed		-0.053 to $+0.048$ R	0.1613	0.096	0.0124	-129 to $+109$	Crack initiation
		$0.25g$	Pinned	2.457	-0.088 to $+0.075$ R	0.1965	0.0249	0.0136	-210 to $+175$	Crack initiation
			Fixed		-0.087 to $+0.076$ R	0.1967	0.0265	0.0154	$-210$to $+175$	Crack initiation
		$0.50g$	Pinned	4.914	-0.146 to $+0.110$ R	**0.197**	0.0484	0.343	-334 to $+276$	Crack initiation
			Fixed		-0.146 to $+0.110$ R	**9.93**	**0.3245**	**1.732**	-334 to $+277$	Severely cracked

Table 6-2: Summary of NLTHA including Roof

In these analyses, the roof part is also included. This naturally increases the overburden load. This helps in the box behaviour of the structure, which provides an intrinsic ability to redistribute seismic load between walls, along with flexible diaphragms, improving ductility and resistance to seismic loads. The resulting base shear values are higher than the previous case, so are the displacements. However, for the analyses along Y-direction, the displacement values are very small compared to that along X-direction. In this case as well, the structure easily resisted the input signals scaled to $0.16g$ and $0.25g$, showing minimal cracking mostly under beam ends and corners of openings. However for $0.50g$, the effect is more significant.

6-1-3 Maximum response acceleration and corresponding relative displacements

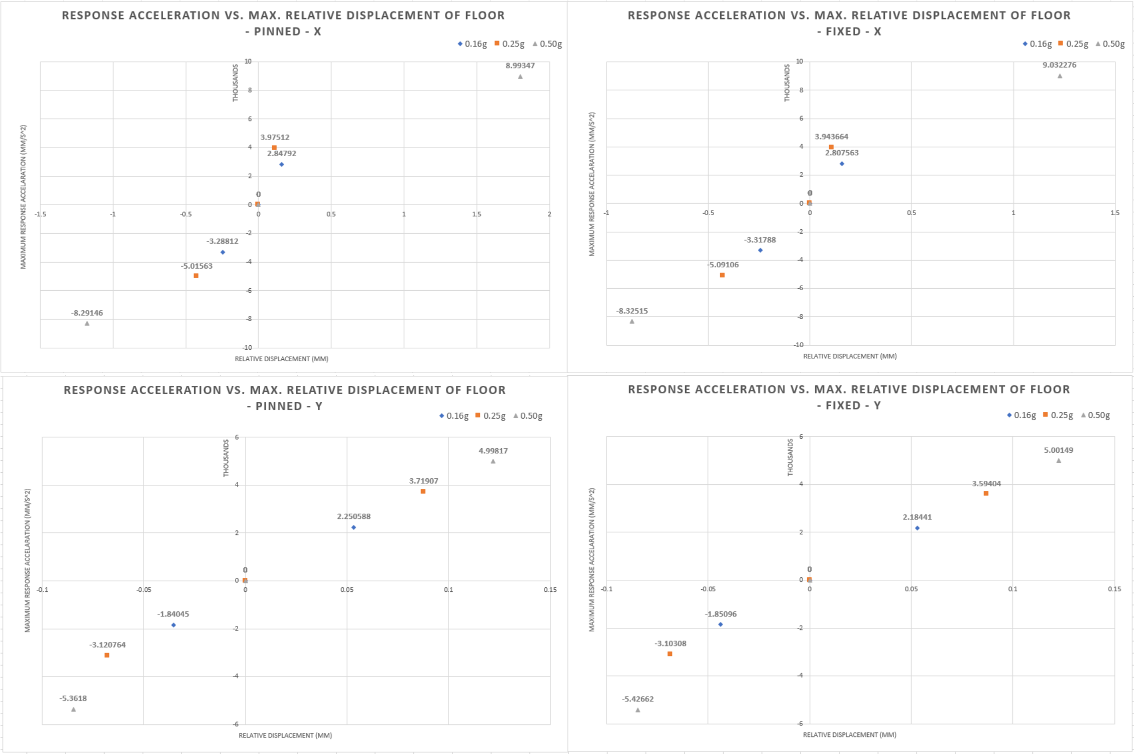

Figure 6-1: Maximum response acceleration plotted against maximum relative floor displacement

These plots show the response acceleration plotted against maximum relative floor displacement for both beam end configurations. It consists of plots for both X-direction and Y-direction analyses for all levels of scaling i.e. from $0.16g$ to $0.50g$. It can be seen here that the plots for X-direction vary greatly for $0.5g$ analysis. However, there is a close match for those of $0.16g$ and $0.25g$ close to origin. In certain cases, the maximum acceleration, though occurring at the back floor centroid impresses a maximum displacement at other floor slabs. Another point of interest is the value of response acceleration which is shown alongside the curves. In certain cases, though the maximum input acceleration is in accordance with the scaling, the response is amplified in the structure to that higher than maximum input acceleration. Such a behaviour is observed only for values of analyses along X-direction. For the Y-direction analyses, the plots match very closely for all levels of scaling i.e. from $0.16g$ to $0.50g$. Even here, it can be seen that the plots for the Y-direction seem linear in nature.

6-2 Comparison of time-history analyses with pushover curves

Pushover analyses carried out here are non-linear but monotonic in nature. Hence, these curves are used as capacity curves for the structure. These serve as a reference, more like an upper limit, for the non-linear time-history analyses as the latter consists of more complex and realistic data following the seismic input. However pushover curves help to estimate the strength and ductility of the structure. It is also important to note that the pushover analyses was also carried out for different beam end conditions and are carefully matched to the corresponding results from time-history analyses.

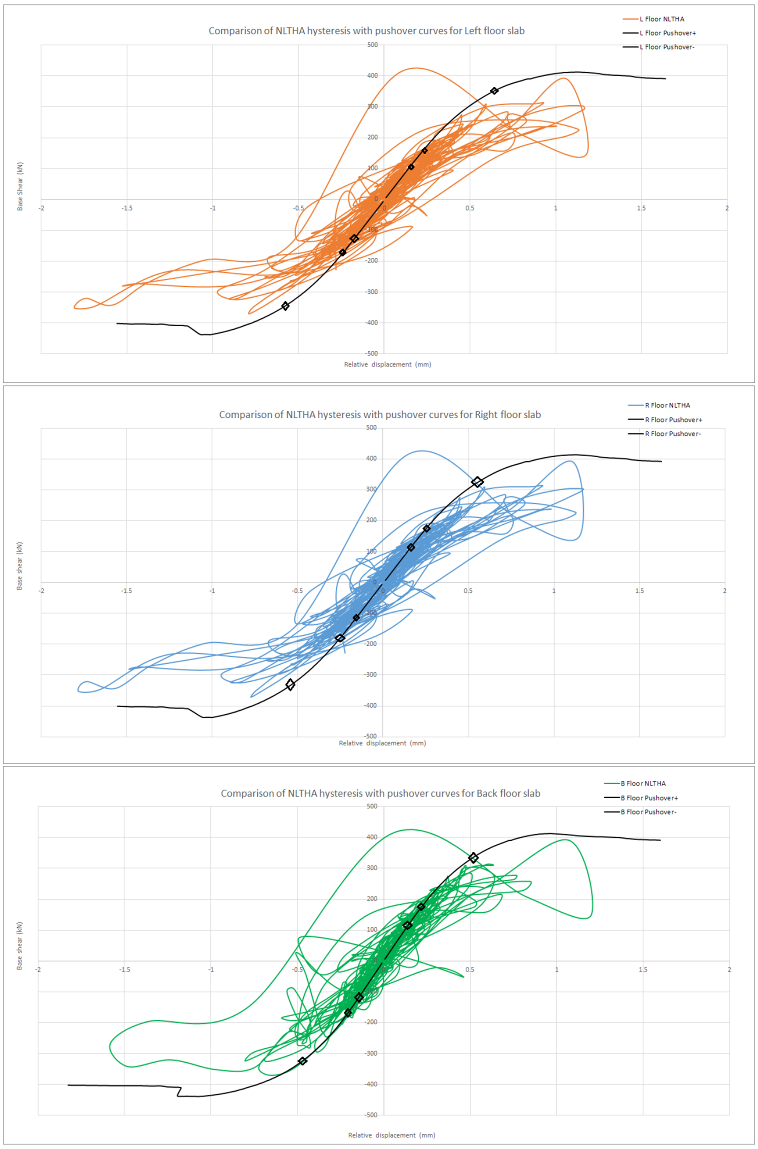

Figure 6-2: Comparison of time-history hysteresis curves ($0.5g$) with pushover curves for X-direction, pinned type beam ends for left, right and back floor repsectively

It can be seen from the above figure 6-2 that the pushover curves envelope the hysteresis curves. The pushover curves also rightly pass through the mean region of the hysteresis curves. The base shear values from the pushover are similar to those obtained from time-history analyses, though not exact. It can also be observed that, in this case, the back floor (green) curve is closely matched to the pushover curve in relation to the base shear and displacement. The markings denote the base shear values (in kN) ±108, ±170 and ±338 corresponding to lateral load of $0.16g$, $0.25g$ and $0.50g$ respectively.

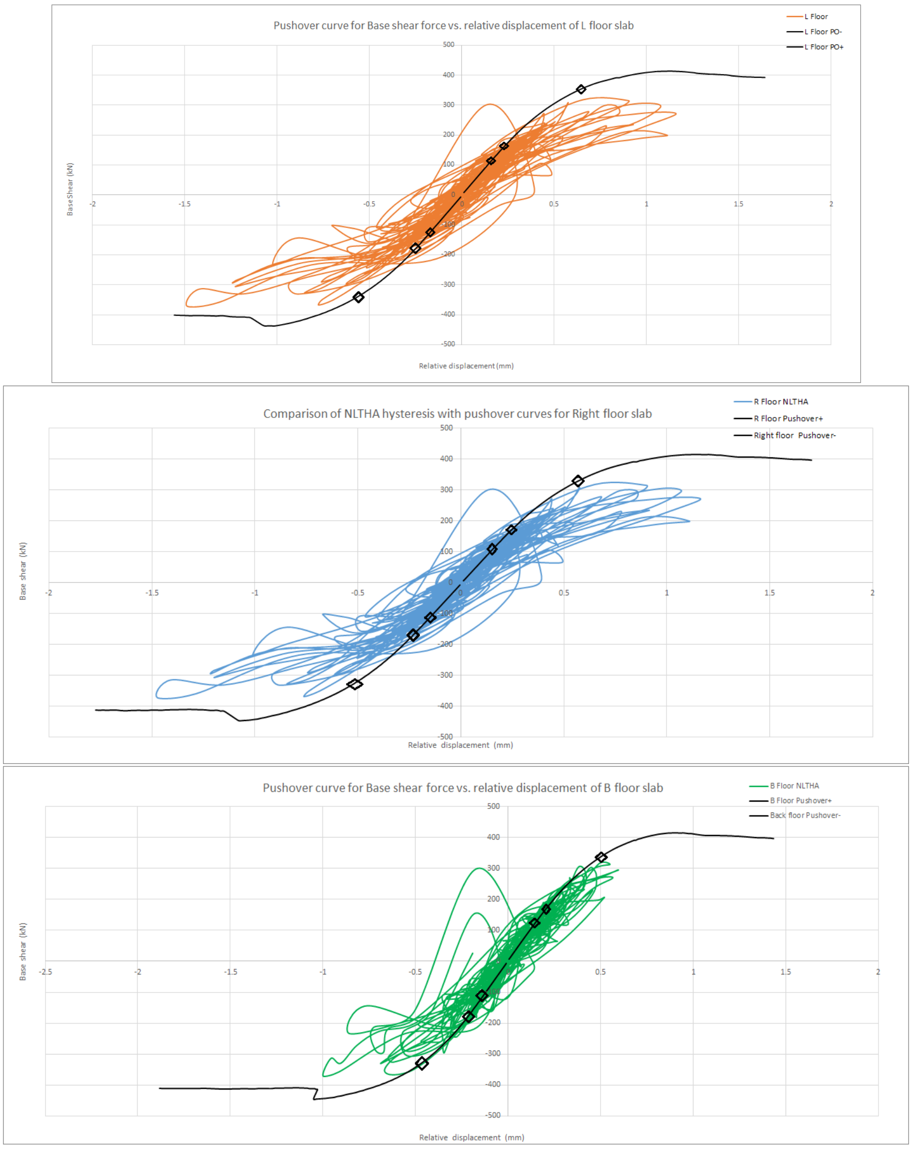

Figure 6-3: Comparison of time-history hysteresis curves ($0.5g$) with pushover curves for X-direction, fixed type beam ends for left, right and back floor repsectively

Referring to the figures 6-2 and 6-3, we can see that the hysteresis curves for the fixed end beam type connection does not vary haphazardly as in the former case. The hysteresis path is close to the pushover curve for all three floor systems. However, for the left floor (orange curve) the base shear does not match exactly, but is still close enough. it is interesting to note that the back floor matches very closely with the pushover curve. Markings denote the base shear values (in kN) ±108, ±175 and ±336.5 corresponding to a lateral load of $0.16g$, $0.25g$ and $0.50g$ respectively.

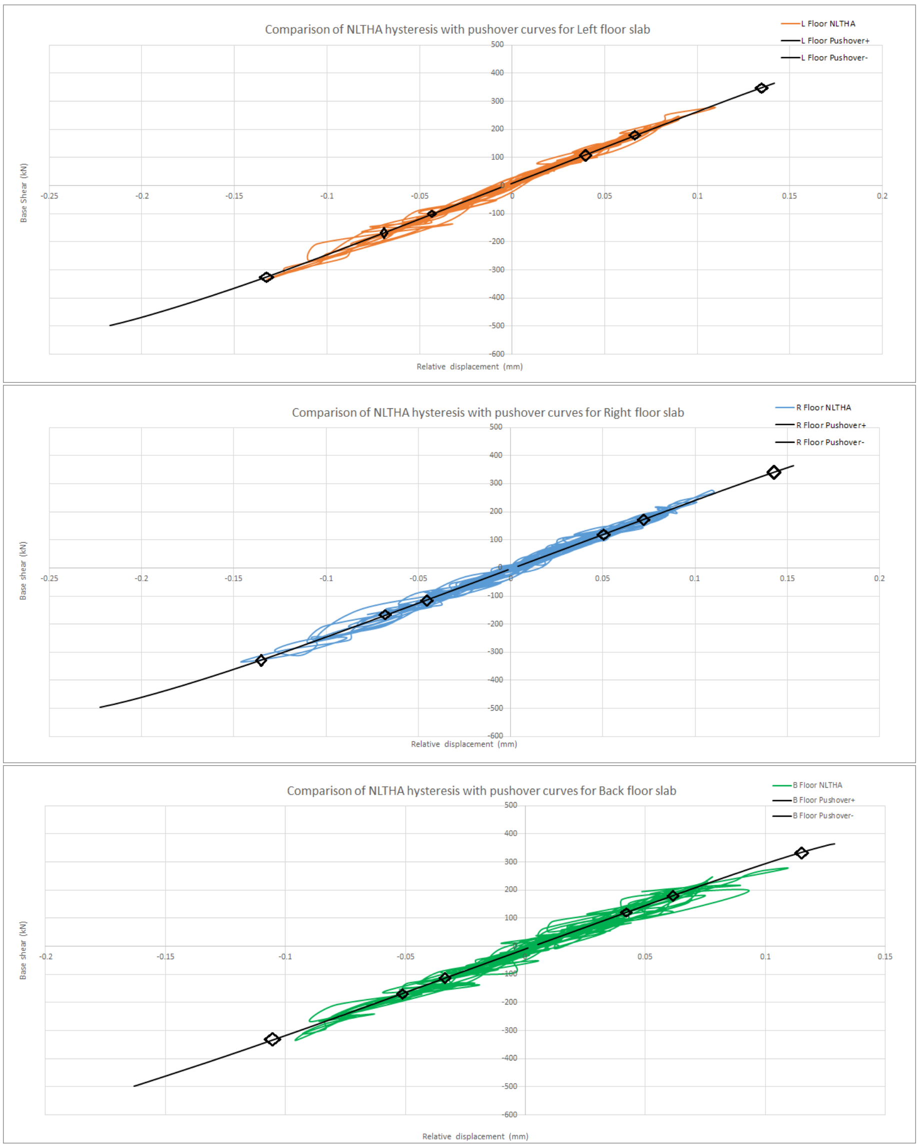

Figure 6-4: Comparison of time-history hysteresis curves ($0.5g$) with pushover curves for Y-direction, pinned type beam ends for left, right and back floor repsectively

Similarly, the pushover analyses was carried out along the Y-direction as well. Firstly for the pinned type beam ends, the pushover curves match closely to the hysteresis curves. It seems to have an almost linear curve. Interestingly, the left floor (orange curve) response is the most closely matched one with the pushover curve. It can also be observed that the other two hysteresis curves show slight deviation on either side of the pushover curves, but still fit well. Another point of interest is that the maximum shear force for the pushover curve in the positive direction is higher compared to hysteresis curves. The markings correspond to the base shear values (in kN) of ±108, ±170 and ±340 at load values of $0.16g$, $0.25g$ and $0.50g$ respectively.

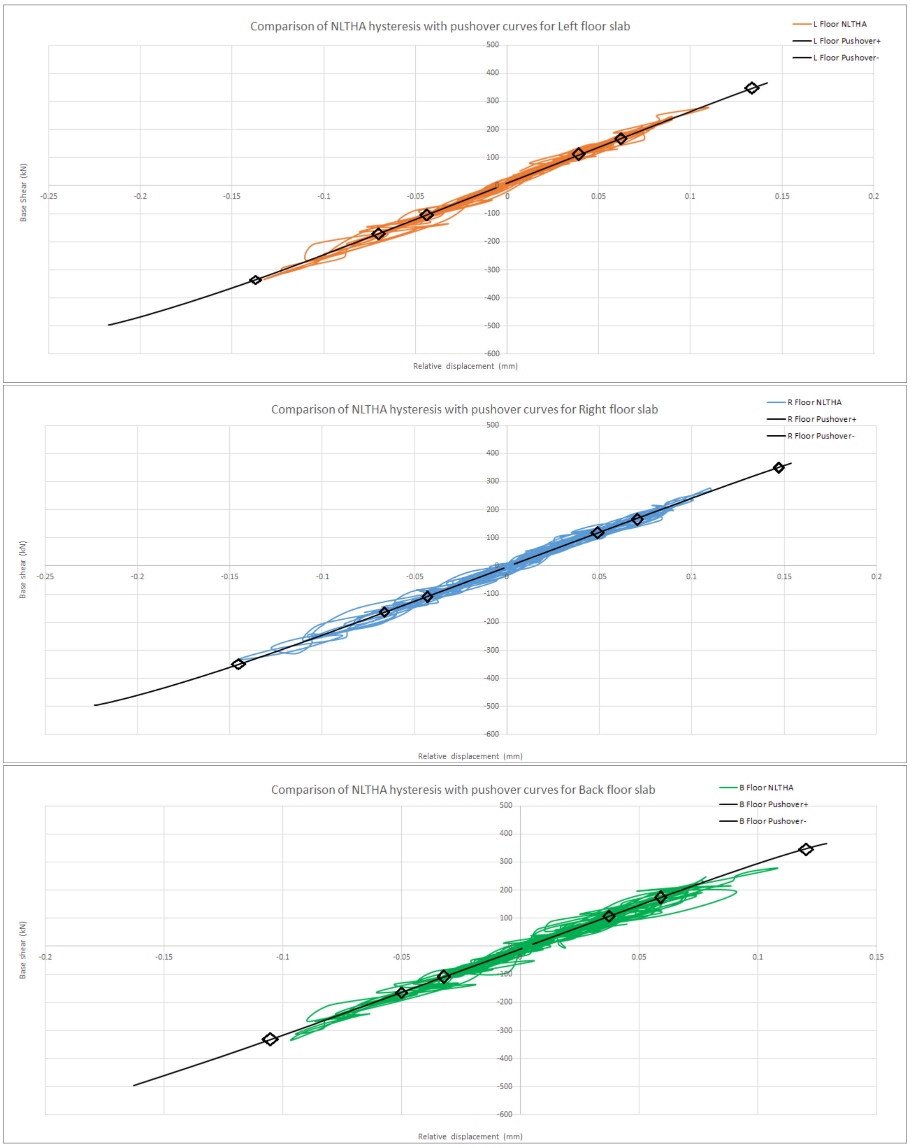

Figure 6-5: Comparison of time-history hysteresis curves $(0.5g)$ with pushover curves for Y-direction, fixed type beam ends for left, right and back floor respectively

As in the previous case, the hysteresis curves from time-history analyses along Y-direction is compared with the pushover curves, but for the fixed end beam type connection. Again, it is evident that the response is almost linear for all the three floor systems. Similar to the previous case, left floor (orange curve) matches best with the pushover curves. Though the other two are also matching well, a slight deviation can be observed. The base shear response from the pushover is slightly higher in the positive direction. The markings correspond to the base shear values (in kN) of ±108, ±169 and ±340 at load values of $0.16g$, $0.25g$ and $0.50g$ respectively.

6-3 Conclusions

By studying and comparing all the analyses, the following inferences are arrived at. They are-

1. The influence of different beam end connections- pinned and fixed has not been significant, owing to non-linearity focused only in masonry and the treatment of all other materials as linear elastic.
2. The inclusion of roof has good influence on the crack strains, principal stress and principal strain values. Referring to tables 6-1 and 6-2, it can be observed that the crack strains, displacements and the base shear response for the model with roof included is more than that for the model without roof.
3. Pushover curves are clearly in agreement with the hysteresis curves from time-history analyses. This proves that, for this model, the hysteresis curves are correct and hence the results valid.
4. It can be observed that the plan of the building is asymmetric. The effect of asymmetry can be seen in the displacement response of the timber floors. Left and right floors have a significant coupling which is also evident from the similar hysteresis curves as well as displacement values. The back floor, however, shows lesser displacement within the time-history regime.
5. The structural behaviour also differs with the direction of excitation. When seismic signal is input along the X-direction, the displacement response is much higher than that in Y-direction.
6. The front left wall (IP1 refer 4-5) undergoes maximum cracking for analyses, both along X-direction and Y-direction.

6-4 Discussion and recommendations for future work

A research project generally makes a few assumptions to guarantee smooth working towards the objectives, however, it is but natural to discover shortcomings through the course of the project. Such points of interests are discussed below. This, in the future, will in turn help to work more efficiently, accurately and improve the quality of research and working on similar such projects. A few recommendations are also provided-

- For a given direction of seismic excitation and scaling level of the signal, beam end types (pinned and fixed) do not show much difference in terms of results. This may be caused due to high stiffness induced by the floor-beam system. It could be improved by using non-linear interface elements to depict reality better.
- Modelling of timber roof and associated components with non-linear properties will help understand the complete systemic functioning of the structure, although this will be more cumbersome, complex and highly time consuming.

- Seismic displacements along X-direction are higher compared to those along Y-direction. This may be due to the alignment of beams along X-direction which provides significant stiffness for the out-of-plane walls when excited along X-direction, and similarly to in-plane walls when excited along Y-direction.
- Comparative studies using other different methods of non-linear analysis to understand and compare the response as well as validating the methodology itself.
- Usage of higher order elements like 8-noded brick element to model masonry, for higher accuracy and clarity.
- Usage of a different modelling approach such as the discrete crack modelling on individual walls or the whole structure to better understand the most vulnerable and damage prone parts of the structure.

Appendix A

Load Calculations

The calculations for static loads that are applied to the structure *T3a* are shown below. These include a total of five different load sets:

1. Self weight of masonry
2. Self weight of beams
3. Self weight of floors
4. Live load on floor slabs
5. Standard dead load on floor slabs

A-1 Material and geometric properties

Firstly, the values for different material properties as provided by ARUP are given -

Density of masonry = $\rho_{masonry}$ = 1900 kg/m^3

Density of timber = ρ_{timber} = 600 kg/m^3

Thickness of walls = t_{walls} = 230 mm = 0.230 m

Thickness of timber floor slabs = $t_{floorslabs}$ = 25 mm = 0.025 m

Cross-sectional area of timber floor beams = $A_{timberbeams}$
= 75 mm * 220 mm = 0.075 m * 0.220 m

Cross-sectional area of timber rafters at roof level = $A_{timberrafters}$
= 38 mm * 100 mm = 0.038 m * 0.100 m

Acceleration due to gravity = g = 9.81 m/s^2

A-2 Floor slabs area

The *T3a* model consists of three timber floor slabs. The area of different floor slabs are given as follows :

1. Left Floor - Length (along Y-axis)= 5.5725 m ; Breadth (along X-axis)= 4.945 m
   Total area = 27.56 m^2
2. Right Floor - Length (along Y-axis)= 6.9475 m ; Breadth (along X-axis)= 4.130 m
   Total area = 28.69 m^2
3. Back Floor - Length (along Y-axis)= 4.825 m ; Breadth (along X-axis)= 4.245 m
   Total area = 20.48 m^2

A-3 Calculation of static loads

A-3-1 Self-weight of masonry

Since 2-D elements are used to model the wall sections, the calculated loads are applied as face pressure on the shell elements.

$$\begin{gathered}\text{Self-weight of masonry walls } = \rho_{masonry} * t_{walls} * g \\ = 1900 * 0.230 * 9.81 = 4287 N/m^2 = 4287 * 10^{-6} N/mm^2\end{gathered} \tag{A-1}$$

A-3-2 Self-weight of timber beams

The timber beams are used at the first floor level below the floor slabs. All the beams lie along X-direction of the structure. Hence, the length of these beams varies relative to their placement in the structure. They are named as Left Beams, Right Beams and Back Beams corresponding to the nomenclature of the floor slabs. Since the floors are supported only along two sides, all the floor slabs are treated as one-way slabs and all the static loads are calculated by converting them to point loads for each end of the beams. The same convention is followed for all the cases such as self-weight of slabs and imposed loads as shown in the following sections A-3-3 and A-3-4.

$$\text{Self-weight of timber beams} = \rho_{timber} * A_{timberbeams} * l_{timberbeams} * g \tag{A-2}$$

$$\begin{gathered}\text{Self-weight of Left Beams} = 600 * (0.075*0.220) * 4.945 * 9.81 = 480.25 N \\ \text{Force applied at each end of the beam} = 240.13 N\end{gathered} \tag{A-3}$$

$$\begin{aligned}\text{Self-weight of Right Beams} &= 600 * (0.075{*}0.220) * 4.130 * 9.81 = 410.10N \\ \text{Force applied at each end of the beam} &= 200.55N\end{aligned} \tag{A-4}$$

$$\begin{aligned}\text{Self-weight of Back Beams} &= 600 * (0.075{*}0.220) * 4.245 * 9.81 = 412.27N \\ \text{Force applied at each end of the beam} &= 206.14N\end{aligned} \tag{A-5}$$

A-3-3 Self-weight of floor slabs

As described in the previous section A-3-2, the self-weight of the floor slabs are distributed to the beam ends as point loads. The number of beams corresponding to different floor slabs is also taken into account and is shown in the calculations below.

$$\begin{aligned}\text{Self-weight of floor slabs} &= \rho_{timber} * A_{leftfloor} * t_{floorslab} * g \\ \text{Force applied at each end of beams} &= \frac{\text{Self-weight of floor slab}}{\text{Number of beams supporting the floor * 2 ends}}\end{aligned} \tag{A-6}$$

$$\begin{aligned}\text{Number of beams under left floor} &= 7 \\ \text{Number of beams under right floor} &= 9 \\ \text{Number of beams under back floor} &= 6\end{aligned} \tag{A-7}$$

$$\begin{aligned}\text{Self-weight of Left Floor} &= 600 * (5.5725{*}4.945) * 0.025 * 9.81 = 4055N \\ \text{Force applied at each end of left beams} &= 289.63N\end{aligned} \tag{A-8}$$

$$\begin{aligned}\text{Self-weight of Right Floor} &= 600 * (6.9475{*}4.130) * 0.025 * 9.81 = 4222N \\ \text{Force applied at each end of right beams} &= 234.57N\end{aligned} \tag{A-9}$$

$$\begin{aligned}\text{Self-weightof Back Floor} &= 600 * (4.8250{*}4.245) * 0.025 * 9.81 = 3014N \\ \text{Force applied at each end of back beams} &= 251.16N\end{aligned} \tag{A-10}$$

A-3-4 Imposed loads on floor slabs

These loads are those prescribed by ARUP on the floor slabs at the first floor level. It is to be noted that there are no imposed loads on the roof of the structure except for standard dead load. The imposed loads are of two types - Live Load (LL) and Standard Dead Load (SDL). The value of the loads are as follows:

$$\begin{aligned}\text{SDL (first floor)} &= 2.5kPa = 2.5kN/m^2 \\ \text{LL (first floor)} &= 1.75kPa = 1.75kN/m^2 \\ \text{SDL (roof)} &= 0.5kPa = 0.5kN/m^2 \\ \text{Total Load Combination} &= \text{Self-weight + SDL + (0.24 * LL)}\end{aligned} \tag{A-11}$$

$$\text{Total imposed loads on floor slabs} = A_{floorslab} * IL_{floorslab} \tag{A-12}$$

$$\begin{aligned}\text{SDL on Left Floor} &= (5.5725{*}4.945) * 2.5 * 10^3 = 68890N\\ \text{Force applied at each end of left beams} &= 4920.72N\\ \text{LL on Left Floor} &= (5.5725{*}4.945) * 0.24 * 1.75 * 10^3 = 11574N\\ \text{Force applied at each end of left beams} &= 826.68N\end{aligned} \tag{A-13}$$

$$\begin{aligned}\text{SDL on Right Floor} &= (6.9475{*}4.130) * 2.5 * 10^3 = 71733N\\ \text{Force applied at each end of right beams} &= 3985.16N\\ \text{LL on Right Floor} &= (6.9475{*}4.130) * 0.24 * 1.75 * 10^3 = 12051N\\ \text{Force applied at each end of right beams} &= 669.51N\end{aligned} \tag{A-14}$$

$$\begin{aligned}\text{SDL on Back Floor} &= (4.8250{*}4.245) * 2.5 * 10^3 = 51205N\\ \text{Force applied at each end of back beams} &= 4267.11N\\ \text{LL on Back Floor} &= (4.8250{*}4.245) * 0.24 * 1.75 * 10^3 = 8602N\\ \text{Force applied at each end of back beams} &= 716.87N\end{aligned} \tag{A-15}$$

Bibliography

[1] M. J. N. Priestley, "Diagonal tension strength of vintage unreinforced clay brick masonry wall panels," *Bull. NEW Zeal. Natl. Soc. Earthq. Eng.*, vol. 18, jun 1985.

[2] K. T. Doherty, *An investigation of the weak links in the seismic load path of unreinforced masonry buildings*. Thesis dissertation, University of Adelaide, 2000.

[3] M. Tomazevic, M. Lutman, and L. Petkovic, "Seismic behaviour of masonry walls: experimental simulation," *J. Struct. Eng.*, 1996.

[4] M. M. AlShebani and S. N. Sinha, "Stress-Strain Characteristics of Brick Masonry under Uniaxial Cyclic Loading," *J. Struct. Eng.*, vol. 125, pp. 600–604, jun 1999.

[5] F. Buccino and E. Vitiello, "Steel anchorages in brick walls: Tests and Design Criteria," in *Pap. No. 195, 11th World Conf. Earthq. Eng.*, 1996.

[6] S. Moreira, D. V. Oliveira, L. F. Ramos, and P. B. Lourenço, "Experimental Study on the Seismic Behavior of SRHSC Columns," in *15 World Conf. Earthq. Eng.*, (Lisboa), C.S. Oliveira, 2012.

[7] T. J. Lin and J. M. LaFave, "Experimental structural behavior of wall-diaphragm connections for older masonry buildings," *Constr. Build. Mater.*, vol. 26, no. 1, pp. 180–189, 2012.

[8] S. Moreira, L. F. Ramos, D. V. Oliveira, and P. B. Lourenço, "Experimental behavior of masonry wall-to-timber elements connections strengthened with injection anchors," tech. rep., ISISE, Department of Civil Engineering, University of Minho, Guimaraes, 2009.

[9] P. B. Lourenço, J. G. Rots, and J. Blaauwendraad, "Two approaches for the analysis of masonry structures: micro and macro-modeling," *HERON*, vol. 40, no. 4, pp. 313–340, 1995.

[10] P. B. Lourenço, R. De Borst, and J. G. Rots, "A plane stress softening plasticity model for orthotropic materials," *Int. J. Numer. Methods Eng.*, vol. 40, no. February 1996, pp. 4033–4057, 1997.

[11] TNO DIANA BV, "DIANA-9.6 User's Manual," 2014.

[12] R. Y. Itani and C. K. Cheung, "Nonlinear Analysis of Sheathed Wood Diaphragms," *J. Struct. Eng.*, vol. 110, pp. 2137–2147, sep 1984.

[13] Y. H. Chui, C. Ni, and L. Jiang, "Finite-Element Model for Nailed Wood Joints under Reversed Cyclic Load," *J. Struct. Eng.*, vol. 124, pp. 96–103, jan 1998.

[14] D. F. Peralta, J. M. Bracci, and M. B. D. Hueste, "Seismic Behavior of Wood Diaphragms in Pre-1950s Unreinforced Masonry Buildings," *J. Struct. Eng.*, vol. 130, pp. 2040–2050, dec 2004.

[15] D. F. Peralta, J. M. Bracci, and M. B. D. Hueste, "Seismic Performance of Rehabilitated Wood Diaphragms," tech. rep., Department of Civil Engineering, Texas A&M University, Texas, 2003.

[16] A. W. Wilson, *Seismic Assessment of Timber Floor Diaphragms in URM Buildings*. Ph.d, University of Auckland, New Zealand, 2012.

[17] A. Holligan, "Groningen gas fields - the Dutch earthquake zone - BBC News," 2013.

[18] T. de Crook, H. W. Haak, B. Dost, and D. T. Crook, "Seismisch risico in Noord-Nederland," tech. rep., KNMI, De Bilt, 1998.

[19] H. R. A. Koster and J. van Ommeren, "Natural Gas Extraction , Earthquakes and House Prices," in *Tinbergen Inst. Discuss. Pap.*, TI 2015, (Amsterdam), Tinbergen Institute, 2015.

[20] KNMI, "Increase in number of quakes," tech. rep., Koninklijk Nederlands Meteorologisch Instituut, 2013.

[21] A. Anthoine, "IN-PLANE BEHAVIOUR OF MASONRY: A LITERATURE REVIEW," tech. rep., European Commission, 1992.

[22] N. W. Kelch, "METHODS USED IN TESTING MASONRY SPECIMENS FOR BENDING, TENSION, AND SHEAR1," *J. Am. Ceram. Soc.*, vol. 14, pp. 125–132, feb 1931.

[23] S. R. Christy, Freeda C; Tensing; Mercy, "In-plane shear behaviour of Brick Masonry-A Literature Review on experimental study.," *Int. J. Civ. Struct. Eng.*, vol. 2, no. 4, pp. 1144–1152, 2012.

[24] D. P. Abrams and N. Shah, "Cyclic Load Testing of Unreinforced Masonry Walls," tech. rep., University of Illinois at Urbana-Champaign, 1992.

[25] M. Corradi, A. Borri, and A. Vignoli, "Experimental study on the determination of strength of masonry walls," *Constr. Build. Mater.*, vol. 17, pp. 325–337, jul 2003.

[26] C. Anderson, "Arching action in transverse laterally loaded masonry wall," *Struct. Eng.*, vol. 62, no. 1, pp. 12–23, 1984.

[27] T. Paulay and M. Priestley, *Seismic design of reinforced concrete and masonry buildings*. John Wiley and Sons, 1992.

[28] R. Brincker, "Yield-Line Theory and Material Properties of Laterally Loaded Masonry Walls," *Mason. Int.*, no. 1, 1984.

[29] C. S. Meisl, K. J. Elwood, and C. E. Ventura, "Shake table tests on the out-of-plane response of unreinforced masonry walls," *Can. J. Civ. Eng.*, vol. 34, no. 11, pp. 1381–1392, 2007.

[30] H. Derakhshan, M. C. Griffith, and J. M. Ingham, "Out-of-Plane Behavior of One-Way Spanning Unreinforced Masonry Walls," *J. Eng. Mech.*, vol. 139, pp. 409–417, apr 2013.

[31] D. Benedetti and A. Castellani, "Dynamic versus static behaviour of a masonry structure under lateral loads," *Eng. Struct.*, vol. 2, no. 3, pp. 163–170, 1980.

[32] M. Tomaževič, "Dynamic modelling of masonry buildings: Storey mechanism model as a simple alternative," *Earthq. Eng. Struct. Dyn.*, vol. 15, pp. 731–749, aug 1987.

[33] M. C. Griffith, J. Vaculik, N. T. K. Lam, J. Wilson, and E. Lumantarna, "Cyclic testing of unreinforced masonry walls in two-way bending," *Earthq. Eng. Struct. Dyn.*, vol. 36, pp. 801–821, may 2007.

[34] H. Derakhshan, M. C. Griffith, and J. M. Ingham, "Airbag testing of multi-leaf unreinforced masonry walls subjected to one-way bending," *Eng. Struct.*, 2013.

[35] D. P. Abrams, "RESPONSE OF UNREINFORCED MASONRY BUILDINGS," *J. Earthq. Eng.*, vol. 1, pp. 257–273, jan 1997.

[36] J. Paquette and M. Bruneau, "Pseudo-Dynamic Testing of Unreinforced Masonry Building with Flexible Diaphragm," *J. Struct. Eng.*, vol. 129, pp. 708–716, jun 2003.

[37] S. A. Mahin and P. S. B. Shing, "Pseudodynamic Method for Seismic Testing," *J. Struct. Eng.*, vol. 111, pp. 1482–1503, jul 1985.

[38] A. S. ELNASHAI, "Do We Really Need Inelastic Dynamic Analysis?," *J. Earthq. Eng.*, vol. 6, no. sup001, pp. 123–130, 2002.

[39] A. K. Chopra and R. K. Goel, "A Modal Pushover Analysis Procedure to Estimate Seismic Demands for Buildings : Theory and Preliminary Evaluation," *Earthquake*, vol. PEER Repor, pp. 561–582, 2001.

[40] M. P. Singh and M. Ghafory-Ashtiany, "Modal time history analysis of non-classically damped structures for seismic motions," *Earthq. Eng. Struct. Dyn.*, vol. 14, pp. 133–146, jan 1986.

[41] E. Salajegheh and A. Heidari, "Time history dynamic analysis of structures using filter banks and wavelet transforms," *Comput. Struct.*, vol. 83, pp. 53–68, jan 2005.

[42] N. T. K. Lam, M. Griffith, J. Wilson, and K. Doherty, “Time-history analysis of URM walls in out-of-plane flexure,” *Eng. Struct.*, vol. 25, no. 6, pp. 743–754, 2003.

[43] J. G. Rots, “Numerical Simulation of Cracking in Structural Masonry,” *HERON*, vol. 36, no. 2, pp. 49–63, 1991.

[44] P. B. Lourenço, *Computational strategies for masonry structures*. PhD thesis, Delft University of Technology, Delft, 1996.

[45] P. Lourenço, “An anisotropic macro-model for masonry plates and shells: implementation and validation,” *TU-DELFT Rep. no. 03.21.1.31.07*, no. 03, p. 102, 1997.

[46] P. B. Lourenço, “Anisotropic Softening Model for Masonry Plates and Shells,” *J. Struct. Eng.*, vol. 126, pp. 1008–1016, sep 2000.

[47] E. N. Dvorkin and K.-J. Bathe, “A continuum mechanics based four-node shell element for general non-linear analysis,” *Eng. Comput.*, vol. 1, pp. 77–88, jan 1984.

[48] D. P. Abrams, “Strength and behavior of unreinforced masonry elements,” in *10th World Conf. Earthq. Eng.*, pp. 3475–3480, 1992.

[49] L. GAMBAROTTA and S. LAGOMARSINO, “DAMAGE MODELS FOR THE SEISMIC RESPONSE OF BRICK MASONRY SHEAR WALLS. PART II: THE CONTINUUM MODEL AND ITS APPLICATIONS,” *Earthq. Eng. Struct. Dyn.*, vol. 26, pp. 441–462, apr 1997.

[50] P. Pegon and A. Anthoine, “Numerical strategies for solving continuum damage problems with softening: Application to the homogenization of Masonry,” *Comput. Struct.*, vol. 64, pp. 623–642, jul 1997.

[51] G. Milani, P. Lourenço, and A. Tralli, “Homogenised limit analysis of masonry walls, Part I: Failure surfaces,” *Comput. Struct.*, vol. 84, pp. 166–180, jan 2006.

[52] G. Milani, P. Lourenço, and A. Tralli, “Homogenised limit analysis of masonry walls, Part II: Structural examples,” *Comput. Struct.*, vol. 84, pp. 181–195, jan 2006.

[53] M. C. Griffith, J. Vaculik, N. T. K. Lam, J. Wilson, and E. Lumantarna, “Cyclic testing of unreinforced masonry walls in two-way bending,” *Earthq. Eng. Struct. Dyn.*, vol. 36, pp. 801–821, may 2007.

[54] M. Patton-Mallory, S. M. Cramer, F. W. Smith, and P. J. Pellicane, “Nonlinear Material Models for Analysis of Bolted Wood Connections,” *J. Struct. Eng.*, vol. 123, no. 8, pp. 1063–1070, 1997.

[55] J. Anderson, V. Bertero, M. Kargahi, and M. Al Satari, “Seismic Performance of an Instrumented Tilt-up Wall Building,” Tech. Rep. July, Pacific Earthquake Engineering Research Center, College of Engineering, University of California, Berkeley, 2004.

[56] T. Yi, *Experimental Investigation and Numerical Simulation of an Unreinforced Masonry Structure with Flexible Diaphragms*. Ph.d, Georgia Institute of Technology, apr 2004.